

Charles University in Prague
Faculty of Mathematics and Physics

DOCTORAL THESIS



Denis Gorbunov

Magnetic and magnetoelastic properties of $f-d$ intermetallics with high content of $3d$ -metal

Institute of Physics, Academy of Sciences of the Czech Republic

Supervisor: Prof. Alexander Andreev, DrSc.

Study program: Physics

Specialization: Physics of Condensed Matter and Materials

Prague 2014

Acknowledgements

During my post-graduate study at the Institute of Physics of the Czech Academy of Sciences and at the Charles University I have been assisted by many people. First and foremost, I express my deepest gratitude to my supervisor Prof. Alexander Andreev, DrSc. for his great efforts in educating me. Thanks to his continual attention, constant guidance, infinite patience, constructive criticism and clear explanations I could grow as a scientist, gain new research skills and advance progressively in the understanding of a number of modern scientific topics.

My special thanks go to the staff of the Joint Laboratory for Magnetic Studies, Ing. Josef Šebek, CSc., Ing. Eva Šantavá, CSc., Ing. Martin Žáček and RNDr. Jan Prokleška, Ph.D. for teaching me to utilize the laboratory equipment and for helping with data collection. I am grateful to RNDr. Zdeněk Arnold, CSc. for his assistance in magnetization measurements under pressure.

I highly appreciate the contribution made by our colleagues from the Faculty of Mathematics and Physics of the Charles University: by Prof. RNDr. Vladimír Sechovský, DrSc. and RNDr. Pavel Javorský, Ph.D. for their support and encouragement; by doc. RNDr. Ladislav Havela, CSc. for his fruitful discussions; doc. RNDr. Stanislav Daniš, Ph.D. and RNDr. Jiří Pospíšil, Ph.D. for their assistance in the laboratory.

I am indebted to Prof. Nikolai Mushnikov, DrSc. and Eugene Rosenfeld, Ph.D. from the Institute of Metal Physics in Ekaterinburg, Russia, for their invaluable consultations about magnetism of $3d-4f$ intermetallic compounds.

I would like to express my gratitude to our colleagues from the High Magnetic Field Laboratory in Dresden, Germany: to Dr. Yurii Skourski, Ph.D., Dr. Shadi Yasin, Ph.D. and Dr. Sergei Zherlitsyn, Ph.D. for their assistance in magnetization and sound propagation measurements in static and pulsed magnetic fields; to Prof. Dr. Joachim Wosnitza for his help in the presentation of results.

I gratefully acknowledge Charles University (grants GAUK-703912, SVV-2012-265303, SVV-2013-267303 and SVV-2014-260091), the Czech Science Foundation (grant P204/12/0150), the Czech Academy of Sciences (project M10010203), the Program of Czech Research Infrastructures (project LM2011025), the EuroMag-NET program under EU Contract No. 228043 and the support of HLD at HZDR, a member of the European Magnetic Field Laboratory (EMFL).

Last but not least, I wish to thank my family and friends for their love and support throughout the whole post-graduate study.

I declare that I carried out this doctoral thesis independently, and only with the cited sources, literature and other professional sources.

I understand that my work relates to the rights and obligations under the Act No. 121/2000 Coll., the Copyright Act, as amended, in particular the fact that the Charles University in Prague has the right to conclude a license agreement on the use of this work as a school work pursuant to Section 60 paragraph 1 of the Copyright Act.

In..... date.....

signature

Název práce: Magnetické a magnetoelastické vlastnosti $f-d$ intermetalik s vysokým obsahem 3d-kovu

Autor: Denis Gorbunov

Katedra/Ústav: Matematicko-fyzikální fakulta, Univerzita Karlova a Oddělení magnetických nanosystémů, Fyzikální ústav, Akademie Věd České Republiky

Vedoucí dizertační práce: Prof. Alexander Andreev, DrSc., Oddělení magnetických nanosystémů, Fyzikální ústav, Praha, Česká republika

Abstrakt: práce zkoumá fundamentální magnetické vlastnosti sloučenin RFe_xAl_{12-x} (R – prvek těžkých vzácných zemin) s tetragonální krystalickou strukturou typu $ThMn_{12}$. Studium $LuFe_xAl_{12-x}$ s nemagnetickým Lu ukázalo, že výměnné interakce a magnetokrystalická anizotropie se v oblasti homogenity, pro $4 \leq x \leq 6$, významně mění. Při zvýšení obsahu Fe antiferromagnetické výměnné interakce zeslabují a naopak ferromagnetické zesilují. Změna výměnných interakcí probíhá v okolí $x = 5$. Podmřížka Fe vykazuje anizotropii typu snadná rovina, anizotropie při zvýšení obsahu Fe slábne. Sloučeniny RFe_5Al_7 s magnetickými R jsou silně anizotropní ferrimagnety s Curieovými teplotami mezi 193 a 262 K. Měření magnetizace a šíření zvuku byly v RFe_5Al_7 odhaleny spontánní a polem vyvolané magnetické fázové přechody anizotropní a výměnné podstaty. Přechody poskytují kvantitativní informace o výměnné interakci mezi podmřížkami. Byla určena korelace mezi prvkem R a fundamentálními magnetickými vlastnostmi RFe_5Al_7 . Magnetický moment Fe je $8 \mu_B$ na buňku. Sloučeniny s Tb, Dy, Ho a Er vykazují kompenzaci magnetizací podmřížek vzácné zeminy a železa. Kompenzační teplota a Curieova teplota jsou úměrné výměnné interakci mezi podmřížkami R a Fe.

Klíčová slova: intermetalika vzácných zemin, výměnné interakce, magnetická anizotropie, polem vyvolané přechody, silná magnetická pole.

Title: Magnetic and magnetoelastic properties of *f-d* intermetallics with high content of 3*d*-metal

Author: Denis Gorbunov

Department/Institute: Faculty of Mathematics and Physics, Charles University and Department of Magnetic Nanosystems, Institute of Physics, Academy of Sciences of the Czech Republic

Supervisor of the doctoral thesis: Prof. Alexander Andreev, DrSc., Department of Magnetic Nanosystems, Institute of Physics, Prague, the Czech Republic

Abstract: Fundamental magnetic properties have been studied in $R\text{Fe}_x\text{Al}_{12-x}$ (R – heavy rare-earth element) compounds with the tetragonal crystal structure of the ThMn_{12} type. In the homogeneity range $4 \leq x \leq 6$, exchange interactions and magnetocrystalline anisotropy of the Fe sublattice are significantly modified as found in $\text{LuFe}_x\text{Al}_{12-x}$ with non-magnetic Lu. With increasing Fe content, antiferromagnetic exchange interactions weaken and ferromagnetic strengthen. The change of the type of magnetic ordering occurs in the vicinity of $x = 5$. The Fe sublattice displays an easy-plane magnetic anisotropy that weakens with growing Fe concentration. $R\text{Fe}_5\text{Al}_7$ compounds with magnetic R are highly anisotropic ferrimagnets with Curie temperatures from 193 to 262 K. Spontaneous and field-induced magnetic phase transitions of anisotropic and exchange nature have been found in $R\text{Fe}_5\text{Al}_7$ by measurements of magnetization and sound propagation. The transitions provide quantitative information on the R -Fe inter-sublattice exchange. A correlation between the R element and the fundamental magnetic properties has been found for $R\text{Fe}_5\text{Al}_7$. The Fe magnetic moment is near $8 \mu_B$ per formula unit. The compounds with R – Tb, Dy, Ho and Er have a compensation of the rare-earth and iron sublattice magnetizations. The compensation point and Curie temperature are proportional to the R -Fe inter-sublattice exchange.

Keywords: rare-earth intermetallics, exchange interactions, magnetic anisotropy, field-induced transitions, high magnetic fields.

Contents

Preface.....	8
Chapter 1: General theory	10
1.1. Localized vs. itinerant magnetism	10
1.1.1. Localized magnetism of rare-earth metals	10
1.1.2. Itinerant magnetism of transition metals.....	12
1.2. Exchange interactions	14
1.2.1. Origin of exchange.....	14
1.2.2. Types of exchange.....	16
1.3. Magnetocrystalline anisotropy	18
1.3.1. Crystal-field induced anisotropy	18
1.3.2. Spontaneous spin-reorientation transitions	21
1.4. Field-induced magnetic phase transitions	22
1.4.1. Transitions of exchange nature	23
1.4.2. Transitions of anisotropic nature.....	24
1.5. Magnetoelasticity	25
1.5.1. Sound propagation in magnetically ordered environment	25
1.5.2. Effects of external pressure on magnetic properties	26
Chapter 2: $R(\text{Fe,Al})_{12}$ compounds: state of the art.....	28
2.1. Crystal structure	28
2.2. Exchange interactions and magnetic order	29
2.3. Magnetic anisotropy and hysteresis properties	33
Chapter 3: Experimental methods.....	37
3.1. Sample preparation.....	37
3.2. Sample characterization	37
3.2.1. X-ray powder diffraction.....	37
3.2.2. Single crystal orientation by Laue back reflection of X-rays	38
3.3. Magnetization measurements.....	40
3.3.1. Static magnetic fields	40
3.3.2. Pulsed magnetic fields.....	42
3.4. Magnetization measurements under pressure	43
3.5. Ultrasound experiments	44
3.6. Heat capacity measurements	45
Chapter 4: Evolution of magnetism in $\text{LuFe}_x\text{Al}_{12-x}$ compounds ($4 \leq x \leq 6$).....	48
4.1. Lattice parameters	48
4.2. Exchange interactions	49
4.2.1. LuFe_4Al_8	50

4.2.2. LuFe _{4.5} Al _{7.5}	53
4.2.3. LuFe ₅ Al ₇	56
4.2.4. LuFe _{5.5} Al _{6.5}	59
4.2.5. LuFe ₆ Al ₆	61
4.3. Magnetic anisotropy.....	64
4.4. Conclusions.....	67
Chapter 5: Magnetic properties of RFe ₅ Al ₇ (R - Gd, Tb, Dy, Ho, Er and Tm) compounds.....	68
5.1. Lattice parameters.....	68
5.2. GdFe ₅ Al ₇	69
5.3. DyFe ₅ Al ₇	74
5.4. TbFe ₅ Al ₇	94
5.5. HoFe ₅ Al ₇	115
5.6. ErFe ₅ Al ₇	134
5.7. TmFe ₅ Al ₇	155
5.8. Summary.....	169
5.9. Conclusions.....	172
References.....	174

Preface

Intermetallic compounds based on rare-earth R and $3d$ transition elements T form a wide group of materials. The rare-earth magnetic moment whose carriers are the $4f$ electrons is localized as the $4f$ electronic shell is considerably screened by the higher shells. The magnetism of the $3d$ metals is itinerant since the $3d$ electrons form conduction bands. The different nature of the $3d$ and $4f$ electronic states results in different magnetic properties provided by the two magnetic sublattices. The rare-earth sublattice combines high magnetic moments and strong magnetocrystalline anisotropy but has low magnetic ordering temperature. The transition metal sublattice is much less anisotropic but provides much higher magnetic ordering temperature. The combination of the $3d$ and $4f$ elements in the same compound makes it possible to obtain high magnetic properties. Extensive magnetic studies of the $3d$ - $4f$ intermetallic compounds led to the discovery of magnetically hard materials, the most prominent being SmCo_5 [1] and $\text{Nd}_2\text{Fe}_{14}\text{B}$ [2], that found vast practical applications [3,4].

At present, due to the wide range of intermetallics and their different stoichiometries and variable rare-earth and transition elements, a huge number of R - T compounds are known, binary and ternary (where a third element most often partly substitutes the T element) [5-7]. It allows a systematic study of each group of compounds in order to investigate complex interactions that involve the $3d$ and $4f$ electrons. The magnetic properties of the $3d$ - $4f$ intermetallic compounds can be described in terms of exchange interactions and magnetocrystalline anisotropy [6] which have been the subject of numerous studies of magnetically ordered R - T intermetallics for the last several decades [5-7].

The present work is focused on the fundamental magnetic properties of ternary R -Fe-Al intermetallic compounds crystallizing in the tetragonal crystal structure of the ThMn_{12} type. The possibility to vary the type of the rare-earth element and the relative content of iron and aluminium allows a systematic study of their exchange interactions and magnetocrystalline anisotropy. Thus, the role of the rare-earth and iron sublattices can be determined in the formation of the fundamental magnetic properties of the $R(\text{Fe},\text{Al})_{12}$ compounds.

The present work is divided into two parts. In the first part, the exchange interactions and magnetocrystalline anisotropy of the Fe sublattice are studied in the whole homogeneity range $4 \leq x \leq 6$ of the $\text{LuFe}_x\text{Al}_{12-x}$ compounds with rare-earth element Lu that carries no ordered magnetic moment. The type of the Fe-Fe exchange interactions is extremely sensitive to the Fe concentration. In the systems with the lowest Fe content, RFe_4Al_8 , the Fe sublattice displays antiferromagnetic order [8-13]. With an increase in x the Fe-Fe exchange interactions tend to ferromagnetic. The Fe sublattice exhibits ferromagnetic order in RFe_6Al_6 systems [14,15]. Since the Fe-Fe exchange interactions are antiferromagnetic in RFe_4Al_8 and ferromagnetic in RFe_6Al_6 , it is reasonable to assume that in RFe_5Al_7 compounds with an intermediate iron content the Fe sublattice displays a transitional magnetic

structure. As regards the magnetic anisotropy, the Fe magnetic moments are confined to the basal plane of the tetragonal lattice [14-18]. However, no quantitative information is available. These data can be obtained on single crystals that are indispensable for magnetic anisotropy investigations. This work is the first systematic study of the exchange interactions and magnetocrystalline anisotropy of the Fe sublattice in the whole homogeneity range of the $R(\text{Fe,Al})_{12}$ intermetallic compounds performed on single crystals.

The second part of the work is devoted to a study of the fundamental magnetic properties of ferrimagnetic $R\text{Fe}_5\text{Al}_7$ compounds with variable magnetic heavy rare-earth components $R = \text{Gd, Tb, Dy, Ho, Er}$ and Tm . Their presence results in the formation of the inter-sublattice $3d-4f$ exchange interactions and strong magnetocrystalline anisotropy. Every rare-earth element should significantly modify the system's energy balance, and different ground states and magnetic properties can be expected. Polycrystalline samples of the $R\text{Fe}_5\text{Al}_7$ compounds display strong magnetic and thermal hysteresis, which suggests strong magnetocrystalline anisotropy [19,20]. Again, the crucial role of single crystals for detailed magnetic studies cannot be overestimated. The magnetocrystalline anisotropy of $R\text{Fe}_5\text{Al}_7$ is determined by the competition between the rare-earth and iron sublattices. Thus, spontaneous spin-reorientation transitions can be expected if the two sublattices give contributions of opposite signs. Furthermore, field-induced transitions should occur as the R and Fe magnetic moments rotate in a magnetic field from the initial ferrimagnetic structure towards the forced ferromagnetic state. Phase transitions can be studied in great detail by existing powerful experimental techniques that involve, first and foremost, high (pulsed) magnetic fields. They not only provide access to new beautiful physics but also make it possible to extract fundamental parameters that determine the system's behavior as a function of temperature and magnetic field. Additional information on the phase transitions can be obtained by measuring physical properties affected by the presence of ordered magnetic moments. In particular, sound propagation turns out to be very sensitive to changes in the magnetically ordered state. Therefore, magnetism and magnetoelasticity of the $R\text{Fe}_5\text{Al}_7$ compounds were investigated in the present work.

Chapter 1: General theory

1.1. Localized vs. itinerant magnetism

1.1.1. Localized magnetism of rare-earth metals

In the periodic table the group of rare-earth metals R includes elements from 57 to 71. In this row the $4f$ orbital is progressively filled from La, having the outer electronic configuration $4f^0 5d^1 6s^2$, to Lu whose structure is $4f^{14} 5d^1 6s^2$. The element Y is also regarded as a representative of the rare-earth metals due to its similar outer electronic configuration $4d^1 5s^2$. With increasing atomic number a lanthanide contraction is observed across the $4f$ series – a quasi-linear decrease in the atomic volume of the rare-earth metals as the nuclear charge increases (Fig. 1.1). Elements Eu and Yb display irregular behavior owing to their divalency, in contrast to the other lanthanides that are trivalent [21].

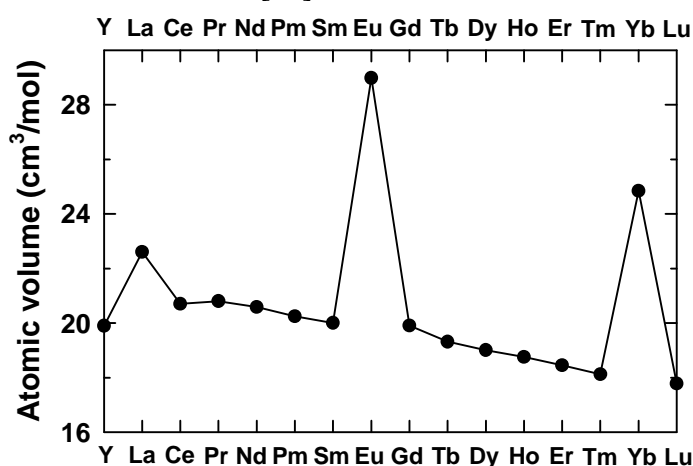


Figure 1.1. Atomic volumes of rare-earth elements [21].

The radius of the $4f$ orbital does not exceed 0.6 \AA . It is considerably screened by the electrons of the higher shells (Fig. 1.2). The rare-earth magnetic moment whose carriers are the $4f$ electrons is localized.

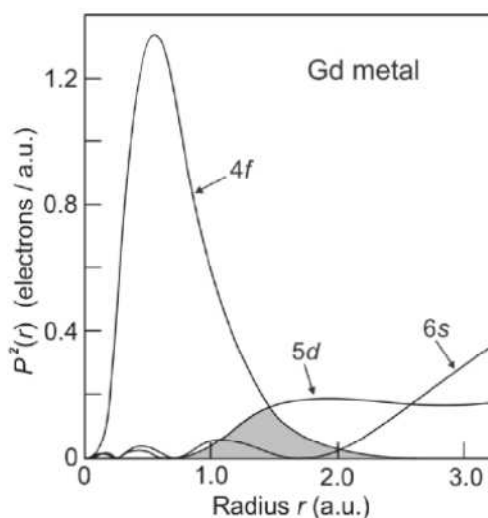


Figure 1.2. Radial charge density for Gd metal ($4f^7 5d^1 6s^2$) [22].

The total Hamiltonian of a rare-earth atom can be written in the following way [21]:

$$H_{\text{tot}} = H_{\text{Coul}} + H_{\text{exch}} + H_{\text{cf}} + H_{\text{ms}} + H_{\text{Z}}, \quad (1.1)$$

where H_{Coul} represents the Coulomb interaction, H_{exch} the exchange interaction, H_{cf} crystalline electric field energy of the $4f$ electrons, H_{ms} magnetoelastic contribution and H_{Z} the Zeeman energy in an applied magnetic field. The terms are written in order of decreasing strength. However, the relative importance of some terms varies due to the spin-orbit coupling.

Orbital and spin motions of electrons as well as the interaction between them hold the key for the atomic origin of magnetism. The Russell-Saunders coupling scheme assumes that the spin-orbit interaction is a weak perturbation to the electrostatic interactions that control the orbital $\mathbf{L} = \sum_i \mathbf{l}_i$ and spin $\mathbf{S} = \sum_i \mathbf{s}_i$ angular momenta to be determined by the summation that extends over all electrons in a given atom. Then the spin-orbit interaction is applied as a weak perturbation to find the total angular momentum $\mathbf{J} = \mathbf{L} + \mathbf{S}$. J can assume values that range from $(L - S)$, $(L - S + 1)$ to $(L + S - 1)$, $(L + S)$. The level lowest in energy is the ground-state level in the multiplet. The ground state can be found by applying Hund's rules. The application of Hund's rules leads to the ground states listed in Table 1.1.

Table 1.1. Ionic properties of the rare-earth elements.

Ion	$4f^n$ n	L	S	J	g_J	$g_J J$	$g_J \sqrt{J(J+1)}$
La ³⁺	0	0	0	–	–	0	0
Ce ³⁺	1	3	1/2	5/2	6/7	2.14	2.54
Pr ³⁺	2	5	1	4	4/5	3.20	3.58
Nd ³⁺	3	6	3/2	9/2	8/11	3.28	3.62
Pm ³⁺	4	6	2	4	3/5	2.40	2.68
Sm ³⁺	5	5	5/2	5/2	2/7	0.72	0.84
Eu ³⁺	6	3	3	0	0	0	0
Gd ³⁺	7	0	7/2	7/2	2	7	7.94
Tb ³⁺	8	3	3	6	3/2	9	9.72
Dy ³⁺	9	5	5/2	15/2	4/3	10	10.63
Ho ³⁺	10	6	2	8	5/4	10	10.60
Er ³⁺	11	6	3/2	15/2	6/5	9	9.59
Tm ³⁺	12	5	1	6	7/6	7	7.57
Yb ³⁺	13	3	1/2	7/2	8/7	4	4.54
Lu ³⁺	14	0	0	–	–	0	0

The magnetic moment $g_J J$ of a free R^{3+} atom and the corresponding effective magnetic moment $g_J \sqrt{J(J+1)}$ can be determined using the Landé factor:

$$g_J = 1 + \frac{J(J+1)+S(S+1)-L(L+1)}{2J(J+1)}. \quad (1.2)$$

There is very good agreement between the $g_J \mu_B \sqrt{J(J+1)}$ values and the effective rare-earth magnetic moment μ_{eff} found experimentally. The μ_{eff} values can be determined from the Curie-Weiss law, according to which in the paramagnetic temperature range the magnetic susceptibility χ is inversely proportional to temperature:

$$\chi = \frac{C}{T - \theta_p}, \quad (1.3)$$

where θ_p is the paramagnetic Curie temperature and C the Curie constant:

$$C = \frac{Ng_J^2 \mu_B^2 J(J+1)}{3k_B T} = \frac{\mu_{\text{eff}}^2}{3k_B T}. \quad (1.4)$$

A discrepancy between $g_J \sqrt{J(J+1)}$ and μ_{eff} does occur for Sm and Eu due to their low-lying excited states that are also significantly populated and shift the $g_J \sqrt{J(J+1)}$ value [23,24].

1.1.2. Itinerant magnetism of transition metals

Transition metals T are characterized by incompletely filled d shell. These are the elements located in the d block of the periodic table: $3d$ (from Sc to Cu), $4d$ (from Y to Ag) and $5d$ metals (from La to Au). The d electrons which are responsible for the magnetism form conduction bands (typically 5 eV for late $3d$ transition metals [3]) in conjunction with the s electrons from the outermost shell. For this reason, the magnetism of the transition metals is itinerant, in contrast to the localized magnetism of the rare-earth metals. The description below is focused on the $3d$ transition elements being the most relevant in the present work.

The magnetic moments in ferromagnets Fe, Co and Ni are 2.216, 1.715 and 0.616 μ_B per atom, respectively [25]. These non-integral values cannot be understood as being due to localized moments on atoms. Therefore, they provide evidence for band magnetism (itinerant magnetism). In the absence of a magnetic field the energies of the spin-up and spin-down $3d$ bands are different. Part of the electrons move from one subband to the other (Fig. 1.3), whereby there appears the magnetic moment equal to the difference between the electronic magnetic moments in the subbands:

$$M = \mu_B (n_{\uparrow} - n_{\downarrow}), \quad (1.5)$$

where n_{\uparrow} and n_{\downarrow} are the number densities of the up-spins and down-spins, respectively.

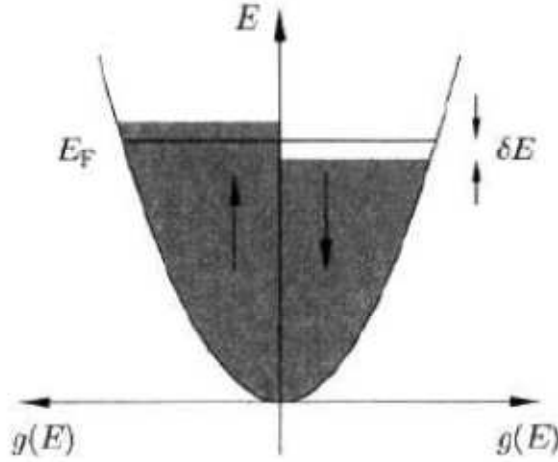


Figure 1.3. Density of states showing spontaneous splitting of energy bands without an applied magnetic field [23].

Ferromagnetism in a system of itinerant electrons is a threshold phenomenon. Its appearance is determined by the Stoner criterion that states that a system will display ferromagnetic order if the exchange integral J and the density of electronic states $g(E_F)$ at the Fermi level are both large:

$$Jg(E_F) \geq 1. \quad (1.6)$$

Due to the formation of the ferromagnetic order, the electronic kinetic energy grows as electrons move from one subband to the other where they can only occupy higher energy states. For this reason, the spontaneous ferromagnetism occurs only if the exchange energy is sufficiently high to compensate for this kinetic energy increase.

If a system of itinerant electrons is far from fulfilling the Stoner criterion, no splitting of the spin-up and spin-down subbands will occur in a zero magnetic field. Application of a magnetic field will either raise or lower the energy of the electrons depending on their spin. Thus, Pauli paramagnetism will be observed – a field-induced splitting of the subbands, which gives rise to a paramagnetic susceptibility of the electron gas:

$$\chi_P = \mu_B^2 g(E_F). \quad (1.7)$$

The Pauli susceptibility displays weak temperature dependence as a consequence of the smearing of the Fermi surface with increasing temperature.

Stoner enhancement is observed in systems on the verge of ferromagnetism such as Pd and Pt [23]. These have a large enough value of the $Jg(E_F)$ parameter to cause a significant enhancement of the magnetic susceptibility but not sufficiently close to 1 to cause spontaneous magnetization. Their enhanced Pauli susceptibility is

$$\chi = \chi_P / (1 - Jg(E_F)). \quad (1.8)$$

Despite providing a good qualitative description of some properties of itinerant ferromagnets, the Stoner model fails to account for their Curie temperature values. Furthermore, the Stoner model leads to temperature-independent magnetic susceptibility in the paramagnetic state, whereas experimentally for $3d$ metals it follows the Curie-Weiss law (see Eq. (1.3)). These difficulties can be overcome in the model developed by Moriya [26]. Whereas within the Stoner model the magnetization is considered homogeneous, Moriya takes into account spin fluctuations. They occur due to thermal excitations in the ferromagnetic system, and their amplitude grows as temperature is raised.

Due to the wide spatial extent of the $3d$ shell it experiences the inhomogeneous crystal electric field produced by neighboring ions [23,27]. The crystal field interaction is much stronger than the spin-orbit interaction. The coupling of the orbital and spin angular momenta is largely broken up, and the states are no longer specified by their J values. Furthermore, the $(2L + 1)$ sublevels belonging to a given L which are degenerate in the free ion may be split in the crystal field. This splitting decreases the contribution of the orbital motion to the magnetic moment. The effective magnetic moment is determined by the expression

$$\mu_{\text{eff}} = 2\mu_{\text{B}}\sqrt{S(S + 1)} \quad (1.9)$$

which suggests that the ground state is such that $L = 0$ and $g_J = 2$. This effect is orbital quenching. Physically it means that in a non-central crystal field the plane of the $3d$ orbit will move about, the angular momentum components are no longer constant and may average to zero. The role of the crystal field in the quenching process is to split the originally degenerate levels into non-magnetic levels separated by energies much higher than $\sim \mu_{\text{B}}H$, so that the magnetic field is a small perturbation in comparison with the crystal electric field. In practice, the orbital angular momentum may not be completely quenched since the spin-orbit interaction cannot be completely ignored. Although the $3d$ magnetic moments are dominated by the spin momentum, the orbital momentum also makes a contribution, of the order of 5-10% [28].

1.2. Exchange interactions

The exchange interactions are responsible for long range magnetic order. These interactions have electrostatic nature and arise because charges of the same sign cost more energy when they are close than when they are apart.

1.2.1. Origin of exchange

The wavefunction for the joint state composed of two electrons a and b having spatial coordinates \mathbf{r}_1 and \mathbf{r}_2 , respectively, can be written as a product of single electron states: $\psi_a(\mathbf{r}_1)\psi_b(\mathbf{r}_2)$. Apart from the spatial part, the overall

wavefunction Ψ also involves the spin part χ . For electrons Ψ should be antisymmetric, which requires that the spin part be either an antisymmetric singlet state χ_S ($S = 0$) in the case of a symmetric spatial state or a symmetric triplet state χ_T ($S = 1$) in the case of an antisymmetric spatial state. Therefore, the wavefunctions for the singlet case Ψ_S and the triplet case Ψ_T are

$$\begin{aligned}\Psi_S &= \frac{1}{\sqrt{2}} [\psi_{a(r_1)}\psi_{b(r_2)} + \psi_{a(r_2)}\psi_{b(r_1)}] \chi_S \\ \Psi_T &= \frac{1}{\sqrt{2}} [\psi_{a(r_1)}\psi_{b(r_2)} - \psi_{a(r_2)}\psi_{b(r_1)}] \chi_T.\end{aligned}\quad (1.10)$$

The energies of the two states can be determined from the following relations:

$$\begin{aligned}E_S &= \int \Psi_S^* \hat{H} \Psi_S d\mathbf{r}_1 d\mathbf{r}_2 \\ E_T &= \int \Psi_T^* \hat{H} \Psi_T d\mathbf{r}_1 d\mathbf{r}_2.\end{aligned}\quad (1.11)$$

The difference between the two energies is

$$E_S - E_T = 2 \int \psi_a^*(\mathbf{r}_1)\psi_b^*(\mathbf{r}_2)\hat{H}\psi_a(\mathbf{r}_2)\psi_b(\mathbf{r}_1)d\mathbf{r}_1d\mathbf{r}_2.\quad (1.12)$$

Equation (1.12) can be parametrized using electron spins \mathbf{S}_1 and \mathbf{S}_2 (see, e.g., [23]). The spin-dependent term in the Hamiltonian is proportional to their product $\mathbf{S}_1 \cdot \mathbf{S}_2$:

$$\hat{H}_1 \sim - (E_S - E_T) \mathbf{S}_1 \cdot \mathbf{S}_2.\quad (1.13)$$

The exchange constant (or exchange integral) is defined by

$$J = \frac{E_S - E_T}{2}.\quad (1.14)$$

Hence the spin-dependent Hamiltonian can be written

$$\hat{H}_1 = -2J \mathbf{S}_1 \cdot \mathbf{S}_2.\quad (1.15)$$

If $J > 0$, the triplet state $S = 1$ is favored. If $J < 0$, the singlet state $S = 0$ is favored. From this results the Hamiltonian of the Heisenberg model:

$$\hat{H} = - \sum_{ij} J_{ij} \mathbf{S}_i \cdot \mathbf{S}_j,\quad (1.16)$$

where J_{ij} is the exchange integral between the i^{th} and j^{th} spins.

According to the Weiss model of ferromagnetism, the exchange interaction is analogous to the presence of a molecular field experienced by electrons. The strength of this field, λ , is proportional to J_{ij} . Assuming that the exchange interaction is effective only over the z nearest neighbors of an ion,

$$\lambda = \frac{2zJ_{ij}(g_J-1)^2}{g_J\mu_B^2}, \quad (1.17)$$

where z is the number of nearest neighbors. The Curie temperature of the system can be written in the following way:

$$T_C = \frac{2zJ_{ij}}{3k_B}(g_J - 1)J(J + 1). \quad (1.18)$$

In order to account for the high values of magnetic ordering temperatures, i.e., of $3d$ metals Fe ($T_C = 1043$ K), Co ($T_C = 1394$ K) and Ni ($T_C = 631$ K), the molecular field should be rather large, $\sim 10^3$ T.

It should be noted that the molecular field is a fiction: the exchange interaction is not an internal magnetic field but it is a purely electrostatic effect. If the molecular field existed and Heisenberg exchange did not, the former would have to be as large as $\sim 10^3$ T to account for the high T_C values.

Equation (1.16) reflects that exchange interactions are proportional to the spin product of two interacting electrons. However, the exchange integral is determined by the type of the exchange interaction. Below follows a description of the most common types of exchange.

1.2.2. Types of exchange

Direct exchange arises as a consequence of the overlap between the magnetic orbitals of two adjacent atoms, i.e., it proceeds directly without the need for an intermediary [23,24]. This interaction is particularly strong for $3d$ metals due to the relatively large extent of their $3d$ electrons clouds. Slater found a correlation between the sign of the exchange constant and the ratio r_{ab}/r_d , where r_{ab} is the interatomic distance and r_d the radius of the incompletely filled d shell [29]. Large values of r_{ab}/r_d correspond to positive exchange constant, while for small r_{ab}/r_d values it is negative. According to the Bethe-Slater curve (Fig. 1.4), the exchange interaction between the moments of two similar $3d$ atoms is comparatively small for large interatomic distances, passes through a maximum and eventually turns negative for small interatomic distances.

Despite serious criticism of the Bethe-Slater curve [30], it is frequently used semi-empirically to explain changes in the magnetic moment coupling when the distance between the corresponding atoms changes.

When there is no direct overlap between electrons of magnetic ions in a solid, indirect exchange comes into play. *Superexchange* arises in ionic solids such as MnO and MnF₂. It is an indirect exchange interaction between non-neighboring magnetic ions which is mediated through a non-magnetic ion placed in between the magnetic ions [23]. The exchange integral within the tight-binding approach is

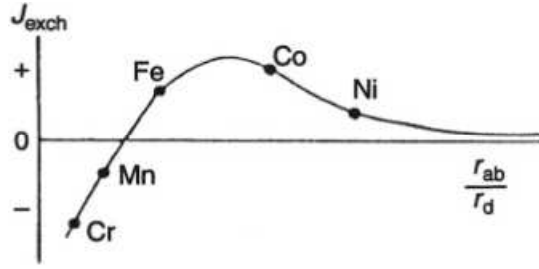


Figure 1.4. Bethe-Slater curve for 3d transition metals [24].

$$J_{\text{super}} \sim -\frac{t^2}{U}, \quad (1.19)$$

where t is the hopping integral proportional to the bandwidth and U the Coulomb energy that represents the energy cost of making an excited state, i.e., when two electrons are on the same atomic site. Superexchange strongly depends on the angle of the bond “magnetic ion – non-magnetic ion – magnetic ion” (Mn-O-Mn in MnO_2). Most often, superexchange is antiferromagnetic.

In metallic solids the indirect exchange is of the *RKKY* (*Ruderman-Kittel-Kasuya-Yosida*) type [23]. In this case, the exchange interaction between magnetic ions is mediated by the conduction electrons. A localized magnetic moment spin-polarizes the conduction electrons. Their spin polarization couples with a neighboring magnetic moment at a distance r from the other magnetic moment. The exchange constant is

$$J_{\text{RKKY}} \sim \frac{-2k_{\text{F}}r \cdot \cos(2k_{\text{F}}r) + \sin(2k_{\text{F}}r)}{2k_{\text{F}}r^4}, \quad (1.20)$$

where k_{F} is the Fermi vector. The RKKY interaction is long range and has an oscillatory dependence on the distance between the magnetic moments (Fig. 1.5). For this reason, it may be either ferromagnetic or antiferromagnetic. The exchange interaction in magnetically ordered rare-earth metals is of the RKKY type.

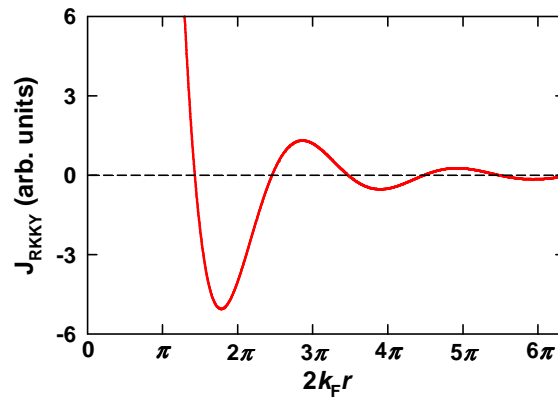


Figure 1.5. Exchange constant of RKKY interaction as a function of $2k_{\text{F}}r$.

In order to describe exchange interactions of $3d$ - $4f$ intermetallic compounds, the two-sublattice model comes into play that states that these compounds consist of two magnetic sublattices: R and T . The T - T exchange interactions dominate, whereas the R - R exchange interactions are much weaker. In the vast majority of R - T compounds the rare-earth and transition metal sublattices become ordered magnetically at the same temperature. It can be explained by the presence of the $3d$ - $4f$ inter-sublattice exchange interactions. The direct overlap between the $3d$ and $4f$ spins is rather small due to the spatial localization of the $4f$ shell. Therefore, the coupling between the transition metal sublattice and the rare-earth sublattice is indirect [6]. According to Campbell [31], the localized $4f$ spins create a positive $5d$ moment through the intra-atomic $4f$ - $5d$ exchange. Subsequently, the direct negative inter-atomic $5d$ - $3d$ exchange is realized. This scheme leads to a parallel moment alignment of the $3d$ and $4f$ magnetic moments for the light rare-earth elements and to an antiparallel alignment for the heavy rare-earth elements (Fig. 1.6). The rare-earth sublattice can be considered an ideal paramagnet situated in the molecular field created by the transition metal sublattice.

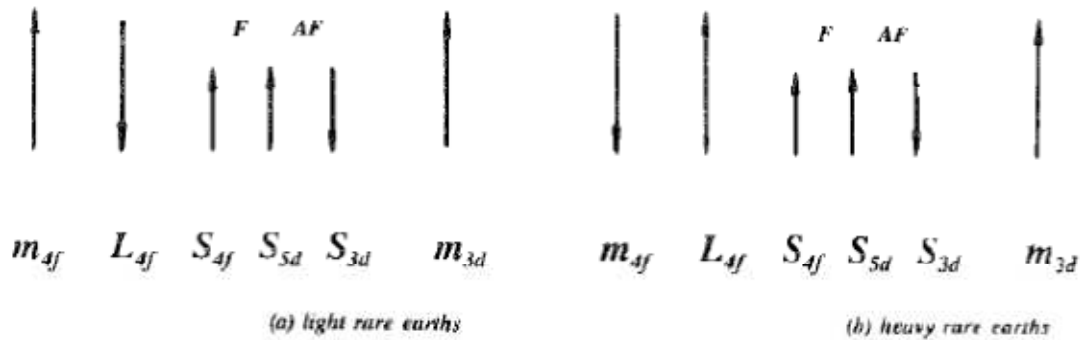


Figure 1.6. Schematic diagram illustrating the coupling between the $3d$ and $4f$ magnetic moments [6]. F and AF indicate ferro- and antiferromagnetic exchange interactions.

1.3. Magnetocrystalline anisotropy

1.3.1. Crystal-field induced anisotropy

Magnetic anisotropy is the dependence of a system's free energy on the direction of the spontaneous magnetization with respect to the crystallographic axes [6,24]. In $3d$ - $4f$ intermetallic compounds both, the rare-earth and transition metal sublattices, make a contribution to the magnetocrystalline anisotropy.

The origin of the rare-earth anisotropy lies in non-zero orbital momentum of the $4f$ elements [24]. The asymmetric $4f$ charge cloud assumes an orientation in the crystal lattice that minimizes its electrostatic interaction with the crystal electric field. Due to the strong spin-orbit coupling it results in a preferred orientation of the spin momentum and, consequently, of the magnetic moment of the $4f$ shell. The main parameters that determine the type and magnitude of the anisotropy are the shape of the $4f$ charge cloud and the nature of the crystal electric field around it. For the majority of the rare-earth metals the $4f$ electron charge density is not spherical as illustrated in Fig. 1.7. Among the rare-earth metals that carry an ordered magnetic

moment, the only exception is Gd whose $4f$ charge cloud is spherically symmetric (orbital quantum number of gadolinium is $L = 0$). The electrostatic potential that acts on the rare-earth ion depends on the symmetry of its position in the crystal lattice, i.e., on the distribution and type of the surrounding atoms. The electrostatic potential is most often not spherical. The interaction with the crystal electric field can be regarded as the interaction between the non-spherical $4f$ charge cloud and the non-spherical electrostatic potential around it. The corresponding anisotropy is called single-ion anisotropy.

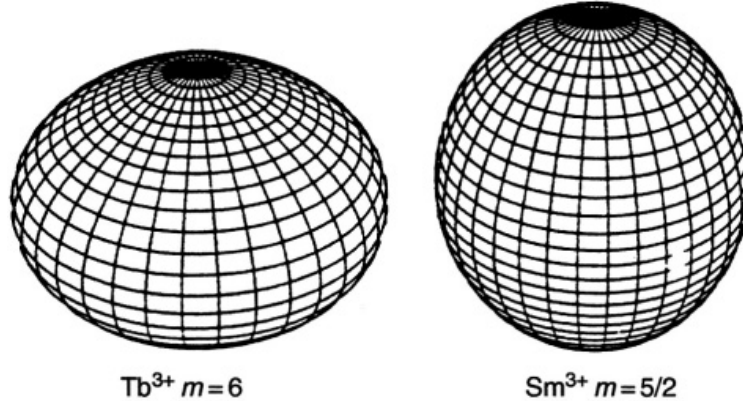


Figure 1.7. Angular distribution of the $4f$ electron charge density of Tb^{3+} ($\alpha_J < 0$) and Sm^{3+} ($\alpha_J > 0$) [24].

In order to analyze the interaction between the $4f$ charge cloud and the crystal electric field, the electrostatic potential is written in terms of a series expansion based on spherical harmonics Y_n^m [3]. Then its effect is considered on the corresponding electric multipole moments associated with the aspherical $4f$ charge cloud. This leads to the following Hamiltonian of the crystal field interaction:

$$H_C = \sum \sum A_n^m \theta_n \langle r^n \rangle O_n^m = \sum \sum B_n^m O_n^m. \quad (1.21)$$

The A_n^m terms are crystal field parameters that reflect the magnitude and symmetry of the electric field. The $\theta_n \langle r^n \rangle O_n^m$ product reflects the nature of the aspherical $4f$ charge cloud. For each magnetic rare-earth ion expressions for the so-called operator equivalents O_n^m are known [32]. Expectation values of the n th power of the $4f$ radius $\langle r^n \rangle$ are available in Ref. [33]. The θ_n quantities are called Stevens' factors. They are usually denoted α_J , β_J and γ_J for $n = 2, 4$ and 6 , respectively. The sign of the second order Stevens' factor reflects the relative orientation between the quadrupole moment and the magnetic moment of the aspherical $4f$ charge cloud. They are perpendicular for $\alpha_J < 0$ and parallel for $\alpha_J > 0$. The $4f$ charge cloud has the shape of an oblate ($\alpha_J < 0$) or prolate ($\alpha_J > 0$) spheroid (see Fig. 1.7).

In case of a simple uniaxial crystal electric field from Eq. (1.21) it follows that the main term of the crystal field interaction E_1 is given by the expectation value of $B_2^0 O_2^0$ [3]:

$$E_1 = B_2^0 \langle O_2^0 \rangle = \alpha_J \langle r^2 \rangle \langle 3J_z^2 - J(J+1) \rangle A_2^0. \quad (1.22)$$

If the exchange interaction significantly exceeds the crystal field interaction, the ground state at $T = 0$ is $|J_z \rangle = -|J \rangle$. In this case

$$E_1 = \alpha_J \langle r^2 \rangle \langle 2J^2 - J \rangle A_2^0. \quad (1.23)$$

This equation represents the interaction of the axial quadruple moment of the $4f$ charge with the local electric field gradient.

Magnetic anisotropy of the $3d$ sublattice is also associated with the occurrence of orbital angular momenta, albeit very small [3]. Magnetism of the $3d$ ions is often described in terms of energy-band parameters [3,6]. However, at present band structure calculations are still not able to reproduce the experimental results for the $3d$ anisotropy due to extremely weak spin-orbit coupling ~ 30 meV that produces a very small spin-orbit splitting relative to the band splitting [3]. It means that the band structure calculations have to be performed to a very high precision in order to reveal magnetic anisotropy. For this reason, the $3d$ anisotropy is experimentally deduced from magnetic measurements on compounds with non-magnetic rare-earth elements ($R - Y, La, Lu$).

For different types of crystal structures there exist mathematical expressions which describe magnetocrystalline anisotropy. For the cubic symmetry anisotropy energy can be written in the following form [34]:

$$E_a = K_0(T) + K_2(T)[\alpha_1^2 \alpha_2^2 + \alpha_2^2 \alpha_3^2 + \alpha_3^2 \alpha_1^2] + K_3(T) \alpha_1^2 \alpha_2^2 \alpha_3^2 + \dots, \quad (1.24)$$

where K_n are anisotropy constants of the $(2n)$ th order, α_1, α_2 and α_3 are direction cosines of the magnetization vector with respect to the crystallographic axes. For the hexagonal symmetry the anisotropy energy is [6,35]

$$E_a = K_0 + K_1 \sin^2 \theta + K_2 \sin^4 \theta + K_3 \sin^6 \theta + K_3' \sin^6 \theta \cos 6\phi + \dots, \quad (1.25)$$

where θ and ϕ are polar and azimuthal angles between the magnetization vector and crystallographic axes. For the tetragonal symmetry

$$E_a = K_0 + K_1 \sin^2 \theta + K_2 \sin^4 \theta + K_2' \sin^4 \theta \cos 4\phi + K_3 \sin^6 \theta + K_3' \sin^6 \theta \cos 4\phi + \dots \quad (1.26)$$

The anisotropy energy of compounds having lower crystallographic symmetries is described by more complicated expressions.

The magnetocrystalline anisotropy can be studied most effectively by applying magnetic field along specific crystallographic directions of single crystalline samples.

1.3.2. Spontaneous spin-reorientation transitions

At low temperatures the anisotropy largely originates from the rare-earth ions and is transferred by the $3d$ - $4f$ exchange interaction to the $3d$ sublattice [6]. With increasing temperature the anisotropy energy of the rare-earth sublattice decreases more rapidly than that of the transition metal sublattice. As a result, their energy balance may change in favor of the $3d$ sublattice. For this reason, spontaneous spin-reorientation transitions may occur in $3d$ - $4f$ compounds if the two magnetic sublattices give contributions of opposite signs to the magnetic anisotropy.

A spin reorientation transition is a phase transition consisting in a change of orientation of ordered magnetic moments with respect to crystallographic axes [35]. These phase transitions do not involve a change of the mutual orientation of the sublattice moments, only their orientation to the crystal axes changes. Spin reorientation transitions can be of first or of second order. In the former case the orientation angle experiences a discontinuity at the transition point. In the latter case the angle itself varies continuously, more specifically, such a spin reorientation involves two second order phase transitions as well as continuous rotation of the magnetization vector in the interval between the transition points. At a transition point the angle θ takes a special high-symmetry value, 0 or $\pi/2$. It should be noted that second-order spin reorientation transitions do not always need to come in pairs. It is possible that the process of spin reorientation starting at a finite temperature may not reach completion before the temperature reaches 0 K as found, e.g., in Gd metal [36] and in $\text{Nd}_2\text{Fe}_{14}\text{B}$ [37,38].

Let us consider a system whose anisotropy energy can be described using second- and fourth-order anisotropy constants:

$$E_a = K_1 \sin^2 \theta + K_2 \sin^4 \theta. \quad (1.27)$$

Minimization with respect to θ yields the following equilibrium states [39]:

1. $\theta = 0$, if $K_1 > \max(0, -K_2)$;
2. $\theta = \arcsin \sqrt{-K_1/2K_2}$, if $-2K_2 < K_1 < 0$;
3. $\theta = \pi/2$, if $K_1 < \min(-2K_2, -K_2)$.

The combination of these statements can be visualized by means of the diagram presented in Fig. 1.8. In the first quadrant and the upper half-plane of the fourth quadrant the anisotropy type is easy axis, which means that the easy magnetization direction lies along the highest symmetry direction in a crystal lattice with uniaxial symmetry (the c axis in the tetragonal or hexagonal symmetry). In the third quadrant and adjacent half-planes of the second and fourth quadrants the anisotropy is of easy plane type: the easy magnetization direction lies within the basal plane. In the „easy cone“ phase the angle θ takes intermediate values between 0 and $\pi/2$. The bold lines separating the domains of different phases are phase transition lines of first (dashed) or second (solid) order.

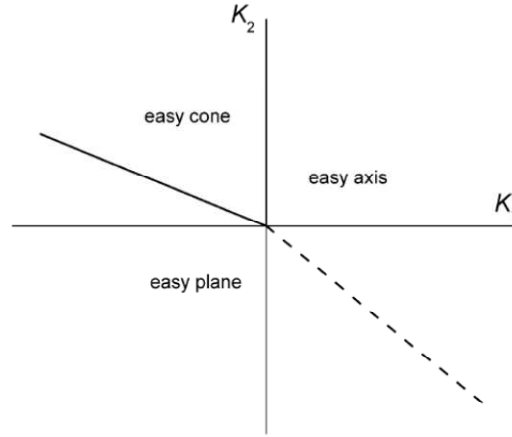


Figure 1.8. Phase diagram of a magnet with two anisotropy constants [39].

Second- and fourth-order anisotropy constants can be found using Sucksmith-Thompson method [40]. Having measured the field dependence of magnetization, $M(H)$, along the hard magnetization direction, the following relations can be applied:

- for easy-plane (or easy cone) anisotropy

$$\frac{H}{M} = -\frac{2K_1+4K_2}{M_s^2} + \frac{4K_2M^2}{M_s^4}, \quad (1.28)$$

- and for uniaxial anisotropy

$$\frac{H}{M} = \frac{2K_1}{M_s^2} + \frac{4K_2M^2}{M_s^4}, \quad (1.29)$$

where M_s is saturation magnetization. $H/M(M^2)$ should be a linear function. Thus, K_1 can be derived from the vertical intercept and K_2 from the slope of the straight line.

1.4. Field-induced magnetic phase transitions

Magnetization curves of magnetically ordered crystals can, under special circumstances, show anomalous discontinuities that appear as jumps of the magnetization with increasing magnetic field. These can be first or second order magnetic phase transitions. Their nature strongly depends on the orientation of the applied magnetic field with respect to the crystallographic directions. The observed jumps in the magnetization curve can be due to a rotation of the magnetization vector, to a change of the modulus of the magnetization vectors, or to a change of the magnetic order [41]. In the first case, changes in the magnetic state of the system can be ascribed to magnetic anisotropy. In the second case, microscopic effects are manifested that may be consequences of particular crystal-field effects, and/or the effect of the magnetic field on the energy-band structure. In the third case exchange interactions are altered, and drastic changes in magnetic structures occur. Below a description is given of the transitions of exchange and anisotropic nature.

1.4.1. Transitions of exchange nature

The effect of a sufficiently strong magnetic field on a simple two-sublattice antiferromagnet is such that it will eventually dominate the internal molecular field and force all magnetic moments to lie parallel to each other. However, how the system comes to this final state depends strongly on the direction of the applied field with respect to the initial direction of sublattice magnetization.

The application of a magnetic field along the hard magnetization axis will cause magnetic moments to bend towards the field direction until both sublattice moments, M_A and M_B , are aligned parallel to the field direction (curve (a) in Fig. 1.9). The slope of the first part of this curve, $\chi_{\text{hard}} = \Delta M / \Delta H$, reflects the strength of the inter-sublattice exchange coupling $n = 1/\chi_{\text{hard}}$.

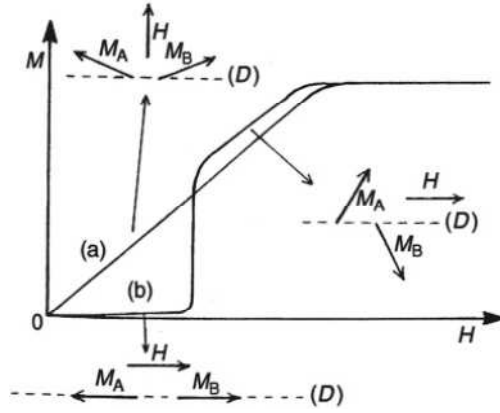


Figure 1.9. Schematic representation of the field dependence of the total magnetization along the hard (a) and easy (b) magnetization directions of an antiferromagnetic single crystal with relatively low magnetocrystalline anisotropy [24].

When a magnetic field is applied along the easy magnetization direction, initially magnetocrystalline anisotropy does not come into play, and the free energy is given by the field susceptibility along this direction:

$$F_{\text{easy}} = -\frac{1}{2}\chi_{\text{easy}}H^2. \quad (1.30)$$

If the sublattice moments become oriented perpendicular to the field direction, i.e., along the hard magnetization direction, the magnetic anisotropy K should be taken into account:

$$F_{\text{hard}} = K - \frac{1}{2}\chi_{\text{hard}}H^2. \quad (1.31)$$

For comparatively low applied field $F_{\text{easy}} < F_{\text{hard}}$, and both sublattice moments will retain the easy magnetization direction. However, since $\chi_{\text{hard}} > \chi_{\text{easy}}$ (see Fig. 1.9), F_{hard} will eventually become the lowest energy state. In this situation, both sublattice moments will become oriented practically parallel to the applied field. The critical field of this transition is determined from the condition $F_{\text{easy}} = F_{\text{hard}}$:

$$H_c = \sqrt{\frac{2K}{\chi_{\text{hard}} - \chi_{\text{easy}}}}. \quad (1.32)$$

This magnetization jump is called spin-flop (curve (b)).

When the magnetocrystalline anisotropy is very large, a different behavior is observed in a magnetic field (Fig. 1.10). Along the hard magnetization direction (curve (a)), the strong anisotropy prevents any sizeable bending of the sublattice moments towards the field direction. Along the easy magnetization direction, the total magnetization remains low for low fields, and at a certain critical field it jumps into the forced parallel configuration. The critical field in this case is determined by the inter-sublattice exchange coupling:

$$H_c = nM. \quad (1.33)$$

It reflects the fact that the sudden change from antiparallel to parallel alignment of the sublattice moments occurs when the applied magnetic field is strong enough to overcome the antiparallel coupling between the two sublattice moments. This phenomenon is called spin-flip or metamagnetic transition.

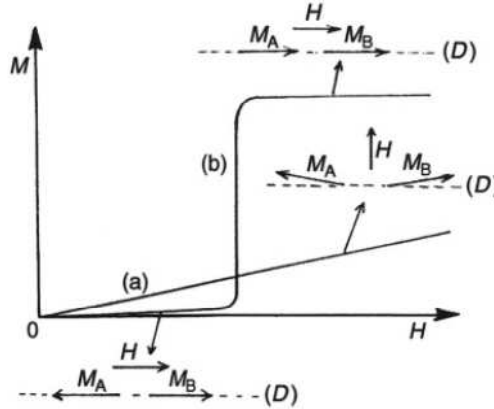


Figure 1.10. Schematic representation of the field dependence of the total magnetization along the hard (a) and easy (b) magnetization directions of an antiferromagnetic single crystal with very strong magnetocrystalline anisotropy [24].

1.4.2. Transitions of anisotropic nature

A first order magnetization process (FOMP) is an irreversible rotation of the magnetization vector under the action of a magnetic field applied along the hard magnetization direction of a ferro- or ferrimagnet [42]. A FOMP manifests itself as a discontinuous change of the magnetization direction. FOMP transitions can be analyzed in terms of the following equation for a uniaxial magnetic crystal [41,42]

$$E = K_1 \sin^2 \theta + K_2 \sin^4 \theta + K_3 \sin^6 \theta - HM_s \cos(\varphi - \gamma) \quad (1.34)$$

that reflects contributions of the anisotropy energy and Zeeman energy to the free energy. In Eq. (1.34) φ is the angle between the magnetization and the easy c axis and γ is the angle between the field and the easy c axis. Higher-order anisotropy constants (at least up to the 6th order) should have non-zero values in order for a FOMP to be observed. Noncollinear structures are not considered in the FOMP model as the exchange energy does not enter into the description. This neglect is equivalent with the assumption of an infinite strength of the inter-sublattice exchange coupling.

The preferred direction of the magnetization in the absence of magnetic field is along the angle where the anisotropy energy is at absolute minimum. For reasons of symmetry the c axis ($\varphi = 0$) and the basal plane ($\varphi = \pi/2$) are always points of extrema. In the conical phase, i.e., for $0 < \varphi < \pi/2$, the easy magnetization direction is determined by the following condition [41,42]:

$$\sin\varphi_c = \sqrt{\left\{ \left[-K_2 \pm \sqrt{K_2^2 - 3K_1K_3} \right] / 3K_3 \right\}}. \quad (1.35)$$

The origin of a FOMP is the presence of two inequivalent minima in the free energy. As the magnetization rotates in a magnetic field, the system shifts from one minimum energy state to the other.

Two types of FOMP can be distinguished depending on the final state after the transition. In case of the saturation state it is type-1 FOMP, otherwise the transition is type-2 FOMP (Fig. 1.11).

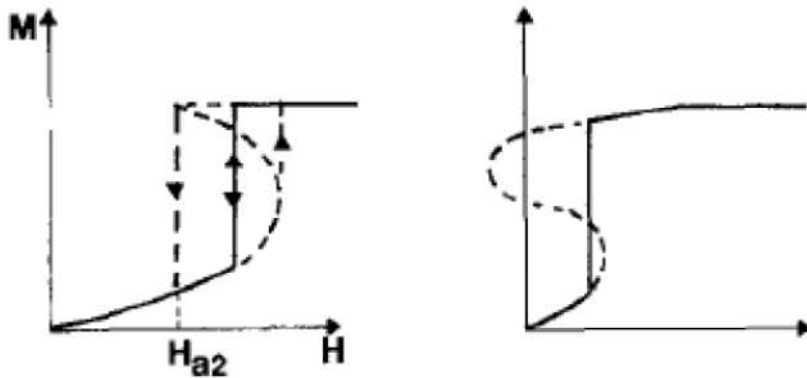


Figure 1.11. Examples of FOMP different types: type-1 (left) and type-2 (right) [41,42].

1.5. Magnetoelasticity

1.5.1. Sound propagation in magnetically ordered environment

Magnetic phase transitions are usually accompanied by pronounced anomalies in the acoustic properties, i.e., sound velocity and sound attenuation. The spin-lattice coupling (or electron-phonon coupling) serves as a highly sensitive probe of magnetic phase transitions, both spontaneous and induced. The ultrasound velocity provides information on variations of atomic bonding, whereas the

ultrasonic attenuation is related to energy dissipation [43]. Spontaneous magnetic transitions are those occurring with changing temperature, mainly „order-disorder“ and spin-reorientation transitions. Field-induced transitions are step-wise rotations of magnetization in a magnetic field, such as spin-flop, spin-flip and FOMP transitions (see section 1.4.2).

The spin-phonon interaction responsible for critical effects observed at phase transitions arises in most cases via the strain modulation of the exchange interaction (volume magnetostrictive coupling) [44]. In Refs. [45,46] it was shown that the relative change of sound velocity $\Delta v/v$ is proportional to the magnetic part of the specific heat C_m . In case of a second-order phase transition, the singularity in $\Delta v/v$ coincides with the one found in $C_m(T)$ function. Furthermore, relative changes of sound velocity are independent of the sound wave frequency [43,44,47].

When anisotropy constants pass through zero in a magnetically ordered state, a spin reorientation transition occurs (see section 1.3.2). The decrease in the magnetic anisotropy is accompanied by a decrease in the magnetostriction. Under these circumstances, a softening of the crystal lattice is expected due to local atomic magnetoelastic interactions. Therefore, the reduction in the Young's modulus E results in a reduction of the sound velocity as follows from the simplest expression:

$$v = \sqrt{\frac{E}{\rho}}, \quad (1.36)$$

where ρ is density. Indeed, clearly defined depressions in the Young's moduli are observed in RFe_2 compounds at temperatures where easy axis rotation takes place [48].

In the approximation that spin fluctuation decay time τ_k is much shorter than the transit time of a sound wave, sound attenuation is proportional to frequency ω squared [44]:

$$\alpha \sim \frac{\omega^2 C_m}{1/\tau_k}. \quad (1.37)$$

1.5.2. Effects of external pressure on magnetic properties

External pressure applied to intermetallic compounds has two major effects: (i) it modifies their electronic properties, the most apparent effect being band broadening, and (ii) it induces changes of their crystal structure. The two effects may have profound implications for magnetically ordered state, and new physics can be expected.

The response of itinerant magnetism to applied pressure is higher than that of localized magnetism. In the former the band broadening involves the electrons responsible for magnetic order, whereas in the latter these electrons do not form bands.

Application of pressure to iron results in a gradual weakening of its magnetic order [25]. The broadening of the $3d$ band due to reduced interatomic distances leads

to a reduction of the density of electronic states at the Fermi level, and the spontaneous magnetic moment and magnetic ordering temperature are reduced. Iron undergoes a phase transition from the bcc to the hcp crystal structure between 14 and 18 GPa, accompanied by the disappearance of the magnetic order [49,50]. Moreover, at a sufficiently high pressure the hcp phase becomes superconducting [51].

Pressure response of itinerant magnetism provides information on elastic properties. In particular, from the variation of the Curie temperature T_C of Fe, Co and Ni with pressure p the compressibility κ can be calculated [52]:

$$\frac{dT_C}{dp} = \frac{5}{3} \kappa T_C. \quad (1.38)$$

The pressure response of magnetization M is related to the change of volume V [53]:

$$\left(\frac{dM}{dp}\right)_{H,T} = -\left(\frac{dV}{dH}\right)_{p,T}. \quad (1.39)$$

Rare-earth metals and alloys display localized magnetism associated with the $4f$ electronic shell that sits deep inside the atom. Changes in interatomic distances induced by applied pressure do not affect directly the $4f$ electrons. Nevertheless, the type of the magnetic order in the rare-earth metals is subject to changes under pressure due to either structural transformations and/or the RKKY exchange interaction that varies with distance in an oscillatory manner (see Section 1.2.2).

At ambient conditions gadolinium has the hcp structure and displays simple ferromagnetic order [21]. Application of pressure results in a slow depression of the Curie temperature, $dT_C/dp \approx 0.16$ K/GPa [54]. At $p = 2.5$ GPa the metal undergoes a structural phase transition from the hcp to the rhombohedral samarium structure [54-56]. This high pressure phase of gadolinium is ordered antiferromagnetically [54,56].

In $3d$ - $4f$ intermetallic compounds the largest changes in the magnetism are associated mainly with the $3d$ sublattice, provided no structural transformations occur (see e.g., [57,58]).

Chapter 2: $R(\text{Fe,Al})_{12}$ compounds: state of the art

Binary R -Fe compounds with the tetragonal crystal structure of the ThMn_{12} type (space group $I4/mmm$) do not exist [59] except for SmFe_{12} obtained as thin films [60,61]. In order to stabilize them, a partial substitution of Fe by a third element M is required. Ternary $R(\text{Fe},M)_{12}$ compounds can be stabilized by M – Al, Si, Ti, V, Cr, Mn, Ga, Nb, Mo, W and Re. These systems form with all rare-earth elements and yttrium [59].

First studies of magnetic properties of the $R(\text{Fe},M)_{12}$ compounds were initiated in the 1970s. More investigations were triggered by the discovery of a new hard magnetic material, $\text{Nd}_2\text{Fe}_{14}\text{B}$, in 1984 [2]. These systems attract considerable interest as potential materials for permanent magnets. Furthermore, a huge variety of their magnetic properties makes them interesting from the fundamental point view [59].

2.1. Crystal structure

Figure 2.1 shows the unit cell of the ThMn_{12} type structure. It contains 2 formula units (26 atoms). Thorium atoms reside on the $2a$ sites, while manganese atoms occupy the three crystallographically inequivalent sites $8f$, $8j$ and $8i$. The coordinates of these sites are listed in Table 2.1. The lattice parameters are $a \approx 8.7 \text{ \AA}$, $c \approx 5.1 \text{ \AA}$, $c/a \approx 0.59$ [62].

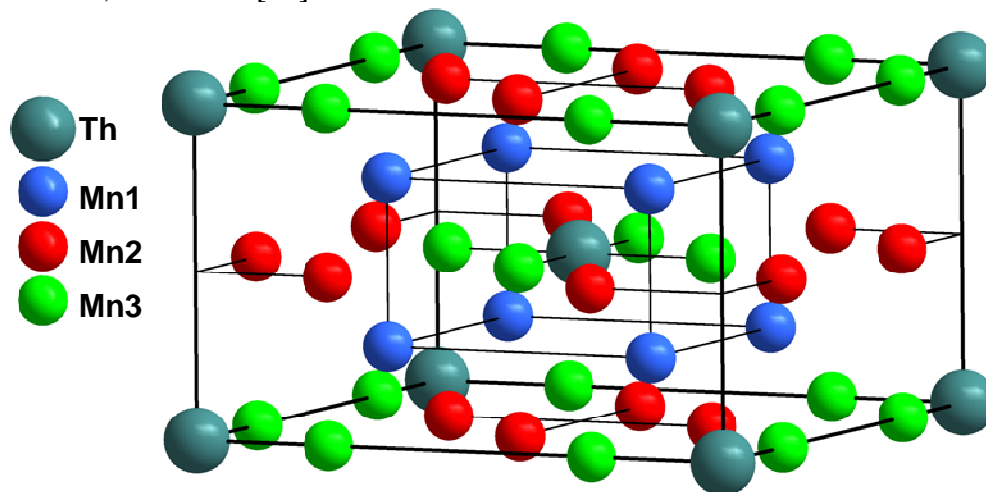


Figure 2.1. Unit cell of the ThMn_{12} type structure.

Table 2.1 – Parameters of atomic positions in a crystal structure of the ThMn_{12} type.

Atom	Position	Coordinates		
		x	y	z
Th	$2a$	0.0	0.0	0.0
Mn1	$8f$	0.25	0.25	0.25
Mn2	$8j$	0.27	0.5	0.0
Mn3	$8i$	0.35	0.0	0.0

The composition of $R(\text{Fe},M)_{12}$ compounds is to a large extent determined by the stabilizing element. For instance, systems with $M - \text{Al}$ exist with a relatively high Al concentration: the homogeneity range of $R\text{Fe}_x\text{Al}_{12-x}$ is $4 \leq x \leq 6$. By contrast, lower concentrations of $M - \text{Ti}$, Si and V are needed to form $R(\text{Fe},M)_{12}$ compounds. $R\text{Fe}_{12-x}\text{Ti}_x$ and $R\text{Fe}_{12-x}\text{Si}_x$ systems are stable at $x \approx 1$ and $x \approx 2$, respectively [63-66], while in $R\text{Fe}_{12-x}\text{V}_x$ the vanadium content can change in the range $1.5 \leq x \leq 3$ [67].

The filling of lattice sites by atoms M is not statistical [68]. In Fe-rich compounds atoms of the stabilizing element occupy the $8i$ sites when it is a transition element $M - \text{Ti}$, V , Mo , W and Re . However, in systems stabilized by s - and p -elements ($M - \text{Si}$), their atoms prefer to reside on the $8f$ and $8j$ sites. In compounds with a low Fe content, $R\text{Fe}_x\text{Al}_{12-x}$, Al atoms occupy mainly the $8i$ sites.

$R\text{Fe}_x\text{Al}_{12-x}$ systems are the subject of the present work, and below follows a more detailed description of their structural properties.

$R\text{Fe}_x\text{Al}_{12-x}$ compounds form with $R - \text{Gd}$, Tb , Dy , Ho , Er , Tm , Yb , Lu , Y and U (in the $R\text{Fe}_5\text{Al}_7$ subgroup the compound with $R - \text{Sm}$ was also reported to exist [20]). In the tetragonal crystal lattice Fe and Al are distributed over the $8f$, $8j$ and $8i$ sites. The main structural feature of the $R\text{Fe}_x\text{Al}_{12-x}$ compounds with respect to their magnetic properties is a gradual filling of the $8j$ sites by Fe atoms from $x = 4$ to $x = 6$. In Al-rich $R\text{Fe}_4\text{Al}_8$, the Fe atoms reside exclusively on the $8f$ site [9,17,69-72]. With increasing x Fe begins to occupy the $8j$ sites which it shares with Al, as was found for $R\text{Fe}_5\text{Al}_7$ [16,19,20,69,73-81] and $R\text{Fe}_6\text{Al}_6$ [69,82-84]. The progressive filling of the $8j$ sites by Fe results in considerable changes of exchange interactions in $R\text{Fe}_x\text{Al}_{12-x}$, which significantly modifies magnetic properties of the system.

In literature different data can be encountered on the filling of crystallographic positions in $R\text{Fe}_x\text{Al}_{12-x}$ compounds. In particular, Mössbauer studies indicated that in $\text{YFe}_x\text{Al}_{12-x}$ and $\text{TbFe}_x\text{Al}_{12-x}$ the filling of the $8f$, $8j$ and $8i$ sites changes continuously from $x = 4$ to $x = 6$ [85-87]. In YFe_4Al_8 and TbFe_4Al_8 the $8f$ sites are occupied by Fe only. With increasing x the Fe concentration decreases for these sites and grows for $8j$ and $8i$. As a result, in the vicinity of the compositions YFe_5Al_7 and TbFe_5Al_7 the distribution of the Fe atoms over the $8f$, $8j$ and $8i$ sites is close to uniform. In YFe_6Al_6 and TbFe_6Al_6 the Fe atoms reside in the $8j$ and $8i$ sites, the $8f$ sites are occupied by Al only. It should be noted that these data contradict the results reported by the same authors in Refs. [19,20] where structural properties of $R\text{Fe}_5\text{Al}_7$ compounds are described including those with $R - \text{Tb}$ and Y . However, in Ref. [79] it was suggested that the filling of the atomic positions in the YFe_5Al_7 compound depends on preparation conditions such as annealing of as-cast alloys.

2.2. Exchange interactions and magnetic order

The Fe sublattice plays the decisive role in the formation of a magnetic order in $R\text{Fe}_x\text{Al}_{12-x}$. This is best seen from a comparison of compounds in the whole homogeneity range $4 \leq x \leq 6$. In systems with the lowest Fe concentration, $R\text{Fe}_4\text{Al}_8$,

with magnetic R elements, the R and Fe sublattices order magnetically independently at different temperatures owing to the weak $3d-4f$ inter-sublattice exchange interactions [17,70,88-91]. The R sublattice orders at temperatures below approximately $T = 80$ K. The Fe sublattice orders at higher temperatures, often in excess of $T = 150$ K. The Fe-Fe interactions were reported to be of antiferromagnetic nature on the basis of magnetic and Mössbauer studies of the compounds with non-magnetic $R = \text{Sc}, \text{Y}, \text{Ce}$ and Lu [8-12]. Neutron diffraction studies led to the determination of more complicated magnetic structures within the Fe sublattice, cycloidal or amplitude-modulated with the magnetic moments confined to the basal plane [17,18,71,92,93]. The presence of a magnetic rare-earth component does not modify the magnetic structure of the Fe sublattice [71,72,88,94]. The R sublattice was found to follow the modulation of the Fe sublattice for DyFe_4Al_8 and HoFe_4Al_8 single crystals [93]. However, the opposite result was obtained for a GdFe_4Al_8 single crystal where the coexistence of two distinct orders associated with the Gd and Fe sublattices was reported [88]. The magnetic structure of the R sublattice displays very high sensitivity to low applied magnetic fields [93]. The Fe magnetic sublattice is thought to be substantially transformed in an external field [95].

The intricate nature of the exchange interactions in the $R\text{Fe}_4\text{Al}_8$ compounds results in their rather unusual behavior in a magnetic field. Magnetization curves measured on the single crystals with $R = \text{Gd}, \text{Dy}$ and Ho display a significant deviation from linearity above saturation at low temperatures along basal-plane directions [88,93]. An example is given for the GdFe_4Al_8 compound in Fig. 2.2 [88]. At $T = 2$ K it displays a spontaneous magnetic moment M_s along the $[110]$ axis, whereas there is no spontaneous component along the $[001]$ axis. Therefore, the magnetic moments lie in the basal plane, the $[001]$ axis is the hard magnetization direction. The M_s value is approximately $4.3 \mu_B/\text{f.u.}$ which is far from the Gd magnetic moment, $7 \mu_B$. It implies a complex magnetic order in the compound.

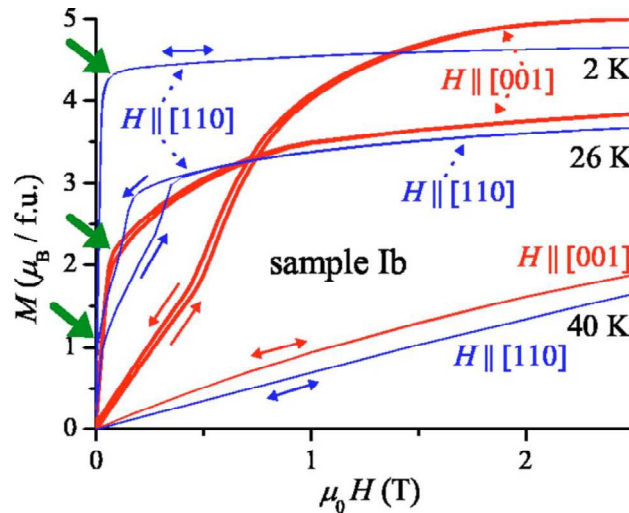


Figure 2.2. Magnetization M as a function of field H at selected temperatures, $\mathbf{H} \parallel [110]$ (blue), and $\mathbf{H} \parallel [001]$ (red). Thin arrows indicate the H direction of the measurements, thick arrows indicate the criterion taken for the estimation of the spontaneous ferromagnetic moment [88].

Moreover, the magnetic structure is transformed with temperature since at $T = 26$ K a spontaneous component appears along the [001] axis as well. The hysteresis observed at $T = 26$ K along the [110] axis may suggest a metamagnetic transition.

In RFe_5Al_7 compounds the $8j$ sites are partly occupied by Fe. This results in strengthening of the $3d-3d$ and $3d-4f$ exchange interactions, and it influences magnetic properties considerably. The R and Fe sublattices order at the same temperature. The magnetic structure of the Fe sublattice is modified due to a tendency towards a ferromagnetic order. Furthermore, in RFe_5Al_7 the transition from the magnetically ordered into the paramagnetic state occurs at $T > 200$ K, even in case of non-magnetic R elements [16,19,20].

Magnetic structures of RFe_5Al_7 (R – Sm, Gd, Tb, Dy, Ho, Er, Tm, Yb, Lu and Y) compounds were suggested on the basis of the results of magnetic and Mössbauer studies [19,20,85-87] and later determined by powder neutron diffraction [16]. Complicated structures were noted in the compounds with non-magnetic R – Yb, Lu and Y [20]. The Fe moments in the $8j$ sites have a collinear ferromagnetic arrangement, whereas those in the $8f$ sites form a canted antiferromagnetic structure. The systems with magnetic heavy rare-earth elements are ferrimagnets, i.e., the total magnetic moments of the R and Fe sublattices are antiparallel. The presence of a magnetic rare-earth component does not modify the magnetic structure of the Fe sublattice [19,20,85-87]. The corresponding compounds with magnetic R have non-collinear magnetic structures. In contrast to these data, a neutron powder diffraction study made it possible to determine collinear magnetic structures of the compounds with R – Tb, Dy, Ho, Er and Tm (Fig. 2.3) [16]. The intra-sublattice exchange interactions in the whole Fe and R sublattices are ferromagnetic. However, neutron powder diffraction cannot distinguish between various axes within the basal plane (e.g., [100] and [110]). For this reason, Fig. 2.3 should be viewed only as a schematic representation.

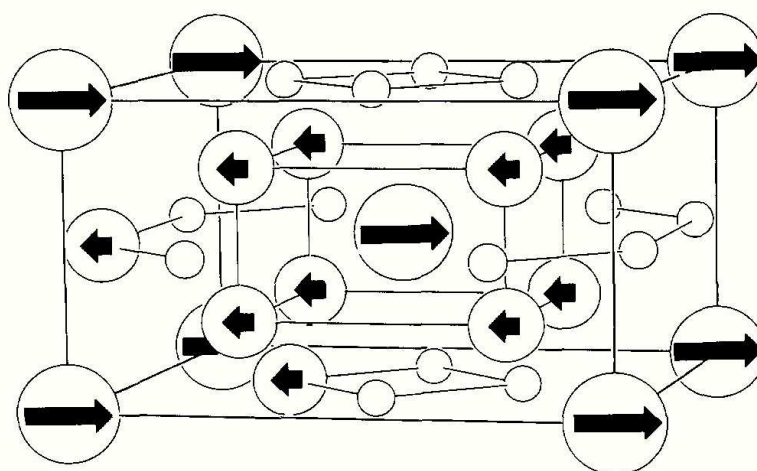


Figure 2.3. Ferrimagnetic unit cell of the RFe_5Al_7 (R – Tb, Dy, Ho and Er) compounds with antiparallel orientation of the collinear R magnetic moments (long arrows) in the $2a$ site and the Fe magnetic moments (short arrows) in the $8f$ and $8j$ sites. The other $8j$ sites (empty circles) and the $8i$ sites (not shown) are occupied by Al [16].

It might be expected that changes in the distribution of Fe atoms over the lattice sites strongly modify exchange interactions. In Refs. [85-87] the Fe atoms were found to occupy the $8f$, $8j$ and $8i$ sites uniformly in YFe_5Al_7 and TbFe_5Al_7 . Under these circumstances, R and Fe magnetic moments become frustrated, and a spin-glass state forms at low temperatures.

In the SmFe_5Al_7 compound with a light rare-earth element the inter-sublattice $3d-4f$ exchange interactions should be ferromagnetic in the whole temperature range of the magnetically ordered state. Surprisingly, the authors of Ref. [20] do not exclude the antiparallel orientation of the Sm and Fe magnetic moments.

Different values of the Curie temperatures T_C of $R\text{Fe}_5\text{Al}_7$ compounds are obtained by different methods. Magnetization measurements yield $T_C = 215$ K for the compound with $R = \text{Y}$ and slightly lower values for those with $R = \text{Yb}$ and Lu [20]. Compounds with magnetic R elements have higher T_C . The maximum value, 268 K, was found for GdFe_5Al_7 . For this system a value of $T_C = 240$ K was also reported [96]. Curie temperature values determined by Mössbauer spectroscopy are lower [20]. The difference is likely to be related to the induction of a magnetic moment in a magnetic field even at $T > T_C$. The discrepancy between the T_C values determined by the two above-mentioned methods is several degrees in case of a magnetic R element and much higher if R is non-magnetic. In general, neutron diffraction studies of the $R\text{Fe}_5\text{Al}_7$ ($R = \text{Y}, \text{Tb}, \text{Dy}, \text{Ho}, \text{Er}, \text{Tm}$) compounds agree well with the previous results. However, in some cases serious contradictions are encountered. Firstly, the YFe_5Al_7 compound is said to not display a long-range magnetic order [79,97]. From this result it follows that the long-range magnetic order is stabilized by interaction with R atoms having a localized magnetic moment. Secondly, the T_C values of HoFe_5Al_7 and ErFe_5Al_7 are much lower, 61 and 62 K, respectively [16]. A short-range magnetic order is said to form in these compounds at the temperature determined to be their T_C by the magnetic measurements and Mössbauer spectroscopy [20]. It is worth mentioning that in Table 1 of Ref. [16] where magnetic characteristics of the $R\text{Fe}_5\text{Al}_7$ ($R = \text{Tb}, \text{Dy}, \text{Ho}, \text{Er}$ and Tm) compounds are listed, the columns for HoFe_5Al_7 and TmFe_5Al_7 are permuted. It follows from incorrect values of the Ho and Tm magnetic moments at low temperatures, $\mu_{\text{Ho}} = 6.29 \mu_B$ and $\mu_{\text{Tm}} = 9.79 \mu_B$, respectively. Whereas the former value is possible, the Tm magnetic moment cannot exceed $7 \mu_B$ under any circumstances. Taking into account this observation, magnetic ordering temperatures of HoFe_5Al_7 determined by neutron diffraction ($T_C = 235$ K) and magnetic measurements ($T_C = 227$ K) are in good agreement [16,20].

In $R\text{Fe}_6\text{Al}_6$ compounds more Fe atoms reside in the $8j$ site. Simple collinear ferrimagnetic structures, similar to that shown in Fig. 2.3, were found by powder neutron diffraction for the systems with $R = \text{Tb}, \text{Ho}$ and Er [14]. Magnetic ordering temperatures exceed $T = 300$ K [82-84]. The only single crystal studied up to now, LuFe_6Al_6 , displays normal ferromagnetic behavior [15].

To summarize, in the whole homogeneity range exchange interactions of RFe_xAl_{12-x} ($4 \leq x \leq 6$) are very sensitive to the Fe concentration. The decisive role is played by the Fe atoms in the $8j$ site. In RFe_4Al_8 , where practically all Fe atoms occupy the $8f$ site, antiferromagnetic $3d-3d$ exchange interactions dominate. As the $8j$ site is filled by Fe atoms, the Fe sublattice tends to a ferromagnetic order. Since the RFe_6Al_6 compounds with non-magnetic R elements are ferromagnets and RFe_4Al_8 antiferromagnets, it is reasonable to assume that the RFe_5Al_7 compounds with an intermediate Fe content display a transitional magnetic structure.

2.3. Magnetic anisotropy and hysteresis properties

Magnetic moments of RFe_4Al_8 compounds lie in the basal plane of the tetragonal lattice [17,18,71,92,93]. To our knowledge, no more information is available in literature on the magnetic anisotropy of these systems.

Magnetic studies of polycrystalline RFe_5Al_7 indicated that practically all of them display strong magnetic hysteresis [20]. The compounds with $R - Yb, Lu$ and Y , whose magnetism originates entirely from the Fe sublattices, exhibit coercivity of the order of 0.1 T at $T = 4.1$ K (Fig. 2.4). Their field variations of magnetization have an interesting shape in that the virgin curve extends outside of the hysteresis loop. This behavior is suggested to be caused by irreversible domain wall motion.

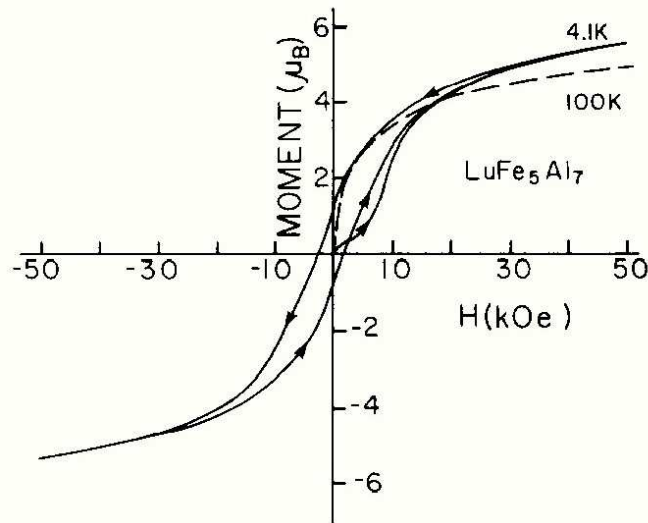


Fig. 2.4. Hysteresis loop of $LuFe_5Al_7$ at $T = 4.1$ K. Practically identical loops were obtained for YFe_5Al_7 and $YbFe_5Al_7$ [20].

The temperature dependence of the magnetization of $SmFe_5Al_7$ was found to be influenced by the cooling rate [20]. This points to strong thermal hysteresis and time dependence of the magnetization. Time effects are observed when measuring magnetization curves of $SmFe_5Al_7$ at $T = 4.1$ K. A rather big time interval, ≈ 3 min, is required for the system to reach an equilibrium after an abrupt change of magnetic field.

RFe_5Al_7 compounds with magnetic heavy rare-earth elements are ferrimagnets. In the whole temperature range of the magnetically ordered state of $GdFe_5Al_7$ the magnetic moment of the Fe sublattice exceeds that of the Gd sublattice: $M_{Fe} > M_{Gd}$ [20,96]. For this reason, no compensation of the Fe and Gd sublattices occurs. Contrary to $GdFe_5Al_7$, in the RFe_5Al_7 compounds with $R - Tb, Dy, Ho$ and Er at low temperatures $M_R > M_{Fe}$ and at high temperatures $M_R < M_{Fe}$ [19,20]. The corresponding temperature variations of magnetization have a compensation point T_{comp} . Its maximum value, 93 K, was found for $R - Dy$, and its minimum value, 29 K, for $R - Er$.

At low temperatures the RFe_5Al_7 compounds with magnetic heavy rare-earth elements display strong magnetic hysteresis [19,20]. At $T = 4.1$ K for $R - Tb, Ho$ and Er the coercivity $\mu_0 H_c$ is about 1 T and for $R - Dy$ it attains 2.5 T. Although H_c rapidly decreases with temperature, its value is still rather high in the vicinity of $T = T_{comp}$. For this reason, the RFe_5Al_7 compounds with $R - Tb, Dy, Ho$ and Er exhibit interesting behavior in a magnetic field at low temperatures. “Negative magnetization” is observed upon cooling from room temperature to $T = 4.1$ K in a low magnetic field $\mu_0 H \leq 0.01$ T (Fig. 2.5). This term is used in Refs. [19,20] for the situation when the total magnetic moment $M_{tot} = M_R - M_{Fe}$ and the magnetic field are antiparallel. The reason for the observed behavior lies in the strong magnetic hysteresis at low temperatures. With decreasing temperature, at the compensation point M_{tot} is reoriented from along the Fe sublattice to along the R sublattice. If the coercivity exceeds the magnetic field at $T = T_{comp}$, the sample’s domain structure does not change, and the total magnetization becomes oriented antiparallel to the magnetic field. For $DyFe_5Al_7$ and $HoFe_5Al_7$ a field of $\mu_0 H = 0.5$ T is sufficiently strong to reorient the majority of the domains along the field at $T = T_{comp}$, and the total magnetization is positive at $T < T_{comp}$. However, for $TbFe_5Al_7$ and $ErFe_5Al_7$ this field is lower than the coercivity at the compensation point, and their total magnetization is antiparallel to the field below it.

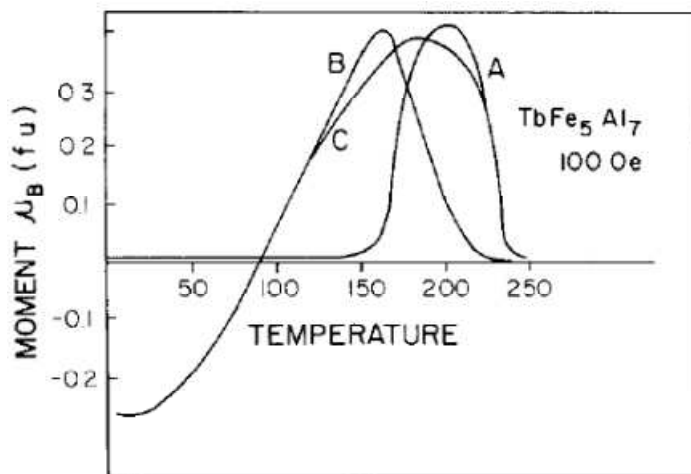


Figure 2.5. Temperature dependence of the magnetization of $TbFe_5Al_7$ measured in 0.01 T with increasing temperature after the sample was first cooled down to $T = 4.1$ K in a zero field (A) and in 0.01 T (B) and measured with decreasing temperature in 0.01 T (C) [20].

Strong thermal and magnetic hysteresis of RFe_5Al_7 suggests strong magnetic anisotropy. Although it has never been studied, powder neutron diffraction provides information on the orientation of magnetic moments in the compounds with $R - Tb, Dy, Ho, Er$ and Tm with respect to the principal crystallographic directions [16]. It was found that the magnetic moments lie in the basal plane of the tetragonal lattice of the systems with $R - Tb, Dy, Ho$ and Er (see Fig. 2.3) and are parallel to the c axis in $TmFe_5Al_7$ (taking into account that in Ref. [16] the columns for $HoFe_5Al_7$ and $TmFe_5Al_7$ in Table 1 are interchanged, see Section 2.2). This result is unexpected for the $ErFe_5Al_7$ compound from the viewpoint of the rare-earth contribution to the magnetocrystalline anisotropy.

At low temperatures the main and much stronger contribution to the magnetic anisotropy of the RFe_5Al_7 compounds is given by the rare-earth sublattice. The anisotropy of the iron sublattice is much weaker. It is expected that the electrostatic interaction between the anisotropic $4f$ electronic shell and the crystalline electric field should lead to different orientations of magnetic moments in two subgroups of the RFe_5Al_7 compounds: those with $R - Tb, Dy$ and Ho and those with $R - Er$ and Tm . As outlined in Section 1.3.1, this is related to the sign of the second order Stevens' factor α_J for the rare-earth ions. For Tb^{3+}, Dy^{3+} and Ho^{3+} $\alpha_J < 0$, while for Er^{3+} and Tm^{3+} $\alpha_J > 0$ [35]. Therefore, one should expect that in $ErFe_5Al_7$ the magnetic moments are oriented along the c axis, similarly to $TmFe_5Al_7$, at least, at low temperatures where the rare-earth anisotropy dominates. On the other hand, the neutron diffraction data might not appear so surprising if one takes into account the $HoFe_{11}Ti$ and $ErFe_{11}Ti$ compounds, isostructural with RFe_5Al_7 . In contrast to all other $RFe_{11}Ti$ systems, the orientation of magnetic moments in those with $R - Ho$ and Er is not in accord with the sign of α_J [98-100]. $HoFe_{11}Ti$ displays easy-axis anisotropy at all temperatures below T_C , whereas in $ErFe_{11}Ti$ the Er sublattice is not uniaxial. One way or another, single crystals are highly desirable for magnetic anisotropy investigations of the RFe_5Al_7 compounds.

Magnetic moments of RFe_6Al_6 compounds also lie in the basal plane of the tetragonal lattice [14]. Strong hysteresis was observed for compounds with magnetic R elements [82]. The magnetic anisotropy of the Fe sublattice was deduced from a magnetic study performed on a $LuFe_6Al_6$ single crystal [15]. The second- and fourth-order anisotropy constants were found to be $K_1 = -0.73 \text{ MJ m}^{-3}$ and $K_2 \leq 0.04 \text{ MJ m}^{-3}$, respectively, by the Sucksmith-Thompson method [40].

From the description above it follows that RFe_xAl_{12-x} ($4 \leq x \leq 6$) compounds represent complex systems from the magnetic point of view. The progressive filling of the $8j$ site in the crystal lattice of the $ThMn_{12}$ type results in significant changes of $Fe-Fe$ intra-sublattice and $R-Fe$ inter-sublattice exchange interactions. In order to understand the magnetism of these compounds, the rare-earth and iron contributions should be separated. Compounds with non-magnetic R elements are best suited to fulfill this condition since they allow one to examine the Fe sublattice alone. Its magnetic properties in RFe_xAl_{12-x} with $4 \leq x \leq 6$ should be clarified by studying its behavior in an external magnetic field along the principal crystallographic directions.

Such a study will (i) reflect the nature of the Fe-Fe intersublattice exchange interactions and (ii) make it possible to obtain information on the magnetic anisotropy of the Fe sublattice.

In order to establish the connection between RFe_4Al_8 and RFe_6Al_6 with magnetic rare-earth elements, it is necessary to study the magnetism of RFe_5Al_7 compounds having an intermediate Fe content. In doing so, the role of individual rare-earth elements should be reflected. This can be achieved by investigating the inter-sublattice R -Fe exchange interactions and magnetic anisotropy. Relatively weak R -Fe exchange interactions might lead to a complex behavior in magnetic field. It might also be suggested that the RFe_5Al_7 compounds display strong magnetic anisotropy on the basis of the results obtained on polycrystalline samples. A detailed systematic study of exchange interactions and magnetic anisotropy requires single crystals with different rare-earth components.

Chapter 3: Experimental methods

3.1. Sample preparation

In the present work all studies of magnetic and magnetoelastic properties of $R\text{Fe}_x\text{Al}_{12-x}$ compounds were performed on single crystals. $\text{LuFe}_x\text{Al}_{12-x}$ ($x = 4, 4.5, 5, 5.5$) and $R\text{Fe}_5\text{Al}_7$ (R - Gd, Tb, Dy, Ho, Er) single crystals were grown by the modified Czochralski method under protective Ar atmosphere in a tri-arc furnace in the Joint Laboratory for Magnetic Studies in Prague, Czech Republic. The crystals were pulled out from a stoichiometric mixture of the pure elements (99.9% R , 99.98% Fe and 99.999% Al) melted on a water-cooled rotating copper crucible. A tungsten rod at room temperature was used as a seed. During the growing process, it was partially immersed in the melt for several seconds and subsequently raised to pull out the solidified alloy stuck to it. The pulling speed, varied between 10 and 20 mm/h, was adjusted in such a way as to create favorable thermodynamic conditions for single crystal growth. The diameter of the obtained single crystals was 2-6 mm, their length varied between 20 and 40 mm.

3.2. Sample characterization

3.2.1. X-ray powder diffraction

X-ray diffraction was performed on parts of the single crystals crushed into a fine powder using a diffractometer Bruker D8 Advance in Cu-K_α radiation. The occurrence of diffraction from a crystal is explained by the Bragg law: constructive interference of a radiation from successive planes occurs when the path difference is an integral number n of wavelengths λ , so that

$$2d\sin\theta_{hkl} = n\lambda, \quad (3.1)$$

where d is the distance between lattice planes (hkl) and θ_{hkl} the angle between them and the incident (reflected) beam [27].

Ideally, in a given powder every possible crystalline orientation occurs with equal probability. In powder X-ray diffraction, the wavelength of the incident radiation is fixed, and the diffraction condition (3.1) is satisfied for specific θ_{hkl} and d .

The X-ray powder diffraction was performed in Bragg-Brentano geometry (Fig. 3.1), that is, the X-ray source and the detector are situated on the same circle [101]. The main condition for constructive interference to occur is that if the powder specimen has a flat surface, it should be tangential to the focusing circle and its normal vector must bisect the angle between the directions to the X-ray source and detector.

The absolute error of an inter-spatial distance for a single reflection can be found using the equation

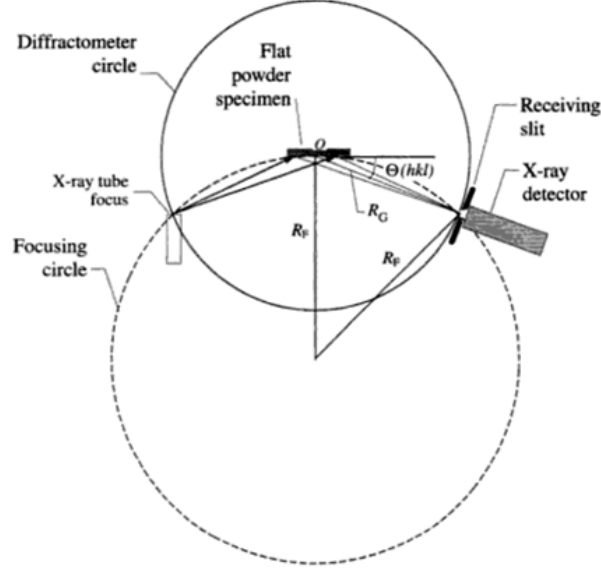


Figure 3.1. Bragg-Brentano geometry for X-ray powder diffraction [101].

$$\delta d = \frac{\partial d}{\partial \theta} \partial \theta = d \cot \theta \delta \theta, \quad (3.2)$$

where $\delta \theta$ is the absolute error of an angle expressed in radians.

Lattice parameters were refined using Fullprof software [102] based on the Rietveld algorithm [103]. It uses the least-square method to calculate an X-ray diffraction pattern according to a given structural model and performs its refinement until it coincides with an experimental X-ray diffraction pattern. Mathematically, the Rietveld method minimizes a function M that analyzes the difference between a calculated profile $y(\text{calc})$ and the observed data $y(\text{obs})$:

$$M = \sum_i W_i \left\{ y_i^{\text{obs}} - \frac{1}{c} y_i^{\text{calc}} \right\}, \quad (3.3)$$

where W_i is the statistical weight and c an overall scale factor, such that $y^{\text{calc}} = cy^{\text{obs}}$.

As an example, Fig. 3.2 demonstrates a powder X-ray diffraction pattern of the LuFe_4Al_8 compound. The figure also shows a calculated X-ray diffraction pattern according to the structural model presented in Chapter 2 for $R\text{Al}_{12-x}\text{Fe}_x$ systems. The R factors obtained for LuFe_4Al_8 are $R_{\text{Bragg}} = 9.54\%$, $R_{\text{F}} = 5.3\%$, and $\chi^2 = 0.147$.

3.2.2. Single crystal orientation by Laue back reflection of X-rays

The back reflection Laue method was used to check the single crystalline state and to orient single crystals on a Mikrometa apparatus. In this case the wavelength of the incident radiation is not fixed, the sample is exposed to a beam of white radiation. For each crystal plane in a given orientation both θ_{hkl} and d are fixed. For a particular n some λ will satisfy the condition (3.1), and the corresponding

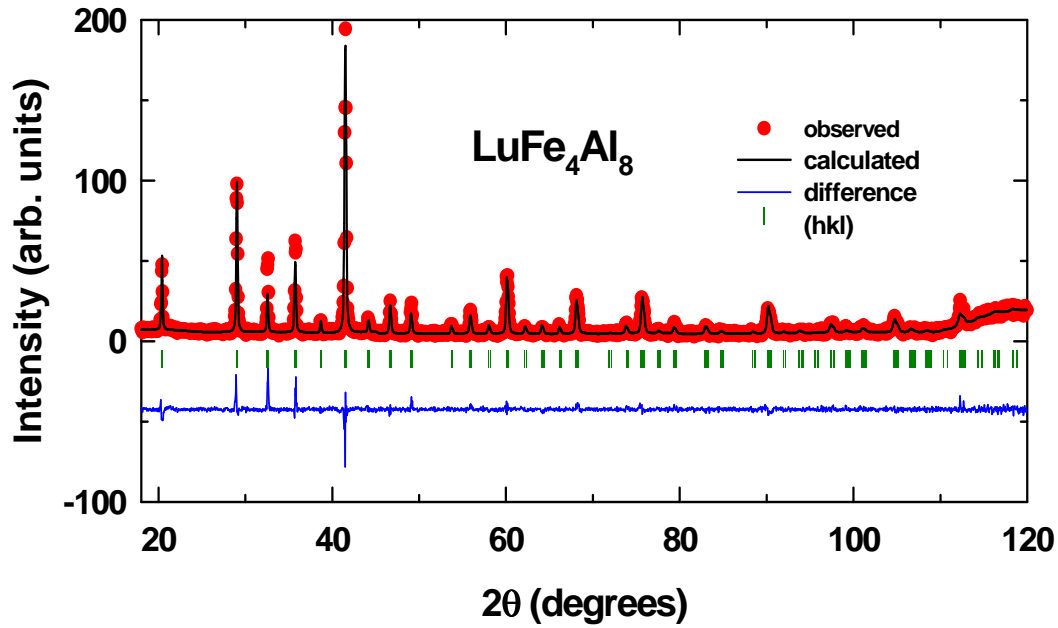


Fig. 3.2. Observed (red circles) and calculated (black line) powder X-ray diffraction patterns of LuFe_4Al_8 , and the difference between them (blue line).

Laue spot will be observed. The symmetry of the Laue pattern corresponds to the symmetry of the crystal and, therefore, reflects its orientation.

Laue diffraction patterns are collected on a film placed between the X-ray source and the crystal (Fig. 3.3). The beams that are diffracted in the backward direction are recorded on the film that intersects the cone of Laue reflections.

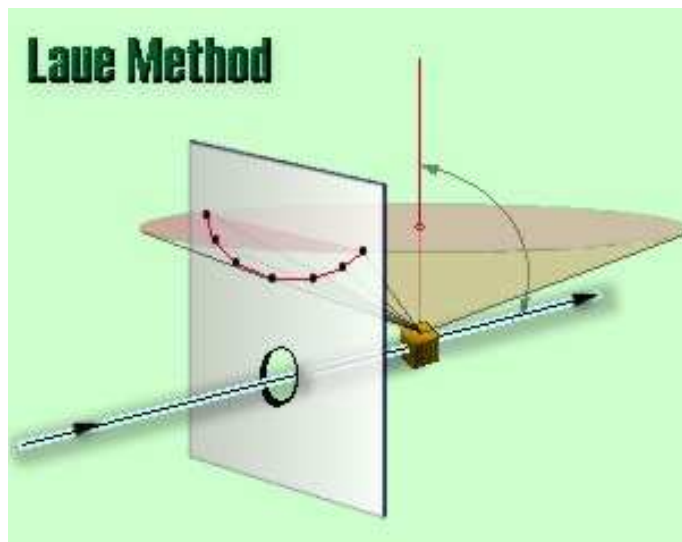


Fig. 3.3. Geometry of the Laue back reflection method.

Typical Laue diffraction patterns are shown in Fig. 3.4 along the [100], [110] and [001] axes of $R\text{Fe}_x\text{Al}_{12-x}$ single crystals studied in the present work.

A goniometric head was used to fix the desired orientation of the single crystals to be cut for further experiments.

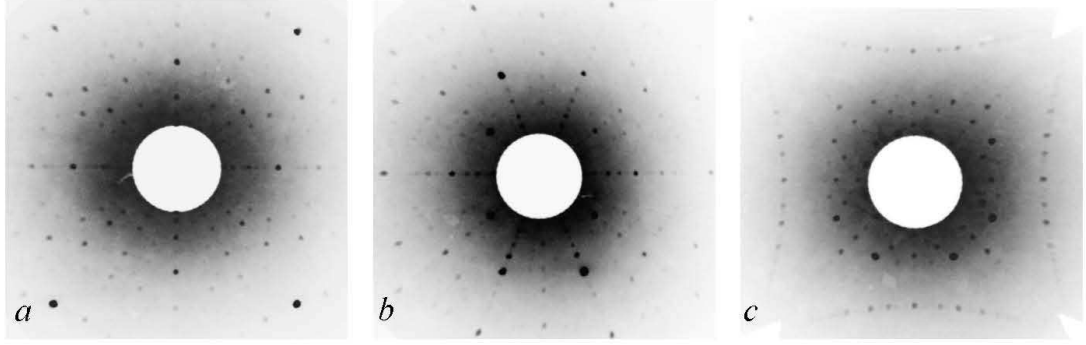


Fig. 3.4. Back-scattered Laue patterns with X-ray beam along the [100] (a), [110] (b) and [001] (c) axes of a DyFe_5Al_7 single crystal.

3.3. Magnetization measurements

Magnetization measurements along the principal crystallographic directions of $\text{RFe}_x\text{Al}_{12-x}$ single crystals were performed in static (up to 14 T) and in pulsed (up to 60 T) magnetic fields.

3.3.1. Static magnetic fields

Magnetization measurements in static magnetic fields were performed by extraction technique using Physical Property Measurement Systems PPMS-9 and PPMS-14 with maximum magnetic fields 9 T and 14 T, respectively. During the measurements, a constant field is applied to the measurement region. The field is created by a superconducting magnet, its value is determined with an error of 5×10^{-5} T. The sample is quickly (~ 0.05 s) moved through a set of coils inducing a signal in them according to Faraday's law, that is, the electromotive force ε is proportional to the rate of change of the magnetic flux Φ through them:

$$\varepsilon = -\frac{d\Phi}{dt}. \quad (3.4)$$

Voltage profile is created that is the time derivative of the net flux through the coils. Then the actual sample moment is obtained by numerically integrating the voltage profile.

The measuring system consists of several coilsets (Fig. 3.5). The AC drive coil set provides an alternating excitation field (not used in the measurements performed in the present work). A compensation coil is situated outside the drive coil to reduce dipole fields to quadruple fields. The drive coil and compensation coil are counterwound and connected in series so that they receive the same excitation signal. The detection coil set responds to the combined sample moment and excitation field. The detection coils are arranged in such a way to help isolate the sample's signal from background sources. There are two sets of counterwound copper coils separated by several centimeters. Each detection coil also contains a low-inductance calibration

coil. These two single-turn calibration coils are situated at the center of each detection coil where the sample measurements occur.

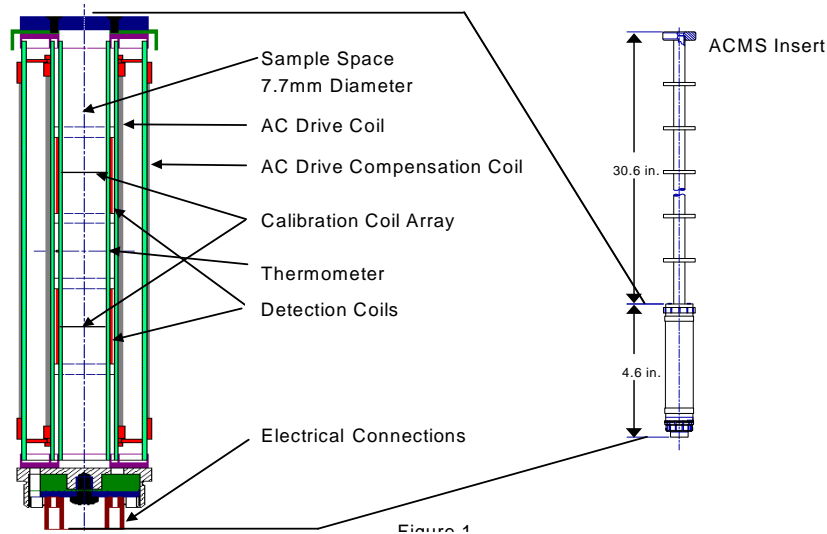


Fig. 3.5. Measuring system insert and coilset.

During DC measurements the amplitude of the detection coil signal is dependent upon both the extraction speed and the sample's magnetic moment. Samples are extracted at speeds of approximately 1 m/s, thus increasing the signal strength and reducing the contribution of time-dependent errors. These advantages result in greater measurement accuracy and sensitivity compared to systems with slower sample extraction speeds.

A sample undergoes a five-point measurement process (Fig. 3.6). The first reading is made with the sample positioned in the center of the bottom detection coil. Then the sample is positioned in the center of the top detection coil, and then in the center of the bottom coil again. Afterwards, the sample is placed at the center of the detection coil array so that it is between the two detection coils. Two more readings are taken with the calibration coil switched into the detection circuit with opposing polarities in order to obtain and subtract environmental and instrumental factors that affect the reading.

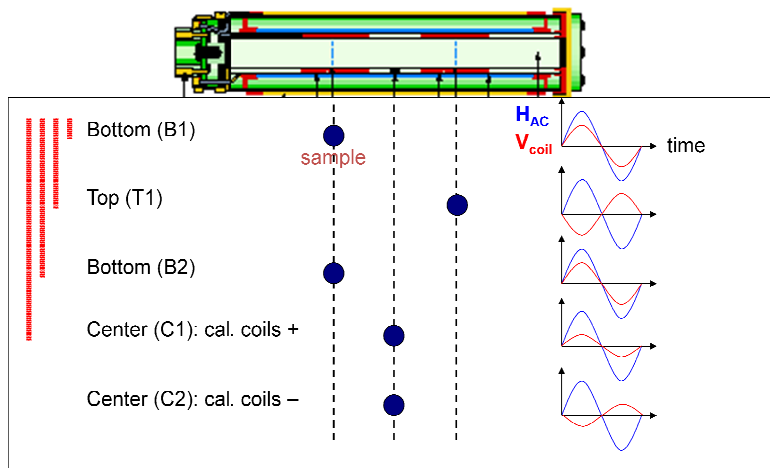


Fig. 3.6. 5-point measurement.

Values of a magnetic moment are determined with a precision of 2.5×10^{-6} emu.

3.3.2. Pulsed magnetic fields

Magnetization curves in pulsed magnetic fields up to 60 T were measured by induction method at the High-field Laboratory in Dresden-Rossendorf [104]. A single 1.44 MJ capacitor module was used. It was charged up to 22 kV and delivered a peak current of 30 kA that produced a maximum magnetic field of 60 T with a rise time of 7 ms (the total pulse duration was 25 ms).

A coaxial system of detection coils was used as it is weakly sensitive to gradients and vibrations. Magnetic field measurements are performed by two coils connected in series (Fig. 3.7). They are located reasonably far above and below from the sample position. The signal induced in the coils is proportional to the time derivative of magnetic field, $\dot{H} = dH/dt$. It is recorded by a digitizer and integrated numerically. The pick-up coil signal was calibrated using a magnetization curve of antiferromagnetic MnF_2 that displays a temperature independent spin-flop transition in a field of 9.27 T [105].

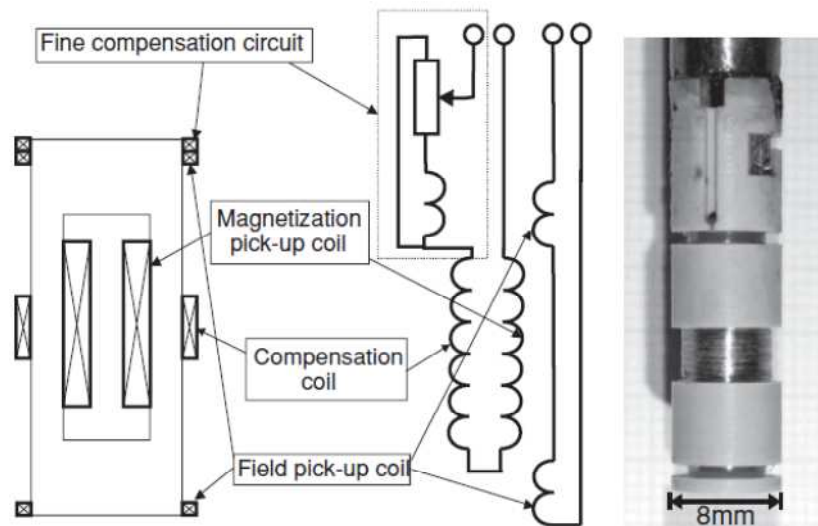


Fig. 3.7. Pickup-coil system used in the pulsed-field magnetometer: (left) the principal sketch, (middle) the electrical scheme, and (right) a picture of the original set up [104].

Since the sample pick-up coil is situated in a varying magnetic field, it is connected with a compensation coil in order to subtract the \dot{H} contribution to the signal. The temperature independent part of the signal was also reduced at each temperature by means of a fine compensation circuit represented by an additional coil. For higher precision, measurements were repeated in the absence of the sample, and the obtained signal was subtracted from the sample's magnetization curve. The absolute values of magnetization were calibrated by static field measurements performed by means of PPMS-9 or PPMS-14.

3.4. Magnetization measurements under pressure

Magnetization measurements under hydrostatic pressure were performed up to $p = 0.86$ GPa in a miniature CuBe pressure cell (Fig. 3.8) up to 7 T using a SQUID magnetometer. The dimensions of the cell (inner diameter 2.5 mm and outer diameter 8.6 mm) are limited by a sample space in the SQUID magnetometer [106]. The pressure transmitting medium was chosen to be spindle oil. A single crystalline sample is mounted on a sample holder sealed by a set of copper and plastic rings. The misalignment owing to the sample holder between the crystal axes and the SQUID axes is less than 3° . Pressure is determined in the low temperature region from a shift of the critical temperature T_{crit} of the superconducting transition of a Pb sensor placed inside the cell (Fig. 3.9) by the following law:

$$p = \frac{T_{\text{crit}}(0) - T_{\text{crit}}(p)}{0.405}, \quad (3.5)$$

$[p] = \text{GPa}$, $[T_{\text{crit}}] = \text{K}$.

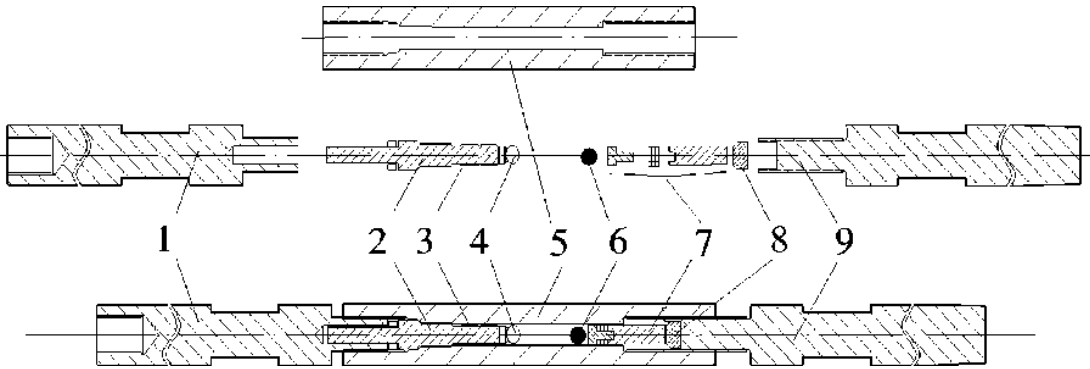


Fig. 3.8. Miniature CuBe pressure cell; 1, 9 - upper and lower pressure clamping bolts, 2 - plug with 3 - sealing, 4 - sample on a holder, 5 - pressure cell, 6 - lead pressure sensor, 7 - piston with Bridgman mushroom-type seal, 8 - piston backup [106].

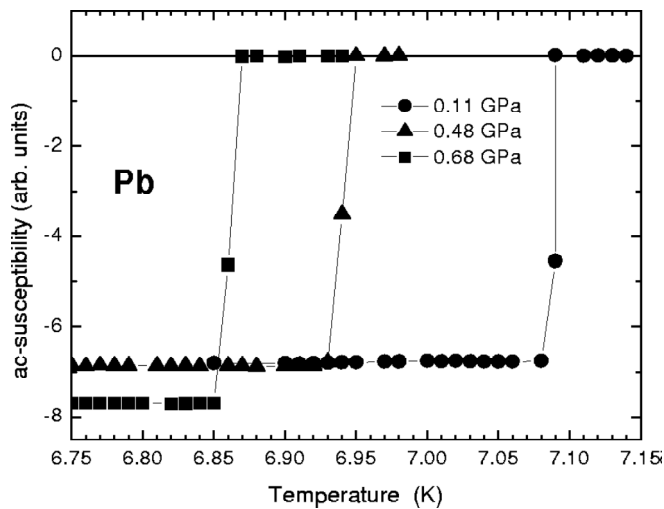


Fig. 3.9. Temperature dependence of ac susceptibility of Pb under different pressures [106].

Pressure inside the cell grows with increasing temperature due to different thermal expansions of the cell and pressure transmitting medium. These changes were taken into account for correct data analysis.

3.5. Ultrasound experiments

Measurements of relative sound velocity changes and sound attenuation were performed in Dresden High Magnetic Field Laboratory in static (up to 18 T) and pulsed magnetic fields (up to 63 T). A pair of piezoelectric transducers is bonded to a single crystalline specimen with parallel polished planes (Fig. 3.10). One transducer acts as an emitter, the other as a receiver. A pulsed electromagnetic signal of $\sim 1 \mu\text{s}$ duration is applied across the transducer. The signal operates at the fundamental frequency of the transducer or at one of its odd harmonics [43]. With the piezoelectric effect, a stress wave is produced which propagates through the specimen. Upon reflection on the surface, a small amount of energy is converted back into an electric pulse. The major part of the pulse is reflected and propagates further.

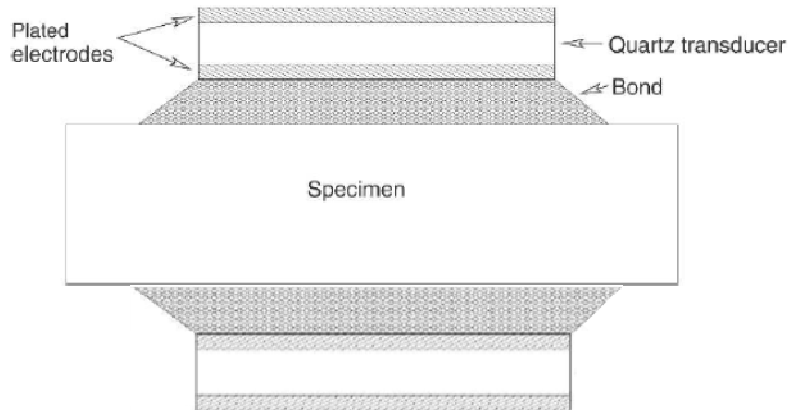


Fig. 3.10. Transducer-bond-specimen arrangement [43].

The apparatus used in Dresden High Magnetic Field Laboratory makes it possible to measure simultaneously relative changes of sound velocity, $\Delta v/v$, and sound attenuation, $\Delta\alpha$, as a function of temperature and magnetic field. The frequency range is 1 – 500 MHz. The procedure to calculate $\Delta v/v$ and $\Delta\alpha$ is the following. Each transit of a sound wave through the sample gives a phase shift

$$\Phi = kL_0, \quad (3.6)$$

where k is the wavevector of the ultrasound, L_0 the sample length. The n -th echo has a phase shift

$$\Phi_0 = kL_0(2n + 1) = \frac{\omega}{v}L_0(2n + 1) \quad (3.7)$$

with respect to the reference signal. The relative sound velocity change is calculated by differentiating Eq. (3.7):

$$\frac{d\Phi_n}{\Phi_n} = \frac{d\omega}{\omega} - \frac{dv}{v} + \frac{dL_0}{L_0}. \quad (3.8)$$

With the constant phase, the frequency change is directly proportional to the velocity change. Usually, the length changes due to temperature variation (thermal expansion) or due to magnetic field (magnetostriction) can be neglected in comparison with the velocity changes [43].

For the sound attenuation measurements, echo trains (see an example of an echo train in Fig. 3.11) can be fitted with an exponential function.

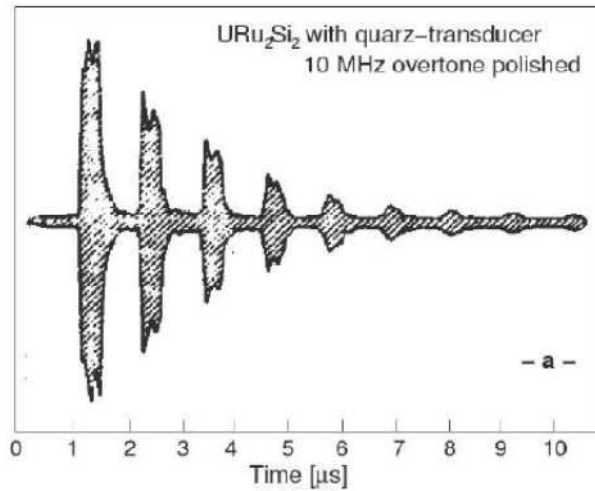


Fig. 3.11. Pulse echo train for ultrasonic waves in URu_2Si_2 with quartz transducers [43].

3.6. Heat capacity measurements

Heat capacity at constant pressure, C_p , was measured by relaxation method using PPMS-9 and PPMS-14 in the temperature range $T = 2 - 300$ K. Heat is added to and then removed from a sample while controlling its temperature change. First, a known amount of heat is supplied at constant power for a fixed time, and then a cooling period of the same duration follows.

A sample is mounted on the sample platform using a thin layer of apiezon grease that provides a good thermal contact between them (Fig. 3.12). A platform heater and platform thermometer are attached to the bottom side of the sample platform. Connecting wires provide electrical connection to the platform heater and platform thermometer.

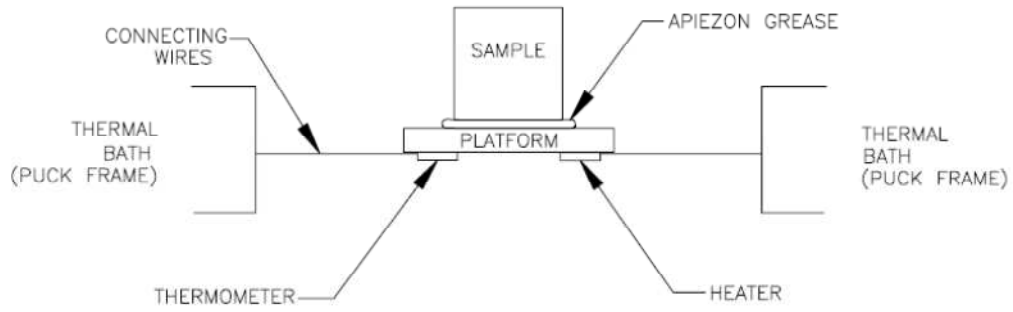


Fig. 3.12. Thermal connections to sample and sample platform used for specific heat measurements.

Measurements are performed at a sufficiently high vacuum ($p \approx 0.01$ mTorr) so that the thermal conductance between the sample platform and the puck is dominated by the conductance of the wires. The measurement time should be long enough to allow both the platform and sample to achieve sufficient thermal equilibrium during the measurement. Furthermore, the sample heat capacity should be large as compared to that of the sample platform. For a high precision in the determination of the sample's heat capacity, measurements were first performed without the sample to determine C_p of the sample platform with apiezon grease. Then, the sample was put onto the platform, and its heat capacity was measured in the same temperature range as that of the platform.

Two models are used in order to convert raw data into specific heat values, depending on how good the thermal contact is between the sample and sample platform. When the contact is good, the simple model comes into play that assumes that the sample and sample platform are at the same temperature during measurements. The temperature of the platform as a function of time is determined by the following equation:

$$C_{\text{total}} \frac{dT}{dt} = -K_w(T - T_b) + P(t), \quad (3.9)$$

where C_{total} is the total heat capacity of the sample and sample platform, K_w the thermal conductance of the connecting wires, T_b the temperature of the thermal bath (puck frame) and $P(t)$ the heater power. The heater power has a finite value during heating of the sample, and it is zero during cooling of the sample. The solution of Eq. (3.9) for the cooling period is

$$T(t) \sim \exp\left(-\frac{t}{\tau}\right), \quad (3.10)$$

where $\tau = C_{\text{total}}/K_w$ is a relaxation time.

The two-tau model is used when there is a poor thermal contact between the sample and sample platform so that they are at different temperatures, T_p and T_s , respectively. The model simulates heat flow between the sample platform and

sample and between the sample platform and puck. The temperatures of the sample platform and sample are separated:

$$\begin{aligned} C_{\text{platform}} \frac{dT_p}{dt} &= P(t) - K_w(T_p(t) - T_b) + K_g(T_s(t) - T_p(t)), \\ C_{\text{sample}} \frac{dT_s}{dt} &= -K_g(T_s(t) - T_p(t)), \end{aligned} \quad (3.11)$$

where C_{platform} and C_{sample} are the heat capacities of the sample platform and sample, respectively, and K_g the thermal conductance between them through the grease. The solution to the system of Eqs. (3.11) for the cooling period is

$$T(t) \sim \exp\left(-\frac{t}{\tau_1}\right), \exp\left(-\frac{t}{\tau_2}\right), \quad (3.12)$$

where τ_1 and τ_2 are relaxation times.

To calculate the heat capacity of a sample, the system compares the solution to the simple model with the actual measurement using a non-linear least-square fitting algorithm. If the heat capacity of the sample platform (in the absence of a sample) is not measured, a fit to the two-tau model is also performed. The system uses C_p values obtained from this model only if the fit deviation is smaller than that to the simple model.

Chapter 4: Evolution of magnetism in $\text{LuFe}_x\text{Al}_{12-x}$ compounds ($4 \leq x \leq 6$)

In $\text{RFe}_x\text{Al}_{12-x}$ ($4 \leq x \leq 6$) compounds with a tetragonal crystal structure of the ThMn_{12} type the $8j$ site is progressively filled with Fe atoms. This not only strengthens the intra-sublattice Fe-Fe and inter-sublattice R -Fe exchange interactions but also changes the type of magnetic order within the Fe sublattice. In order to understand magnetic properties of the $\text{RFe}_x\text{Al}_{12-x}$ ($4 \leq x \leq 6$) compounds it is necessary to separate contributions made by the Fe and R sublattices. The magnetic properties of the Fe sublattice can be determined by studying compounds with R elements that carry no magnetic moment, e.g., with Lu. Although the magnetic properties of $\text{LuFe}_x\text{Al}_{12-x}$ ($4 \leq x \leq 6$) have been studied on polycrystalline samples, no systematic investigations have been performed of the concentration evolution of their exchange interactions and magnetocrystalline anisotropy. This Chapter presents results of a systematic study of the fundamental magnetic properties of $\text{LuFe}_x\text{Al}_{12-x}$ single crystals with the Fe content $x = 4, 4.5, 5, 5.5$ and 6 grown by the Czochralski method.

4.1. Lattice parameters

Figure 4.1 shows concentration dependence of the lattice parameters a and c of $\text{LuFe}_x\text{Al}_{12-x}$ ($x = 4 - 6$). The parameter a decreases by 1.2% from $x = 4$ to 6 , whereas the parameter c is practically unchanged. Such anisotropic shrinkage results in 1% increase of the c/a ratio shown in Fig. 4.1 as well. The decrease in the lattice parameters is also reflected in the change of the unit cell volume V .

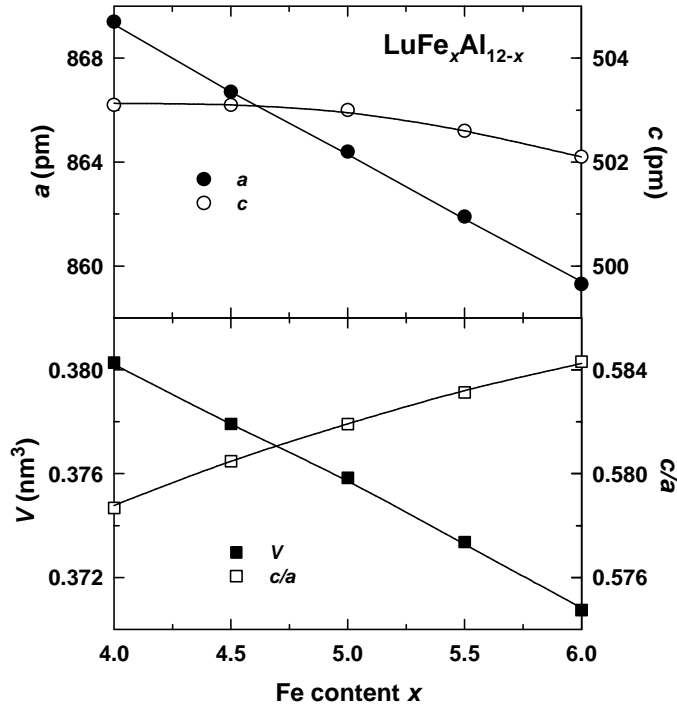


Fig. 4.1. Lattice parameters a and c , ratio c/a and unit cell volume V as a function of the Fe content x in $\text{LuFe}_x\text{Al}_{12-x}$ ($x = 4 - 6$).

From LuFe_4Al_8 to LuFe_6Al_6 the overall volume reduction is 2.6%, which is attributed to the smaller atomic radius of Fe (126 pm) than that of Al (143 pm).

4.2. Exchange interactions

Changes in the field dependencies of magnetization M of $\text{LuFe}_x\text{Al}_{12-x}$ ($x = 4 - 6$) are shown in Fig. 4.2 that presents the concentration evolution of the magnetization curve in ascending field (hysteresis will be discussed below) along the [100] axis at $T = 2$ K. A gradual transition is observed from antiferromagnetic to ferromagnetic behavior. The magnetization of LuFe_4Al_8 grows rather slowly. The compound with $x = 4.5$ exhibits much higher low-field susceptibility. It still does not exhibit spontaneous magnetic moment but in 1-2 T it displays an S-shape anomaly that can be treated as a metamagnetic transition. At $x = 5$, the transition field is close to zero, and the compounds with $x = 5.5$ to 6 exhibit spontaneous magnetization.

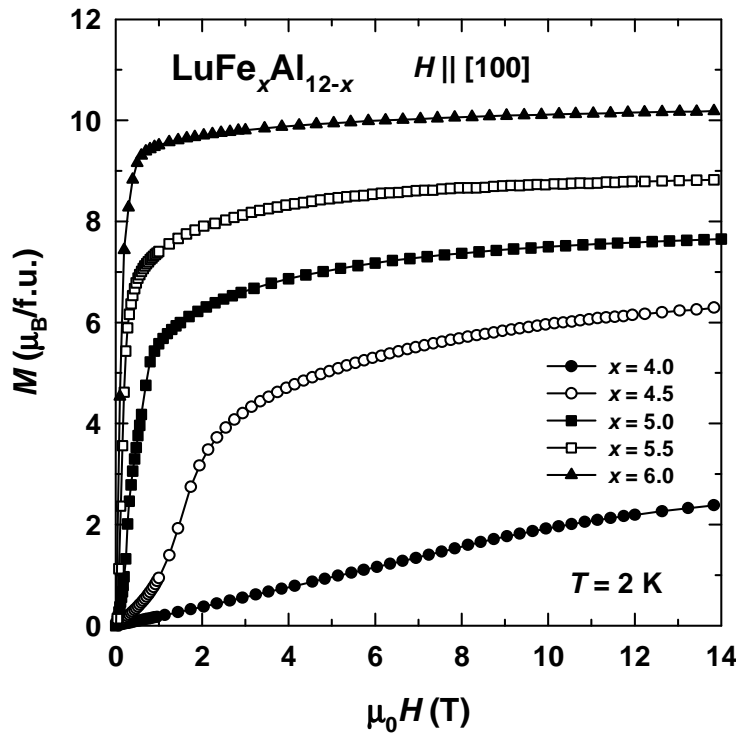


Fig. 4.2. Magnetization curves along the [100] axis of the $\text{LuFe}_x\text{Al}_{12-x}$ single crystals with $x = 4, 4.5, 5, 5.5$ and 6 at $T = 2$ K.

The observed changes in the behavior of $\text{LuFe}_x\text{Al}_{12-x}$ in a magnetic field as x increases from 4 to 6 indicate that the addition of Fe strongly modifies the magnetic exchange interactions of the compounds. In the following discussion the magnetic properties of the five $\text{LuFe}_x\text{Al}_{12-x}$ ($x = 4, 4.5, 5, 5.5$ and 6) compounds will be presented in detail.

4.2.1. LuFe₄Al₈

Figure 4.3 shows the temperature dependence of the magnetization along the [100] axis of the LuFe₄Al₈ single crystal in a magnetic field of 0.1 T. One observes very low practically constant M values at low temperatures followed by a decrease in the magnetization at $T > 120$ K. The change in the behavior of magnetization at $T = 120$ K is attributed to a phase transition into the antiferromagnetic state. Similar $M(T)$ dependence for a polycrystalline LuFe₄Al₈ sample, but with an anomaly at approximately $T = 105$ K, was observed in Ref. [91]. The specific heat also shown in Fig. 4.3 does not display any anomalies whatsoever, neither in the vicinity of the Néel temperature $T_N = 120$ K nor at lower temperatures. The absence of any anomaly in C_p implies a very low magnetic entropy change at the magnetic phase transition. It should be noted that in Ref. [107] an anomaly was reported in C_p of a polycrystalline LuFe₄Al₈ sample at $T = 24$ K that was attributed to a phase transition into a superconducting state. The anomaly is not confirmed by the single crystal study in this work.

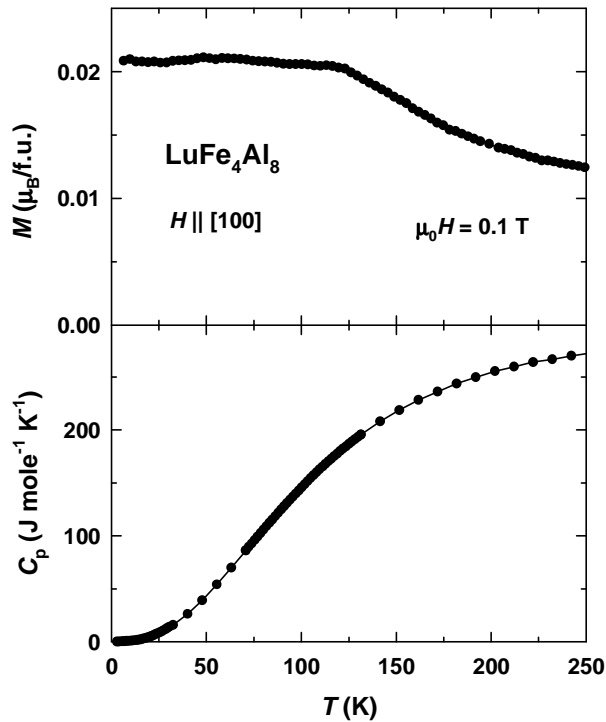


Fig. 4.3. Temperature dependence of the magnetization along the [100] axis in a field of 0.1 T (top) and temperature dependence of the specific heat (bottom) of the LuFe₄Al₈ single crystal.

Magnetization curves along the [100] and [001] axes of the LuFe₄Al₈ single crystal are presented in Fig. 4.4 at several selected temperatures. There is no spontaneous component along either axis. With increasing temperature, the field-induced magnetic moment gradually decreases. Whereas in Fig. 4.2 where $M(H)$ of LuFe₄Al₈ is shown in comparison with other compounds having much larger magnetization no special feature is seen, a detailed examination of the magnetization

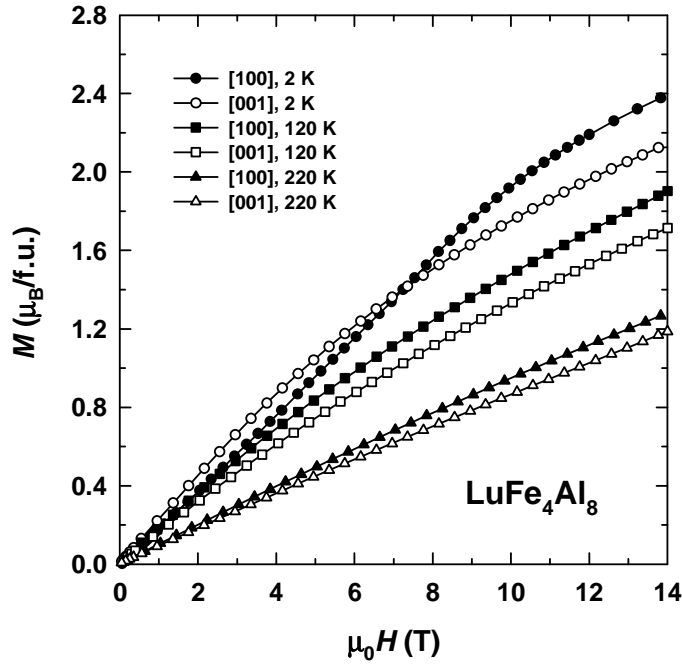


Fig. 4.4. Magnetization curves along the [100] and [001] axes of the LuFe_4Al_8 single crystal at several selected temperatures.

curve along the [100] axis at $T = 2$ K shows that it displays weak S-shape (similar to a much more pronounced S-shape in $\text{LuFe}_{4.5}\text{Al}_{7.5}$ and LuFe_5Al_7 , see below). The S-shape implies rotation of magnetic moments lying in the basal plane from the initial antiferromagnetic to a non-collinear ferromagnetic configuration through a metamagnetic transition. The transition is very broad. In order to determine the critical field H_{cr} of the transition, the field derivative of the magnetization, dM/dH , was calculated. It is shown in Fig. 4.5 with the magnetization curves at $T = 2$ and 80 K to allow a comparison between the two temperatures. At $T = 2$ K dM/dH displays a non-monotonous behavior with a maximum at 8 T which can be treated as $\mu_0 H_{\text{cr}}$. With increasing temperature the anomaly becomes less pronounced and shifts to a lower field. At $T = 80$ K no anomaly is present on the dM/dH curve. The temperature dependence of the transition field (inset in Fig. 4.5) shows that H_{cr} gradually decreases with temperature. The transition is no longer seen at $T > 80$ K.

The small ferromagnetic component induced by an external field is preserved when switching the field in the opposite direction. Figure 4.5 shows that LuFe_4Al_8 displays magnetic hysteresis with a low remanent magnetization. The coercive field is equal to 0.16 T at $T = 2$ K and rapidly diminishes with increasing temperature (inset in Fig. 4.6). However, the hysteresis disappears completely only in a rather high field of 10 T. This is rather unusual since the hysteresis originates only from the Fe sublattice.

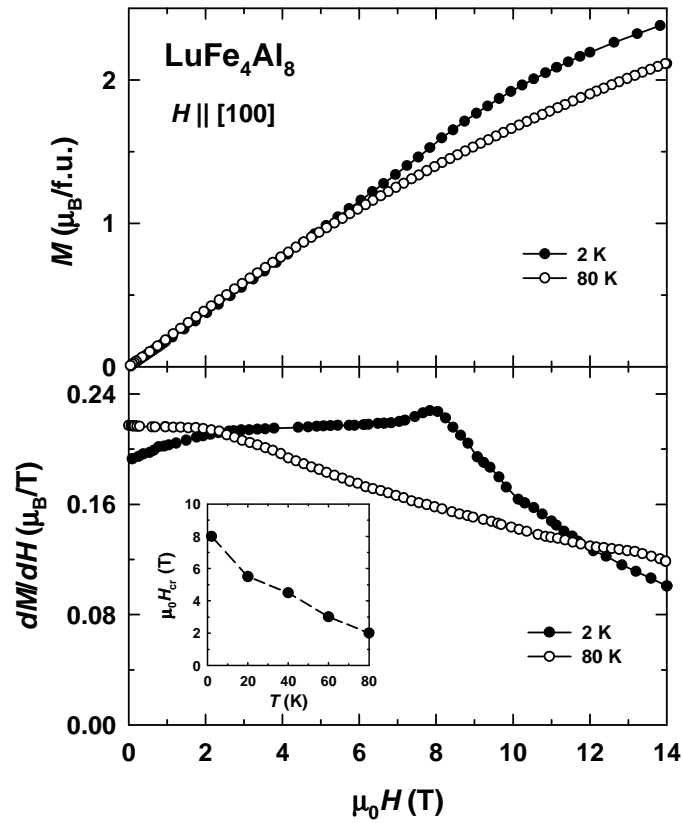


Fig. 4.5. Magnetization curves along the [100] axis of the LuFe_4Al_8 single crystal at $T = 2$ K and 80 K (top) and their field derivatives (bottom). The inset shows the temperature dependence of the critical field of the metamagnetic transition.

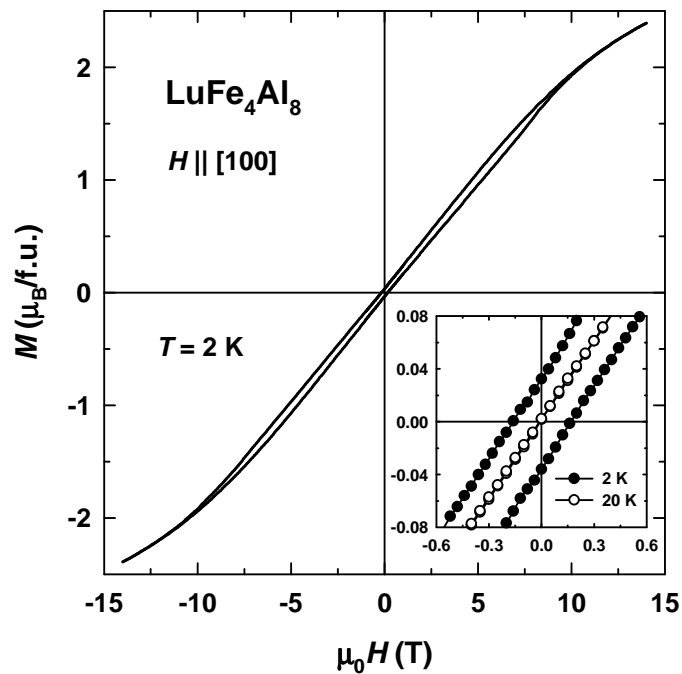


Fig. 4.6. Hysteresis loop along the [100] axis of the LuFe_4Al_8 single crystal at $T = 2$ K. The inset shows low-field details of the hysteresis loops at $T = 2$ and 20 K.

4.2.2. LuFe_{4.5}Al_{7.5}

Figure 4.7 shows the temperature dependence of the magnetization along the [100] and [001] axes of the LuFe_{4.5}Al_{7.5} single crystal. The addition of Fe results in much higher M values, in comparison with LuFe₄Al₈. The main feature on both curves is a broad maximum observed in the vicinity of $T = 120$ K followed by a steep decrease in the magnetization with increasing temperature. The specific heat (not shown) displays no anomalies, similarly to that of LuFe₄Al₈ (Fig. 4.3).

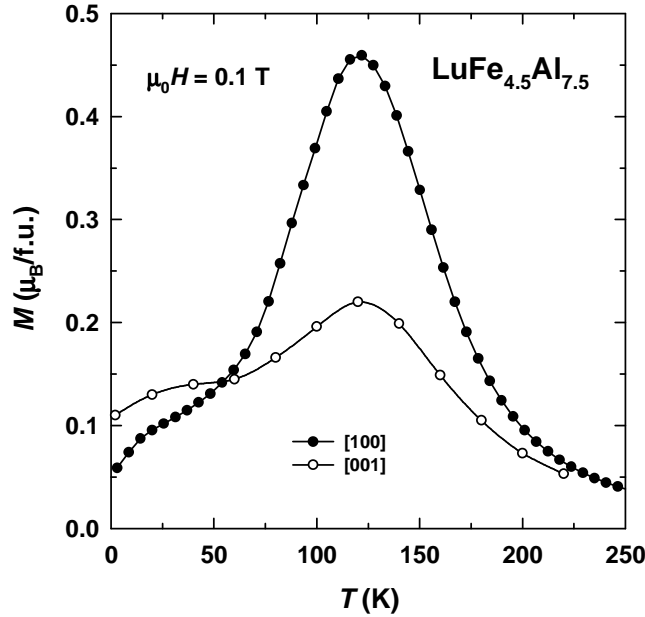


Fig. 4.7. Temperature dependence of the magnetization along the [100] and [001] axes of the LuFe_{4.5}Al_{7.5} single crystal in a field of 0.1 T.

Figure 4.8 presents magnetization curves along the [100] and [001] axes of the LuFe_{4.5}Al_{7.5} compound at several selected temperatures. For clarity, only field-ascending branches are shown, the low-field details will be discussed below. Magnetization along both axes assumes rather high values as compared to LuFe₄Al₈. In addition, the magnetization along the [100] axis displays a field-induced magnetic transition with $\mu_0 H_{cr} = 1.5$ T at $T = 2$ K. Above the transition the magnetization continues to grow as a function of field. The magnetic susceptibility in a field below the transition is lower along the [100] axis than along the [001] axis, which is also seen in Fig. 4.7. In a field of 14 T the [100] and [001] curves exhibit close values of magnetization of about $6 \mu_B/f.u.$ If we assume a value of $\sim 1.5 \mu_B/Fe$ atom as was found in isostructural RFe_5Al_7 compounds with $R = Gd$ [108,109], Tb [110], Dy [111], Ho [112], Er [113] and Tm [114], the saturation ($\sim 6.5 \mu_B$) will be reached in a field slightly higher than 14 T. From the observed anisotropy of magnetization it follows that the magnetic moments in LuFe_{4.5}Al_{7.5} lie in the basal plane, the [001] axis is the hard magnetization direction. No anisotropy within the basal plane was detected as found from a comparison between magnetization curves along the [100] and [110] axes (not shown).

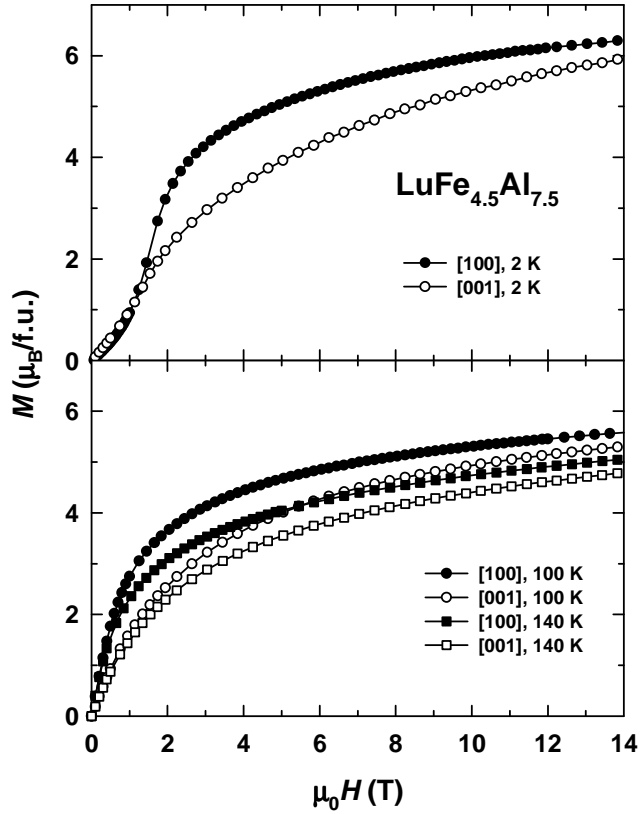


Fig. 4.8. Magnetization curves along the [100] and [001] axes of the $\text{LuFe}_{4.5}\text{Al}_{7.5}$ single crystal at several selected temperatures

Since the $\text{LuFe}_{4.5}\text{Al}_{7.5}$ compound does not display a spontaneous magnetic moment in the whole temperature range of the magnetically-ordered state, it is an antiferromagnet, similarly to LuFe_4Al_8 . From the broad maximum in magnetization (Fig. 4.7) it can be concluded that the antiferromagnetic exchange interactions are suppressed at $T_N \approx 120$ K. For a more precise determination of T_N a neutron diffraction study is necessary.

The temperature evolution of the magnetization curve along the easy [100] axis of $\text{LuFe}_{4.5}\text{Al}_{7.5}$ is shown in Fig. 4.9. With increasing temperature the transition is shifted to lower fields, becomes less pronounced and finally disappears at $T > 80$ K. The inset in Fig. 4.9 shows the variation of the transition field H_{cr} with temperature.

The observed jump in magnetization is a metamagnetic transition. It reflects that the initial antiferromagnetic configuration is broken, and a ferromagnetic component is induced along the magnetic field. The fact that the transition shifts to a much lower field as x grows (8 T at $x = 4$ vs. 1.5 T at $x = 4.5$ at $T = 2$ K) reflects that the antiferromagnetic exchange interactions are weakened with increasing Fe concentration.

Details of hysteresis loops along the [100] axis of the $\text{LuFe}_{4.5}\text{Al}_{7.5}$ single crystal at low temperatures are shown in Fig. 4.10. The ferromagnetic component induced at the metamagnetic transition is preserved in zero field at low temperatures. Both the remanent magnetization and the width of the hysteresis loop rapidly diminish with increasing temperature. At $T = 2$ K the virgin curve extends to a region

outside of the hysteresis loop. The reason is that the virgin curve reflects the irreversible transition from the antiferromagnetic to the ferromagnetic state with a much larger hysteresis than that provided by ferromagnetic domains that determine the hysteresis loop.

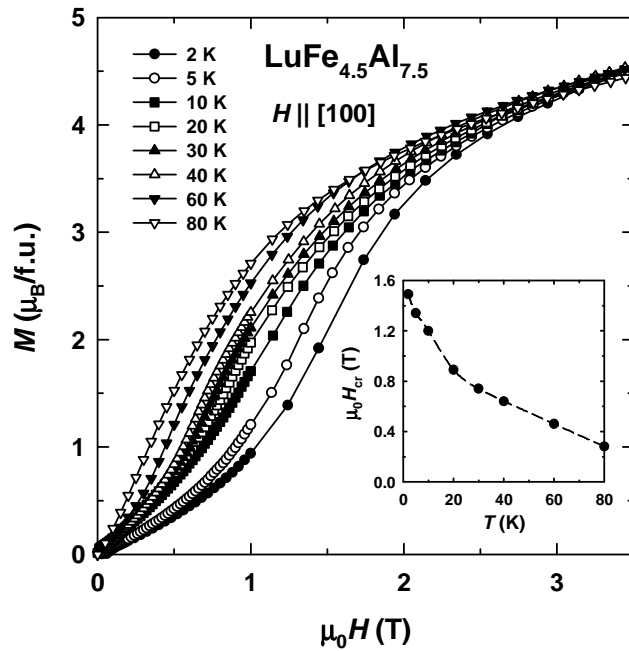


Fig. 4.9. Temperature evolution of the magnetization curve along the [100] axis of the $\text{LuFe}_{4.5}\text{Al}_{7.5}$ single crystal in the range $T = 2 - 80$ K. The inset shows the temperature dependence of the critical field of the metamagnetic transition.

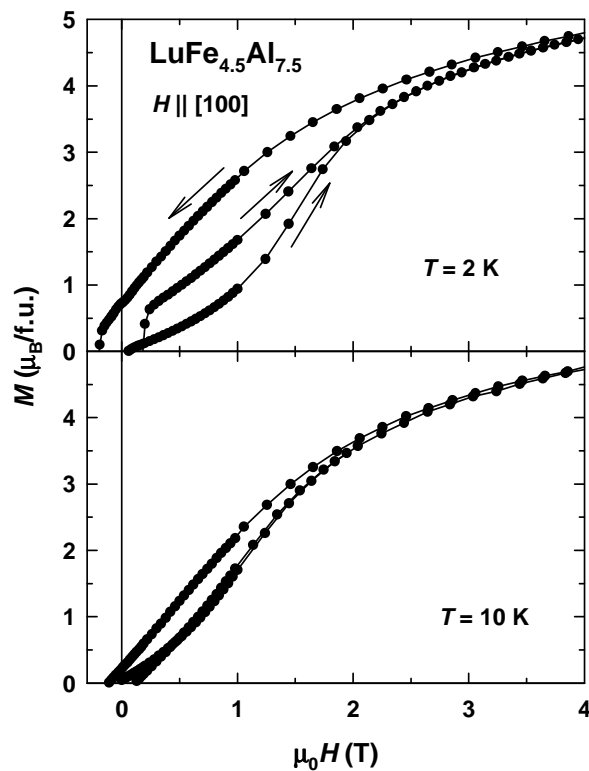


Fig. 4.10. Low-field details of the hysteresis loops measured along the [100] axis of the $\text{LuFe}_{4.5}\text{Al}_{7.5}$ single crystal at $T = 2$ and 10 K.

4.2.3. LuFe₅Al₇

The temperature dependence of the magnetization along the [100] and [001] axes of the LuFe₅Al₇ single crystal is presented in Fig. 4.11. On the curve along the [100] axis one observes a broad maximum in the vicinity of $T = 120$ K and a drop in magnetization around $T = 200$ K. The specific heat (not shown) is again a featureless function of temperature. This makes it difficult to determine the exact values of the temperatures of magnetic phase transitions.

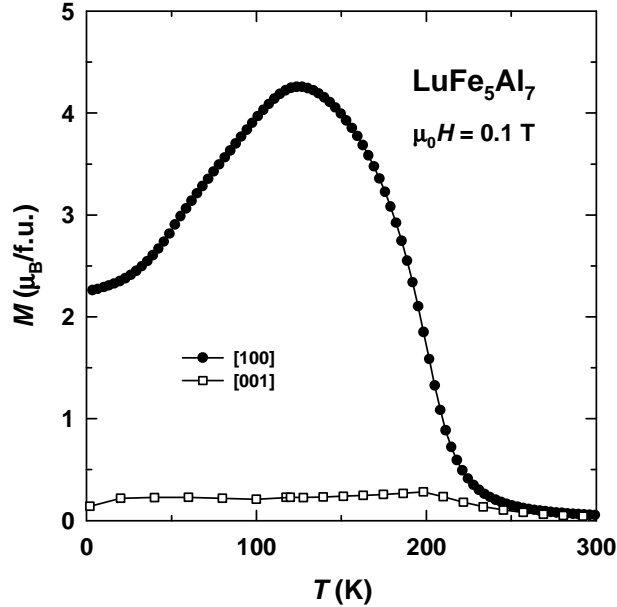


Fig. 4.11. Temperature dependence of the magnetization along the [100] and [001] axes of the LuFe₅Al₇ single crystal in a field of 0.1 T.

Magnetization isotherms of the LuFe₅Al₇ single crystal along the [100] and [001] axes are presented in Fig. 4.12 at several selected temperatures. Only field-ascending branches are shown for clarity of the presentation (hysteresis will be discussed later). Similarly to LuFe_{4.5}Al_{7.5}, the easy magnetization direction in LuFe₅Al₇ lies in the basal plane. At $T = 2$ K and 40 K the compound does not display a spontaneous magnetic moment. Instead, the curves along the easy [100] axis exhibit a field-induced magnetic transition. At higher temperatures the transition is not seen, the magnetization grows rapidly from the lowest field. Then the magnetization still increases considerably as a function of field. Such a high susceptibility reflects a non-collinear structure of the Fe magnetic moments that rotate continuously towards the field direction. In a field of 14 T the magnetization of LuFe₅Al₇ is about 7.5 μ_B/f.u. (at $T = 2$ K) Therefore, the field-induced collinear ferromagnetic state should be reached in a field just slightly higher than 14 T, in accordance with the magnetic moment of the Fe sublattice determined in RFe₅Al₇ with magnetic *R* elements [108-113].

The temperature evolution of the magnetization isotherm along the easy [100] axis at low temperatures is shown in Fig. 4.13. A field-induced magnetic transition is

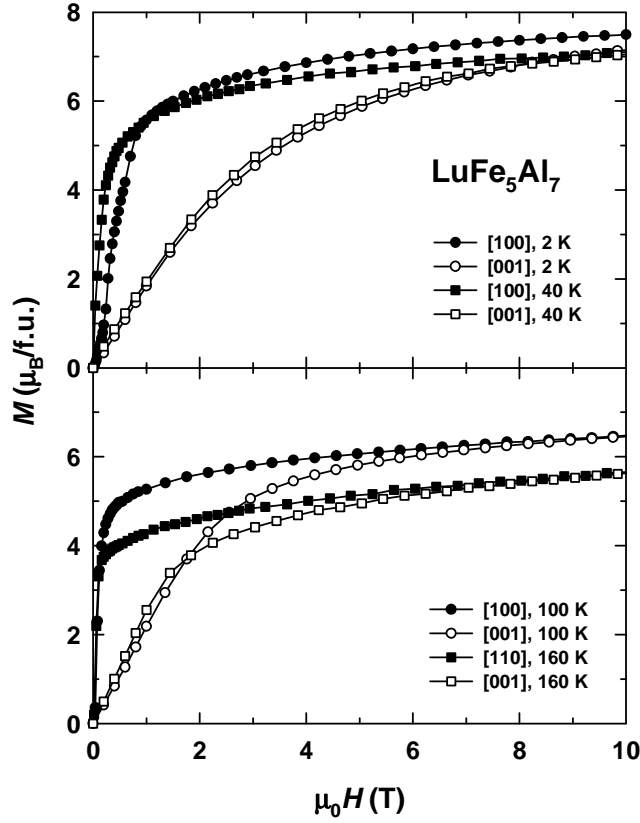


Fig. 4.12. Magnetization curves along the [100] and [001] axes of the LuFe_5Al_7 single crystal at several selected temperatures.

observed at $T < 80$ K. The inset in Fig. 4.13 shows the temperature dependence of the transition field H_{cr} .

Since no spontaneous magnetic moment is present in LuFe_5Al_7 at low temperatures, the compound is in an antiferromagnetic state. The magnetization jump can be interpreted as a metamagnetic transition. It should be noted that the critical field of the transition is much lower in LuFe_5Al_7 as compared to $\text{LuFe}_{4.5}\text{Al}_{7.5}$ and LuFe_4Al_8 . This finding reflects the general trend that the antiferromagnetism in the $\text{LuFe}_x\text{Al}_{12-x}$ systems is weakened with increasing Fe content.

Hysteresis loops along the easy [100] axis of the LuFe_5Al_7 single crystal at $T = 2$ K and 20 K are shown in Fig. 4.14. The loops display similarities to those of $\text{LuFe}_{4.5}\text{Al}_{7.5}$ (Fig. 4.10). Since the induced ferromagnetic component is preserved in a zero field, a non-zero remanent magnetization and a coercivity are observed. It is interesting to note that the virgin curve is not located outside the hysteresis loops, in contradiction with the results published previously on polycrystalline LuFe_5Al_7 [20]. A possible reason consists in a slightly different composition of the polycrystalline sample used in Ref. [20], shifted towards $\text{LuFe}_{4.5}\text{Al}_{7.5}$, where the effect of the virgin curve lying outside the hysteresis loop is indeed observed (Fig. 4.10). In the present work it has been found that the field of the metamagnetic transition in LuFe_5Al_7 is considerably lower than in $\text{LuFe}_{4.5}\text{Al}_{7.5}$ (0.35 T vs. 1.5 T at $T = 2$ K) and thus falls in the same range as the coercivity of ferromagnetic domain walls.

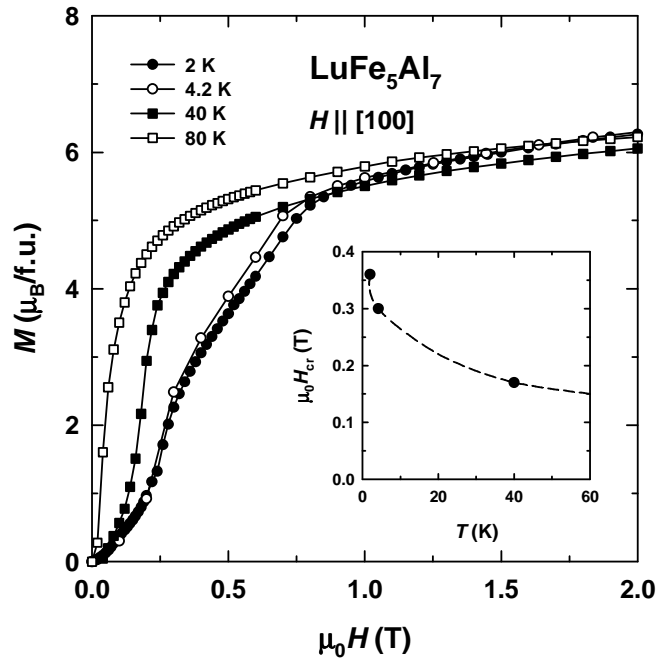


Fig. 4.13. Temperature evolution of the magnetization curve along the [100] axis of the LuFe_5Al_7 single crystal in the range $T = 2 - 80$ K. The inset shows the temperature dependence of the critical field of the metamagnetic transition.

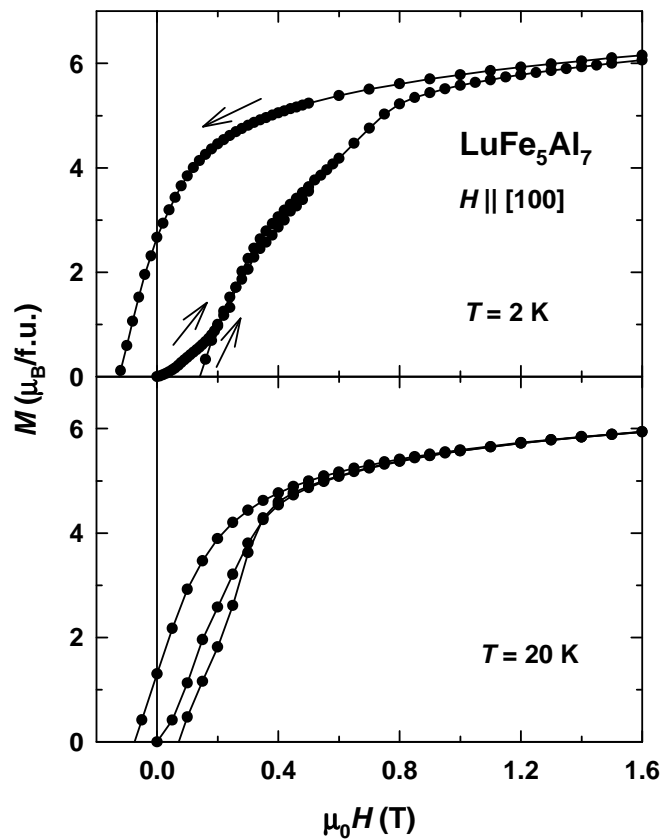


Fig. 4.14. Low-field details of the hysteresis loops measured along the [100] axis of the LuFe_5Al_7 single crystal at $T = 2$ and 20 K.

The low-temperature antiferromagnetic state in LuFe_5Al_7 changes at elevated temperatures. The rapid growth of the magnetization at $T > 80$ K in a low field (Fig. 4.12) without traces of the metamagnetic transition implies that ferromagnetic exchange interactions start to dominate in the compound. They are most likely to co-exist with antiferromagnetic exchange interactions, which leads to the non-monotonous temperature dependence of the magnetization (Fig. 4.11). However, here the maximum in $M(T)$ at $T = 120$ K cannot be considered as the Néel temperature because of the spontaneous magnetization observed already above $T = 80$ K. Therefore, we can estimate $T_N \approx 80$ K where features of the antiferromagnetic state disappear. This is different from $\text{LuFe}_{4.5}\text{Al}_{7.5}$ where no temperature range with a spontaneous magnetization is observed. The ferromagnetism disappears in LuFe_5Al_7 at $T_C = 200$ K.

4.2.4. $\text{LuFe}_{5.5}\text{Al}_{6.5}$

Field dependences of the magnetization along the [100] and [001] axes of the $\text{LuFe}_{5.5}\text{Al}_{6.5}$ single crystal at several selected temperatures are shown in Fig. 4.15. The magnetic moments of the compound lie in the basal plane. Along the easy magnetization direction $\text{LuFe}_{5.5}\text{Al}_{6.5}$ displays a spontaneous magnetic moment at all temperatures. It reflects a ferromagnetic nature of the exchange interactions in $\text{LuFe}_{5.5}\text{Al}_{6.5}$.

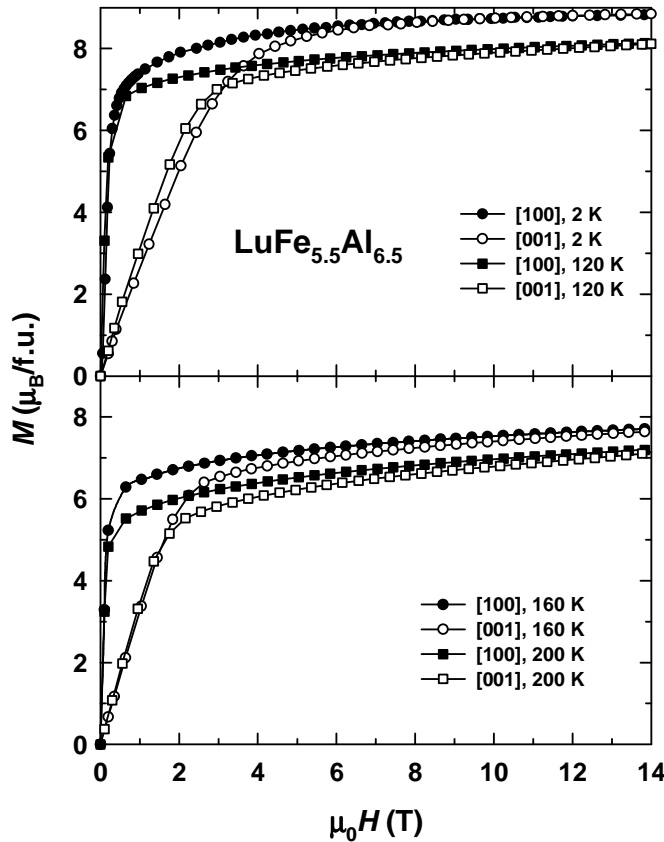


Fig. 4.15. Magnetization curves along the [100] and [001] axes of the $\text{LuFe}_{5.5}\text{Al}_{6.5}$ single crystal at several selected temperatures.

Magnetization in 0.1 T as a function of temperature along the [100] axis of the $\text{LuFe}_{5.5}\text{Al}_{6.5}$ single crystal is shown in Fig. 4.16. At low temperatures the magnetization displays growth that is followed by a plateau up to about $T = 250$ K, where it abruptly decreases. The low-temperature anomaly can be attributed to the presence of antiferromagnetic exchange interactions. Their presence is further supported by the $M(H)$ dependence (Fig. 4.15): magnetization still increases after the domain-wall motion is completed (although this effect is less intensive than those observed in $\text{LuFe}_x\text{Al}_{12-x}$ with $x < 5.5$). Nevertheless, it is clear that the ferromagnetic $\text{LuFe}_{5.5}\text{Al}_{6.5}$ compound displays only traces of antiferromagnetism. The steep decrease in the $M(T)$ dependence is associated with the phase transition into the paramagnetic state. This is confirmed by the specific heat C_p , also shown in Fig. 4.16. C_p displays a weak anomaly in the temperature region where the magnetization exhibits the pronounced drop. The anomaly in C_p shows that the Curie temperature of $\text{LuFe}_{5.5}\text{Al}_{6.5}$ is $T_C = 263$ K.

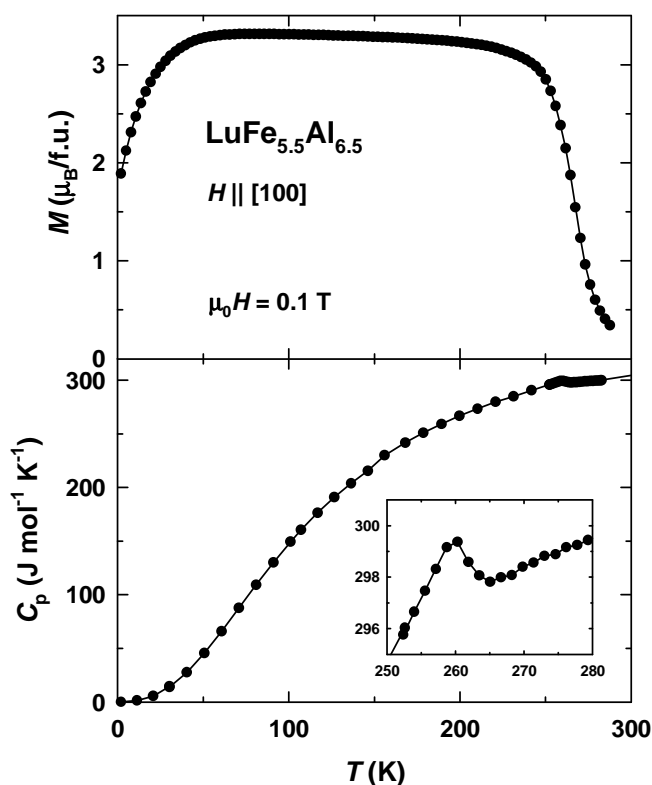


Fig. 4.16. Temperature dependence of the magnetization along the [100] axis in a field of 0.1 T (top) and temperature dependence of the specific heat (bottom) of the $\text{LuFe}_{5.5}\text{Al}_{6.5}$ single crystal. The inset shows the specific heat in the vicinity of the Curie temperature $T_C = 263$ K.

It should be noted that since saturation is not reached, and magnetization continues to grow up to the highest available field of 14 T, the unambiguous determination of the spontaneous magnetic moment M_s of $\text{LuFe}_{5.5}\text{Al}_{6.5}$ is complicated. The temperature variation of M_s determined from Arrott plots is shown in Fig. 4.17. At low temperatures M_s displays a very weak temperature dependence, and then a monotonous decrease is observed upon approaching $T = T_C$. The low-temperature behavior of $\text{LuFe}_{5.5}\text{Al}_{6.5}$ is likely to be related to the presence of

antiferromagnetic interactions in the compound. The plateau in the $M_s(T)$ dependence reflects a higher degree of non-collinearity of the magnetic moments at low temperatures than at high temperatures. The spontaneous magnetic moment starts the monotonous decrease with increasing temperature around $T = 60$ K, which correlates well with the temperature dependence of the magnetization in 0.1 T (Fig. 4.16). The temperature dependence of the magnetic moment in 14 T, also shown in Fig. 4.17, is ferromagnetic-like. At low temperatures this dependence is qualitatively different from $M_s(T)$. The reason is that with increasing magnetic field the magnetic moments become more collinear, and in a field of 14 T $\text{LuFe}_{5.5}\text{Al}_{6.5}$ is a practically collinear ferromagnet.

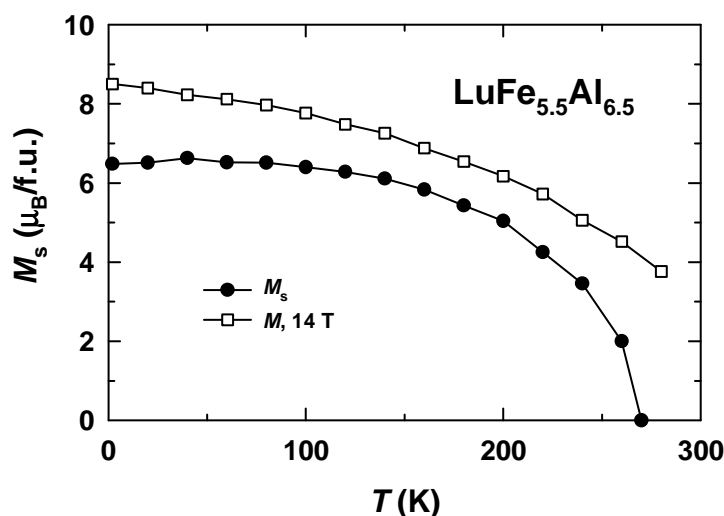


Fig. 4.17. Temperature dependence of the spontaneous magnetization and of the magnetization in a field of 14 T of the $\text{LuFe}_{5.5}\text{Al}_{6.5}$ single crystal.

4.2.5. LuFe_6Al_6

The LuFe_6Al_6 compound was studied on a single crystal in Ref. [15]. Here, its magnetic properties are briefly presented for completeness (the present study was done on the same single crystal used in Ref. [15]).

The temperature dependence of the magnetization along the [100] axis of the LuFe_6Al_6 single crystal displays a monotonous decrease with temperature (Fig. 4.18). This behavior suggests that the exchange interactions in the compound are mostly of a ferromagnetic nature. The specific heat, shown in the bottom of Fig. 4.18, exhibits a maximum related to the phase transition associated with the magnetically ordered state. The Curie temperature is $T_C = 327$ K (inset in Fig. 4.18).

Magnetization isotherms along the [100] and [001] axes of the LuFe_6Al_6 single crystal are shown in Fig. 4.19. Along the easy [100] axis the saturation is reached in a rather low field followed by a practically zero differential susceptibility. It serves as an indication that LuFe_6Al_6 is indeed a ferromagnet. However, the slight deviation of the [100]-axis magnetization curve observed at $T = 2$ K just below saturation may imply that part of the magnetic moments in the compound are still not collinear, and a field of about 0.6 T is required to align them along the field direction.

Nevertheless, it is clear that ferromagnetism in $\text{LuFe}_x\text{Al}_{12-x}$ ($4 \leq x \leq 6$) is strengthened with increasing Fe content. The spontaneous magnetic moment displays a typical ferromagnetic temperature variation (Fig. 4.20).

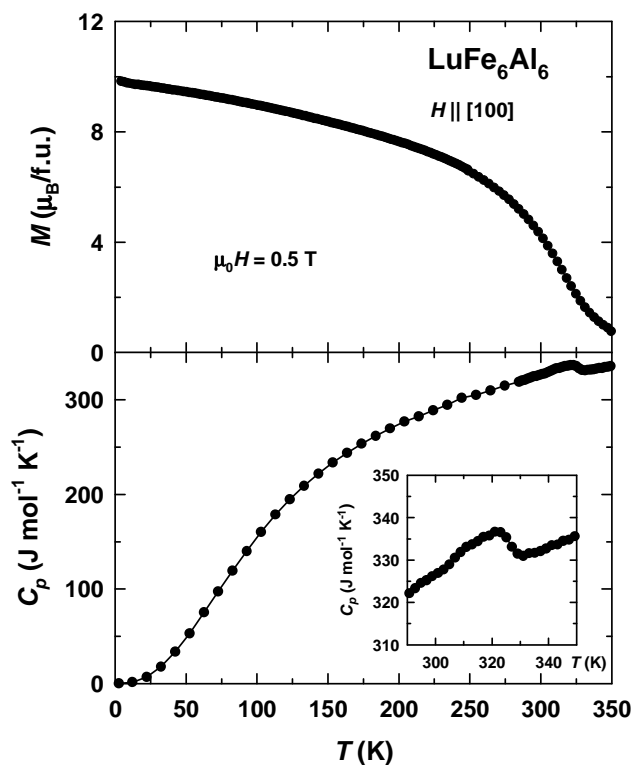


Fig. 4.18. Temperature dependence of the magnetization along the [100] axis in a field of 0.5 T (top) and temperature dependence of the specific heat (bottom) of the LuFe_6Al_6 single crystal. The inset shows the specific heat in the vicinity of the Curie temperature $T_C = 327$ K.

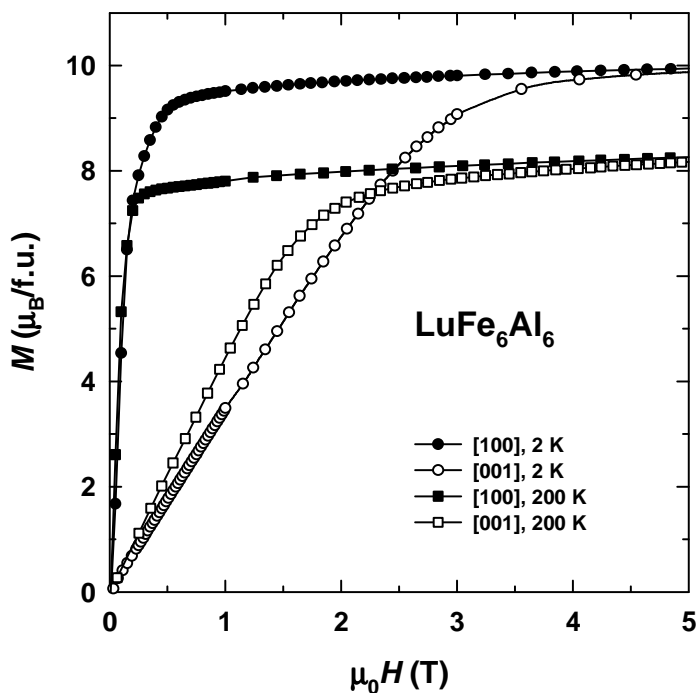


Fig. 4.19. Magnetization curves along the [100] and [001] axes of the LuFe_6Al_6 single crystal at several selected temperatures.

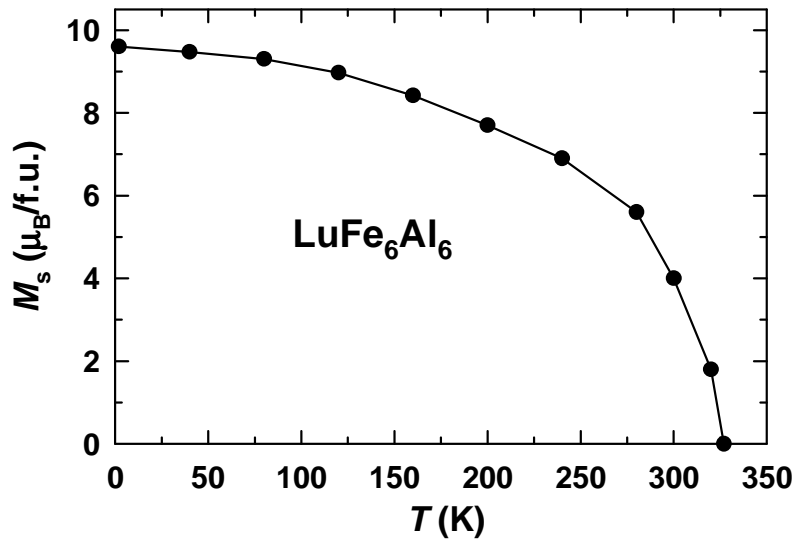


Fig. 4.20. Temperature dependence of the spontaneous magnetization of the LuFe_6Al_6 single crystal.

To summarize the information on the exchange interactions, Fig. 4.21 presents a phase diagram that reflects the variation of the magnetic order in the $\text{LuFe}_x\text{Al}_{12-x}$ ($4 \leq x \leq 6$) compounds with the Fe content. LuFe_4Al_8 and $\text{LuFe}_{4.5}\text{Al}_{7.5}$ are antiferromagnets with the Néel temperature around $T_N = 120$ K. A temperature region where ferromagnetism exists appears in LuFe_5Al_7 between $T_N = 80$ K and the Curie temperature $T_C = 200$ K. This region broadens towards higher x as T_C increases and T_N decreases due to a weakening of the antiferromagnetic exchange interactions. Finally, LuFe_6Al_6 is a ferromagnet, perhaps with a very low fraction of antiferromagnetic exchange interactions.

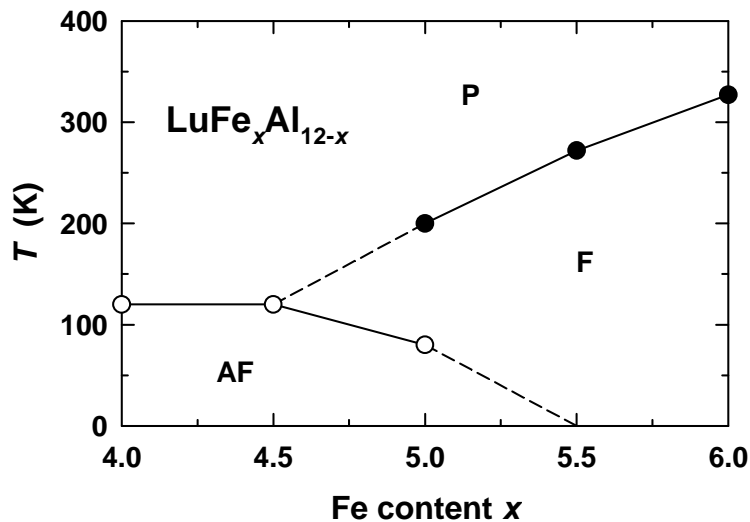


Fig. 4.21. Magnetic phase diagram in the x - T coordinates for the $\text{LuFe}_x\text{Al}_{12-x}$ ($x = 4-6$) systems.

The observed change of the magnetic order in the $\text{LuFe}_x\text{Al}_{12-x}$ compounds with increasing Fe content reflects the presence of competitive exchange interactions.

The balance between them undergoes significant changes as the 8j site is filled with Fe atoms in the tetragonal crystal lattice of the ThMn₁₂ type.

4.3. Magnetic anisotropy

The present single-crystalline study of the LuFe_xAl_{12-x} ($4 \leq x \leq 6$) compounds has also made it possible to obtain information on their magnetic anisotropy. The magnetic moments of all the compounds studied lie in the basal plane of the tetragonal lattice. No magnetic anisotropy was found within the basal plane. For the compounds with $x \geq 5$ it is possible to estimate the magnetic anisotropy energy E_a as the area between the magnetization isotherms along the easy and hard axes. At $T = 2$ K such an estimation yields $E_a \approx -1$ MJ/m³, -0.85 MJ/m³ and -0.7 MJ/m³ for LuFe₅Al₇, LuFe_{5.5}Al_{6.5} and LuFe₆Al₆, respectively. This result reflects a weakening of the anisotropy with increasing Fe content. As regards the compounds with $4 \leq x < 5$, on account of their dominant antiferromagnetic exchange interactions such calculations are rather complicated. Their magnetization curves reflect not only the magnetic anisotropy but a field-induced non-collinearity of magnetic moments makes a contribution to the resulting magnetization as well.

For the determination of anisotropy constants the Sucksmith-Thompson method is usually used [40]. The method relies on a negligible increase in the magnetization above the field where domain wall motion is completed. The method cannot be applied to the LuFe₅Al₇ and LuFe_{5.5}Al_{6.5} compounds because of their high differential susceptibility dM/dH in a magnetic field (see Figs. 4.12 and 4.15). For the LuFe₆Al₆ compound that displays a normal ferromagnetic behavior the second- and fourth-order anisotropy constants were found in Ref. [15]: $K_1 = -0.73$ MJ/m³ and $K_2 \leq 0.04$ MJ/m³ at $T = 2$ K. With increasing temperature K_1 and K_2 monotonously diminish to zero.

The anisotropy field H_a of ferro- and ferrimagnets is reflected in a change of the slope of their magnetization curves measured along the hard magnetization direction near saturation. Precise H_a values can be determined by the singular point detection method (SPD) [119]. The method consists in calculating the second field derivative of magnetization, d^2M/dH^2 . The $d^2M/dH^2(H)$ function has one minimum whose position on the field axis corresponds to the anisotropy field. As an example, Fig. 4.22 shows $d^2M/dH^2(H)$ curves for the LuFe_{5.5}Al_{6.5} and LuFe₆Al₆ compounds at $T = 200$ K in conjunction with the respective magnetization curves (the SPD cannot be applied to the compounds with $x < 5.5$ owing to the antiferromagnetic exchange interactions). The temperature variations of their anisotropy field are presented in Fig. 4.23. The H_a values decrease linearly. The LuFe_{5.5}Al_{6.5} compound has higher H_a values. This is in accord with the estimation of their anisotropy energy made above.

From the quantitative analysis of E_a and H_a it can be concluded that the magnetic anisotropy of the LuFe_xAl_{12-x} ($4 \leq x \leq 6$) compounds weakens with increasing Fe content.

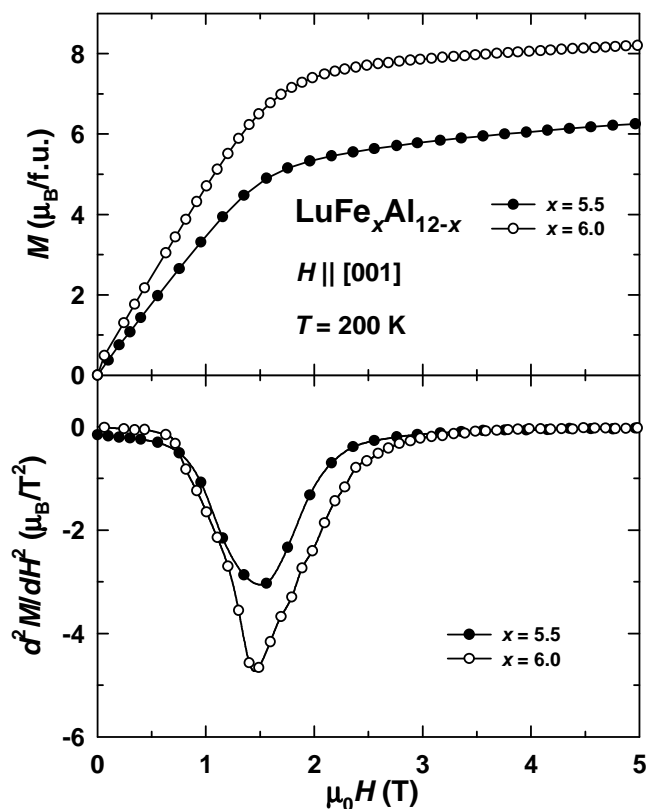


Fig. 4.22. Magnetization curves along the [100] axis of the $\text{LuFe}_x\text{Al}_{12-x}$ single crystals with $x = 5.5$ and 6.0 at $T = 200$ K, and their second field derivatives.

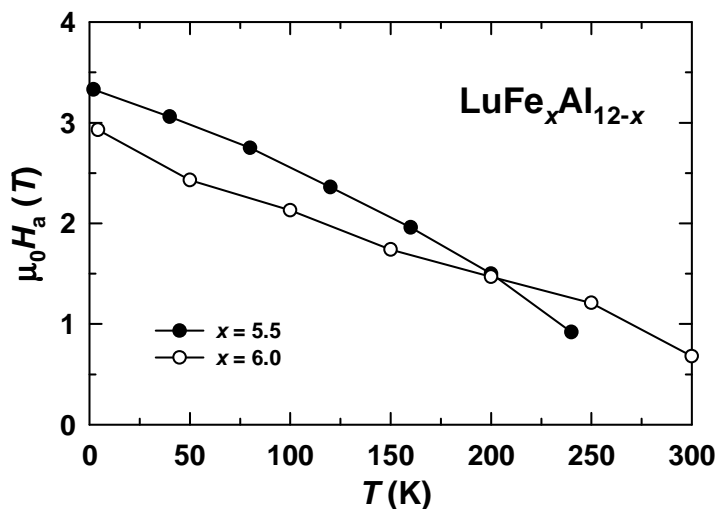


Fig. 4.23. Temperature variations of the anisotropy field of the $\text{LuFe}_x\text{Al}_{12-x}$ compounds with $x = 5.5$ and 6.0 determined by the SPD method.

It should be taken into account that, in contrast to $\text{LuFe}_x\text{Al}_{12-x}$ ($4 \leq x \leq 6$) studied in the present work, the Fe sublattice in isostructural compounds with a high content of Fe (e.g., $R\text{Fe}_{10}\text{V}_2$ [115,116], $R\text{Fe}_{11}\text{Ti}$ [116]) is known to display an easy-axis anisotropy. It means that the type of the Fe magnetic anisotropy changes in the intermediate region between 6 and 10 Fe atoms per formula unit. Although ternary compounds with this Fe content do not exist, quasiternaries can be stabilized. In particular, $\text{LuFe}_x\text{Al}_{10-x}\text{Si}_2$ ($7 \leq x \leq 10$) systems have been studied before [117]. A

gradual weakening of the easy-axis magnetic anisotropy was observed with an increase in the Al content. Considering the results of Ref. [117] and those of the present work, we can propose a concentration spin reorientation from the easy-plane to the uniaxial anisotropy between $x = 7$ and $x = 8$. However, in Ref. [117] polycrystalline samples were studied, so the anisotropy energy could only be estimated with a high error. It might be interesting to extend the present single-crystalline study to $x > 6$ in order to investigate in more detail the change of the Fe magnetic anisotropy in compounds with the tetragonal crystal structure of the ThMn_{12} -type. For such a study, a 1-12 system should be found where the homogeneity range of Fe extends at least from $x = 6$ to 8.

The observed variation of the magnetic properties reflects, apart from competitive exchange interactions, the presence of competitive anisotropic interactions in the Fe sublattice in R -Fe compounds with the tetragonal structure of the ThMn_{12} -type. The gradual filling of the $8j$ sites by Fe atoms in $\text{LuFe}_x\text{Al}_{12-x}$ as x increases results in a weakening of the easy-plane anisotropy as found in the present work, and in Fe-rich compounds an easy-axis anisotropy is induced. This finding suggests that, in contrast to those in the $8f$ sites, the Fe atoms in the $8j$ sites give a uniaxial contribution to the magnetic anisotropy. As regards the $8i$ sites, they are occupied mainly by Fe atoms in Fe-rich compounds such as $R\text{Fe}_{11}\text{Ti}$. The contribution of the $8i$ positions to the magnetic anisotropy can be estimated by a linear extrapolation of the E_a values obtained for $\text{LuFe}_{5.5}\text{Al}_{6.5}$ and LuFe_6Al_6 to $x = 11$. The extrapolation yields $E_a \approx 0.8 \text{ MJ/m}^3$. However, for $\text{LuFe}_{11}\text{Ti}$ a much higher value, $E_a = +1.4 \text{ MJ/m}^3$, was obtained [118]. Therefore, it can be concluded that the Fe atoms in the $8i$ sites give an even stronger uniaxial contribution to the magnetic anisotropy than those in the $8j$ sites.

4.4. Conclusions

1. Within the homogeneity region $4 \leq x \leq 6$ of the $\text{LuFe}_x\text{Al}_{12-x}$ compounds a small anisotropic compression of the tetragonal lattice is observed with increasing Fe concentration. Parameter a decreases by 1.2% as the Fe atoms substitute the Al atoms in the $8j$ site.

2. In the $\text{LuFe}_x\text{Al}_{12-x}$ compounds whose magnetic order originates from the Fe sublattice, competitive exchange and anisotropic interactions have been found. Both undergo considerable changes with increasing Fe content.

3. The compounds with $x = 4$ and 4.5 are antiferromagnets with the Néel temperature $T_N \approx 120$ K. Antiferromagnetic exchange interactions weaken with increasing Fe content. In the compounds with $4 \leq x \leq 5$ a metamagnetic transition occurs that reflects a rotation of the magnetic moments from the initial antiferromagnetic to a non-collinear ferromagnetic state. The critical field of the transition decreases as the Fe concentration grows.

4. The type of the magnetic order changes near $x = 5$. In the compounds with $x = 5$ and 5.5 antiferromagnetic exchange interactions are suppressed at low temperatures, and above a ferromagnetic order is stabilized. The temperature interval where ferromagnetic exchange interactions dominate broadens with increasing Fe content since the Néel temperature decreases and the Curie temperature grows. Antiferromagnetic exchange interactions are practically absent in LuFe_6Al_6 that displays normal ferromagnetic behavior.

5. The $\text{LuFe}_x\text{Al}_{12-x}$ ($4 \leq x \leq 6$) compounds display an anisotropy of the easy-plane type. No anisotropy was detected in the basal plane of the tetragonal lattice. With increasing Fe content the magnetic anisotropy is weakened. A concentration spin-reorientation transition in the Fe sublattice from easy plane to easy axis is likely to occur in Fe-rich compounds in the interval $7 \leq x \leq 8$.

6. In contrast to the Fe atoms in the $8f$ site that make a planar contribution to the magnetic anisotropy, the Fe atoms in the $8j$ site make a uniaxial contribution. In Fe-rich compounds where Fe atoms also reside in the $8i$ site, their contribution to the anisotropy is also uniaxial, and it exceeds that of the Fe atoms in the $8j$ site.

Chapter 5: Magnetic properties of RFe_5Al_7 (R - Gd, Tb, Dy, Ho, Er and Tm) compounds

In the previous Chapter it was found that exchange interactions and magnetic anisotropy of $LuFe_xAl_{12-x}$ ($4 \leq x \leq 6$) compounds are strongly dependent on the Fe content. Significant changes in the fundamental magnetic properties are also expected with varying rare-earth components. It is related to the formation of (i) inter-sublattice R -Fe exchange interaction and (ii) single-ion magnetocrystalline anisotropy of the rare-earth sublattice. This Chapter presents a systematic study of the magnetic properties of the RFe_5Al_7 (R - Gd, Tb, Dy, Ho, Er and Tm) compounds performed on single crystals. In literature the existence of the compounds with R - Sm and Yb was also reported [20]. Their single crystals were not prepared and studied in this work since their growth by a modified Czochralski method is substantially more complicated due to intensive evaporation of the rare-earth components.

5.1. Lattice parameters

Figure 5.1 shows parameters a and c of the tetragonal crystal lattice of RFe_5Al_7 compounds. Parameter a decreases from R - Gd to R - Lu by 0.7%, whereas parameter c stays practically constant. This anisotropic compression of the crystal

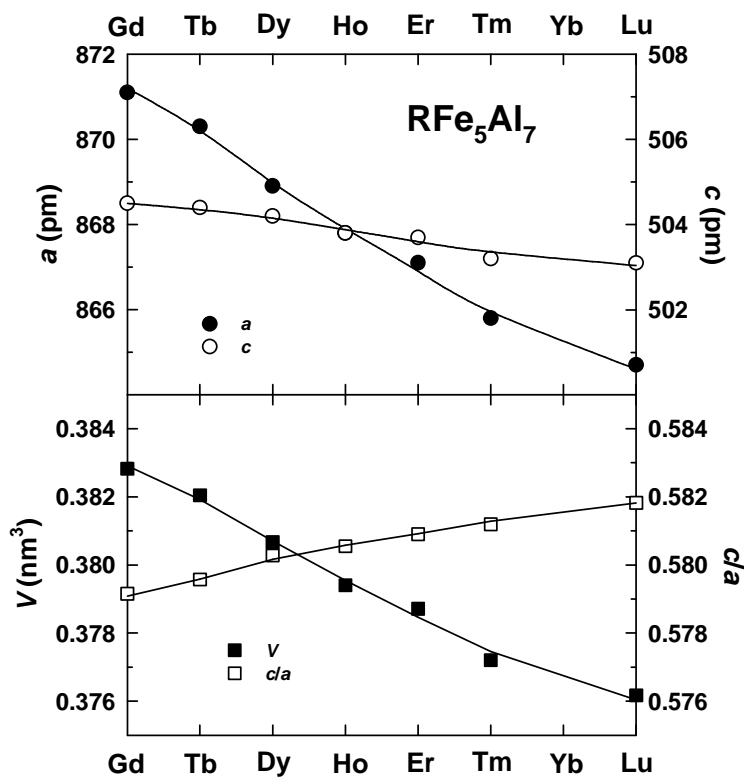


Fig. 5.1. Lattice parameters a and c , ratio c/a and unit cell volume V of RFe_5Al_7 compounds (R - Gd, Tb, Dy, Ho, Er, Tm and Lu).

lattice leads to an increase in the c/a ratio. As a result of lanthanide contraction the unit cell volume shrinks by 1.8% from $R - \text{Gd}$ to $R - \text{Lu}$.

5.2. GdFe_5Al_7

It is convenient to describe first the GdFe_5Al_7 compound. Gadolinium has orbital quantum number $L = 0$, and its $4f$ electron shell is spherical. Therefore, the single-ion anisotropy of Gd is zero. It simplifies the analysis regarding the influence of this rare-earth component on magnetic properties of the compound.

Figure 5.2 presents magnetization curves measured along the principal crystallographic axes at $T = 2$ K. One observes that $[110]$ is the easy magnetization direction, the spontaneous magnetization at $T = 2$ K being $M_s = 0.58 \mu_B/\text{f.u.}$ There is also a nonzero projection of the spontaneous moment onto the $[100]$ axis, $0.43 \mu_B/\text{f.u.}$ The spontaneous moment ratio, $M_s^{100}/M_s^{110} \approx \cos 45^\circ$, corresponds well to the tetragonal symmetry and reflects good quality of the crystal and its proper orientation. There is no spontaneous component along $[001]$, which is the hard magnetization direction. After domain-wall motion is completed, the magnetization continues to grow due to a non-collinear magnetic structure in the applied magnetic field. The field susceptibility, dM/dH , is higher along $[100]$ than along $[110]$, and the corresponding magnetization curves intersect. No anomalies are observed at the

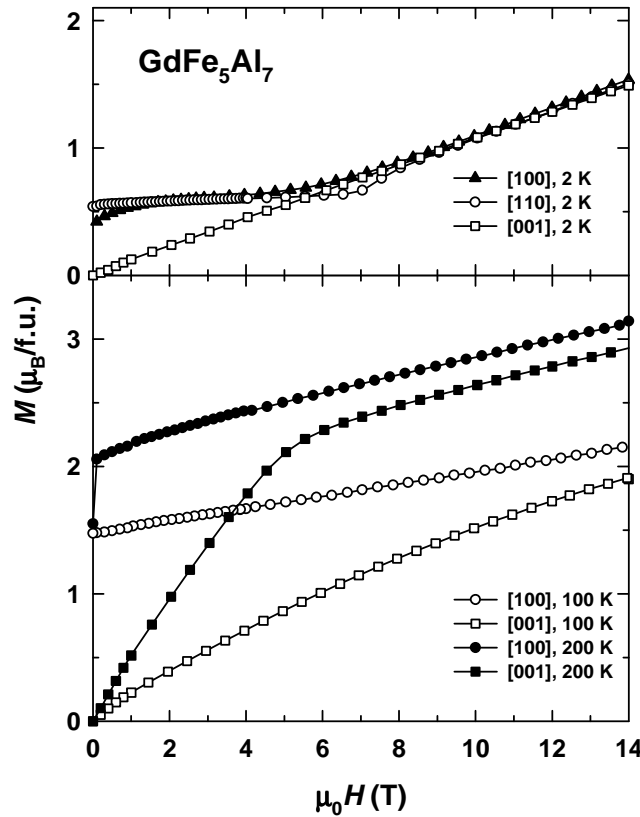


Fig. 5.2. Magnetization curves measured along the $[100]$, $[110]$ and $[001]$ axes of the GdFe_5Al_7 single crystal at several selected temperatures.

intersection point. Above 8 T all three curves are close to each other. The common high-field part at $T = 2$ K is linear and extrapolates to the origin according to the expression $M = H/n_{\text{GdFe}}$, where n_{GdFe} is the inter-sublattice Gd-Fe exchange constant. It is found to be 8.3 T f.u./ μ_{B} . This n_{GdFe} value is lower than, e.g., $n_{\text{GdFe}} = 12.2$ T f.u./ μ_{B} determined for the isostructural $\text{GdFe}_{10}\text{Si}_2$ compound by inelastic neutron scattering [120]. Yet, the difference is not unreasonable, given that $\text{GdFe}_{10}\text{Si}_2$ contains twice as many iron atoms per formula unit. For clarity at $T > 2$ K Fig. 5.2 presents only magnetization along the easy and hard directions although the in-plane anisotropy survives approximately up to $T = 200$ K. Its evolution will be presented below.

It is also seen in Fig. 5.2 that at $T = 2$ K the magnetization isotherms along the easy [110] and hard [001] directions intersect at around 6 T. At fields 6 - 8 T, the magnetization along the easy axis is lower than that along the hard axis, and at higher fields the magnetization along the two axes is the same. Obviously, the intersection point does not correspond to the anisotropy field between the basal plane and the tetragonal c axis and the area between the easy [110] and hard [001] directions is not the anisotropy energy of GdFe_5Al_7 . The area between the easy- and hard-magnetization isotherms of GdFe_5Al_7 varies non-monotonically: it is much smaller at $T = 2$ K than at higher temperatures (e.g., $T = 100$ and 200 K), whereas anisotropy energy usually decreases with temperature. For this reason it appears difficult to determine the anisotropy energy of GdFe_5Al_7 at low temperatures.

Temperature dependences of magnetization along the [100] and [110] axes measured in a field of 0.1 T are presented in Fig. 5.3. In the whole temperature range of the magnetically ordered state the magnetization in GdFe_5Al_7 is along the Fe sublattice and therefore does not exhibit a compensation point. Assuming that the Gd magnetic moment in the ground state of GdFe_5Al_7 is equal to its free-ion Gd^{3+} value, $M_{\text{Gd}} = g_J J = 7 \mu_{\text{B}}$, and the magnetic structure is collinear and antiparallel, the total moment of the Fe sublattice can be determined as $M_{\text{Fe}} = M_{\text{s}} + M_{\text{Gd}} = 7.58 \mu_{\text{B}}$, which corresponds to $\mu_{\text{Fe}} \approx 1.5 \mu_{\text{B}}$ for an average moment of an Fe atom. The temperature dependence of the specific heat C_{p} of GdFe_5Al_7 shown in the lower panel of Fig. 5.3 displays a single anomaly at $T = 262$ K which corresponds to the Curie temperature T_{C} of the compound. This T_{C} value is in agreement with the temperature dependences of magnetization (upper panel in Fig. 5.3) and lies in between the data of Refs. [20] ($T_{\text{C}} = 268$ K) and [96] ($T_{\text{C}} = 240$ K). The electronic contribution to the specific heat was estimated to be $\gamma \approx 55 \text{ mJ mol}^{-1} \text{ K}^{-2}$.

In Chapter 4 it was found that the transition from the magnetically ordered state into the paramagnetic state of the LuFe_5Al_7 compound occurs around $T = 200$ K. In GdFe_5Al_7 the magnetic ordering temperature is higher by 60 K, which is equivalent to about 30%. This increase is related mainly to the inter-sublattice Gd-Fe exchange interaction (the intra-sublattice Gd-Gd exchange interaction also makes a contribution but it should be much smaller). Since exchange interactions in $3d-4f$ intermetallic compounds are of the Heisenberg type [6], the reason for such a big

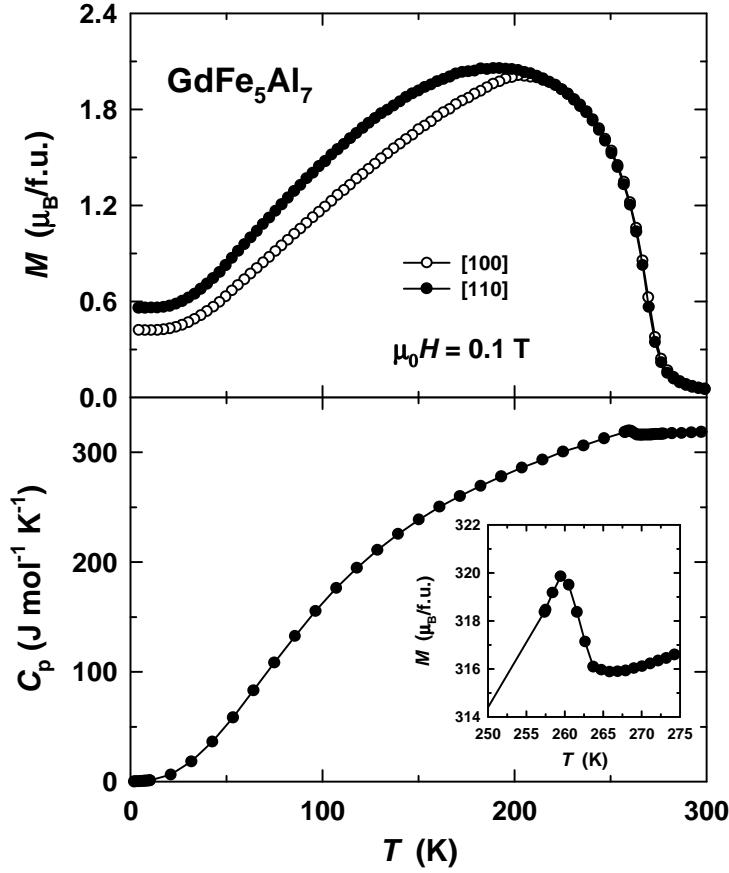


Fig. 5.3. Temperature dependence of the magnetization along the [100] and [110] axes measured in a field of 0.1 T (top) and of the specific heat (bottom) of the GdFe_5Al_7 single crystal. The inset shows the specific heat in the vicinity of $T_C = 262$ K.

increase in T_C is the high spin momentum of Gd (the spin quantum number of Gd is $S = 7/2$).

Figure 5.4 shows the temperature evolution of the anisotropy between the [100] and [110] axes of the GdFe_5Al_7 single crystal. The in-plane anisotropy field gradually decreases from 2 T at $T = 2$ K to approximately 0.2 T at $T = 180$ K and disappears at about $T = 200$ K. This is also seen in the temperature dependence of magnetization (Fig. 5.3) where above $T = 200$ K the $M(T)$ curves in 0.1 T along the [100] and [110] axes coincide.

The presence of the in-plane anisotropy in GdFe_5Al_7 is rather unusual. Since Gd has orbital quantum number $L = 0$, its contribution to the anisotropy within the single-ion anisotropy model is zero. In this situation, the magnetic anisotropy in GdFe_5Al_7 should originate from the Fe sublattice. However, its magnetic anisotropy should be rather weak and not visible in the basal plane as found for numerous rare-earth-iron intermetallics [15,121,122]. Indeed, the in-plane anisotropy energy, expressed in terms of an effective constant K_{eff} , is very low: $K_{\text{eff}} \approx 7 \text{ kJ/m}^3$ at $T = 2$ K. However, as can be demonstrated on the simplest model, regarding the Gd and Fe sublattices strictly antiparallel, the smallness of K_{eff} does not necessarily mean that the in-plane anisotropy field, $H_{\text{a,p}} = 2K_{\text{eff}}/|M_{\text{Gd}} - M_{\text{Fe}}|$, should be small as well, if

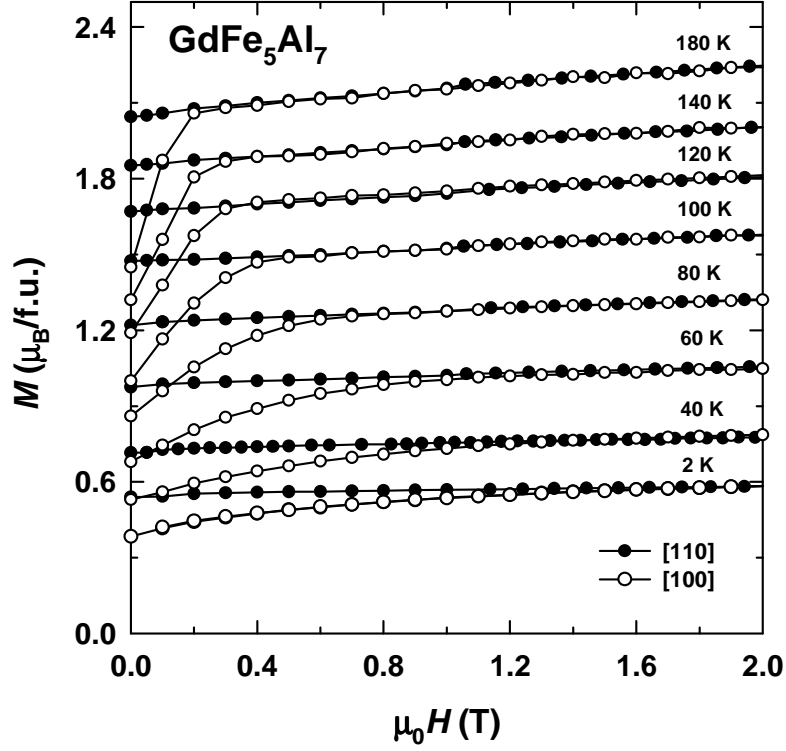


Fig. 5.4. Temperature evolution of the magnetization curves along the [100] and [110] axes of the GdFe_5Al_7 single crystal.

$M_{\text{Gd}} \approx M_{\text{Fe}}$. The low value of $M_s = M_{\text{Fe}} - M_{\text{Gd}}$ at low temperatures ($0.58 \mu_{\text{B}}/\text{f.u.}$ at $T = 2 \text{ K}$) clearly corresponds to this situation. As a result, one observes a rather high in-plane anisotropy field (2 T at $T = 2 \text{ K}$) despite the smallness of the anisotropy energy.

Figure 5.5 shows magnetization isotherms measured along the hard [001] axis of the GdFe_5Al_7 single crystal. The curves are linear below $T = 100 \text{ K}$, which means that the anisotropy field H_a between the basal plane and the c axis exceeds the maximum applied field of 14 T. A change of the slope reflecting H_a appears at $T = 120 \text{ K}$ at about 10 T and at lower fields at higher temperatures. The observed H_a values are rather high at $T > 100 \text{ K}$, taking into account that the anisotropy should come only from the Fe sublattice.

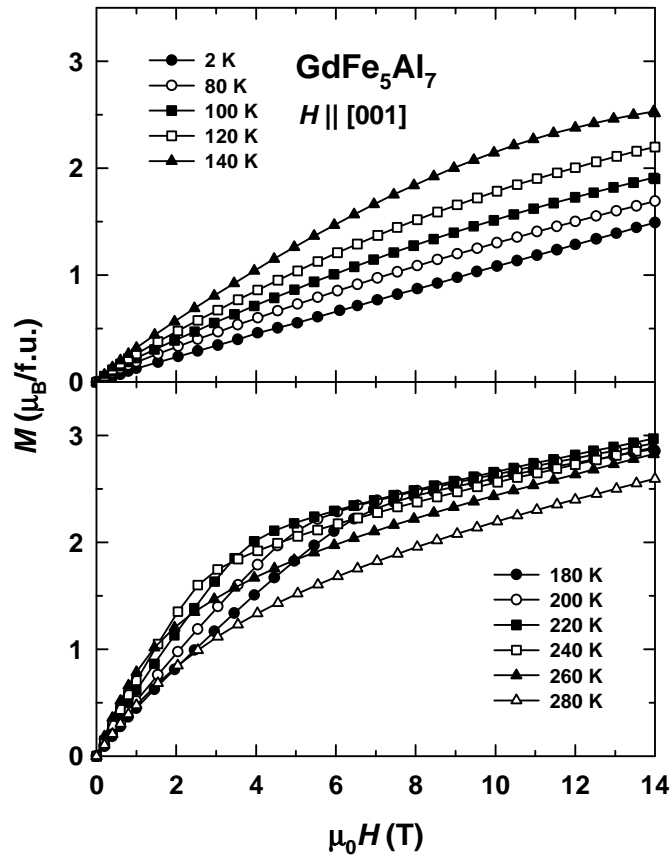


Fig. 5.5. Temperature evolution of the magnetization curve along the [001] axis of the GdFe₅Al₇ single crystal.

5.3. DyFe₅Al₇

Next, it would be logical to present magnetic properties of the TbFe₅Al₇ compound since, following gadolinium, terbium is the next representative of the lanthanides. However, the compound with *R* – Tb displays a special feature (see Chapter 5.4 below) and it is better to continue by the DyFe₅Al₇ compound for the following reason. A nearly complete picture of the compound's magnetization process was obtained in a magnetic field up to 60 T. The high-field data were analyzed using two different approaches to extract the inter-sublattice exchange parameter n_{DyFe} . The obtained results will be useful later when discussing other members of the *R*Fe₅Al₇ family.

Figure 5.6 shows magnetization curves (without details of the magnetic hysteresis to be shown and discussed below) measured along the [100], [110] and [001] axes of the DyFe₅Al₇ single crystal at several selected temperatures. The compound exhibits a spontaneous magnetization along the [100] and [110] axes, whereas there is no spontaneous component along the [001] direction. Therefore, the magnetic moments of DyFe₅Al₇ lie in the basal plane of the tetragonal lattice, in agreement with the neutron diffraction data [16]. The clear difference between the curves measured along the [100] and [110] axes points to a strong anisotropy within

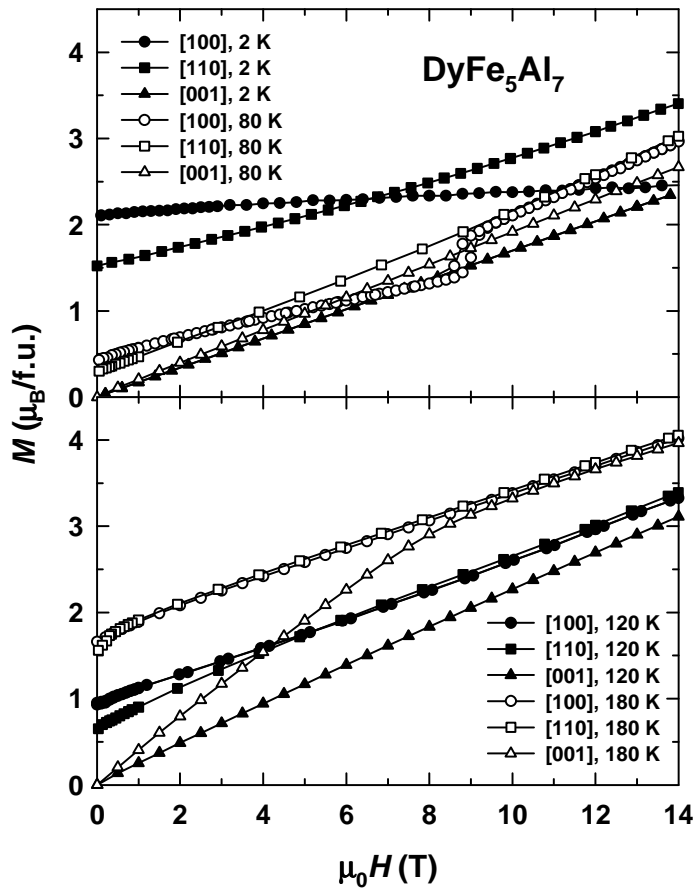


Fig. 5.6. Magnetization isotherms measured along the principal axes of the DyFe₅Al₇ single crystal at selected temperatures.

the basal plane with the [100] axis being the easy-magnetization direction. The ratio of the spontaneous moments along the [110] and [100] axes ($1.55 \mu_B$ and $2.12 \mu_B$, respectively, at $T = 2$ K), $M_s^{110}/M_s^{100} \approx \cos 45^\circ$, corresponds well to the tetragonal symmetry and reflects good quality of the crystal and its proper orientation.

Temperature dependences of M_s determined from the magnetization isotherms along the [100] axis and its projection onto the [110] axis are presented in Fig. 5.7. The compound has the compensation point at $T_{\text{comp}} = 93$ K and $T_C = 231$ K. Both values are in good agreement with those obtained in Refs. [16,19,20] for polycrystalline samples. Assuming that the Dy magnetic moment in the ground state of DyFe_5Al_7 is equal to the moment of a free Dy^{3+} ion, $M_{\text{Dy}} = 10 \mu_B$, and the magnetic structure is collinear and antiparallel, the total moment of the Fe sublattice can then be determined as $M_{\text{Fe}} = M_{\text{Dy}} - M_s = 7.9 \mu_B$, which corresponds to $\mu_{\text{Fe}} = 1.6 \mu_B$ for an average moment of the Fe atom. Such a high M_{Fe} value practically excludes the possibility of a non-parallel arrangement within the Fe sublattice which can originate from the presence of antiferromagnetic coupling between the Fe atoms in the $8f$ sites, as was observed for the isostructural LuFe_5Al_7 compound with non-magnetic Lu (see Chapter 4). Perhaps, negative interactions within the Fe sublattice are suppressed by the Dy-Fe interactions, which leads to the formation of the collinear ferrimagnetic structure. A close μ_{Fe} value ($1.65 \mu_B$) was found on a single crystal of LuFe_6Al_6 which is evidently a collinear ferromagnet [15].

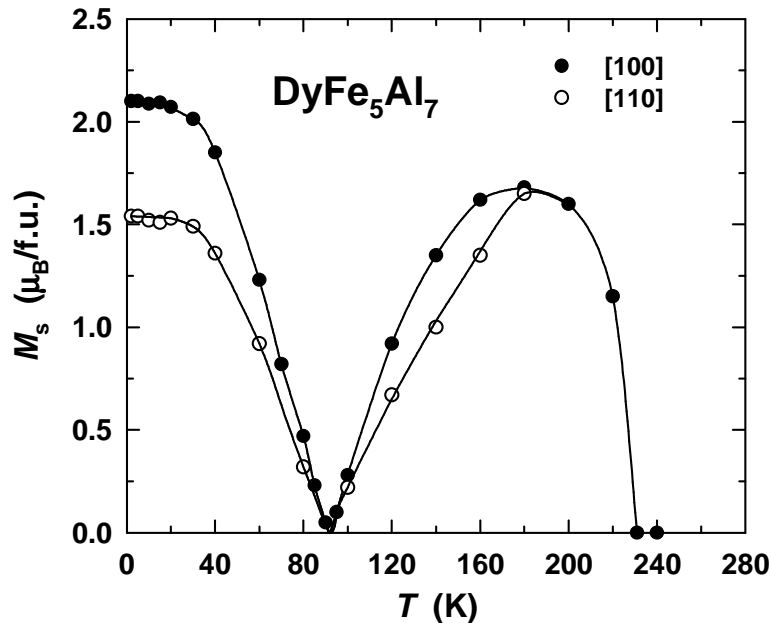


Fig. 5.7. Temperature dependence of the spontaneous moment M_s obtained from magnetization isotherms along the [100] axis and its projection onto the [110] axis.

A high magnetic susceptibility above the spontaneous magnetization even along the easy magnetization direction can be attributed to a strong bending of magnetic moments with increasing magnetic field. The bending of the moments is

more intensive along the [110] direction. As a result, the magnetization isotherms along the [100] and [110] axes intersect at a certain field at temperatures below $T = 100$ K. At $T = 80$ K, a hysteretic transition is seen in Fig. 5.6 along the easy [100] direction in a field ~ 9 T. Above the transition, the curves along the [100] and [110] axes coincide. At $T = 120$ K, the transition is no longer seen and the two curves are almost identical except in the low-field region (< 4 T). The temperature evolution of the transition will be discussed below. Finally, the in-plane anisotropy vanishes at $T = 180$ K (it is also seen in Fig. 5.7, where M_s^{100} and M_s^{110} coincide) whereas the anisotropy between the basal plane and the c axis persists up to T_C . As seen from Fig. 5.6, the anisotropy field H_a is still rather high, about 8 T at $T = 180$ K.

Figure 5.8 shows magnetization curves along the [110] axis at different temperatures. Below $T = 120$ K, the curves are characterized by a small positive curvature. This can be considered a precursor to a transition at higher fields. At higher temperatures, the magnetization isotherms become practically linear up to T_C . The $M(H)$ curves measured along the [001] axis (Fig. 5.9) are linear below 160 K, which shows that the anisotropy field H_a exceeds the maximum field of 14 T applied in the experiment. A change of the $M(H)$ curve's slope reflecting H_a appears only at $T = 160$ K at about 12 T and at lower fields at higher temperatures. Magnetization curves just below and just above T_C along the basal plane and the [001] axis are presented in Fig. 5.10. It is seen that the magnetic anisotropy persists even in the

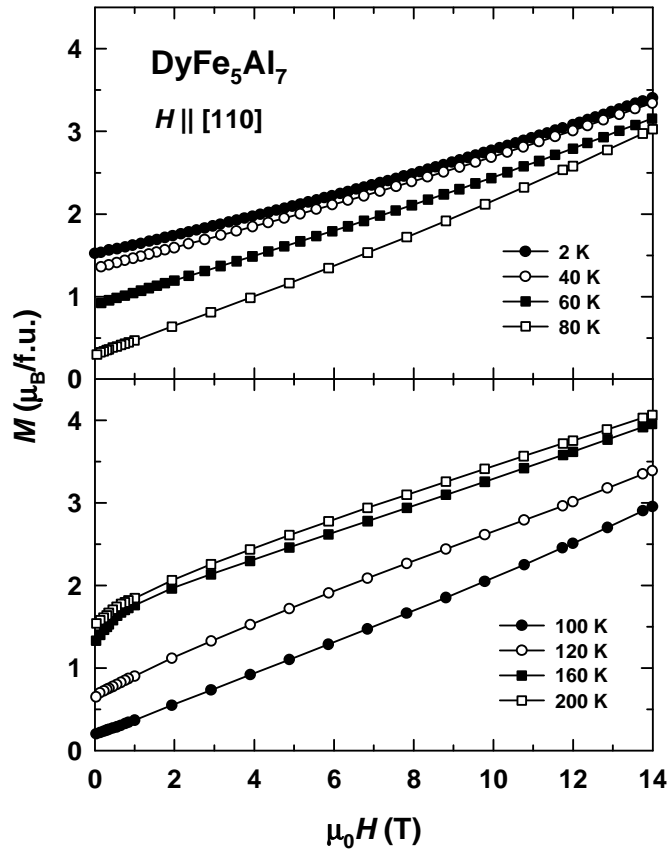


Fig. 5.8. Temperature evolution of the [110] axis magnetization curve below (top) and above (bottom) the compensation point $T_{\text{comp}} = 93$ K.

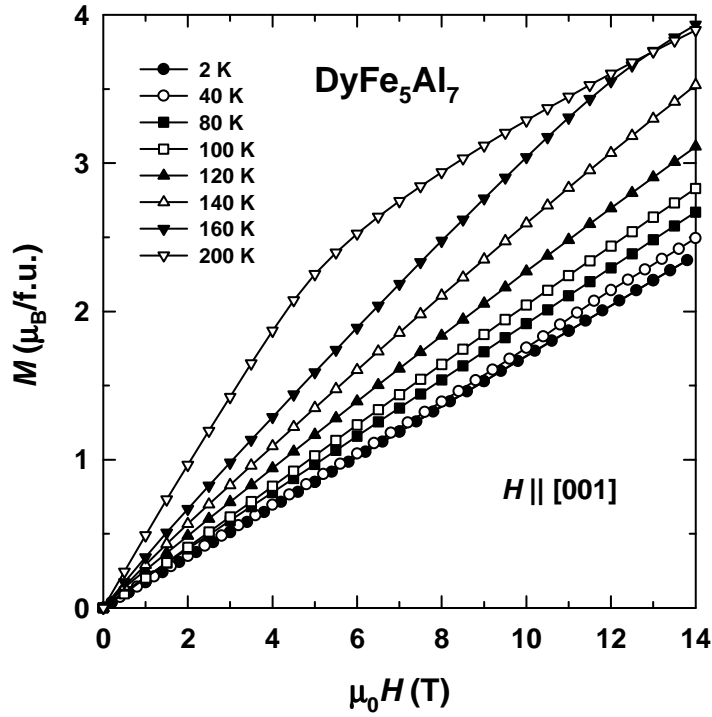


Fig. 5.9. Temperature evolution of the [001] axis magnetization curve.

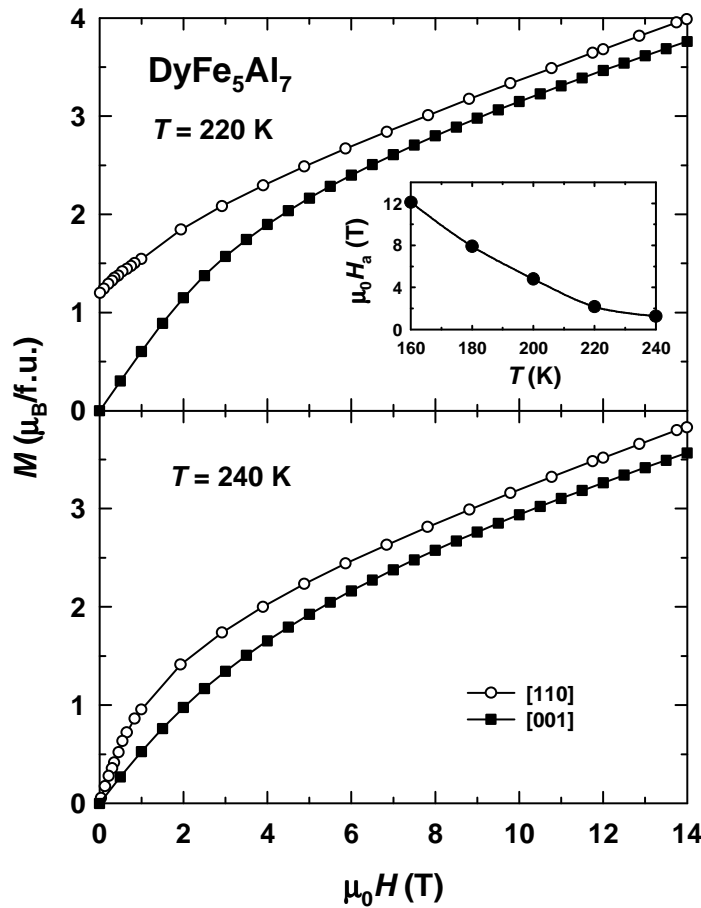


Fig. 5.10. Magnetization curves along the [001] and [110] axes at $T = 220$ and 240 K. The inset shows the temperature dependence of the anisotropy field determined by the SPD method.

paramagnetic state. The inset in Fig. 5.10 shows temperature dependence of H_a in the temperature range where the H_a values do not exceed the maximum applied field of 14 T. H_a was determined by the SPD (singular-point detection) method [119] as the field corresponding to the minimum of d^2M/dH^2 for the hard-axis magnetization curve.

The magnetization curves along the [100] axis presented in Fig. 5.11 show that a transition with a hysteresis of ~ 0.5 T is seen between $T = 75$ and 100 K. The critical field $H_{cr,1}$ of the transition decreases rapidly upon approaching T_{comp} from above and below (the transition field is marked by $H_{cr,1}$ since a second transition is observed in a higher field, at $H_{cr,2}$, see below). Figure 5.12 shows that $H_{cr,1}$ falls down to 2-3 T at $T = 90$ and 95 K. The temperature dependence of H_{cr} shown in Fig. 5.13 is very sharp. Extrapolation of $H_{cr,1}(T)$ to low temperatures explains why we did not observe the transition below $T = 70$ K: the $H_{cr,1}$ values exceed the maximum applied field of 14 T. The transition is observed above T_{comp} as well. Above $T = 100$ K, it becomes broad and is smeared out at $T = 120$ K.

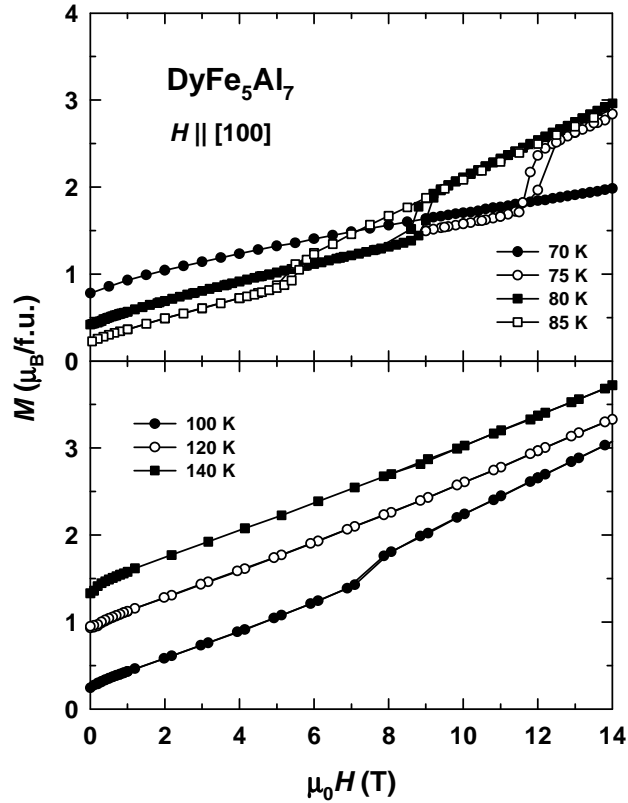


Fig. 5.11. Temperature evolution of the [100] axis magnetization curve below (top) and above (bottom) the compensation point $T_{comp} = 93$ K.

Since below T_{comp} the magnetic field is parallel to the magnetic moments of the Dy sublattice, the transition can be considered as the breaking of the antiparallel coupling between the Dy and Fe sublattices and a rotation of the Fe moments. In this case, the Dy sublattice should rotate at the transition above T_{comp} . However, the interpretation of the transition as occurring in only one of the sublattices contradicts

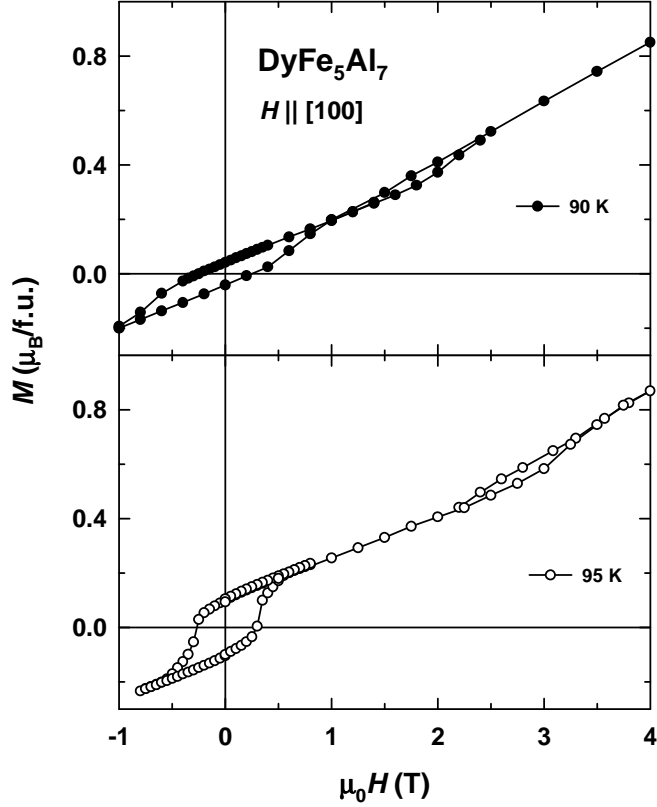


Fig. 5.12. Magnetization isotherms measured along the [100] axis in the vicinity of T_{comp} .

the temperature dependence of the magnetization jump ΔM_1 upon the transition (Fig. 5.13). First, the observed ΔM_1 is rather small, not exceeding $0.8 \mu_B/\text{f.u.}$ (at $T = 75 \text{ K}$), whereas the magnetic moment of each sublattice should be an order of magnitude higher. Second, $\Delta M_1(T)$ approaches zero at T_{comp} , i.e., it clearly follows the temperature dependence of the total moment and not those of individual sublattice moments which should be rather flat in such a narrow temperature interval and certainly do not pass through zero. The non-monotonous behavior of $H_{\text{cr},1}(T)$ passing through zero at T_{comp} , similarly to $\Delta M_1(T)$, also contradicts the notion of a transition in only one sublattice. Therefore, the transition should involve a rotation of both, the Dy and Fe sublattices.

In the basal plane of the tetragonal crystal, the [100] and [010] crystallographic directions are both the easy magnetization directions. Let us consider two possible orientations of the magnetic moments of the Dy and Fe sublattices in a relatively small field applied along the [100] axis (Fig. 5.14). In this figure α and φ denote the angles between M_{Fe} and M_{Dy} and between M_{Dy} and the [010] axis, respectively. It is evident that the anisotropy energy for these two cases is similar, while the Zeeman energy depends on the value of the spontaneous magnetization. For $M_s > 0$ in a small field the Dy and Fe magnetic moments will be oriented along the [100] direction. However, the susceptibility for a collinear ferrimagnet in this direction is expected to be low. On the other hand, near the

compensation point the value of the susceptibility due to the sublattice bending is higher for the case when the magnetic sublattices are normal to the field direction.

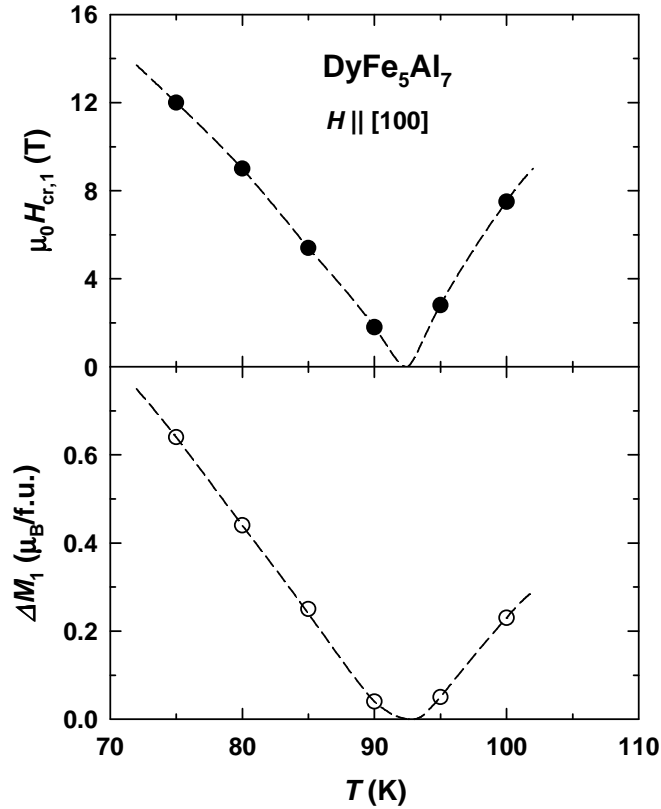


Fig. 5.13. Temperature dependence of the critical field $\mu_0 H_{cr,1}$ of the field-induced transition and of the magnetization gain ΔM_1 at the transition.

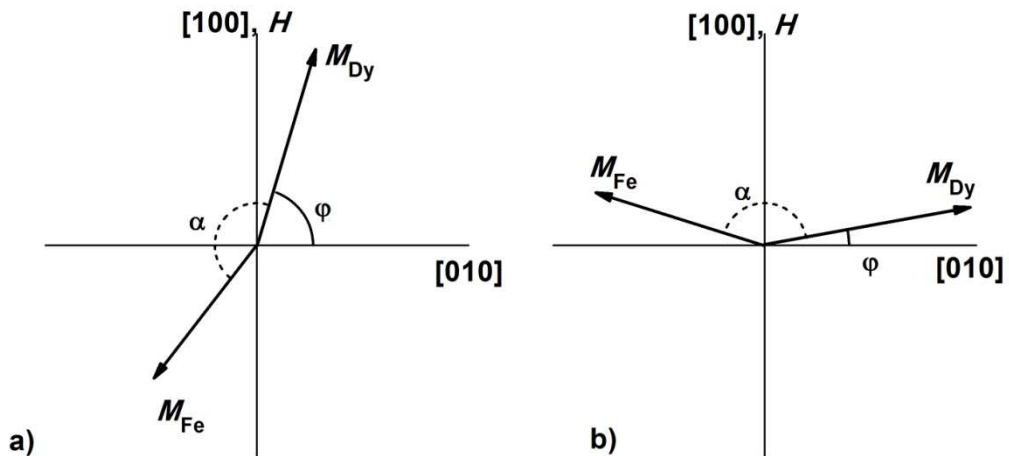


Fig. 5.14. Possible orientations of the magnetic moments of the Dy and Fe sublattices in a field applied along the $[100]$ axis: low field (a) and higher field (b).

Therefore, with increasing field we can expect the spin-reorientation transition of M_{Dy} and M_{Fe} from $[100]$ to a direction close to the $[010]$ axis. The higher the spontaneous moment, the higher should be the transition field. At very high fields, the ferromagnetic saturation along the field direction will be reached. Hence, in high

fields we can expect the inverse transition of the moments from nearly [010] to the [100] direction.

In order to estimate the critical fields of the spin-reorientation transitions let us consider the free energy of the system comprising the energies of intersublattice exchange interaction, magnetic anisotropy and the Zeeman energy:

$$E(\alpha, \varphi, H) = M_{\text{Dy}}M_{\text{Fe}}n_{\text{DyFe}}\cos(\alpha) - K\cos(4\varphi) - \mu_0H[M_{\text{Dy}}\sin(\varphi) + M_{\text{Fe}}\sin(\alpha + \varphi)], \quad (5.1)$$

where K is the in-plane anisotropy constant, and n_{DyFe} is the intersublattice exchange parameter. Here we neglect the anisotropy of the Fe sublattice. In order to determine the equilibrium angles α_0 and φ_0 of the orientation of the magnetic moments in a magnetic field H we should find the minimum of the free energy (5.1) with respect to the angles α and φ . Then the magnetization curve will be given by the expression:

$$M(\alpha, \varphi, H) = M_{\text{Dy}}\sin(\varphi_0) + M_{\text{Fe}}\sin(\alpha_0 + \varphi_0). \quad (5.2)$$

The exchange parameter n_{DyFe} for DyFe_5Al_7 can be estimated using the molecular field theory for a collinear two-sublattice ferrimagnet. Comparing the magnetic ordering temperatures of the $R\text{Fe}_5\text{Al}_7$ compounds with different R elements [16,20] one can conclude that the energy of the Fe-Fe exchange interaction is much higher than that of the R - R interactions in these compounds. For this case the temperature dependence of the magnetic moment of the Dy sublattice is determined by the Dy-Fe exchange interaction:

$$M_{\text{Dy}}(T) = M_{\text{Dy}}(0)B_J\left(\frac{g_J\mu_B\mu_0H_{\text{mol}}}{k_B T}\right), \quad (5.3)$$

where B_J is the Brillouin function, J the quantum number of the total moment of Dy ion, g_J the Landé factor, and H_{mol} the molecular field at the Dy ion produced by the Fe magnetic moments. The value of the molecular field is proportional to the Fe sublattice magnetic moment:

$$\mu_0H_{\text{mol}} = n_{\text{DyFe}}M_{\text{Fe}}, \quad (5.4)$$

and its temperature dependence is determined by the temperature dependence of the Fe sublattice magnetization:

$$H_{\text{mol}}(T) = H_{\text{mol}}(0)\frac{M_{\text{Fe}}(T)}{M_{\text{Fe}}(0)}. \quad (5.5)$$

Typically, the temperature behavior of the Fe magnetic moment can be taken from the $M(T)$ dependence for an isostructural compound of a similar composition with a non-magnetic R element. However, for LuFe_5Al_7 the temperature dependence

of the magnetization is complicated because of the competition between positive and negative exchange interactions within the Fe sublattice (see Chapter 4). Therefore, for an estimation we used the $M(T)$ dependence for the LuFe_6Al_6 compound with a collinear ferromagnetic structure [15]. Reducing this dependence to the values of M_{Fe} and T_C for DyFe_5Al_7 and subtracting it from the experimental $M_s(T)$ curve we obtained the temperature dependence of M_{Dy} for DyFe_5Al_7 (Fig. 5.15). The best fit of the experimental data with Eq. (5.3) is observed for the molecular field value $\mu_0 H_{\text{mol}}(0) = 42$ T, which corresponds to the exchange parameter $n_{\text{DyFe}} = 5.3$ T f.u./ μ_B .

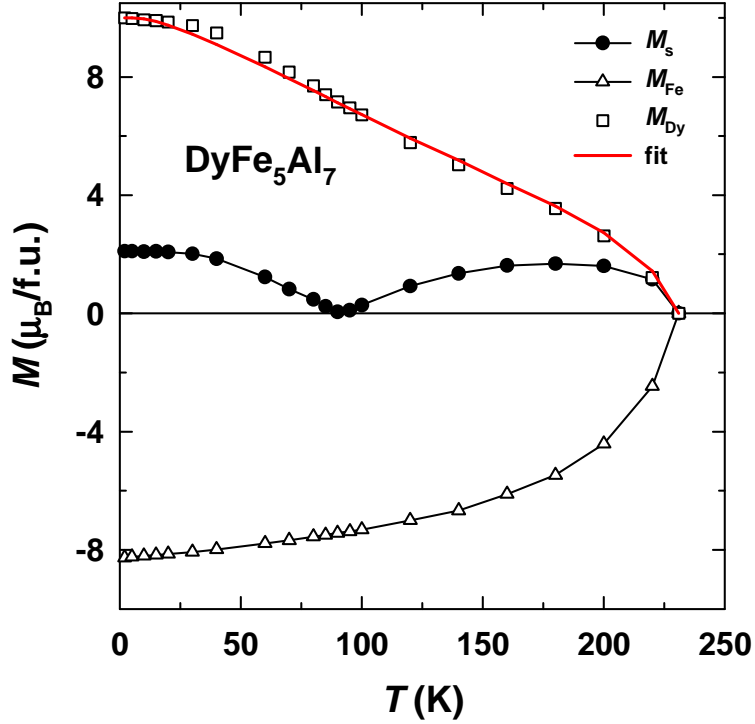


Fig. 5.15. Experimental temperature dependence of the spontaneous magnetic moment along the easy [100] axis and calculated temperature dependences of the magnetic moment of the Dy and Fe sublattices in DyFe_5Al_7 . The Fe magnetic moment is assumed to be negative as it is antiparallel to the Dy magnetic moment. The red line represents the fit according to Eq. (5.3).

Alternatively, the exchange parameter can be estimated from the magnetization curve of the antiferromagnetic state. In a magnetic field applied along the easy axis at the compensation point the intersublattice exchange parameter is equal to the inverse high-field susceptibility:

$$n_{\text{DyFe}} = \frac{d(\mu_0 H)}{dM}. \quad (5.6)$$

The experimental magnetization curve at $T = 95$ K (Fig. 5.12) gives $d(\mu_0 H)/dM = 4.3$ T f.u./ μ_B that is lower than the value 5.3 T f.u./ μ_B obtained from the $M(T)$ dependence. Therefore, the field-induced bending of the magnetic sublattices is somewhat higher than can be expected for the simple collinear two-sublattice model.

Nevertheless, in order to calculate the magnetization curves using Eqs. (5.1) and (5.2) we fixed the intersublattice exchange parameter to be $n_{\text{DyFe}} = 5.3 \text{ T f.u.}/\mu_{\text{B}}$.

For the limiting case $K = 0$, the calculations give the magnetization curve typical of that observed for a free-powder sample [123]. For the field interval $0 < \mu_0 H < n_{\text{DyFe}}(M_{\text{Dy}} - M_{\text{Fe}})$, the ferrimagnetic saturation is realized. At higher fields a canted magnetic structure is formed, and the magnetization linearly increases with field. Finally, the ferromagnetic saturation is reached in the field $\mu_0 H = n_{\text{DyFe}}(M_{\text{Dy}} + M_{\text{Fe}})$.

The anisotropy in the basal plane leads to the formation of two magnetization jumps in the magnetization curve. The values of the critical fields and the shape of the magnetization curve depend on the K value at small K , and are almost independent of K at $K > 0.5 \text{ MJ/m}^3$. From the magnetization slope along the [110] direction at different temperatures we can roughly estimate that the in-plane anisotropy constant is $K \sim 2.5 \text{ MJ/m}^3$ at $T = 0 \text{ K}$ and drops to nearly zero values above $T = 180 \text{ K}$. The calculated T - H magnetic phase diagram is presented in Fig. 5.16. It is seen that the behavior of the critical field of the transition near the compensation point correlates well with experimental data. At the same time, the values of the calculated and experimental critical fields are different. A better agreement with the critical fields can be obtained at higher values of the intersublattice exchange parameter, but this contradicts the high-field susceptibility data at T_{comp} . Moreover, in fields below $H_{\text{cr},1}$ the calculations give no bending of the sublattice magnetic moments, while the experimental magnetization curve is characterized by a non-zero susceptibility along the easy axis. All these data point to the formation of a non-collinear magnetic structure of the Fe moments in magnetic fields.

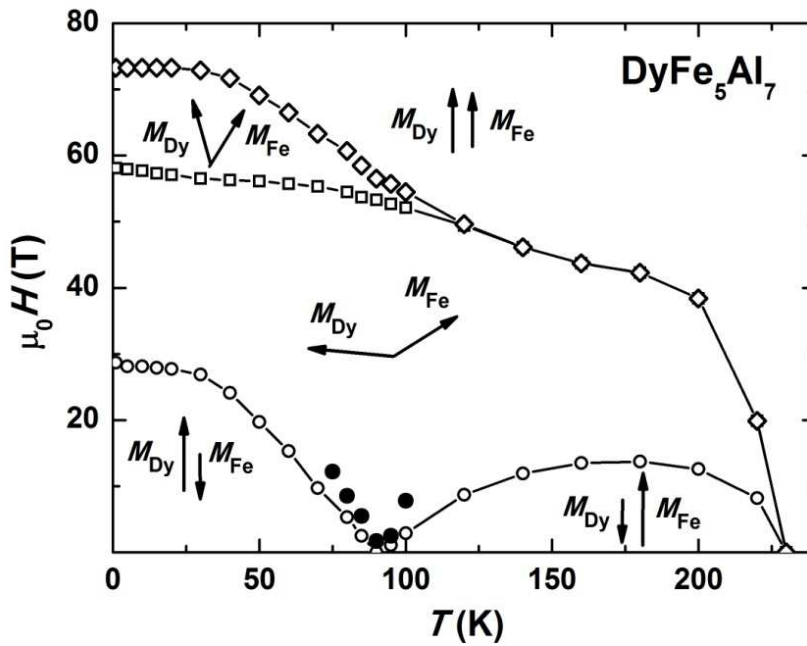


Fig. 5.16. Calculated T - H magnetic phase diagram. M_{Dy} and M_{Fe} denote the vectors of the Dy and Fe sublattice magnetizations, respectively.

To understand the field-induced magnetic transition more deeply, it is necessary to observe it at low temperatures, for which the magnetic study of the DyFe_5Al_7 single crystal should be extended to higher magnetic fields. A further goal of such a study is to either confirm or disprove the presence of a second transition in the compound.

Figure 5.17 shows magnetization curves of DyFe_5Al_7 measured in pulsed magnetic fields up to 60 T at $T = 2$ K. Two hysteretic transitions are observed along the easy [100] axis. There are no magnetization jumps along the other two principal axes. The transitions along [100] occur at about 30 T and 53 T. At the highest available field the magnetization equals $17 \mu_{\text{B}}/\text{f.u.}$. In order to reach the forced ferromagnetic state in DyFe_5Al_7 , a slightly higher field is required (~ 64 T), as follows from the sum of the Dy- and Fe-sublattice moments, $M_{\text{Dy}} + M_{\text{Fe}} = 10 + 7.9 = 17.9 \mu_{\text{B}}/\text{f.u.}$. The magnetization along the [110] axis experiences rapid growth up to 60 T. The pronounced difference between the magnetization curves measured along the [100] and [110] axes confirms the high anisotropy in the basal plane. The magnetization along the hard [001] axis grows linearly. Extrapolation of the hard-axis magnetization curve to higher fields shows that the saturated value of $17.9 \mu_{\text{B}}/\text{f.u.}$ will be reached in a field of 95 T.

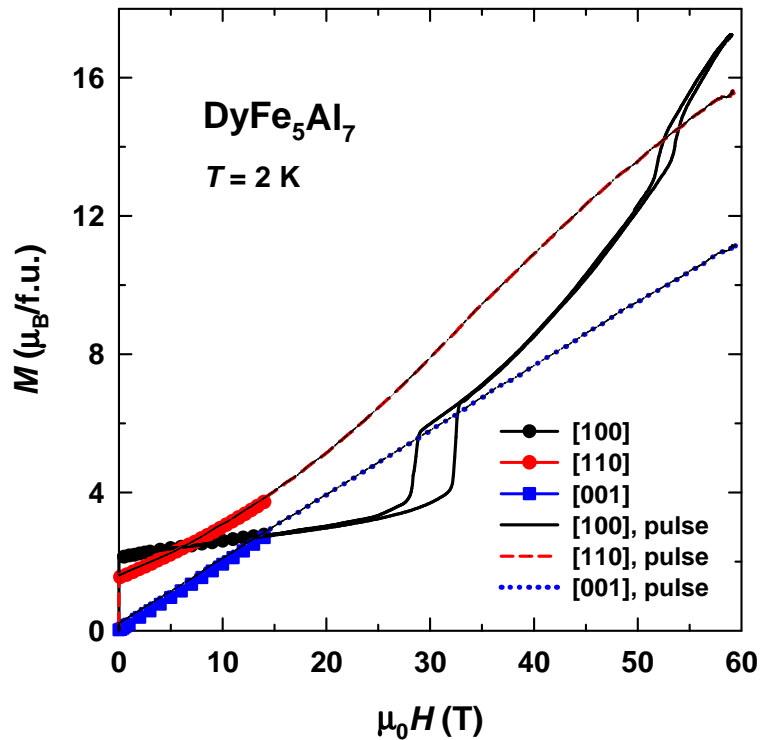


Fig. 5.17. Magnetization curves of the DyFe_5Al_7 single crystal measured along the principal axes in pulsed magnetic fields at $T = 2$ K (lines). The symbols represent steady-field results.

Temperature evolution of the magnetization curve along the easy [100] axis of DyFe_5Al_7 in the temperature range $T = 20 - 80$ K is shown in Fig. 5.18. The first transition is clearly seen at all temperatures, its critical field $H_{\text{cr},1}$ rapidly decreases with temperature. The second transition becomes less pronounced at higher

temperatures but its critical field $H_{cr,2}$ stays constant. Thus, at $T = 80$ K the first jump is still clearly seen on the magnetization curve, whereas the second jump has practically disappeared.

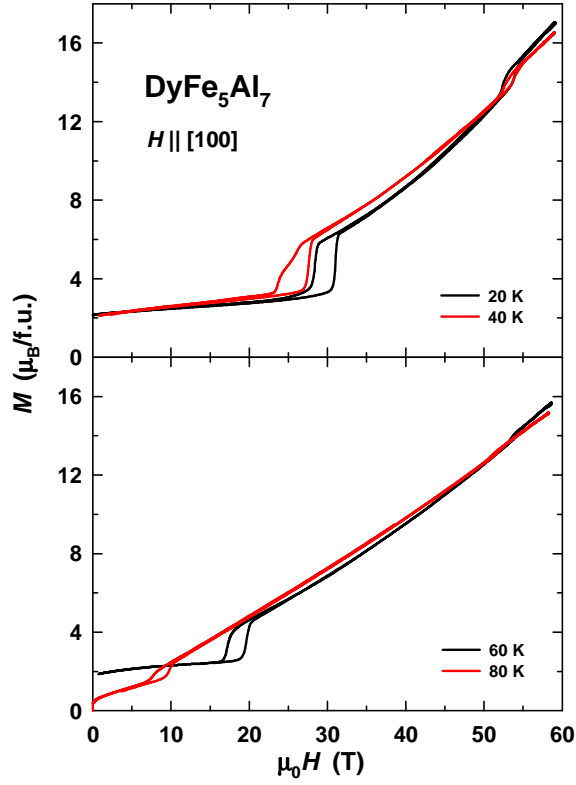


Fig. 5.18. Magnetization curves of the DyFe_5Al_7 single crystal measured along the [100] axis in pulsed magnetic fields at $T = 20 - 80$ K.

The temperature dependence of the critical fields of the first and second transitions in DyFe_5Al_7 is shown in Fig. 5.19 ($H_{cr,1}$ and $H_{cr,2}$ were determined as the average fields between the ascending and descending branches). $H_{cr,1}$ decreases rapidly from about 30 T at $T = 2$ K to zero at $T_{\text{comp}} = 93$ K and then increases as the temperature is raised to $T = 100$ K. At $T < T_{\text{comp}}$ the critical field $H_{cr,1}$ can be fitted to the following equation:

$$H_{cr,1} = H_{cr,0} \left[1 - \left(\frac{T}{T_{\text{comp}}} \right)^2 \right], \quad (5.7)$$

where $\mu_0 H_{cr,0} \approx 30.5$ T is the value of the critical field at $T = 0$. As regards the second transition, its critical field $H_{cr,2}$ does not appear to depend on temperature. For comparison, Fig. 5.19 also shows the T - H magnetic phase diagram (see Fig. 5.16). The calculations predict slightly different values of $H_{cr,1}$ and $H_{cr,2}$, nevertheless, they are in general agreement with the obtained results.

The temperature dependence of the magnetization jump ΔM_1 at the first transition, also shown in Fig. 5.19, is similar to that of the transition field. The jump amounts to about $2.4 \mu_B/\text{f.u.}$ at $T = 2$ K, passes through zero at the compensation

point and then grows, thereby following the spontaneous magnetization. The magnetization jump ΔM_2 at the second transition decreases monotonously with temperature.

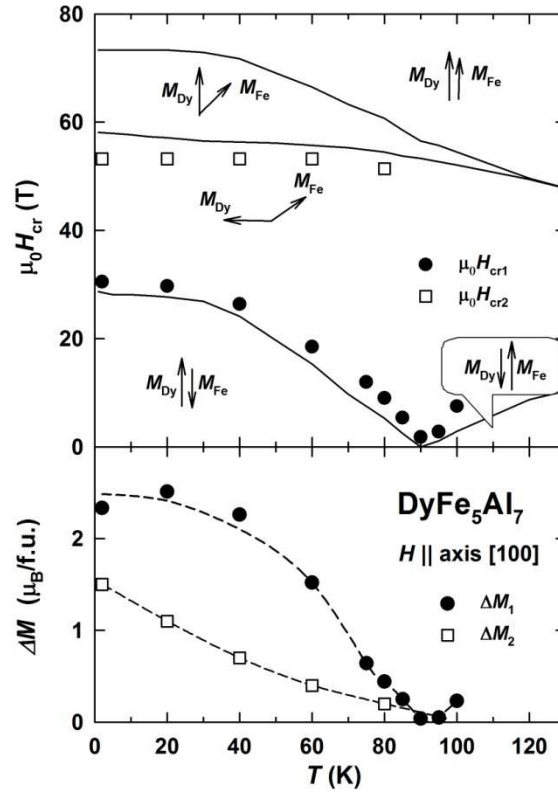


Fig. 5.19. Temperature dependence of the critical fields of the first (circles) and second (squares) field-induced transitions obtained experimentally and calculated for the diagram in Fig. 5.16 (lines) and temperature dependence of the magnetization jumps at the transitions of the DyFe₅Al₇ single crystal.

High-field magnetization measured at $T = 40$ and 80 K along the $[110]$ and $[001]$ axes of DyFe₅Al₇ is shown in Fig. 5.20. None of the curves exhibits any transitions. The magnetization along the $[110]$ axis displays rapid growth at all temperatures. The magnetization along the hard $[001]$ axis grows linearly and much more slowly.

It is suggested to use a different approach to determine the inter-sublattice Dy-Fe exchange interaction in DyFe₅Al₇, i.e., by using the obtained high-field magnetization data. According to the model for an easy-plane ferrimagnet with an anisotropic dominant sublattice [124,125], the first field-induced transition along the easy magnetization direction carries sufficient information for the determination of the inter-sublattice exchange interaction. Below it is demonstrated how this theory works for the DyFe₅Al₇ compound.

We consider a two-sublattice ferrimagnet at $T = 0$. The sublattice moments are regarded as fully saturated, $|M_{Fe}| = \text{const}$, $|M_{Dy}| = \text{const}$. Rotation of the magnetic moments under a magnetic field applied in the basal plane is described by the following thermodynamic potential

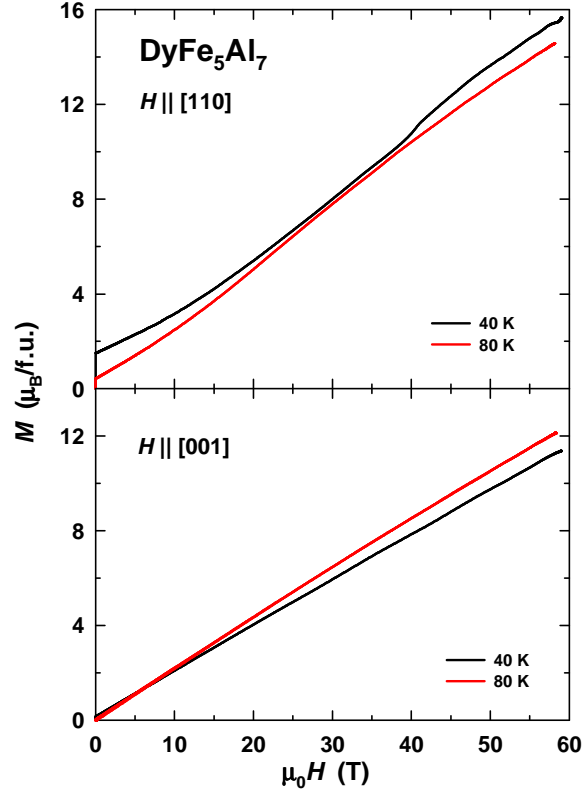


Fig. 5.20. Magnetization curves of the DyFe_5Al_7 single crystal measured along the [110] and [001] axes in pulsed magnetic fields at $T = 40 - 80$ K.

$$\Phi = n_{\text{DyFe}}M_{\text{Fe}}M_{\text{Dy}}\cos(\alpha + \beta) - M_{\text{Fe}}H\cos(\alpha) - M_{\text{Dy}}H\cos(\beta) + K_{\text{Dy}}\cos(4\beta). \quad (5.8)$$

Here, the first term is the intersublattice exchange energy, n_{DyFe} , M_{Fe} and M_{Dy} have the same meaning as those in Eq. (5.1), α and β are the angles between \mathbf{M}_{Fe} and \mathbf{M}_{Dy} , respectively, and the applied magnetic field. The second and third terms are the Zeeman energies of the sublattices. The fourth term is the anisotropy energy of the Dy sublattice in the basal plane as appropriate for the tetragonal symmetry of DyFe_5Al_7 . The in-plane anisotropy of the Fe sublattice is weak and can be neglected as follows from a magnetic study of isostructural GdFe_5Al_7 (this Chapter) and LuFe_5Al_7 (Chapter 4).

For the following analysis it is convenient to introduce dimensionless variables,

$$\varphi = \frac{\Phi}{n_{\text{DyFe}}M_{\text{Fe}}^2}, \quad h = \frac{H}{n_{\text{DyFe}}M_{\text{Fe}}}, \quad m = \frac{M_{\text{Dy}}}{M_{\text{Fe}}}, \quad \kappa = \frac{K_{\text{Dy}}}{n_{\text{DyFe}}M_{\text{Fe}}^2}. \quad (5.9)$$

In terms of these variables, the thermodynamic potential (5.8) is re-written as follows:

$$\varphi(\alpha, \beta) = m\cos(\alpha + \beta) - h\cos(\alpha) - mh\cos(\beta) + \kappa\cos(4\beta). \quad (5.10)$$

The calculation consists in finding the minimum of the free energy (5.10) with respect to the angles α and β for a given h and setting those values in the expression for the reduced magnetization

$$\sigma = \frac{\cos(\alpha) + m\cos(\beta)}{1-m}. \quad (5.11)$$

The angle β was found by going over all values between 0 and $\pi/2$. For a given β , the angle α was determined from the equation

$$\alpha = \frac{\pi}{2} - \arctan \frac{h - m\cos(\beta)}{m\sin(\beta)} \quad (5.12)$$

which made it possible to calculate α in the whole range from 0 to π . Note that Eq. (13) of Ref. [124] is only valid for α acute.

The shape of the magnetization curve $\sigma(h)$ depends on two parameters: the ratio of the sublattice moments m and the anisotropy constant κ of the rare-earth sublattice. All possible shapes of the magnetization curve were obtained in Ref. [126] for the special case $0 < m < 1$. In the present work, the analysis is extended to the case $1 < m < 2$ since $M_{\text{Dy}} > M_{\text{Fe}}$ as appropriate for DyFe_5Al_7 . In contrast to m , κ is usually unknown. Similarly to Ref. [126], a detailed examination has been performed of all possible types of behavior of a system with various m and κ . The results are summarized in Fig. 5.21 showing 10 different curve types according to the classification proposed in ref. [127]. In fact, most of the magnetization curves shown in Fig. 5.21 are the same as those in Ref. [126]. The two new curves, namely, f and t , appear in the region $m > 1$ as seen in Fig. 5.22 showing part of the $m\kappa$ plane for $0 < m < 2$. The curve f is observed at moderate values of κ and contains one magnetization jump preceded and followed by kinks. With an increase in the anisotropy constant, a second discontinuity and yet another kink appear on the magnetization curve (curve t).

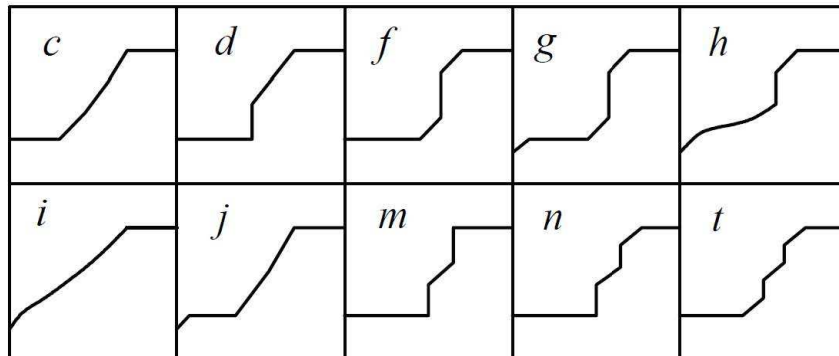


Fig. 5.21. Ten archetypal patterns of high-field magnetization curves.

The lines cd , mn , dn , cf and df/nt drawn in Fig. 5.22 were determined using the same formulas as in the case $0 < m < 1$ [126]. In order to find the coordinates of the triple point 3, one should set $\kappa_1 = -8\kappa$ and $\kappa_2 = 8\kappa$ in Eqs. (50-52) of ref. [127] and equate them to zero. Then the ordinate is $m = \frac{21}{50} \times (1 + \sqrt{\frac{21}{5}}) \approx 1.281$, the abscissa is $\kappa = -21/5^5 = 0.00672$. It is interesting to note that the triple points 2 and 3 have the same ordinates, and their abscissas differ by exactly 0.84. The boundary ct is a vertical line at $m = \sqrt{2}$. It is related to features in the behavior of the angles α and β as functions of field h in the vicinity of the hard magnetization direction $\beta = \pi/4$. It follows from $\beta = \pi/4$ that $\sin(\alpha) = m/\sqrt{2}$ for arbitrary κ . At $m < \sqrt{2}$ there are two values of the angle α that correspond to $\beta = \pi/4$ and there are no such values in case $m > \sqrt{2}$, i.e., $\beta = \pi/4$ is not reached, $\max \beta < \pi/4$. At $m = \sqrt{2}$ the angle β attains its maximum value $\pi/4$ at $h = 1$, in this case $\alpha = \pi/2$.

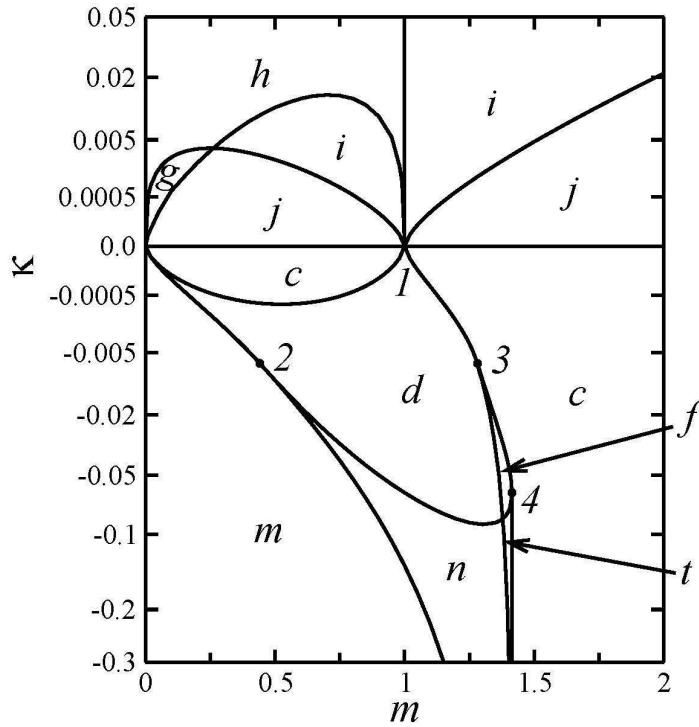


Fig. 5.22. Partition of the parameter plane m - κ among the curve types sketched in Fig. 5.21. Note the nonlinear vertical scale: $\kappa \sim y^3$, where y is the ordinate in the drawing.

In case of a strong anisotropy, $\kappa < -\frac{1}{16}$, the orientation of the spins along the hard magnetization direction $\beta = \pi/4$ is unstable – $\varphi(\alpha, \beta)$ has a saddle point at $\alpha = \pi/2$, $\beta = \pi/4$. It is easy to prove by a direct calculation of the second derivatives with $m = \sqrt{2}$ and $h = 1$. For this reason, there is a discontinuity where β can exceed $\pi/4$ (i.e., at $m < \sqrt{2}$) in order to avoid an unstable state near $\beta = \pi/4$. Two discontinuities appear on the magnetization curve – on increasing and decreasing β .

In case $\kappa > -\frac{1}{16}$, the state with $\beta = \pi/4$ (and $\alpha = \pi/2$) is stable and no discontinuities appear. For this reason, the line ct ends in the triple point 4, whose coordinates are $m = \sqrt{2}$, $\kappa = -\frac{1}{16}$.

The line ij at $m > 1$ was calculated using the same formula as at $m < 1$:

$$\kappa = \frac{1}{16} m (1 - \sqrt{m})^2. \quad (5.13)$$

Figure 5.22 shows that a rich variety of magnetization curves is expected in the vicinity of $m \sim 1.3$. By contrast, the behavior is much simpler for $m > \sqrt{2}$. The ratio of the sublattice moments in DyFe_5Al_7 is $m = 1.27$. For this m and $\kappa > 0$ there are two curve types (i and j), whereas for $\kappa < 0$ as many as four different shapes of the magnetization curve are possible (n , d , f , and c). The magnetization curve along the easy [100] axis of the DyFe_5Al_7 compound at $T = 2$ K displays two jumps, both of them are followed by slanting sections (Fig. 5.17). According to Fig. 5.21, such a shape corresponds to type n . Magnetization curves of type n are of rare occurrence in systems with $M_R < M_{\text{Fe}}$ ($m < 1$). At $m = 1.27$ curves of type n should be observed within the interval $-0.7 < \kappa < -0.09$, delimited by the lines dn and mn (Fig. 5.22). As regards the magnetization curves along the [001] and [110] axes, they correspond to types a (defined in Ref. [127]) and i , respectively.

According to the method used in Refs. [124,125], the inter-sublattice molecular field can be determined from the high-field magnetization data by $H_{\text{mol}} = H_1/h_1$, where $H_1 = 30$ T is the critical field of the first field-induced transition along the EMD and h_1 is the dimensionless critical field determined as

$$h_1 = \frac{m-1}{1-\frac{m}{2}}. \quad (5.14)$$

The expression (5.14) is the analogue of Eq. (A8) in Ref. [126] for the case $m > 1$. At $T = 2$ K the intersublattice molecular field on Dy in DyFe_5Al_7 is $\mu_0 H_{\text{mol}} = n_{\text{DyFe}} M_{\text{Fe}} = 41$ T. Using molecular field theory, a value of $\mu_0 H_{\text{mol}} = 42$ T was obtained at $T = 0$, in good agreement with this result. From the obtained value of the intersublattice molecular field the range of values of the basal plane Dy anisotropy constant is found to be $-150 < K_{\text{Dy}} < -20$ K/f.u. ($-10.90 < K_{\text{Dy}} < -1.45$ MJ/m³).

It is worth noting that in an isomorphous compound $\text{DyFe}_{11}\text{Ti}$ K_{Dy} is similarly large in magnitude but positive: $K_{\text{Dy}} \approx \frac{4095}{2} B_{44} = 22$ K/f.u. (1.56 MJ/m³) [128] where $B_{44} = 1.05 \times 10^{-2}$ K is the corresponding crystal-field parameter [129], the sign of B_{44} has been corrected to positive, according to Ref. [130]. Therefore, the easy magnetization direction in $\text{DyFe}_{11}\text{Ti}$ is [110] rather than [100], Refs. [130,131]. In this connection, it would be interesting to investigate Dy-Fe intermetallics with the ThMn_{12} structure where the ratio of Dy to Fe content changes from 1/5 to 1/11 and thus, K_{Dy} is expected to change sign. Ternary compounds with such composition range do not exist, however, it might be possible to find some quasiterminals. In particular, $\text{LuFe}_x\text{Al}_{10-x}\text{Si}_2$ ($7 \leq x \leq 10$) compounds have been studied before [117].

For clarity Figs. 5.6, 5.8 and 5.11 showed only the field-descending branch of the magnetization curves in the basal plane or, in the case of the transition, also the ascending part but only above 4 T. Now a domain hysteresis observed in the

DyFe₅Al₇ single crystal will be described. Figures 5.23 and 5.24 show hysteresis loops in a field applied along the [100] and [110] axes, respectively, at different

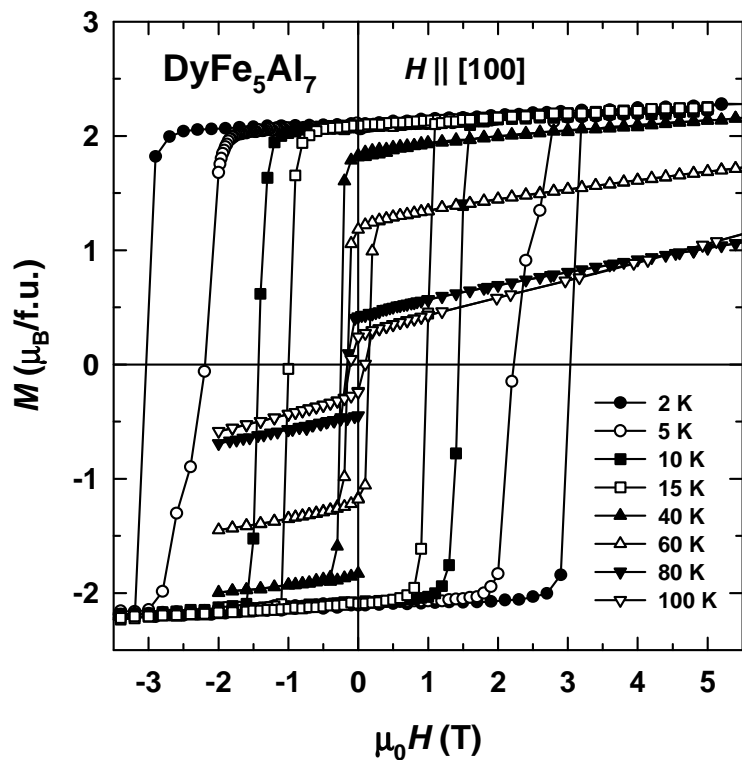


Fig. 5.23. Low-field details of hysteresis loops measured along the [100] axis at different temperatures.

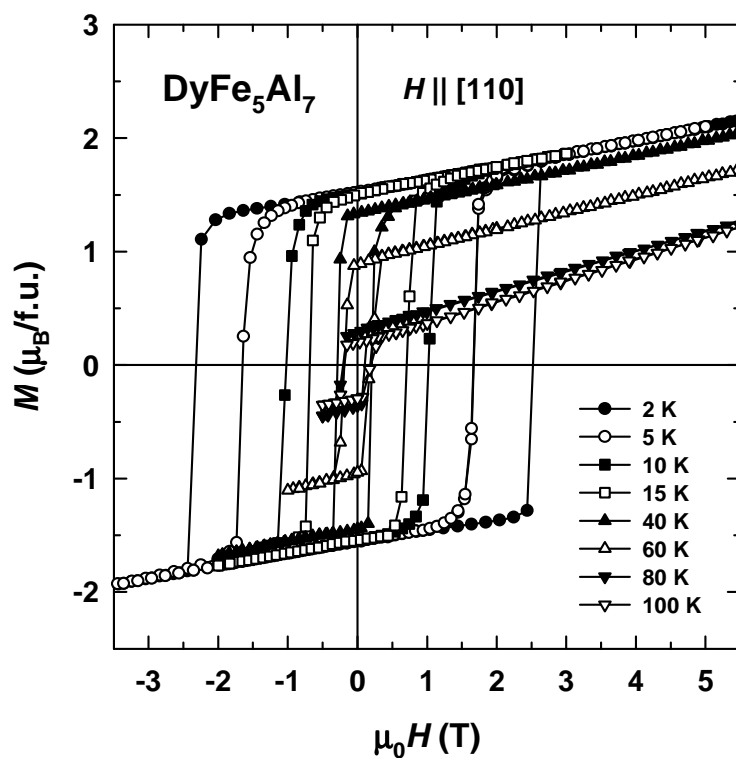


Fig. 5.24. Low-field details of hysteresis loops measured along the [110] axis at different temperatures.

temperatures. The coercive field H_c is very large especially taking into account the easy-plane type of magnetic anisotropy. H_c reflects the fact that, apart from the anisotropy between the basal plane and the tetragonal axis, the in-plane anisotropy is also very strong in DyFe_5Al_7 . At $T = 2$ K, H_c reaches very large values of 3 T and 2.4 T along the [100] and [110] axes, respectively, and rapidly decreases with increasing temperature (Fig. 5.25). Below approximately $T = 20$ K, $H_c(T)$ exhibits a drastic exponential decrease, $H_c(T) = H_c(0)\exp(-\beta T)$, corresponding with the model of a high intrinsic coercivity of narrow domain walls applicable to systems with a very high magnetic anisotropy [132]. At higher temperatures, a different less temperature-dependent mechanism of coercivity dominates leading to a much slower decrease in H_c with a moderate maximum in the vicinity of T_{comp} .

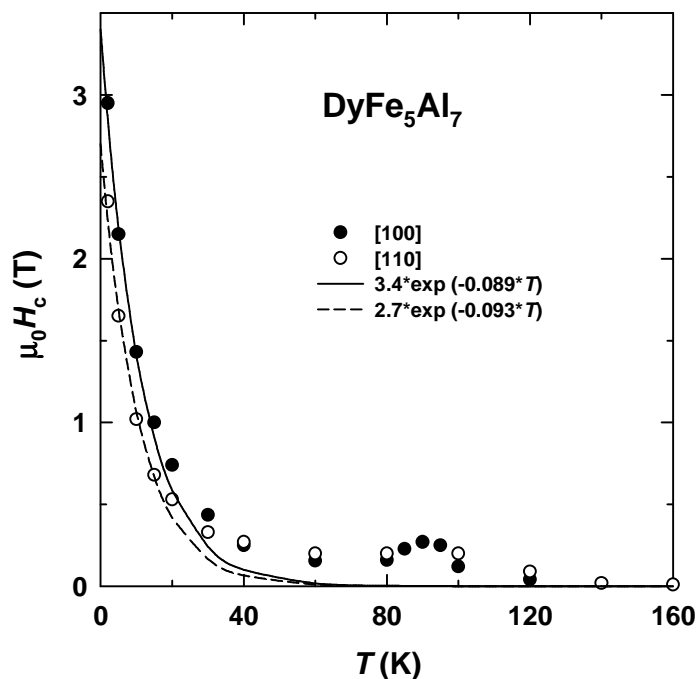


Fig. 5.25. Temperature dependence of the coercive field $\mu_0 H_c$ along the [100] and [110] axes. The dashed lines represent the fit $\mu_0 H_c(T) = \mu_0 H_c(0)\exp(-\beta T)$.

Apart from the field hysteresis, DyFe_5Al_7 also exhibits a thermal hysteresis. Figure 5.26 shows the temperature dependence of the magnetization measured in a 0.1 T field applied along the main axes in the basal plane upon heating and cooling. First, the sample was cooled down from room temperature to $T = 2$ K in a magnetic field of 0.5 T. Since this field is considerably higher than the coercivity just below T_{comp} , the crystal became saturated along the moments of the Dy sublattice. Qualitatively the same result was obtained in Refs. [19,20] under the same conditions. Upon heating this single-domain sample in a field of 0.1 T through the compensation point, the magnetization reorients itself along the moments of the Fe sublattice, i.e., it becomes negative with respect to the applied field of 0.1 T because the coercivity is larger than this field in the vicinity of T_{comp} (Fig. 5.25). However,

the magnetization remains negative only in a narrow temperature interval because above $T = 100$ K H_c becomes lower than the applied field and the crystal becomes magnetized along the field. Upon subsequent cooling of the sample, since H_c below T_{comp} is always higher than 0.1 T, the crystal remains single-domain after the inversion of the magnetization from the Fe to the Dy sublattice, and the “negative magnetization effect” is seen in a wide range up to the lowest temperatures. Under particular conditions of the experiment, “the single-domain state” is valid, however, only for the [110] axis where the magnetization of the cooled crystal reaches at $T = 2$ K the absolute value of $1.55 \mu_B$, i.e., the same as the projection of M_s onto this axis. For the [100] axis, a slightly lower minimal H_c below T_{comp} , (at $T = 60$ -80 K), 0.16 T instead of 0.2 T along [110], leads to a partially demagnetized state, and the absolute value of the negative magnetization at $T = 2$ K ($1.7 \mu_B$) is lower than $M_s = 2.1 \mu_B$.

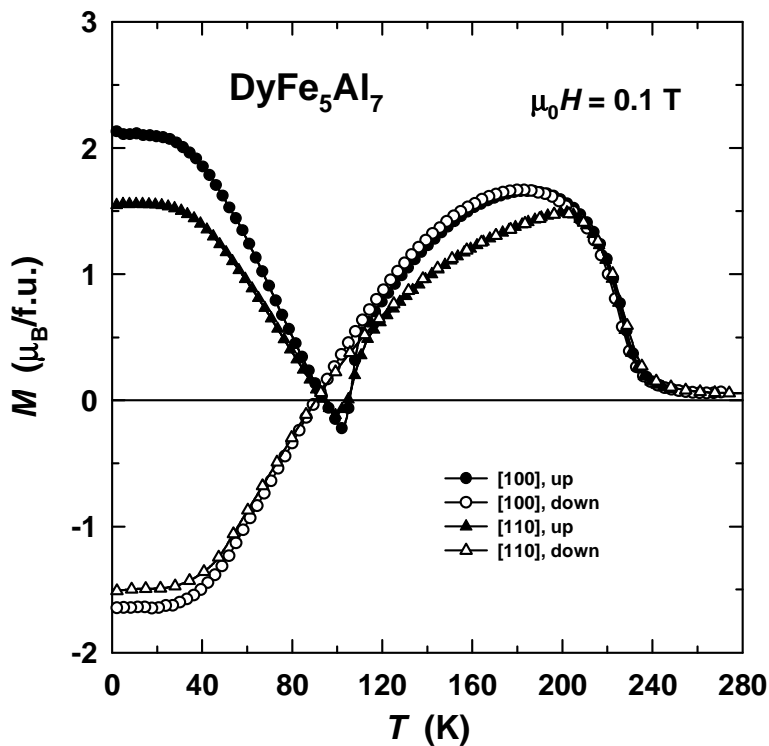


Fig. 5.26. Temperature dependence of magnetization measured in a field of 0.1 T applied along the [100] and [110] axes. First the sample was cooled to $T = 2$ K in a field of 0.5 T. Then, the magnetization was measured in 0.1 T upon heating the sample up to $T = 280$ K and subsequent cooling down to $T = 2$ K.

5.4. TbFe₅Al₇

A magnetic study of the DyFe₅Al₇ compound in the previous section demonstrated that the presence of a rare-earth ion having an anisotropic 4*f* electronic shell results in a strong magnetocrystalline anisotropy. It substantially affects the behavior in a magnetic field and manifests itself by a strong magnetic and thermal hysteresis.

Equally interesting physics is expected for other representatives of the RFe₅Al₇ family with different magnetic heavy rare-earth elements. Magnetism and magnetoelasticity of the TbFe₅Al₇ compound are investigated in this section. Strong magnetic anisotropy and field-induced magnetic transitions should be observed as well. Moreover, in Ref. [87] a spin-glass behavior at low temperatures was reported for this material.

Figure 5.27 shows magnetization isotherms along the principal crystallographic directions of the TbFe₅Al₇ single crystal at several selected temperatures (only field-descending branches are shown, low-field details will be discussed below). The compound exhibits a spontaneous magnetic moment along the [100] and [110] axes, and no spontaneous component is present along the [001] axis. Therefore, the magnetic moments of TbFe₅Al₇ lie in the basal plane. The [001] axis is the hard magnetization direction. Anisotropy is also present within the basal plane of the compound since the magnetization along the [100] and [110] axes displays different behavior in the magnetic field. At $T = 2$ K the EMD is the [100] axis with the spontaneous magnetic moment $M_s = 1.24 \mu_B/\text{f.u.}$ The spontaneous moment ratio, $M_s^{110}/M_s^{100} \approx \cos 45^\circ$, corresponds to the tetragonal symmetry and reflects good quality of the crystal and its proper orientation. Under the assumption that the Tb magnetic moment is equal to its theoretical value, $\mu_{\text{Tb}} = 9 \mu_B$, the magnetic moment of the Fe sublattice in ferrimagnetic TbFe₅Al₇ can be calculated as follows: $M_{\text{Fe}} = M_{\text{Tb}} - M_s = 7.76 \mu_B$. This corresponds to the Fe moment $\mu_{\text{Fe}} = 1.55 \mu_B$ per Fe atom. It is also seen from Fig. 5.27 that at $T = 120$ and 200 K $M_s^{100} < M_s^{110}$, in contrast to the situation at $T = 2$ and 40 K. It means that TbFe₅Al₇ displays a spin-reorientation transition within the basal plane from the [100] axis to the [110] axis. Strong paraprocess is observed above the field in which the domain-wall motion is completed. It reflects field-induced non-collinearity of magnetic moments and causes the [100]- and [110]-magnetization curves to intersect at low temperatures. The intensive paraprocess is similar to those found in GdFe₅Al₇ and DyFe₅Al₇ and originates from the relatively weak Tb-Fe intersublattice exchange interactions caused by the heavy dilution of the Fe sublattice with Al.

Figure 5.28a shows the temperature dependence of the spontaneous magnetization M_s for fields applied along the [100] and [110] axes. The non-monotonous temperature dependence of M_s for both directions reflects a ferrimagnetic order with changing sublattice magnetizations in the compound. A compensation of the Tb and Fe sublattices is observed at $T_{\text{comp}} = 84$ K. A spin-reorientation transition occurs near this compensation point. In this temperature

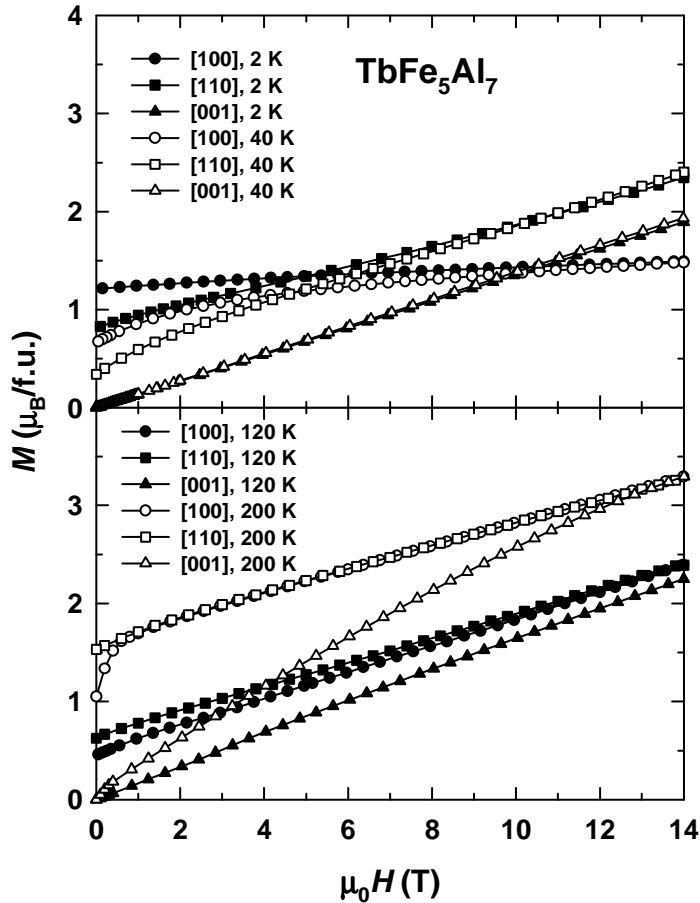


Fig. 5.27. Magnetization curves along the principal crystallographic directions of the TbFe_5Al_7 single crystal at several selected temperatures.

range, the ratio $M_s^{110}/M_s^{100} \approx \cos 45^\circ$ (or $M_s^{100}/M_s^{110} \approx \cos 45^\circ$) is not fulfilled, M_s^{110} values become very small. Magnetization curves along the [100] and [110] axes at $T = 95$ and 98 K show the transition in more detail (Fig. 5.29). At $T = 95$ K the EMD is still along the [100] axis, whereas at $T = 98$ K the [110] axis is the EMD with the ratio $M_s^{100}/M_s^{110} \approx \cos 45^\circ$. It was also found that there is no component of the spontaneous magnetic moment along the [001] axis which is the hard magnetization direction in the whole magnetically ordered state. The low M_s^{110} values can be explained by the fact that the highest applied field of 14 T is not sufficient to induce a single domain state in TbFe_5Al_7 due to a considerable growth of coercivity (see below). From the magnetization measurements the spin-reorientation temperature T_{sr} could not be determined precisely.

The spin-reorientation transition affects strongly the sound propagation through TbFe_5Al_7 . Figure 5.28b shows the temperature dependence of the relative change of the sound velocity, $\Delta v/v$, and sound attenuation, $\Delta\alpha$, for a longitudinal acoustic wave propagating along the [100] axis. $\Delta v/v$ displays a broad minimum and $\Delta\alpha$ a broad maximum in the vicinity of T_{comp} . Figure 5.28c shows the acoustic properties for a longitudinal wave propagating along the [110] direction of TbFe_5Al_7 . Both, $\Delta v/v$ and $\Delta\alpha$, also display clear, but less pronounced broad anomalies in the

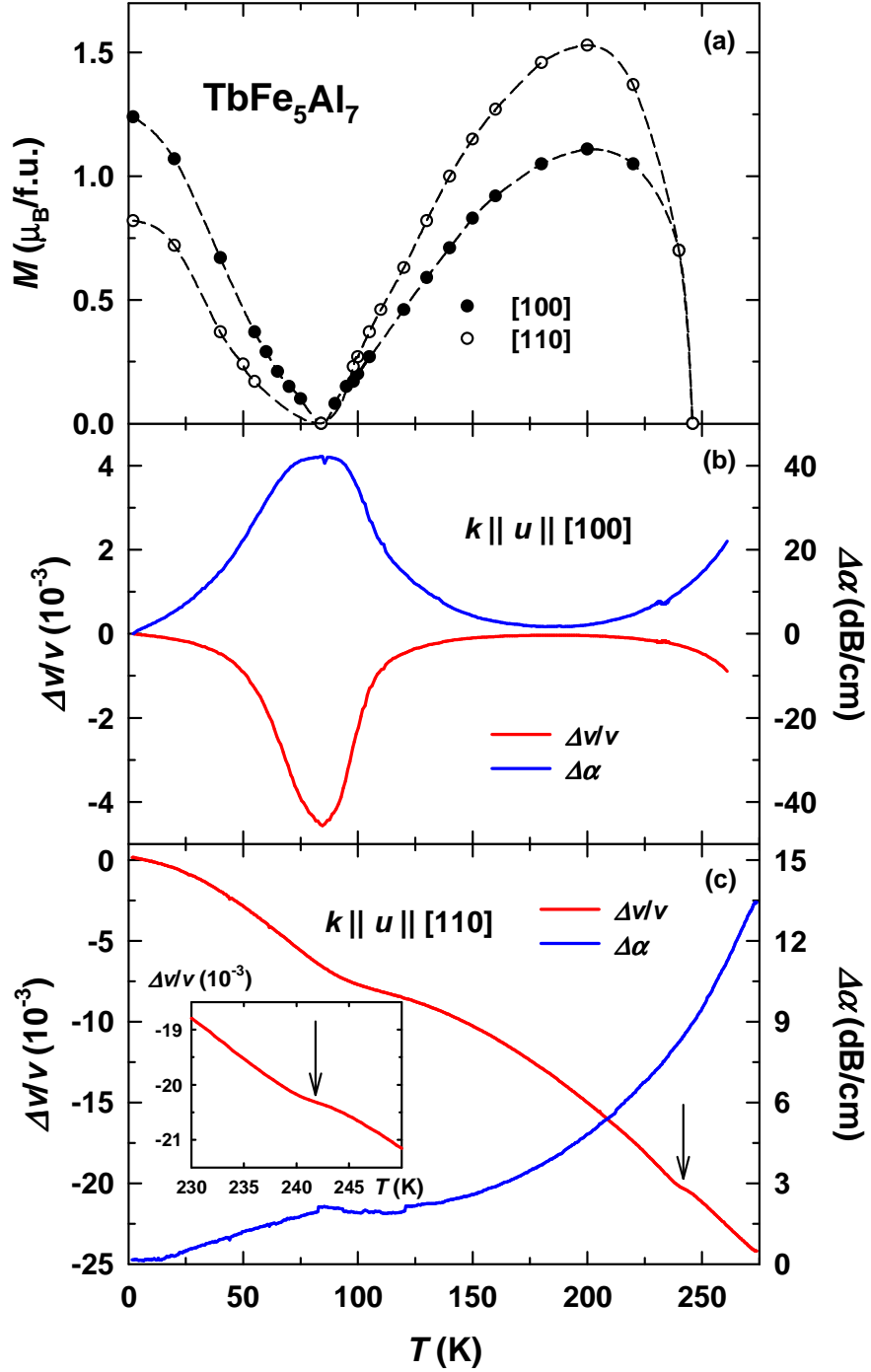


Fig. 5.28. Temperature dependence of (a) spontaneous magnetization along the $[100]$ and $[110]$ axes, (b) of the relative change of the sound velocity and sound attenuation of a longitudinal acoustic wave propagating along the $[100]$ axis, and (c) along the $[110]$ axis of TbFe_5Al_7 . The inset shows the relative change of sound velocity in the vicinity of $T_C = 242$ K.

same temperature range. The compensation point is not a phase transition since no additional symmetry is broken or new order parameter evolves at this temperature. Therefore, the observed features in the acoustic properties of TbFe_5Al_7 are associated

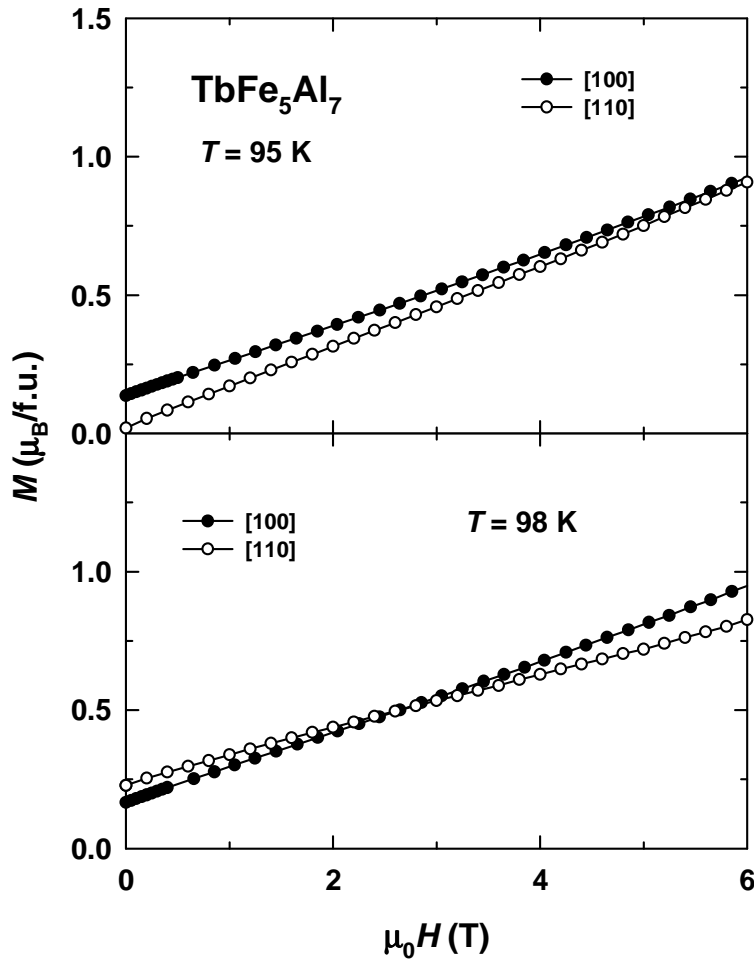


Fig. 5.29. Magnetization curves along the [100] and [110] axes of the TbFe_5Al_7 single crystal at $T = 95$ and 98 K.

with the spin reorientation. Note that similar anomalies were observed in highly magnetostrictive $R\text{Fe}_2$ compounds near their spin-reorientation transitions (see Ref. [48] and references therein). The origin of those anomalies was attributed to a softening of the lattice due to magnetoelastic interactions. The specific heat does not display any anomaly related to the spin-reorientation transition (Fig. 5.30). The most likely reason is a very low change in entropy of TbFe_5Al_7 at the transition since in the whole temperature range of the magnetically-ordered state the magnetic moments of TbFe_5Al_7 do not leave the basal plane. By contrast, a more significant effect is expected in case of a spin-reorientation transition from the basal plane to the c axis of the tetragonal lattice or *vice versa*. The order of the transition can be determined by a microscopic technique, such as neutron diffraction, or by magnetic dilatometry, similarly to Refs. [133,134] where the isostructural $\text{TbFe}_{11}\text{Ti}$ compound was studied. The magnetostrictive distortions are related to the orientation of the magnetic moments in TbFe_5Al_7 . At $T < T_{\text{sr}}$, the magnetic moments lie along the [100] axis, which should lead to orthorhombic distortions of the tetragonal lattice that can be detected by a splitting of the $(h00)$ lines by use of X-ray diffraction. At $T > T_{\text{sr}}$, the magnetic moments lie along the [110] axis, and different orthorhombic distortions are expected, i.e., the $(hh0)$ lines should be split. One type of orthorhombic

distortions should abruptly change to the other in case of a first-order phase transition – a step-wise reorientation of the magnetic moments. By contrast, a gradual rotation of the magnetic moments from one axis to the other should be accompanied by monoclinic distortions. In this case two second-order phase transitions should occur: first, as the magnetic moments begin to deviate from the [100] axis, and second, as they become aligned along the [110] axis. Routine X-ray powder diffraction cannot be used for this task since a large magnetostrictive distortion $\sim 1 \times 10^{-3}$ is rather low from the structural viewpoint, and such a study should be performed in very high 2θ angles using lines which are very weak on powders.

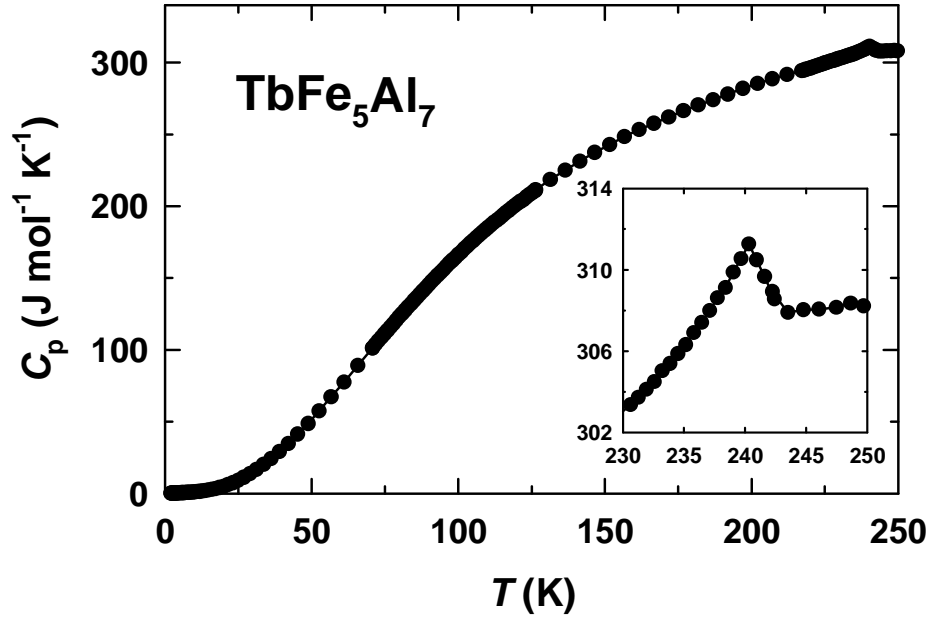


Fig. 5.30. Temperature dependence of the specific heat of the TbFe_5Al_7 single crystal. The inset shows the specific heat in the vicinity of $T_C = 242$ K.

The closeness of T_{sr} to T_{comp} might not be accidental in TbFe_5Al_7 . From the experiment it follows that in a magnetic field there exists a non-collinear magnetic structure in the compound (see Fig. 5.27). The field-induced non-collinearity occurs due to the relatively weak Tb-Fe exchange interaction since the Fe sublattice is significantly diluted with Al. It was shown in Ref. [135] that such a canting of magnetic moments considerably reduces the effective anisotropy energy caused by the intrinsic sublattice anisotropies. Under these circumstances, in a hexagonal crystal the effective anisotropy constant is determined in the following way:

$$K_{\text{eff}} \approx \frac{n_{\text{TbFe}}(K_R + K_T) + 36K_R K_T}{n_{\text{TbFe}} + 36 \frac{M_T^2}{(M_R - M_T)^2} K_R + 36 \frac{M_R^2}{(M_R - M_T)^2} K_T}, \quad (5.15)$$

where K_R and K_T are the basal plane anisotropy constants of the rare-earth and transition metal sublattices, respectively, M_R and M_T their magnetic moments, and

n_{TbFe} the inter-sublattice exchange parameter. We used the same approach as that of Ref. [135] and obtained the following expression for a tetragonal crystal:

$$K_{\text{eff}} \approx \frac{n_{\text{TbFe}}(K_R + K_T) + 16K_R K_T}{n_{\text{TbFe}} + 16 \frac{M_T^2}{(M_R - M_T)^2} K_R + 16 \frac{M_R^2}{(M_R - M_T)^2} K_T}, \quad (5.16)$$

where K_R and K_T are the basal plane anisotropy constants of the tetragonal lattice. For TbFe_5Al_7 Eq. (5.16) can be simplified taking into account that $K_T = 0$:

$$K_{\text{eff}} \approx \frac{n_{\text{TbFe}} K_R}{n_{\text{TbFe}} + 16 \frac{M_T^2}{(M_R - M_T)^2} K_R}, \quad (5.17)$$

The reason is that no anisotropy within the basal plane was detected in isostructural $\text{LuFe}_x\text{Al}_{12-x}$ compounds where magnetic order originates only from the Fe sublattice (see Chapter 4). If the Tb and Fe magnetic moments would rotate rigidly antiparallel in a magnetic field, the corresponding anisotropy energy would be the sum of the two magnetic-sublattice contributions (consider $n_{\text{TbFe}} \rightarrow \infty$ in Eq. (5.16)). In the vicinity of the compensation point the magnetic moments of the Tb and Fe sublattices have close absolute values. Therefore, K_{eff} is reduced as compared to its values away from T_{comp} . A dominant contribution to the anisotropy energy might be given by higher-order terms leading to the observed spin-reorientation transition in TbFe_5Al_7 .

The spontaneous magnetic moments along the [100] and [110] axes drop to zero at 246 K (Fig. 5.28a). The anomaly corresponding to the phase transition from the ordered into the paramagnetic state is observed in $\Delta v/v$ for sound along the [110] axis at about 242 K, as shown by the arrow in Fig. 5.28c and in the inset. The latter value of the Curie temperature T_C is more accurate since sound propagation was measured in zero magnetic field. Moreover, $T_C = 242$ K also follows from the zero-field specific-heat measurements (inset in Fig. 5.30).

The in-plane anisotropy is observed in TbFe_5Al_7 almost up to the magnetic ordering temperature (see Fig. 5.28a, M_s along the [100] and [110] are still different at $T = 220$ K). Figure 5.31 presents the temperature variation of the anisotropy between the [100] and [110] axes in the temperature range $T = 120 - 240$ K where the anisotropy field $H_{\text{a,p}}$ is lower than 14 T. A gradual reduction of the in-plane anisotropy is seen with increasing temperature. It should be noted that the determination of $H_{\text{a,p}}$ is not unambiguous since it is hard to find the exact intersection point between the $M(H)$ curves along the [100] and [110] axes.

The temperature evolution of the magnetization isotherm along the easy [100] axis of the TbFe_5Al_7 single crystal is presented in Fig. 5.32. At $T < 70$ K the magnetization is a featureless function of field up to 14 T. At $T = 70$ K a field-induced transition is seen. The $M(H)$ dependence at $T = 100$ K exhibits a small downward curvature, which might serve as a prerequisite to a transition in a field

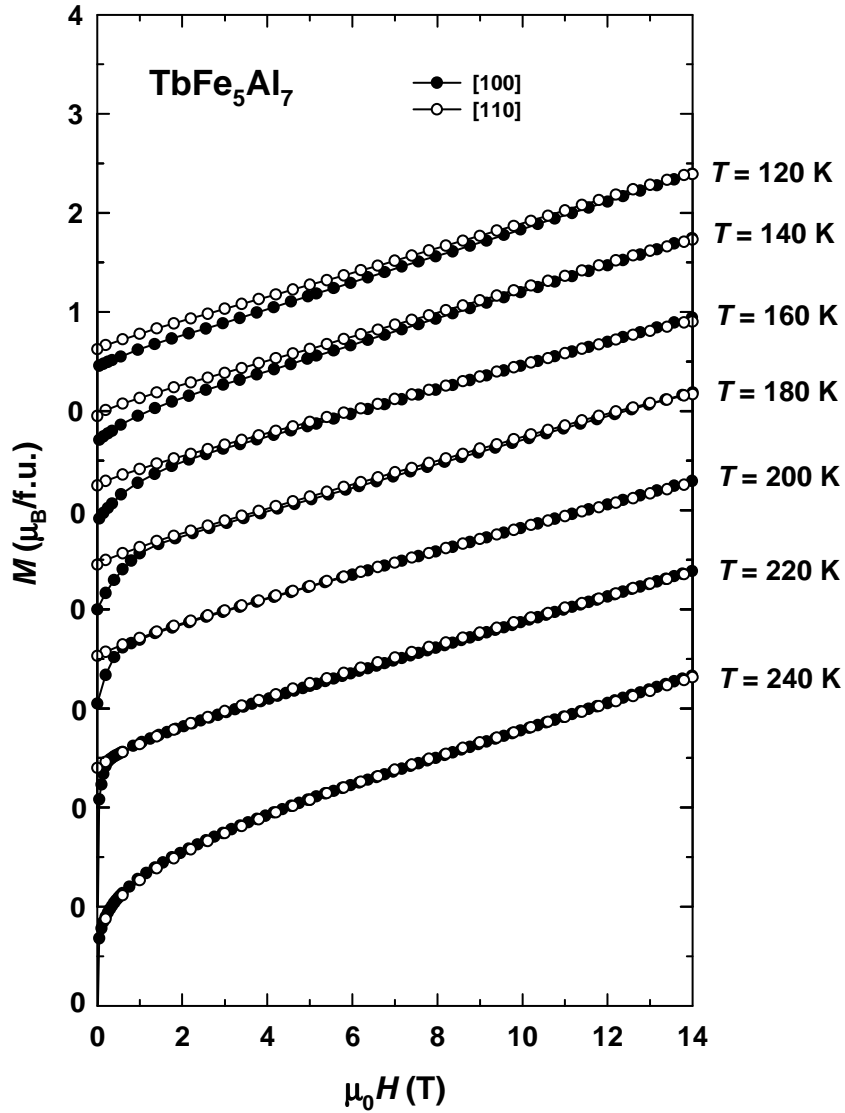


Fig. 5.31. Temperature evolution of the in-plane magnetic anisotropy of the TbFe_5Al_7 single crystal in the range $T = 120 - 240$ K.

higher than 14 T. The magnetization curves at $T > 100$ K are generally linear functions of field.

The magnetization isotherms along the [110] axis change with field in a similar manner (Fig. 5.33). Nevertheless, special attention should be given to the $M(H)$ dependence at $T = 40 - 60$ K. As discussed above (see Fig. 5.28a), the projection of the spontaneous magnetic moment onto the [110] axis cannot be properly determined and is underestimated down to zero. As a result, at $T = 60$ K M_s^{110} looks equal to zero, although the compensation of the Tb and Fe sublattices occurs only at $T_{\text{comp}} = 84$ K.

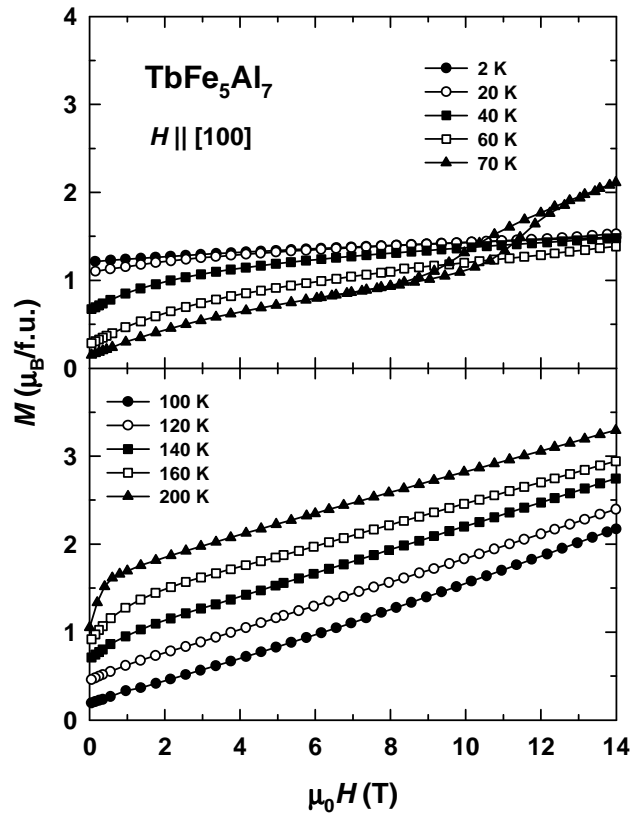


Fig. 5.32. Temperature evolution of the magnetization curve along the [100] axis of the TbFe₅Al₇ single crystal.

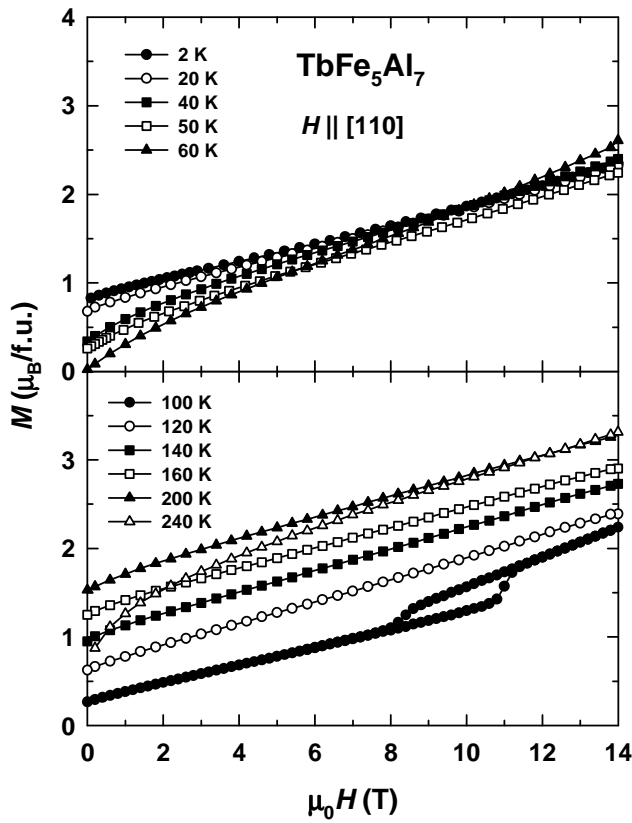


Fig. 5.33. Temperature evolution of the magnetization curve along the [110] axis of the TbFe₅Al₇ single crystal.

The temperature evolution of the magnetization isotherm along the hard [001] axis is presented in Fig. 5.34. Below about $T = 200$ K all the isotherms are linear, the anisotropy field H_a exceeds the highest available field of 14 T. A change of the slope reflecting $\mu_0 H_a = 8$ T appears at $T = 220$ K (the H_a value was determined by the singular-point detection method [119]). At $T = 240$ K, just below $T = T_C$, still a high value $\mu_0 H_a = 6$ T was obtained. The anisotropy field found for isostructural DyFe_5Al_7 has much lower values upon approaching its magnetic ordering temperature. H_a values obtained in the vicinity of $T = T_C$ suggest that the TbFe_5Al_7 compound exhibits a very strong anisotropy at lower temperatures. The large anisotropy is associated with the Tb single-ion anisotropy since the Fe sublattice displays a moderate anisotropy.

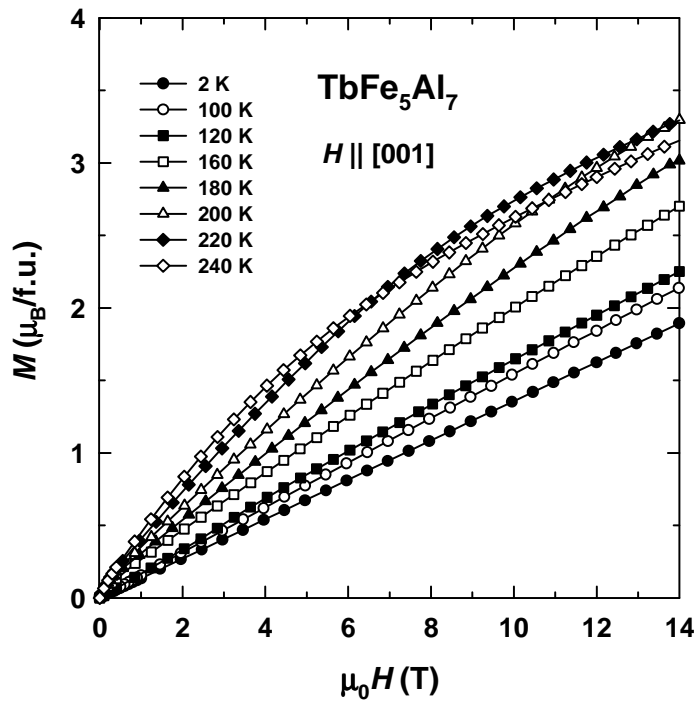


Fig. 5.34. Temperature evolution of the magnetization curve along the [001] axis of the TbFe_5Al_7 single crystal.

Figures 5.32 and 5.33 indicate that in the vicinity of the compensation point $T_{\text{comp}} = 84$ K TbFe_5Al_7 displays field-induced magnetic transitions along the [100] and [110] axes, respectively. Figures 5.35 and 5.36 show that anomalies appear both in the magnetization as in the sound velocity. For fields applied along the [100] axis (Fig. 5.35) the anomalies, observed below T_{comp} , display hysteresis evidencing first order transitions. The critical field decreases with increasing temperature. The anomalies in $\Delta v/v$ are rather broad.

For fields applied along the [110] axis (Fig. 5.36), anomalies in M and $\Delta v/v$ are observed above the compensation temperature. In this case, the transition field increases with increasing temperature. In the sound velocity, sharp hysteretic minima appear at the same field values where the steps in the magnetization occur. The

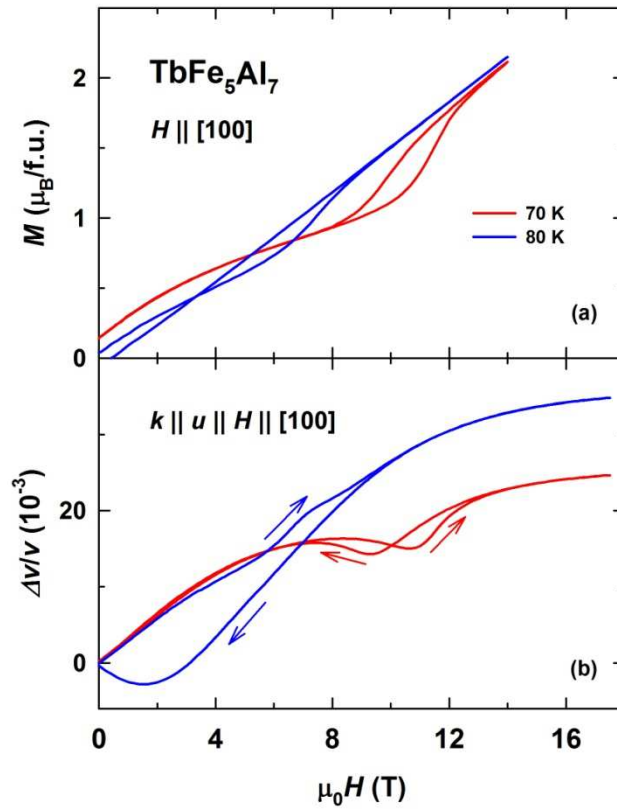


Fig. 5.35. (a) Magnetization and (b) relative change of the sound velocity of TbFe_5Al_7 below $T_{\text{comp}} = 84$ K as a function of magnetic field applied along the [100] direction.

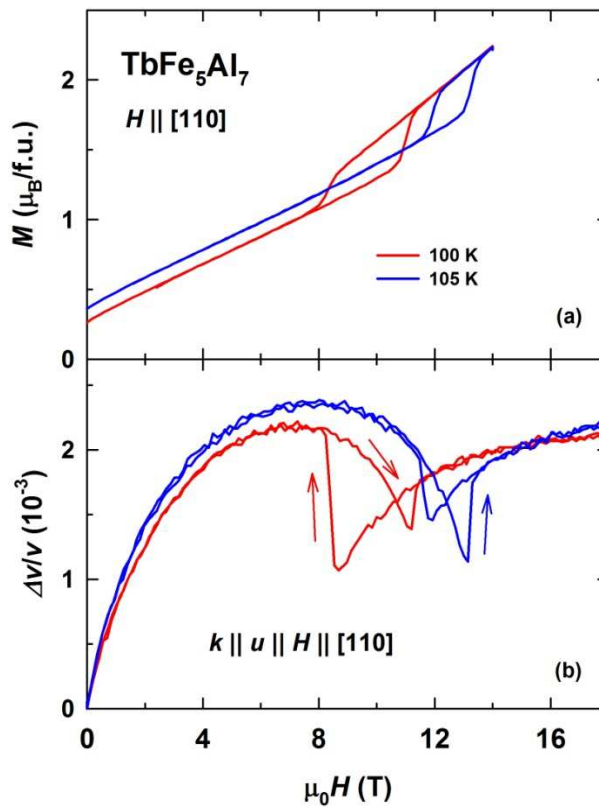


Fig. 5.36. (a) Magnetization and (b) relative change of the sound velocity of TbFe_5Al_7 above $T_{\text{comp}} = 84$ K as a function of magnetic field applied along the [110] direction.

different shapes and magnitudes of the acoustic anomalies in $\Delta v/v$ below and above T_{comp} suggest different magnetoelastic couplings. The total magnetization of TbFe_5Al_7 is dominated by the highly anisotropic Tb sublattice below the compensation point and by the much less anisotropic Fe sublattice above the compensation point. Since the Fe magnetic moment can rotate more freely than that of Tb, in an applied magnetic field the magnetic susceptibility dM/dH is larger below T_{comp} than above T_{comp} (this is confirmed by a careful analysis of the magnetization curves around the compensation point). Therefore, the canting of the magnetic sublattices is larger when the Fe sublattice is antiparallel to the field. Under these conditions, the magnetoelastic interaction may be expected to be larger, which would result in a stronger influence of the magnetic field on the sound-velocity change.

The critical fields of the field-induced transitions in TbFe_5Al_7 grow rapidly above and below the compensation point. For this reason, we used pulsed magnetic fields up to 60 T to further study the magnetization and sound propagation in TbFe_5Al_7 .

Figure 5.37 presents magnetization curves for fields applied along the [100], [110], and [001] directions at 2 K. Along the easy [100] direction, the magnetization grows very slowly. A very weak anomaly is seen between 20 and 30 T (inset in Fig. 5.37). This result is unexpected since in general with decreasing temperature field-induced magnetic transitions should become more pronounced. Moreover, in the

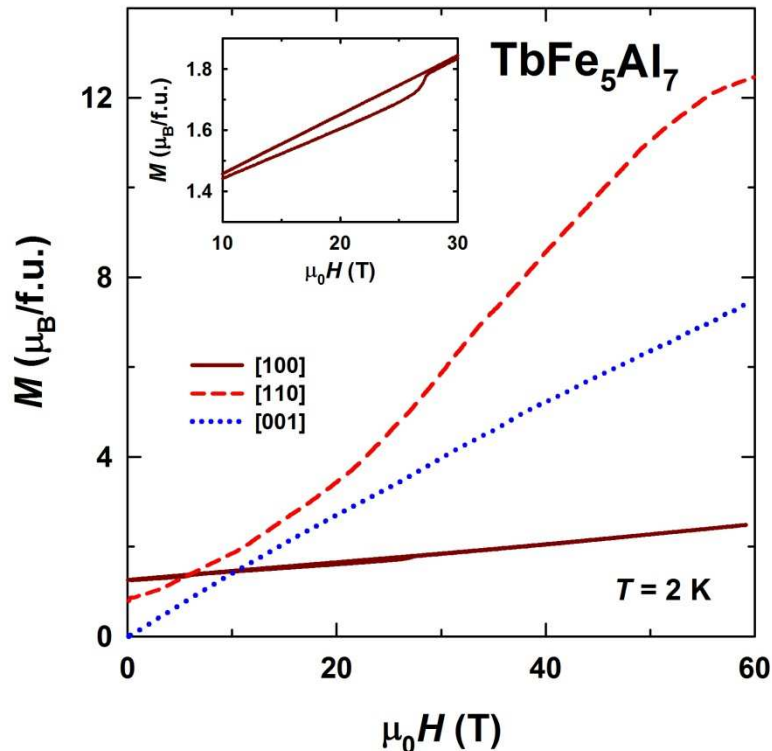


Fig. 5.37. Magnetization curves of TbFe_5Al_7 for fields applied along the principal crystallographic directions in pulsed magnetic fields at 2 K. The inset shows the magnetization curve along the [100] axis in the vicinity of the field-induced transition.

isostructural $R\text{Fe}_5\text{Al}_7$ compound with R - Dy much sharper magnetization jumps were observed at low temperatures than at high temperatures. A possible reason for the weak magnetization jump and the small magnetic susceptibility is that the transition occurs only in small parts of the single crystal where the local anisotropy might be reduced due to crystallographic defects. A strong increase in the magnetic anisotropy energy upon cooling prevents domain-wall motion even in fields up to 60 T. On the one hand, the coercivity of 180° domain walls is much lower than 60 T, and the single domain state along the [100] axis is reached much below the highest available field. One should expect zero (or very low) magnetic susceptibility up to the field-induced transition. On the other hand, since the transition reflects a rotation of the magnetic moments from [100] to [010] (see below), the domains with the magnetization along the [010] axis either do not emerge or do not grow up to the highest available fields. The appearance or growth of such domains is prevented by the strong Tb anisotropy. In the highest available field, the magnetization is equal to $2.5 \mu_B/\text{f.u.}$, i.e., it is very far from the forced ferromagnetic state that corresponds to the collinear parallel alignment of the Tb and Fe magnetic moments. The magnetization of this state can be calculated as $M_{\text{sat}} = M_{\text{Tb}} + M_{\text{Fe}} = 9 + 7.8 = 16.8 \mu_B/\text{f.u.}$

No field-induced magnetic transitions are observed for fields applied along the [110] and [001] axes. The magnetization along the [110] axis in the basal plane grows rapidly, at 60 T it reaches $12.5 \mu_B/\text{f.u.}$ This value is much higher than along the easy [100] axis since, even in case of an infinite Tb anisotropy, from the lowest fields the Fe sublattice moment is subject to a rotation. Along the hard [001] axis the magnetization increases linearly. Extrapolation to high fields indicates that the value $M_{\text{sat}} = 16.8 \mu_B/\text{f.u.}$ will be reached at about 130 T.

In ultrasound measurements no anomaly was observed below 20 K. At higher temperatures pronounced anomalies can be observed in the magnetization and acoustic properties. Figure 5.38 shows data for the magnetization (a and b), sound velocity (c and d), and sound attenuation (e and f) for field applied along the [100] axis at 50 and 60 K. A hysteretic magnetization jump is seen between 10 and 20 T. The sound velocity grows strongly at low fields and then displays a pronounced softening with a sharp minimum at the transition. At $T = 50$ K, two anomalies appear for the down sweep. Also in $\Delta\alpha$ anomalies at the transition can be resolved.

As shown above (Figs. 5.35 and 5.36), the critical field approaches zero at T_{comp} and grows rapidly with temperature. In pulsed magnetic fields we could follow the transition to temperatures far below T_{comp} (see Fig. 5.38). Figure 5.39 shows field dependences of the magnetization and the acoustic properties for fields applied along the [110] direction at 110 and 130 K. At 110 K the magnetization displays a hysteretic transition (Fig. 5.39a). $\Delta v/v$ displays a minimum (Fig. 5.39c), and $\Delta\alpha$ exhibits a sharp maximum (Fig. 5.39e) corresponding to a large energy dissipation at the transition. At 130 K, the magnetization step becomes substantially reduced and broadened (Fig. 5.39b). However, the highly sensitive acoustic properties still maintain similar sharp anomalies at the transitions (Figs. 5.39d and f) as at 110 K.

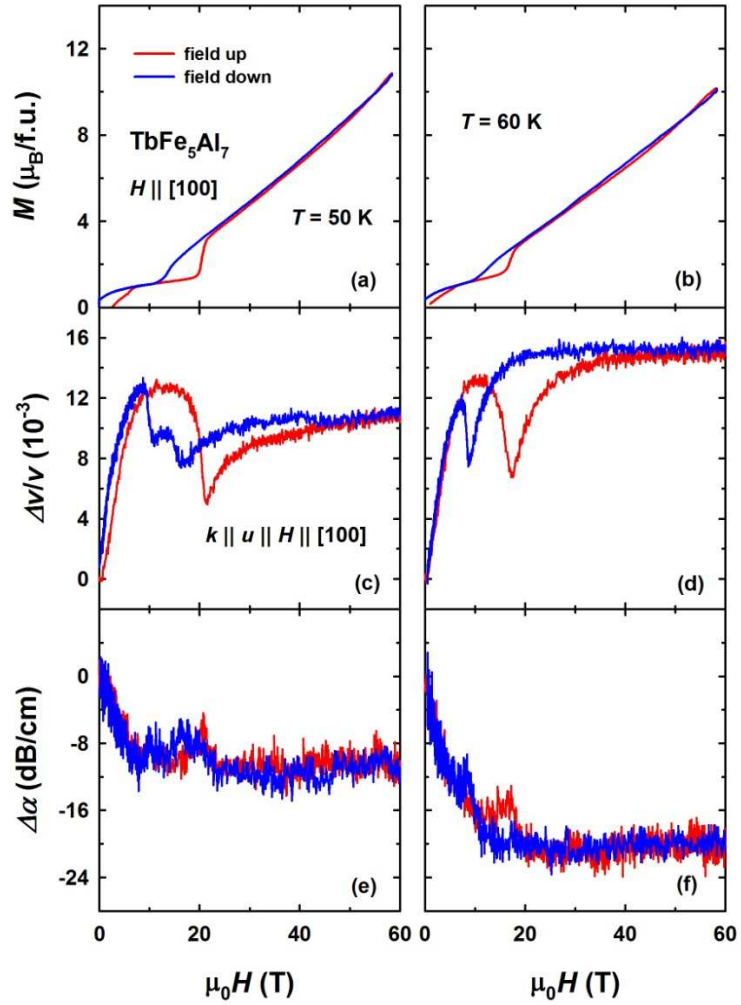


Fig. 5.38. Magnetization (a and b), relative change of the sound velocity (c and d), and sound attenuation (e and f) measured for fields applied along the [100] axis of TbFe_5Al_7 in pulsed magnetic fields at 50 and 60 K.

In order to determine the temperature dependence of the critical fields $H_{\text{cr},100}$ and $H_{\text{cr},110}$ of the transitions for fields applied along the [100] and [110] directions, respectively, two different approaches were used. $H_{\text{cr},100}$ was taken as the average field of the magnetization jumps for rising and falling field. For the acoustic properties, their behavior near the transition makes the determination of $H_{\text{cr},100}$ ambiguous. On the contrary, $H_{\text{cr},110}$ was obtained from the acoustic properties since they display single sharp anomalies, whereas at high temperatures the transitions practically disappear in the magnetization.

The resulting magnetic phase diagram is shown in Fig. 5.40. A gradual reduction of $H_{\text{cr},100}$ occurs upon approaching T_{comp} . The dashed lines at low temperatures show rough estimates of the transition field since the corresponding transitions are hardly visible in the magnetization. Above T_{comp} , $H_{\text{cr},110}$ grows rapidly. For $T > 145$ K, the transition is no longer observed.

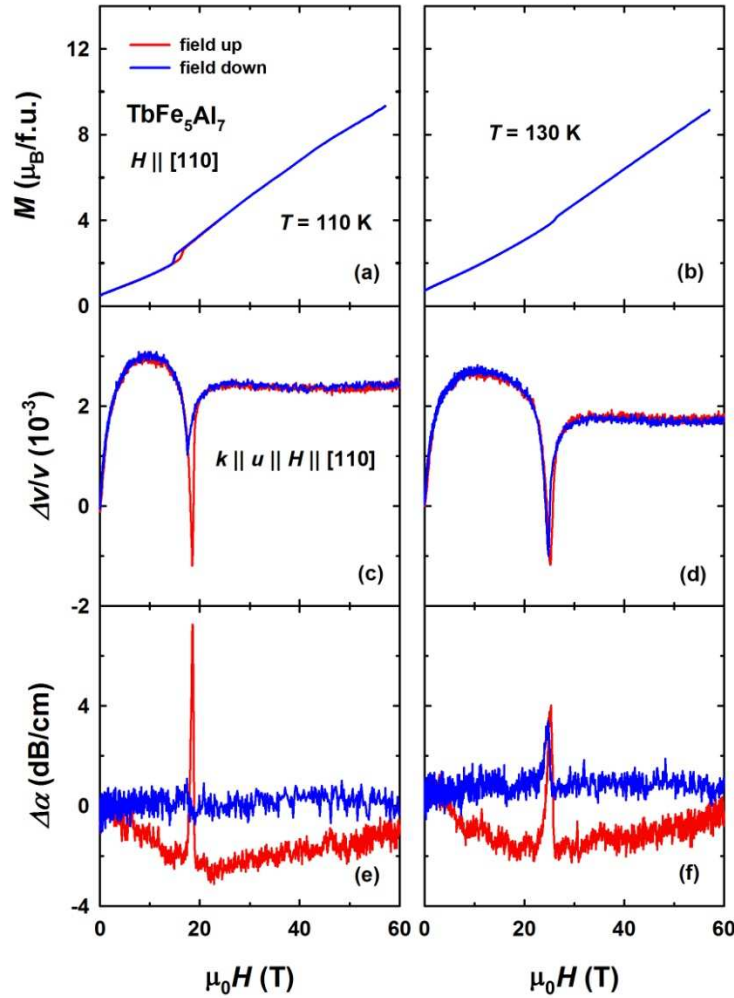


Fig. 5.39. Magnetization (a and b), relative change of the sound velocity (c and d) and sound attenuation (e and f) measured for fields applied along the [110] direction in pulsed magnetic fields at 110 and 130 K.

Since at $T < T_{sr}$, the EMD in TbFe_5Al_7 is the [100] axis and at $T > T_{sr}$ the [110] axis becomes the EMD, it is clear that the field-induced transitions are observed only along the EMD.

For fields applied along the [100] axis at $T < T_{sr}$, TbFe_5Al_7 has a low susceptibility since the magnetic moments are already aligned along the EMD. At T_{comp} , the compound is antiferromagnetic. Therefore, it has a higher susceptibility when the magnetic moments are perpendicular to the magnetic field. One can expect a magnetization jump when the moments rotate from [100] to [010], another EMD in the basal plane perpendicular to the field. The higher the spontaneous magnetic moment, the higher is the transition field. A similar situation is observed at $T > T_{sr}$ when the EMD changes. In this case the magnetic moments reorient themselves from [110] to [1-10] at the transition.

The transition fields of the $R\text{Fe}_5\text{Al}_7$ compounds with R - Tb and Dy, reveal similar characteristics, that is, H_{cr} passes through zero at the compensation point.

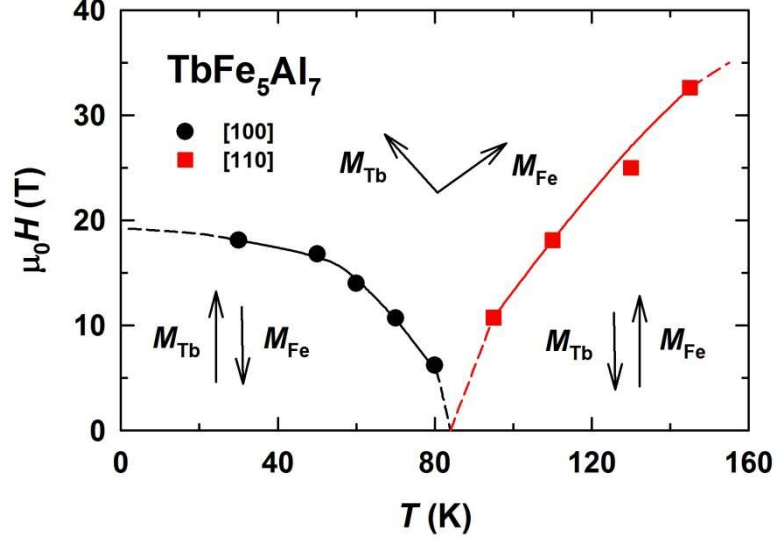


Fig. 5.40. T - H magnetic phase diagram for fields applied along the [100] and [110] directions.

This strongly suggests a similar origin of their field-induced magnetization jumps. Moreover, in $TbFe_5Al_7$ an additional step can be expected above 60 T since two transitions were observed in high magnetic fields in $DyFe_5Al_7$.

The presence of an additional transition above 60 T at 2 K is strongly supported by the results presented in Fig. 5.22. In this figure, the partition of the parameter plane m - κ among different types of high-field magnetization curves is shown, where $m = M_R/M_{Fe}$, $\kappa = K_R/(n_{RFe}M_{Fe}^2)$, K_R is the in-plane anisotropy constant of the rare-earth sublattice and n_{RFe} is the inter-sublattice exchange constant. For $TbFe_5Al_7$ $m = 1.16$ and κ has a large negative value leading to a m -, or n - type material, which means that the corresponding magnetization curve should display two field-induced magnetic transitions before reaching the ferromagnetic saturation.

Since the field-induced magnetic transitions occur along the EMD of $TbFe_5Al_7$, the Zeeman energy competes against the inter-sublattice exchange interaction, and the anisotropy energy involved in the process can be neglected (this is only true for the first magnetization jump; after that the anisotropy energy has to be taken into account). In this case, the field-induced magnetic transition reflects the strength of the Tb-Fe inter-sublattice exchange interaction. The obtained high-field magnetization data contains sufficient information to calculate the inter-sublattice exchange constant n_{TbFe} [124], a quantity that expresses the strength of this interaction. This constant is related to the molecular field created by the Fe sublattice on Tb: $H_{mol} = n_{TbFe}M_{Fe}$. The molecular field can be determined directly from the high-field magnetization data [124] at 2 K:

$$H_{mol} = \frac{H_{cr,100}}{h_1}, \quad (5.18)$$

where the dimensionless parameter h_1 in the denominator is determined by [136]

$$h_1 = \frac{m-1}{1-\frac{m}{2}} \quad (5.19)$$

Using $m = 1.16$ and $\mu_0 H_{cr,100} = 19.3$ T extrapolated to $T = 0$ (see Fig. 5.40), we arrive at $\mu_0 H_{mol} = 50.6$ T which results in $n_{TbFe} = 6.5$ T f.u./ μ_B .

Since the inter-sublattice exchange constant was found using an estimated value of $H_{cr,100}$, it is appropriate to use a different approach to determine n_{TbFe} which can be calculated as well using molecular-field theory. To this end, the same approach was used as for $DyFe_5Al_7$. The temperature dependence of the Tb magnetic moment, M_{Tb} , was determined experimentally and then fitted with the Brillouin function using Eqs. 5.3 - 5.5 for the case $R - Tb$ (Fig. 5.41). The best fit to the temperature dependence of M_{Tb} was obtained for a molecular field $\mu_0 H_{mol} = 54$ T. This corresponds to $n_{TbFe} = 6.9$ T f.u./ μ_B .

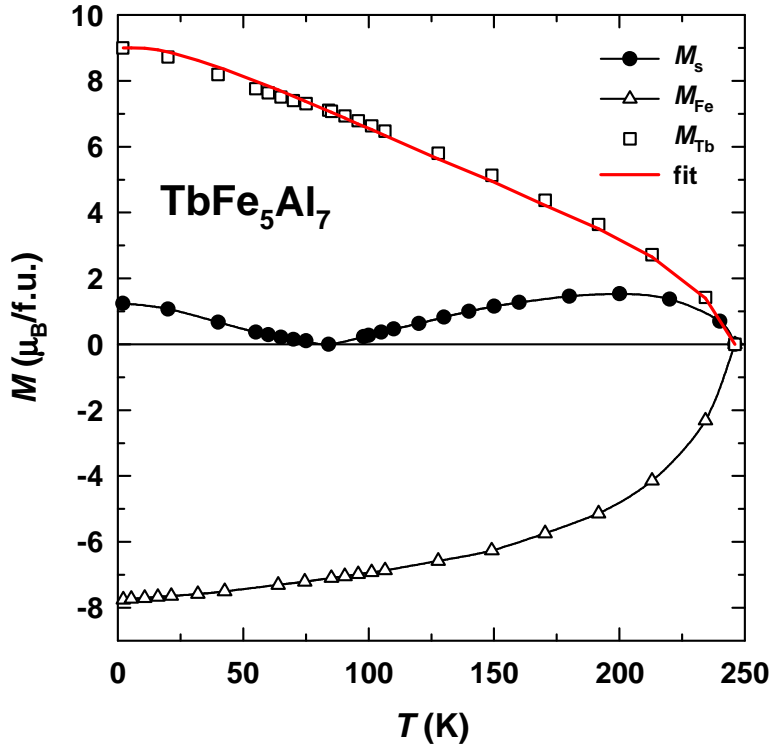


Fig. 5.41. Measured (closed circles) temperature dependence of the spontaneous magnetic moment along the easy magnetization direction ([100] at $T < T_{comp}$ and [110] at $T > T_{comp}$) together with the calculated temperature dependence of the magnetic moment of the Tb and Fe sublattices. The Fe magnetic moment is assumed to be negative as it is antiparallel to the Tb magnetic moment. The red line represents the fit according to the molecular-field theory.

Thus, the values of the Tb-Fe inter-sublattice exchange constant determined by two different methods are in good agreement. The obtained n_{TbFe} correlates well with those found for $GdFe_5Al_7$ ($n_{TbFe} = 8.3$ T f.u./ μ_B) and $DyFe_5Al_7$ ($n_{TbFe} = 5.3$ T f.u./ μ_B).

The above presented results indicate that $TbFe_5Al_7$ is a highly anisotropic ferrimagnet. The strong magnetic anisotropy is manifested by a strong magnetic

hysteresis at low temperatures. Figure 5.42 shows hysteresis loops measured along the [100] axis at $T = 2$ K and 20 K of the TbFe_5Al_7 single crystal. The two loops were measured on the crystal initially in the single-domain state that was obtained by cooling the sample in a field of 14 T from room temperature. Both loops are strongly asymmetric. Moreover, the magnetization displays very different behavior as the field is swept towards -14 T and then back to 14 T. It is clear that the highest available field of 14 T cannot fully saturate the sample due to strong hysteresis, and both loops should be considered as minor.

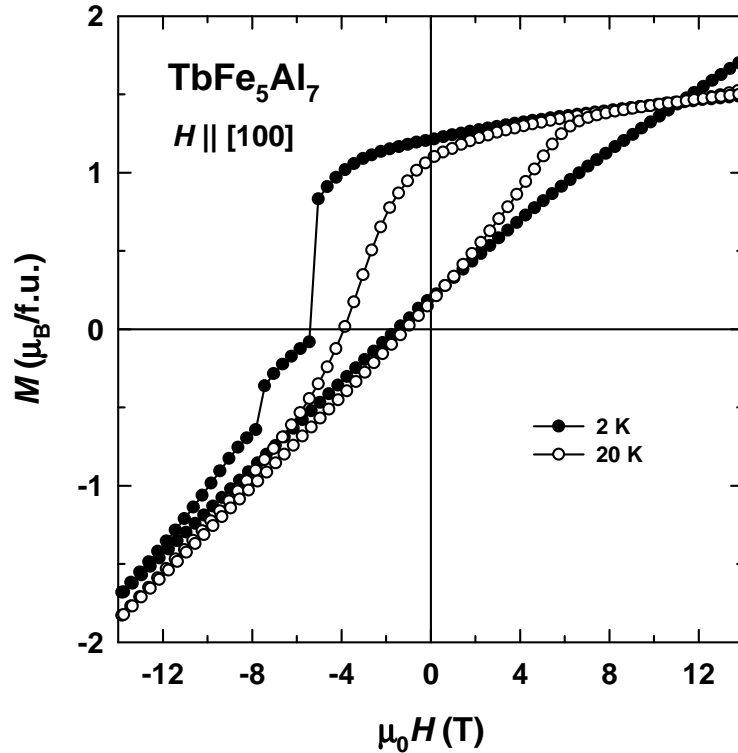


Fig. 5.42. Hysteresis loops along the [100] axis of the TbFe_5Al_7 single crystal at $T = 2$ and 20 K.

The asymmetric shape of the hysteresis loops presented in Fig. 5.42 may also imply a spin-glass state of TbFe_5Al_7 at low temperatures. It is interesting to note that spin-glass behavior of TbFe_5Al_7 was already reported in Ref. [87] where it was associated with an almost equal Fe population of the $8f$, $8j$ and $8i$ sites leading to the frustration of the magnetic moments. This unusual site occupation is, however, in contradiction with the results reported by the same authors on the basis of Mössbauer spectroscopy [20] and the results obtained in a powder neutron diffraction study by a different group [16]. It should also be noted that no indication of a spin-glass state was observed in GdFe_5Al_7 and DyFe_5Al_7 and LuFe_5Al_7 where the Fe atoms evidently show preference for the $8f$ and $8j$ sites. It is expected that the site occupation in TbFe_5Al_7 is similar. In this connection, the observed highly asymmetric hysteresis loops should be associated with the strong magnetic hysteresis at low temperatures.

As seen from Fig. 5.43, at $T > 20$ K along the [100] axis symmetric loops are observed reflecting a domain hysteresis that weakens with increasing temperature.

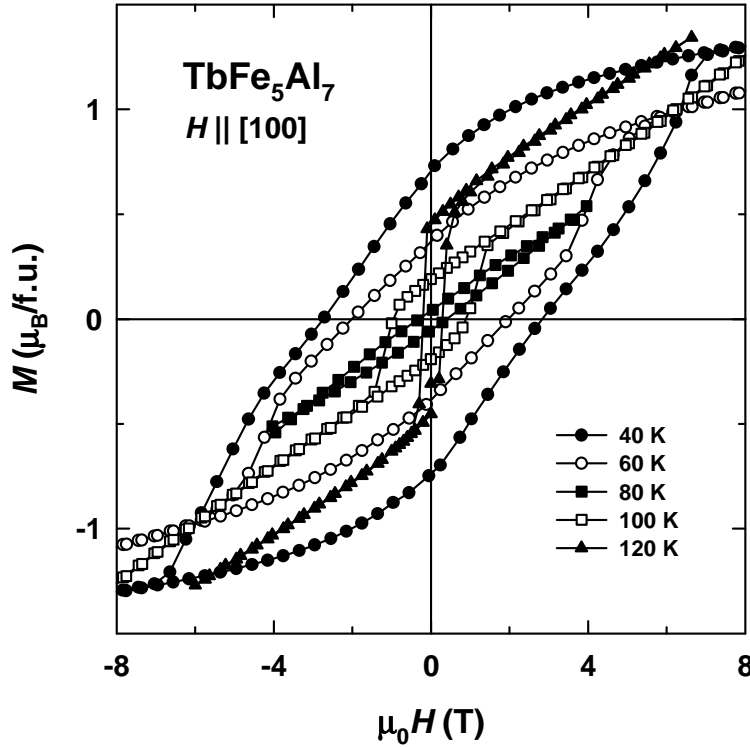


Fig. 5.43. Hysteresis loops along the [100] axis of the TbFe_5Al_7 single crystal in the range $T = 40 - 120$ K.

Fig. 5.44 shows that along the [110] axis hysteresis loops have a symmetric shape at all temperatures. It is related to weaker hysteresis in comparison with that along the [100] axis. A particularly interesting feature observed in Fig. 5.44 is that the loop at $T = 2$ K has a parallelogram shape, whereas all the other loops are characterized by round edges. Such a shape at $T = 2$ K suggests that the domain walls are frozen and start to move only at a particular activation field. Already at $T = 4.2$ K the mechanism of the magnetic hysteresis changes as seen from the change of the loop shape. This is also supported by the abrupt increase of the coercivity H_c from $T = 2$ to 4.2 K.

The H_c values are very high, especially at low temperatures (Fig. 5.45). Since even the highest available field of 14 T is not strong enough to magnetize the sample completely along the [100] axis at $T \leq 20$ K, the coercive field cannot be measured in this temperature interval. Therefore, at low temperatures the H_c values should be even higher than what follows from the sharp temperature dependence measured between $T = 40$ and 70 K. Since the magnetization vector rotates within the basal plane in the external field, such high H_c values reflect very strong in-plane anisotropy in TbFe_5Al_7 . The steep fall of the coercive field might be related to narrow domain walls of the highly-anisotropic compound, in analogy with isostructural DyFe_5Al_7 . The fast decrease of H_c along [100] and [110] is followed by its sharp growth upon approaching $T = T_{\text{comp}}$, where the $H_c(T)$ function shows a discontinuity. At higher temperatures the coercivity decreases monotonously and becomes negligible at $T > 140$ K.

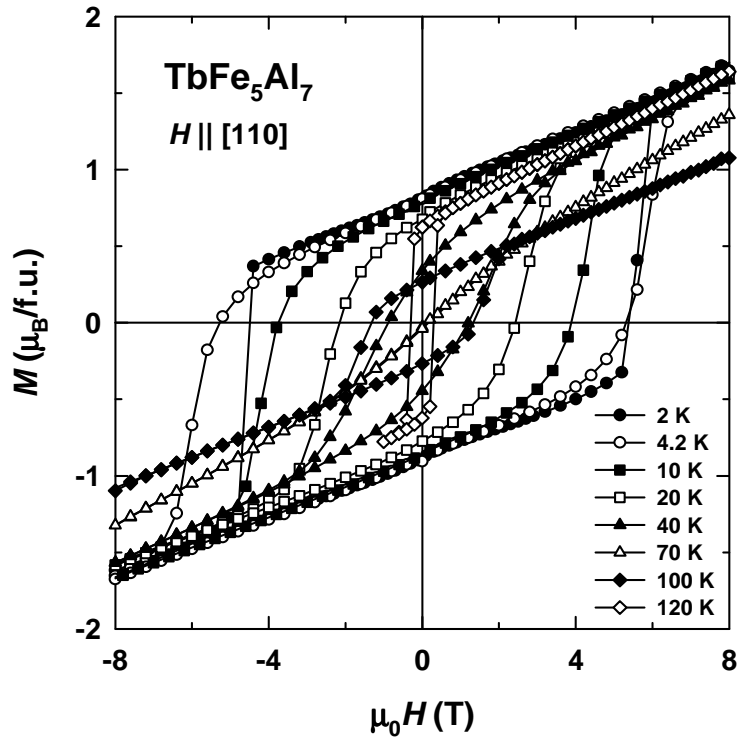


Fig. 5.44. Hysteresis loops along the [110] axis of the TbFe_5Al_7 single crystal in the range $T = 2 - 120$ K.

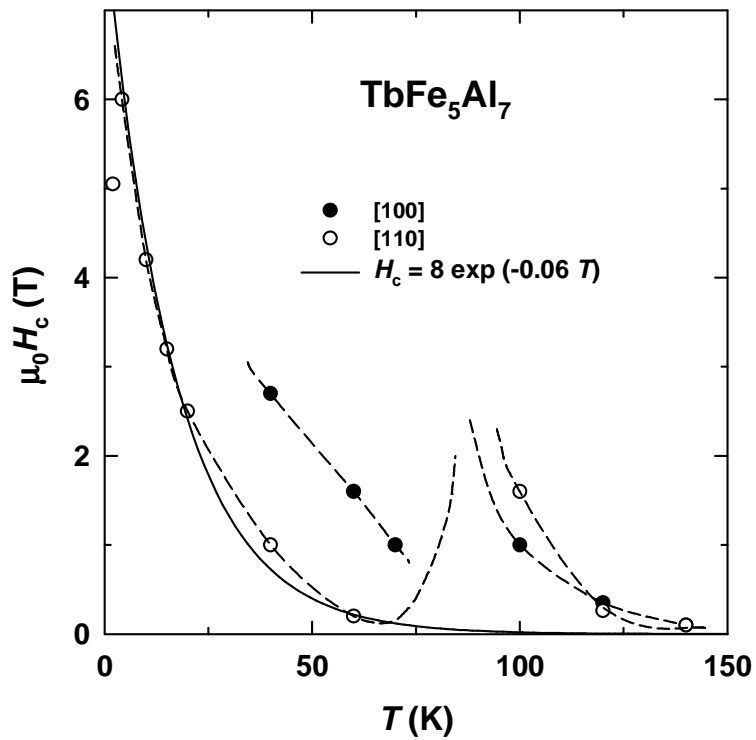


Fig. 5.45. Temperature dependence of the coercive field along the [100] and [110] axes of the TbFe_5Al_7 single crystal.

Figure 5.46 shows the temperature dependence of magnetization along the [100] and [110] axes of the TbFe_5Al_7 single crystal upon heating and cooling in a field of 0.1 T. First the sample was cooled down to $T = 60$ K where a field of 14 T was applied in order to overcome the coercive field that is at the minimum at this temperature (see Fig. 5.45) and obtain the sample in the single-domain state. Then the crystal was cooled down to $T = 2$ K where the magnetic field was reduced to 0.1 T, and the $M(T)$ dependence was measured up to $T = 300$ K. It was followed by measuring the $M(T)$ curve in 0.1 T to $T = 2$ K.

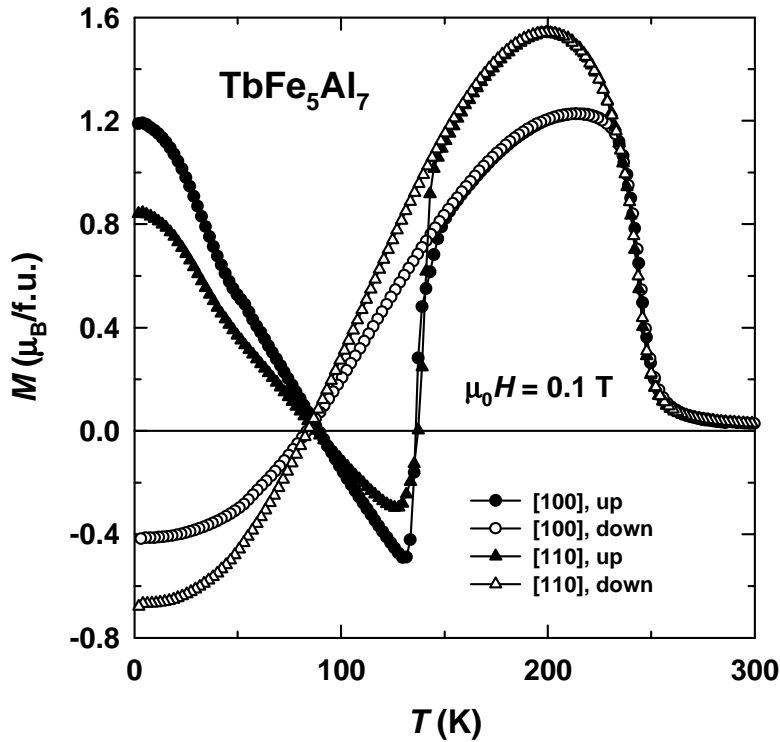


Fig. 5.46. Temperature dependence of the magnetization measured in a field of 0.1 T applied along the [100] and [110] axes of the TbFe_5Al_7 single crystal. First, the sample was cooled down to $T = 2$ K in a field of 14 T. Then, the magnetization was measured in 0.1 T upon heating the sample up to $T = 300$ K and subsequent cooling to $T = 2$ K.

Upon heating the magnetization turns negative just above $T = T_{\text{comp}}$. This effect is caused by a high coercive field that exceeds the external magnetic field 0.1 T in the vicinity of the compensation temperature. As a result, the single-domain state of the crystal does not change at $T = T_{\text{comp}}$, and the reorientation of the total magnetization from the Tb to the Fe sublattice leads to negative M values. The coercive field rapidly decreases with temperature and assumes lower values than 0.1 T around $T = 140$ K (Fig. 5.45) where the magnetization turns positive.

Upon cooling in a field of 0.1 T the magnetization turns negative at $T = T_{\text{comp}}$ since the coercivity exceeds 0.1 T. At all temperatures below the compensation point $\mu_0 H_c > 0.1$ T, and the “negative magnetization” effect is observed to the lowest temperatures. However, at $T = 2$ K neither along the [100] axis nor along the [110] axis the magnetization reaches the absolute value of the spontaneous magnetic

moment. The reason is that the hysteresis loops are not squared, and just below the compensation point the sample turns out to be partially demagnetized. Moreover, upon cooling at $T < T_{\text{comp}}$ the magnetization along the [110] axis is higher in the absolute value than that along the easy [100] axis. This is obviously not a fundamental property of TbFe_5Al_7 but rather a hysteresis-related effect as well. Thermal hysteresis was also observed in highly-anisotropic DyFe_5Al_7 (Fig. 5.26).

From Fig. 5.46 it also follows that the magnetic moment along the [110] axis exceeds the moment along the [100] axis only at $T > 140$ K. Thus, Fig. 5.46 does not support the earlier results that the spin-reorientation transition occurs between 95 and 98 K (Figs. 5.28 and 5.29). It should be noted that at $T \geq 98$ K the ratio $M_s^{100}/M_s^{110} \approx \cos 45^\circ$ holds, which confirms that the easy magnetization direction is the [110] axis in this temperature range. A more complicated situation is encountered in the interval $T = 60\text{-}95$ K, where this ratio is not fulfilled. We do not exclude the possibility that the spin-reorientation transition occurs at $T < 95$ K in TbFe_5Al_7 . However, since the magnetization measurements do not lead to an unambiguous conclusion about the value of the spin-reorientation temperature, a different technique, e.g., neutron diffraction, is necessary.

5.5. HoFe₅Al₇

This section describes magnetic and magnetoelastic properties of the HoFe₅Al₇ compound. The Ho³⁺ ion provides a strong magnetic anisotropy, and HoFe₅Al₇ displays a complex behavior in a magnetic field.

Figure 5.47 shows static-field magnetization curves measured along the [100], [110] and [001] axes of the HoFe₅Al₇ single crystal at several selected temperatures. The compound is ordered ferrimagnetically at these temperatures and displays a high easy-plane anisotropy. The absence of a spontaneous component along the [001] axis indicates that it is the hard magnetization direction. Large anisotropy is present within the basal plane, as seen from the marked difference between the magnetization isotherms along the [100] and [110] axes. The EMD is along the [110] axis with a spontaneous magnetic moment $M_s = 2.0 \mu_B/\text{f.u.}$ at $T = 2$ K. The in-plane anisotropy disappears at 160 K. Assuming that in the ground state the Ho magnetic moment is equal to its free Ho³⁺ ion value, $10 \mu_B$, the magnetic moment of the Fe sublattice may be calculated as $M_{\text{Fe}} = M_{\text{Ho}} - M_s = 8 \mu_B$ (below $T_{\text{comp}} = 65$ K the total magnetic moment is dominated by the Ho sublattice).

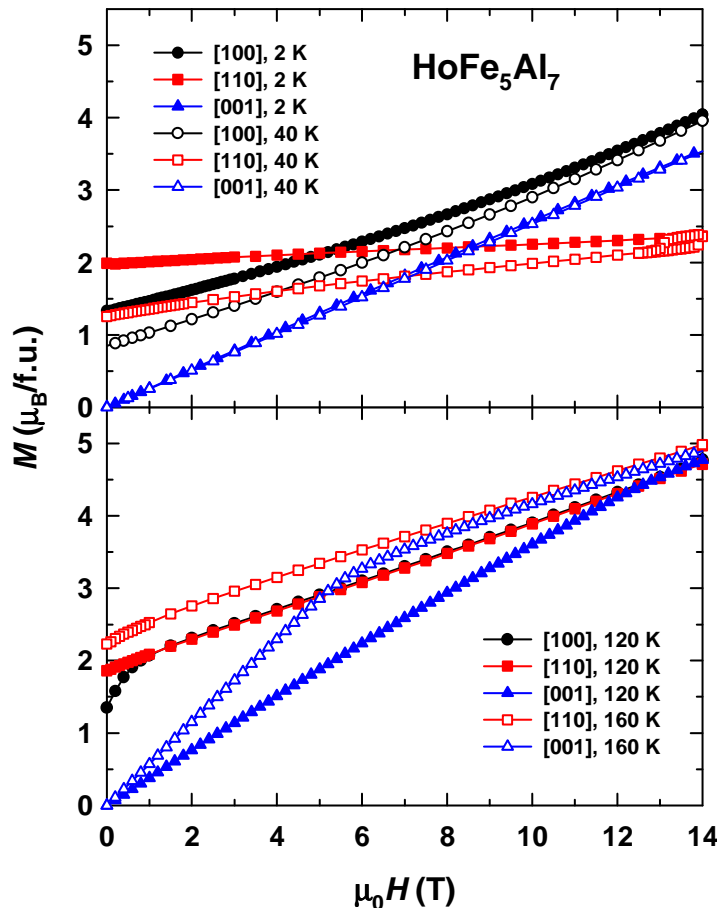


Fig. 5.47. Field dependence of the magnetization measured along the principal axes of the HoFe₅Al₇ single crystal at selected temperatures.

None of the curves along the [100] and [110] axes saturates up to 14 T, which can be attributed to a non-collinearity of the magnetic moments. The magnetization

along the hard [100] axis in the basal plane displays a higher susceptibility, as a result the magnetization curves along the [100] and [110] directions intersect at low temperatures (5 T at $T = 2$ K). No peculiarities are observed at the crossover point.

The temperature dependence of the specific heat, C_p , and spontaneous magnetic moment, M_s , of HoFe_5Al_7 in the vicinity of T_C is presented in the upper part of Fig. 5.48. The two curves give somewhat different values of T_C . The weak and relatively broad anomaly observed on the $C_p(T)$ curve indicates that the phase transition occurs at $T = 216$ K, whereas M_s (obtained from the Arrott plots along the easy [110] axis) drops to zero around $T = 220$ K. This points to the induction of a magnetic moment in the compound by a small applied field above T_C . For this reason, only measurements in zero magnetic field provide the correct value of T_C .

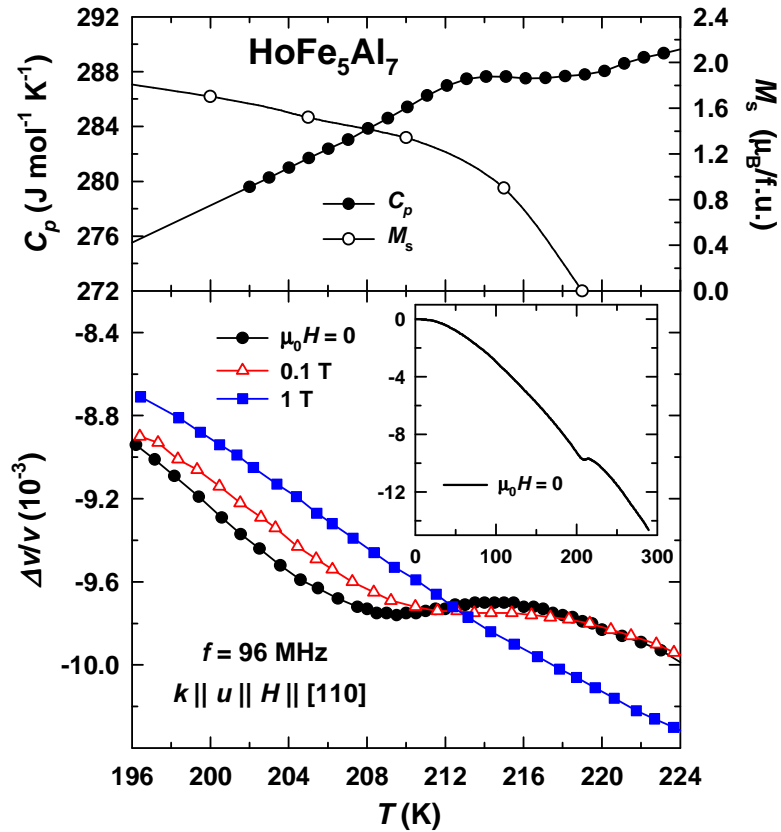


Fig. 5.48. Temperature dependence of the specific heat, C_p , spontaneous magnetic moment, M_s , and relative changes of the sound velocity, $\Delta v/v$, of longitudinal ultrasonic waves propagating along the [110] axis of the HoFe_5Al_7 single crystal in the vicinity of $T_C = 216$ K. The inset shows the temperature dependence of the relative changes of the sound velocity between 2 and 300 K.

Measurements of the relative changes of the sound velocity, $\Delta v/v$, of longitudinal acoustic waves, shown in the lower part of Fig. 5.48, indicate that at the phase transition magnetic fields affect the sound propagation as well. With increasing temperature, $\Delta v/v$ displays a monotonous softening and a cusp well-defined in zero field but considerably broadened at 0.1 T. The anomaly corresponding to the phase transition of HoFe_5Al_7 in zero field is observed between 210 and 216 K. The anomaly shifts to higher temperatures, as seen from the curve

measured in 0.1 T. A field of 1 T strongly affects $\Delta v/v$ that exhibits a very smooth temperature variation in the vicinity of T_C without any anomaly indicative of a phase transition. The inset in Fig. 5.48 indicates that $\Delta v/v$ displays no other anomalies in the temperature range from 2 to 300 K, including the compensation temperature $T_{\text{comp}} = 65$ K.

Figure 5.49 shows magnetization isotherms of HoFe_5Al_7 along the [100] axis in the temperature range 2 – 160 K. The spontaneous moment decreases with increasing temperature upon approaching the compensation point $T_{\text{comp}} = 65$ K. Above T_{comp} the spontaneous moment increases up to approximately 160 K and then decreases below the Curie temperature $T_C = 216$ K.

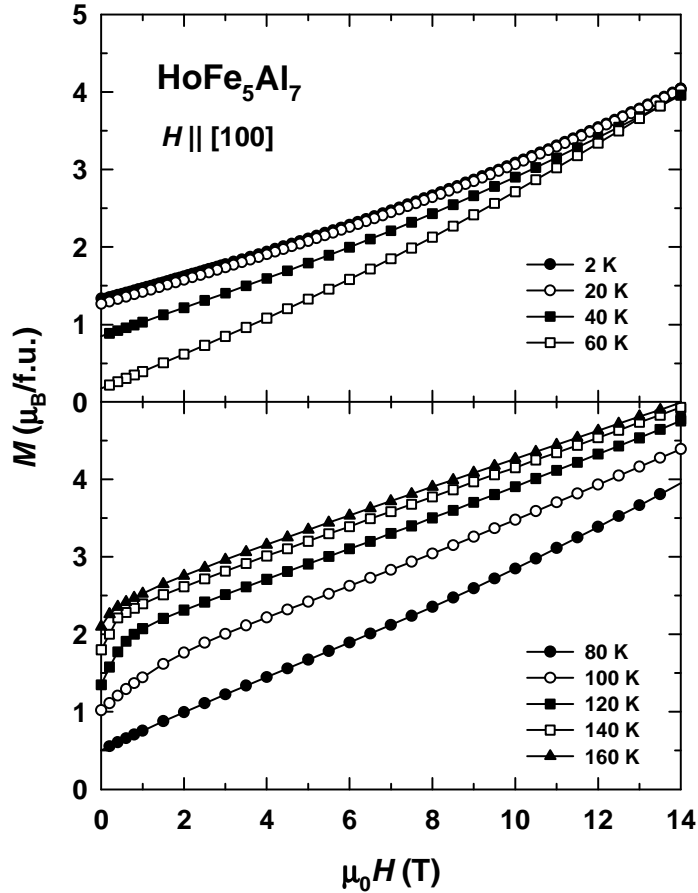


Fig. 5.49. Magnetization curves of the HoFe_5Al_7 single crystal measured along the [100] axis at $T = 2 - 160$ K.

The $M(H)$ curves measured along the hard [001] axis (Fig. 5.50) are linear below 100 K, which shows that the anisotropy field H_a exceeds the maximum applied field of 14 T. A change of the $M(H)$ curve's slope reflecting H_a appears only at 120 K at about 13 T. The inset in Fig. 5.50 shows the temperature dependence of H_a in the temperature range where the H_a values do not exceed 14 T. H_a was determined by the singular-point detection method [119].

The magnetization curves along the easy [110] axis display a field-induced magnetic transition appearing in the temperature range from 40 to 80 K in fields up to 14 T (Fig. 5.51). As temperature increases, the critical field of the transition,

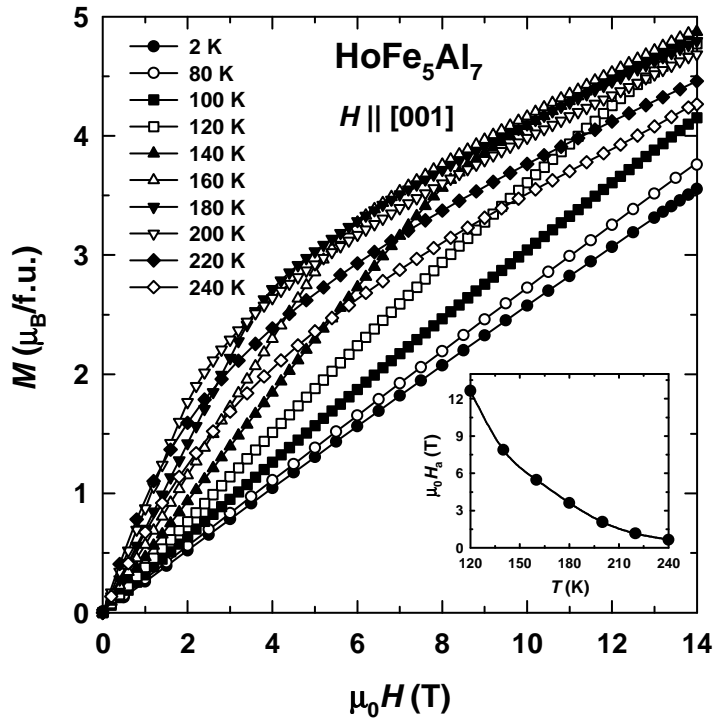


Fig. 5.50. Magnetization curves of the HoFe₅Al₇ single crystal measured along the [001] axis at $T = 2 - 240$ K. The inset shows the temperature dependence of the anisotropy field.

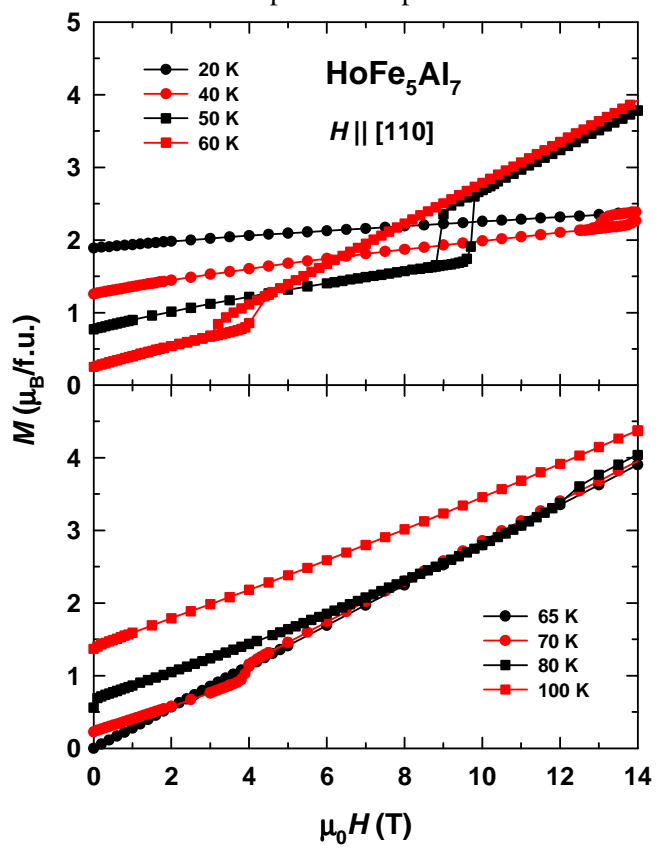


Fig. 5.51. Temperature evolution of the magnetization for fields applied along the [110] axis below (top) and above (bottom) $T_{\text{comp}} = 65$ K.

$\mu_0 H_{cr,1}$, decreases and passes through zero at $T = T_{comp}$ (we mark the transition field by $\mu_0 H_{cr,1}$ since a second transition is observed in a higher field, at $\mu_0 H_{cr,2}$, see below). The transition exhibits hysteresis and is of first order. At $T > T_{comp}$ the transition is observed as well. Although $\mu_0 H_{cr,1}$ increases with temperature, the transition becomes increasingly smeared out and eventually disappears above $T = 80$ K.

Figures 5.52 and 5.53 show that the jump in the magnetization is accompanied by well-pronounced anomalies with hysteresis effects in the sound velocity, $\Delta v/v$, and sound attenuation, $\Delta\alpha$. In order to allow a direct comparison with magnetization data, $M(H)$ curves are given in Figs. 5.52a and 5.53a. At $T < T_{comp}$, the acoustic mode exhibits a softening by about 0.1% with increasing magnetic field (Fig. 5.52b). $\Delta v/v(H)$ at $T = T_{comp}$ displays a descending branch indicative of a field-induced transition, however, its ascending branch is likely to be observed only in

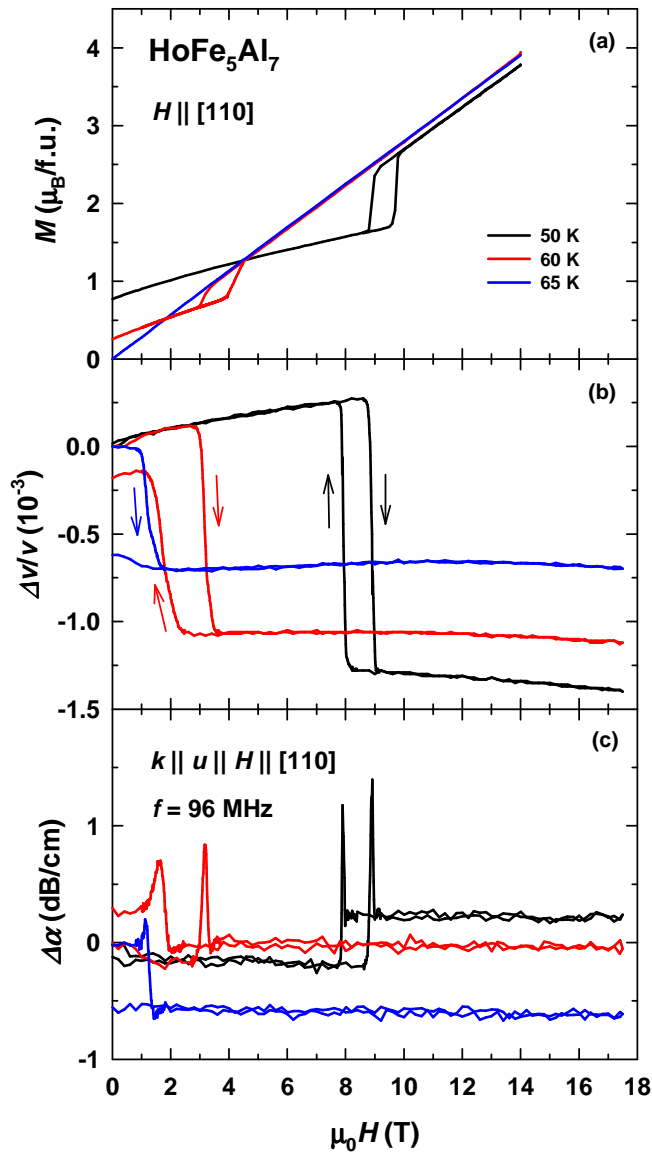


Fig. 5.52. (a) Temperature evolution of the [110] axis magnetization curve, (b) of the relative changes of the sound velocity and (c) of the sound attenuation of HoFe_5Al_7 below $T_{comp} = 65$ K.

negative fields resulting in an average $\mu_0 H_{\text{cr},1}$ close to zero as found from the magnetization measurements. The sound attenuation also clearly indicates the presence of the transition (Fig. 5.52c).

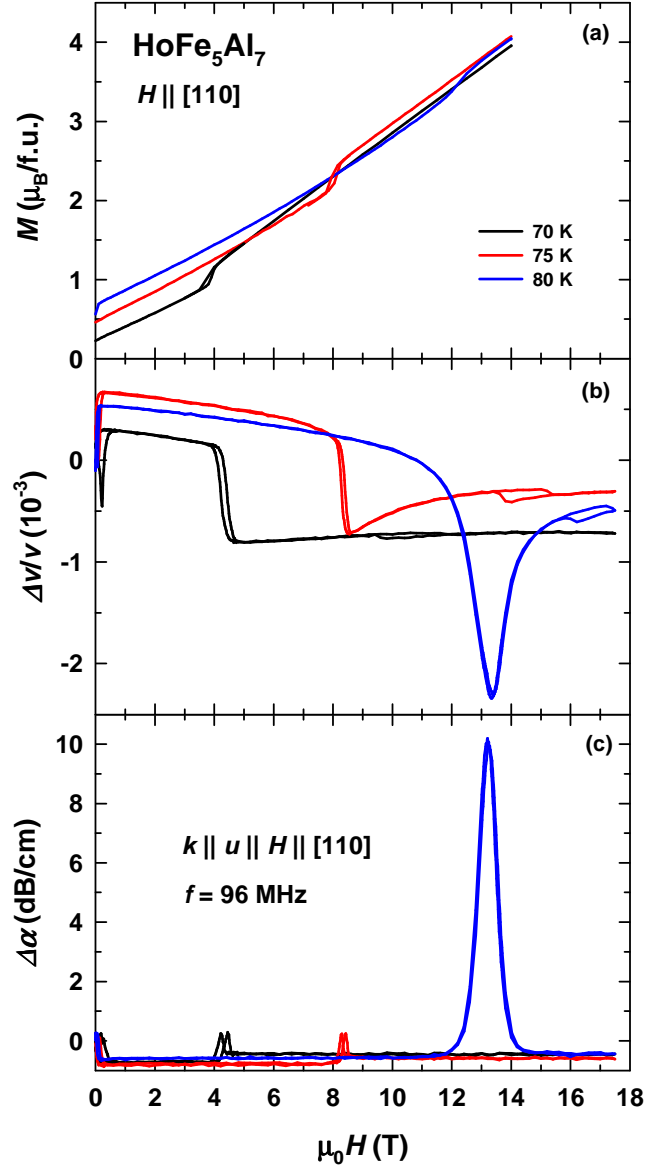


Fig. 5.53. (a) Temperature evolution of the [110] axis magnetization curve, (b) of the relative changes of the sound velocity and (c) of the sound attenuation of HoFe_5Al_7 above $T_{\text{comp}} = 65$ K.

At $T = 70$ K, the shape of the $\Delta v/v(H)$ curve is rather similar to those at $T < T_{\text{comp}}$ except for a (rather weak) hysteretic anomaly seen between 9.5 and 12 T (Fig. 5.53b). This weak anomaly is most probably related to a change of the magnetic structure of the compound. Above 70 K, a sharp minimum develops at the transition. The second anomaly at higher fields becomes more apparent as well. The $\Delta\alpha(H)$ dependence at $T = 70$ and 75 K varies with magnetic field in a manner similar to that at $T < T_{\text{comp}}$ (Fig. 5.53c). However, a pronounced maximum is observed at $T = 80$ K that corresponds to a large energy dissipation at the transition. The longitudinal wave

experiences a total change in the attenuation of about 10 dB/cm, an order of magnitude larger than at other temperatures. It is surprising that such significant changes are observed at 80 K in the acoustic properties, in contrast to the magnetization that displays a rather weak anomaly (Fig. 5.53a).

The temperature dependence of the critical field $\mu_0 H_{cr,1}$ shows very steep slopes, $dH_{cr,1}/dT$ (Fig. 5.54a). Due to the transition hysteresis, $\mu_0 H_{cr,1}$ was determined from both the ascending and descending branches of the corresponding $M(H)$ and $\Delta v/v(H)$ data. The magnetic transition cannot be interpreted as a rotation of the magnetic moment within one magnetic sublattice. Firstly, the temperature dependence of the magnetization jump, ΔM_1 , at the transition clearly follows the temperature dependence of the total magnetic moment that passes through zero at $T = T_{comp}$ (Fig. 5.54b). By contrast, the individual magnetic moments of the Ho and Fe sublattices should vary smoothly with temperature between 40 and 80 K. Secondly, the observed ΔM_1 values are rather small ($\Delta M_1 = 1 \mu_B/f.u.$ at $T = 50$ K), whereas the magnetic moment of either magnetic sublattice is several times larger. The non-monotonous temperature dependence of the transition field passing through zero at $T = T_{comp}$ also contradicts the notion of a transition in only one magnetic sublattice. Thirdly, the change of $(\Delta v/v)_1$ at the transition, also shown in Fig. 5.54b, passes through a minimum at $T = T_{comp}$ and, therefore, correlates well with $H_{cr,1}$ and ΔM_1 . All this indicates that the transition is caused by a simultaneous rotation of the magnetic moments within both, the Ho and Fe sublattices.

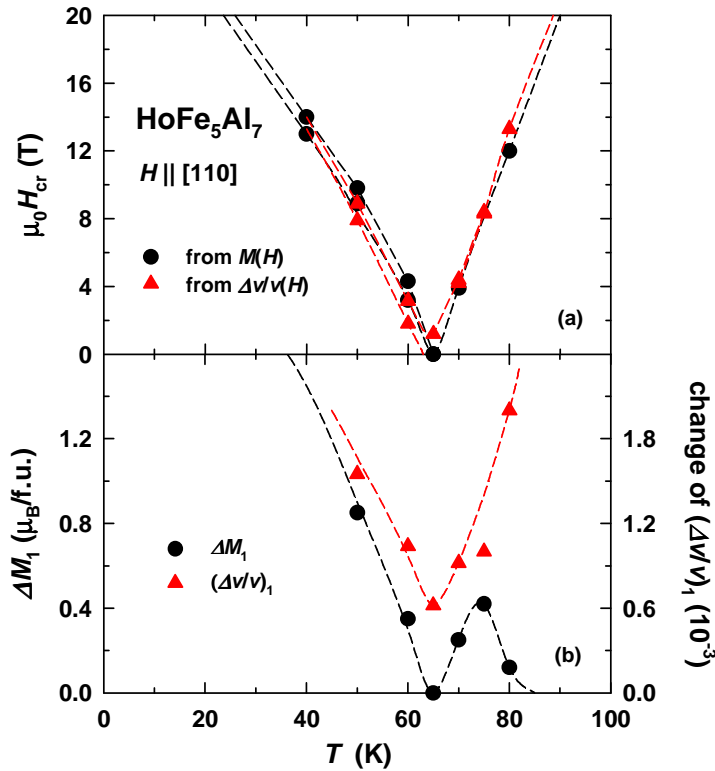


Fig. 5.54. Temperature dependence of the critical field $\mu_0 H_{cr,1}$ of the first field-induced transition (a), the magnetization gain ΔM_1 and change of $(\Delta v/v)_1$ at the transition (b).

The strong temperature dependence of $H_{cr,1}$ in the vicinity of the compensation point (Fig. 5.54) does not make it possible to follow the transition in static magnetic fields far away from T_{comp} . Therefore, pulsed magnetic fields up to 60 T were used to investigate that further.

Figure 5.55 shows the magnetization of HoFe_5Al_7 measured in pulsed magnetic fields up to 60 T applied along the [100], [110] and [001] axes at $T = 2$ K. Along the easy [110] axis the magnetization experiences two magnetic transitions represented by step-wise anomalies, at 13-20 T and 34-38 T. Both transitions exhibit wide hysteresis and, therefore, are of first order. The magnetization gain at the transitions is rather low, with values not exceeding $\Delta M_1 = 1.4 \mu_B/\text{f.u.}$ and $\Delta M_2 = 2.1 \mu_B/\text{f.u.}$ for the first and second jump, respectively. Due to the high anisotropy within the basal plane, the magnetization along the [100] and [110] axes approaches somewhat different values at highest fields. Above the intersection of the two magnetization curves at 5 T, the magnetization is higher along the [100] axis, the hard direction in the basal plane. The saturation value of the magnetic moment expected for the parallel alignment of the Ho and Fe sublattices is $M_{ferro} = M_{Ho} + M_{Fe} = 10 + 8 = 18 \mu_B/\text{f.u.}$ Just below 60 T the saturation is almost reached. The inset in Fig. 5.55 shows the high-field part of a measurement along the easy [110] axis extended to a field of 64 T. At the highest applied field the magnetization is as high as $17.7 \mu_B/\text{f.u.}$, very close to M_{ferro} .

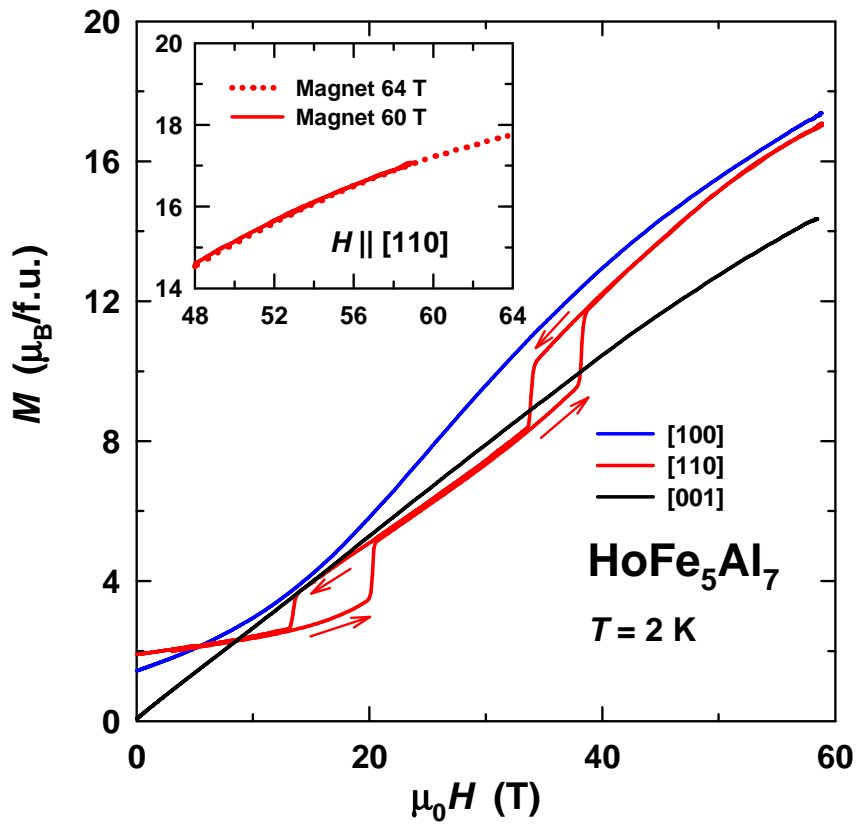


Fig. 5.55. Magnetization curves of HoFe_5Al_7 measured along the principal axes in pulsed magnetic fields at $T = 2$ K. The inset shows the extension of the curve along the [110] axis to 64 T.

No magnetization jumps are observed along the [100] axis. The magnetization rapidly increases as the magnetic moments gradually turn away from the easy [110] direction towards the applied magnetic field. The magnetization along the [001] axis displays an almost linear growth. The observed increase is unlikely to be caused by a rigid rotation of the magnetic moments since the field dependence of the magnetization is clearly dominated by a non-collinear arrangement of the magnetic moments even along the easy [110] axis (see Fig. 5.47) as discussed above.

Similar to HoFe_5Al_7 , a high-field magnetization study of the isostructural DyFe_5Al_7 also indicated the presence of two magnetization jumps along the EMD which is the [100] axis (see Fig. 5.17). At $T = 2$ K, the transitions in DyFe_5Al_7 were observed at 28-33 T and 52-54 T. The first jump was attributed to a simultaneous rotation of the Dy and Fe magnetic moments. The second jump was found to be temperature independent. Apparently, DyFe_5Al_7 and HoFe_5Al_7 behave similarly in a magnetic field. However, the magnetization jumps are observed at much higher fields in the former compound. Both materials display transitions along the EMD and possess similar sublattice magnetic moments (with similar values of the Zeeman energy) due to the same values of the magnetic moments of free Dy^{3+} and Ho^{3+} ions. This means that the observed difference in $\mu_0 H_{\text{cr}}$ of the two compounds is caused by the strength of the $4f$ - $3d$ exchange interactions. A similar situation was also reported, e.g., for DyMn_6Sn_6 and HoMn_6Sn_6 , where field-induced transitions from the ferrimagnetic to a canted-moment phase were found at 22 and 17 T, respectively [137].

The complex magnetic phases observed for fields aligned along the easy [110] axis have also been studied by acoustic measurements in pulsed magnetic fields. Figure 5.56 shows $M(H)$, $\Delta v/v(H)$ and $\Delta\alpha(H)$ at $T = 2$ K. Just as the magnetization (Fig. 5.56a), the sound velocity exhibits anomalies with pronounced hystereses at both magnetic transitions (Fig. 5.56b). In $\Delta v/v(H)$ the shapes of the anomalies are clearly different, in contrast to the magnetization data. This difference indicates a different origin for the two transitions. Moreover, the second anomaly on the $\Delta v/v(H)$ curve has a fine structure. Sharp jumps at 34 and 38 T coincide with the magnetization jumps. These are the same features as observed at the first transition. Besides, there is a smoother and bigger increase at 40 T accompanied by hysteresis. That could mean an additional transformation of the magnetic structure above the second field-induced transition. Since the magnetization has no anomalies in this field range, one can speculate that the normal components of the magnetic moments are involved in the transformation, because structural changes are unlikely. Furthermore, the change of the slope in the sound velocity at ~ 52 T correlates with the change of the slope in the magnetization (see Fig. 5.56a). No anomaly is seen in $\Delta\alpha$ (Fig. 5.56c) within resolution of about 2 dB/cm.

Figure 5.57 presents the magnetization and relative changes of the sound velocity of HoFe_5Al_7 in pulsed magnetic fields at $T = 20, 40,$ and 60 K. The magnetization data show that the low-field transition rapidly diminishes with

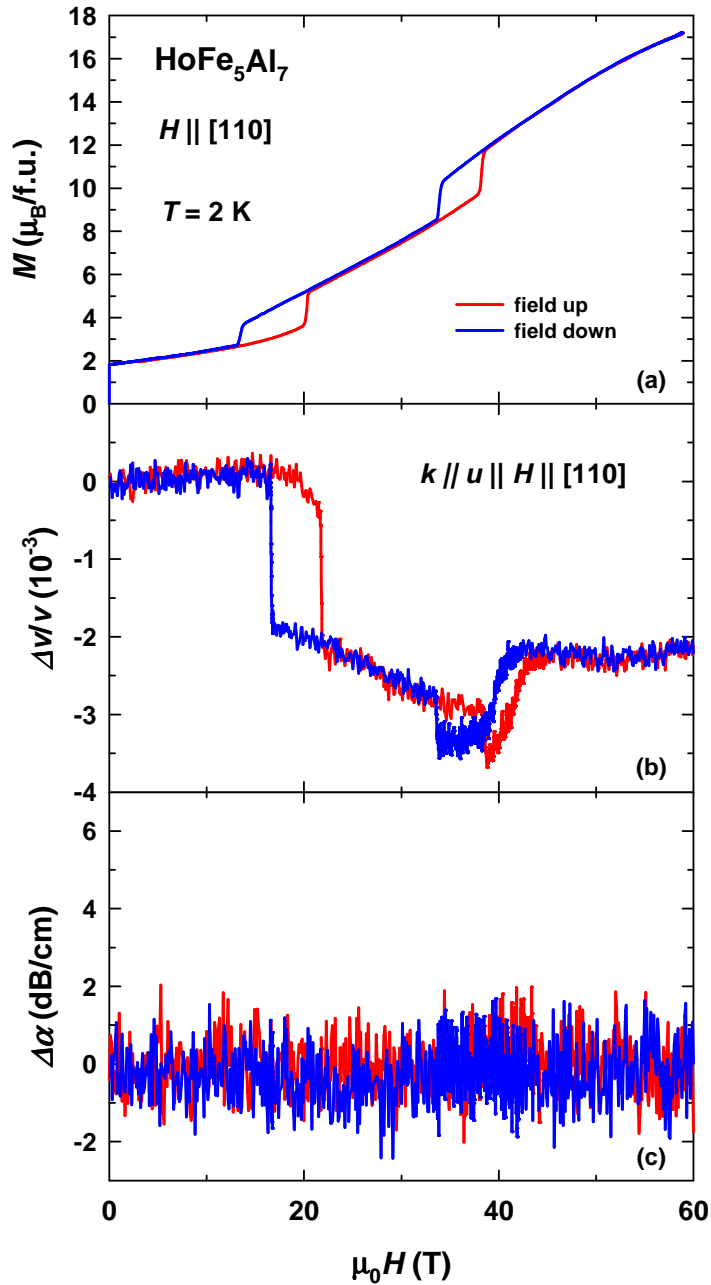


Fig. 5.56. Magnetization (a), relative change of sound velocity (b) and sound attenuation (c) measured along the [110] axis of the HoFe_5Al_7 single crystal in pulsed magnetic fields at $T = 2$ K.

increasing temperature (Figs. 5.57a,b,c). The hysteresis and the magnetization jump at the transition are shrinking rapidly as well. In striking contrast, $\mu_0 H_{\text{cr},2}$ remains practically temperature independent, although, as expected, the transition becomes less pronounced with increasing temperature. The different temperature dependences of critical fields indicate again that they are of different origin. (This point has been mentioned above in the discussion of the relative changes of sound velocity (Fig. 5.56)). In $\Delta v/v(H)$, $\mu_0 H_{\text{cr},1}$ can be resolved as well at all temperatures (Figs. 5.57d,e,f). The shape of the anomaly is similar to that observed at $T = 2$ K (Fig. 5.56) but its magnitude gradually decreases with temperature. The anomaly related to $\mu_0 H_{\text{cr},2}$ is

seen at $T = 20$ K but disappears at higher temperatures, although the transition is still present on the magnetization curves.

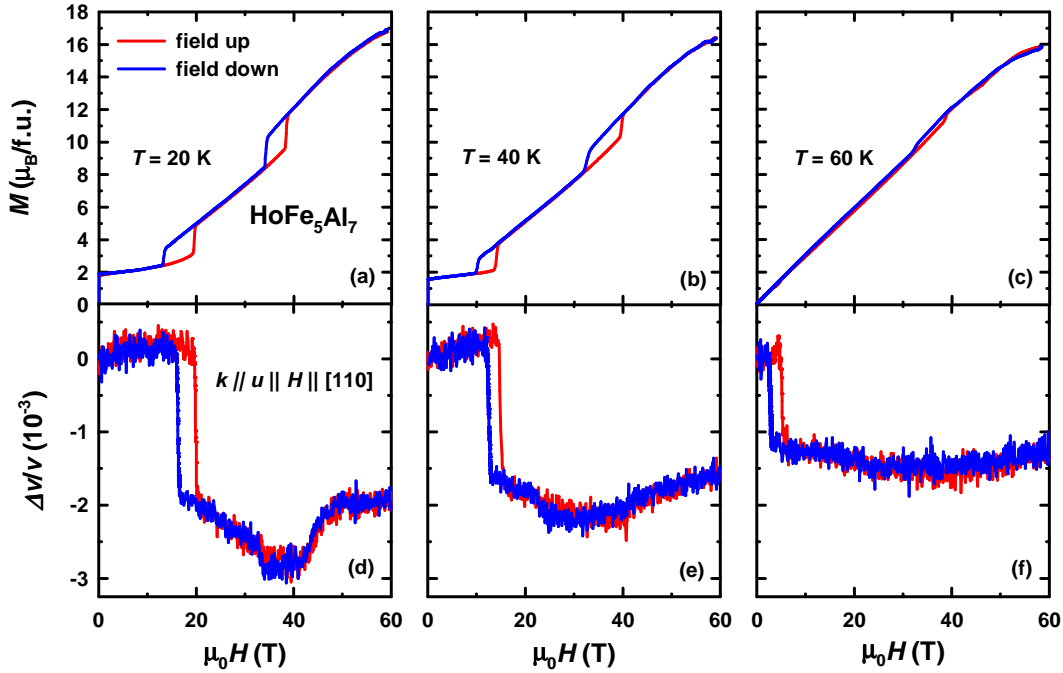


Fig. 5.57. Magnetization (a, b and c) and relative changes of sound velocity (d, e and f) measured along the [110] axis of the HoFe_5Al_7 single crystal in pulsed magnetic fields at $T = 20, 40$ and 60 K.

The field dependences of the magnetization and acoustic properties at $T = 80$ K are shown in Fig. 5.58. Two weak anomalies are observed in $M(H)$ at about 11 and 36 T (Fig. 5.58a). The relative changes of the sound velocity and sound attenuation demonstrate very sharp changes at the low-field transition, as has been observed in static magnetic fields (see Fig. 5.53b). The second transition, accessible only in pulsed magnetic fields, is also clearly resolved in the acoustic properties. However, the changes in $\Delta v/v(H)$ and $\Delta\alpha(H)$ at the second transition are not as big as those at the low field transition.

Finally, Fig. 5.59a presents the T - H magnetic phase diagram of HoFe_5Al_7 for fields applied along the easy [110] axis. The critical field of the first transition rapidly decreases from the average value of 17 T at 2 K to zero at $T_{\text{comp}} = 65$ K and then increases as the temperature is raised to 80 K. Above $H_{\text{cr},1}$, the magnetic structure is characterized by a non-collinear arrangement of the Ho and Fe magnetic moments. $H_{\text{cr},2}$ of the second transition stays constant at about 36 T at all temperatures. Anyhow, fields higher than 36 T are required to reach the ferromagnetic saturation. Fig. 5.59a also shows wide hysteresis at both transitions. Qualitatively, the temperature dependence of the critical field of the first magnetization jump is consistent with the diagram obtained for DyFe_5Al_7 (see Fig. 5.19). However, in contrast to the present data, the second transition in DyFe_5Al_7 displays a temperature dependence, albeit rather weak. The temperature dependences

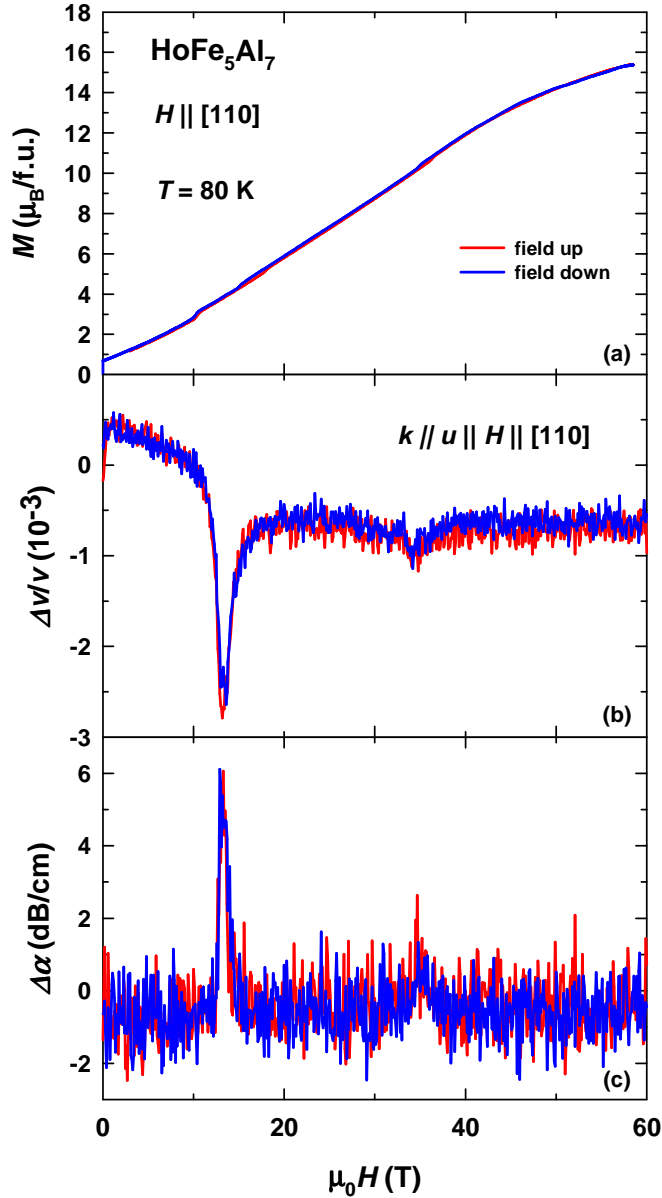


Fig. 5.58. Magnetization (a), relative change of sound velocity (b) and sound attenuation (c) measured along the [110] axis of the HoFe_5Al_7 single crystal in pulsed magnetic fields at $T = 80$ K.

of the magnetization jumps ΔM_1 and ΔM_2 are shown in Fig. 5.59b. ΔM_1 displays a similar temperature dependence as $H_{\text{cr},1}$. The jump amounts to about $1.5 \mu_B/\text{f.u.}$ at $T = 2$ K, passes through zero at the compensation point and then grows again. Although the magnetization gain at the second transition is higher than that at the first transition, ΔM_2 can still be considered rather low taking into consideration the large magnetic moments of the Ho and Fe sublattices. This observation along with the fact that ΔM_2 decreases monotonously to zero at $T = T_{\text{comp}}$ suggests that the second magnetic transition is a consequence of simultaneous rotations of the magnetic moments of both, the Ho and Fe sublattices, similar as for the first transition. Changes in $\Delta v/v$ at the first and second transition decrease with increasing temperature and pass through a minimum at the compensation point (Fig. 5.59c). At

$T > T_{\text{comp}}$ a steep growth is observed in the change of $\Delta v/v_1$, which might evidence magnetoelastic mechanisms different from those at $T < T_{\text{comp}}$.

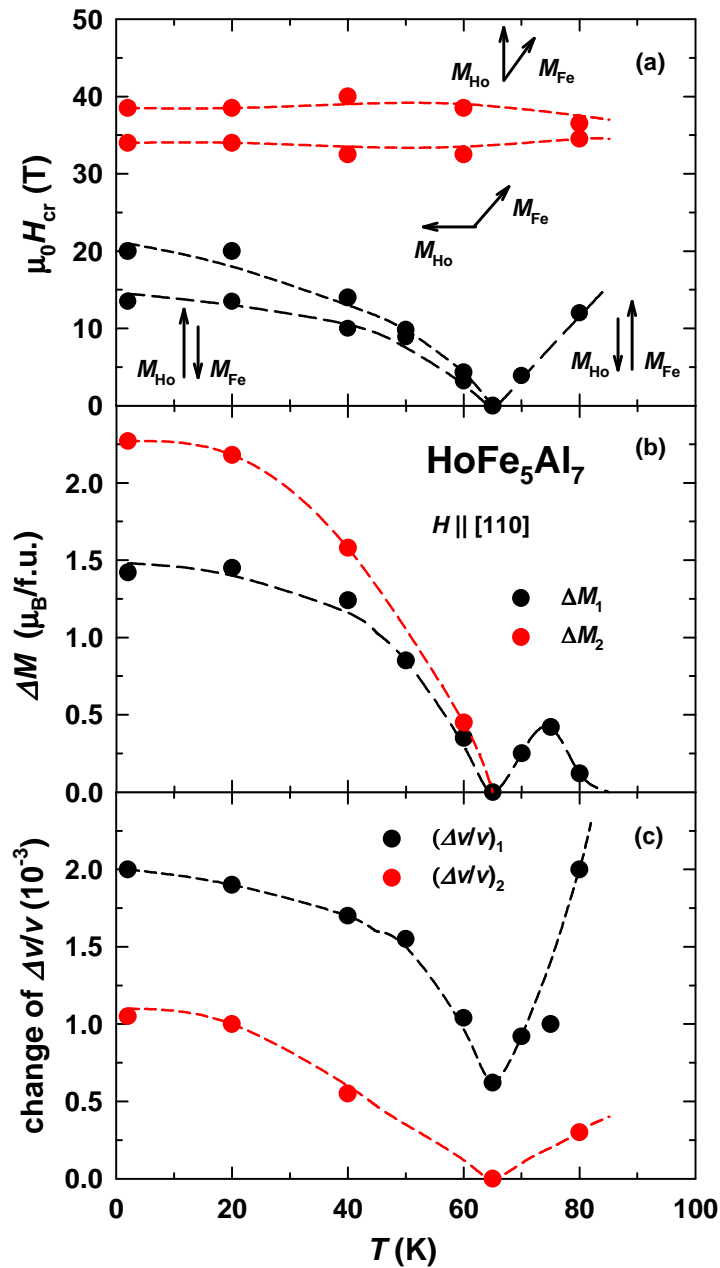


Fig. 5.59. T - H magnetic phase diagram (a), temperature dependence of the magnetization gain ΔM (b) and change of $\Delta v/v$ (c) at the first and second transitions of the HoFe_5Al_7 single crystal.

For the interpretation of the transitions, it should be noted that there are two crystallographically equivalent perpendicular easy magnetization directions in the basal plane of the tetragonal lattice of HoFe_5Al_7 , $[110]$ and $[1-10]$. When the field is applied along the $[110]$ axis, the ferrimagnet HoFe_5Al_7 has a relatively low magnetic susceptibility. At the compensation temperature the ferrimagnet behaves as an antiferromagnet. Therefore, a higher magnetic susceptibility should be observed

when the magnetic moments of the two sublattices are perpendicular to the field. In this situation, one may expect a magnetization jump from one EMD (the [110] axis) to the other (the [1-10] axis). The higher the spontaneous magnetic moment, the higher is the transition field. Upon further increasing the field, the ferromagnetic saturation will be reached along the field direction, and an additional transition may be expected from the [1-10] axis back to the [110] axis.

Since the field-induced magnetic transitions in HoFe_5Al_7 reflect the breaking of (almost) antiparallel coupling between the Ho and Fe sublattices, it is necessary to analyze the inter-sublattice $3d-4f$ molecular field that reflects the intensity of the relevant exchange interactions.

The inter-sublattice exchange parameter, n_{HoFe} , on Ho was determined using two different approaches, namely, molecular field theory and the model for a ferrimagnet with an anisotropic dominant sublattice, in the same way as for DyFe_5Al_7 and TbFe_5Al_7 . The temperature dependence of the magnetic holmium moment in HoFe_5Al_7 , $M_{\text{Fe}}(T)$, determined within molecular field theory is shown in Fig. 5.60 in conjunction with $M_{\text{s}}(T)$ and the Fe magnetic moment $M_{\text{Fe}}(T)$. The best fit of the experimental data, also shown in Fig. 5.60, was obtained for the inter-sublattice exchange parameter $n_{\text{HoFe}} = 4 \text{ T f.u.}/\mu_{\text{B}}$.

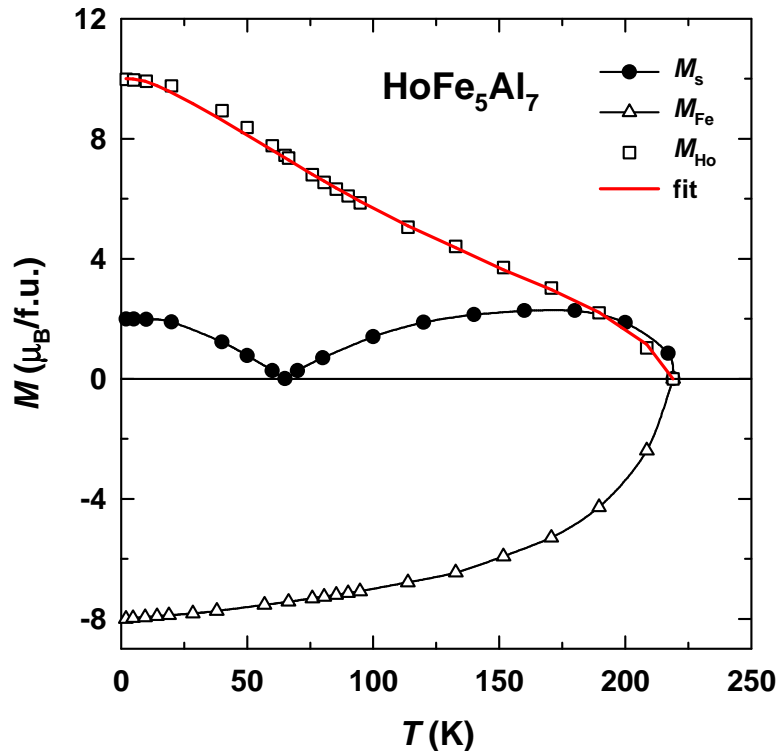


Fig. 5.60. Measured (closed circles) temperature dependence of the spontaneous magnetic moment along the easy magnetization direction together with the calculated temperature dependence of the magnetic moment of the Ho and Fe sublattices. The Fe magnetic moment is assumed to be negative as it is antiparallel to the Ho magnetic moment. The red line represents the fit according to the molecular-field theory.

The determination of the inter-sublattice exchange interaction using the high-field magnetization data obtained in the present work is complicated since the low-field transition shows a large hysteresis (Figs. 5.55 and 5.56). From the average value of this transition, $\mu_0 H_{cr,1} = 16.5$ T, the lower value $n_{\text{HoFe}} = 3.1$ T/ μ_B is obtained. Apparently, due to the wide hysteresis at the transition the determination of n_{HoFe} using this method is ambiguous. With increasing field the transition occurs at 20 T. From this value we arrive at $n_{\text{HoFe}} = 3.8$ T f.u./ μ_B , in good agreement with the result obtained within the framework of the molecular-field theory.

For GdFe_5Al_7 , TbFe_5Al_7 and DyFe_5Al_7 , $n_{\text{GdFe}} = 8.3$, 6.7 and 5.3 T f.u./ μ_B were found, respectively. The molecular field in HoFe_5Al_7 obtained in the present work correlates well with these three values. Since the exchange interactions in the $3d$ - $4f$ compounds are mainly of the Heisenberg type [6], the observed decrease of the inter-sublattice molecular field with atomic number of the rare-earth component is related to the spin reduction.

Apart from the Zeeman energy and the $3d$ - $4f$ intersublattice exchange interactions, the magnetic anisotropy plays a very important role in the formation of the field-induced transitions in HoFe_5Al_7 as well. It is known that in the vicinity of the compensation point of ferrimagnets its effects become most conspicuous [138]. We analyzed the field-dependent magnetization of HoFe_5Al_7 within the two-sublattice model. In the absence of magnetic anisotropy, no magnetization jumps occur up to the ferromagnetic saturation, and the corresponding magnetization curve is that of a powder free to rotate in a magnetic field [123]. The strong easy-plane magnetic anisotropy results in the appearance of two field-induced magnetic transitions along the EMD. The easy-plane anisotropy constant, K_{Ho} , associated with the dominant Ho sublattice, can be estimated from Figs. 5.21 and 5.22 showing schematically how high-field magnetization curves depend on the magnetization ratio M_R/M_{Fe} and anisotropy constant. With $-150 < K_{\text{Ho}} < -20$ K/f.u., the anisotropy falls in the same ballpark as that of the Dy sublattice in DyFe_5Al_7 .

Application of external pressure is expected to introduce changes to the coupling between the Ho and Fe sublattices, which should be reflected in the temperature and field dependences of the magnetization. Figure 5.61 shows the temperature dependent magnetization of the HoFe_5Al_7 single crystal for different hydrostatic pressures in a field of 0.1 T. For $T > T_{\text{comp}}$, the absolute value of the magnetic moment decreases with increasing pressure, whereas at $T < T_{\text{comp}}$, an increase in the magnetic moment is observed. As a result, T_C and T_{comp} shift oppositely with respect to their values at ambient pressure. T_C decreases with a rate $dT_C/dp = -10$ K/GPa, whereas T_{comp} increases with $dT_{\text{comp}}/dp = 3.5$ K/GPa (inset in Fig. 5.61). These effects are a result of the weakening of the Fe magnetic moment in HoFe_5Al_7 under pressure. The itinerant character of the Fe sublattice makes it more sensitive to external pressure that results in a reduction of its magnetic moment. The magnetic moment of the Ho sublattice is unlikely to be influenced noticeably by the pressures applied due to the localization of the $4f$ electrons.

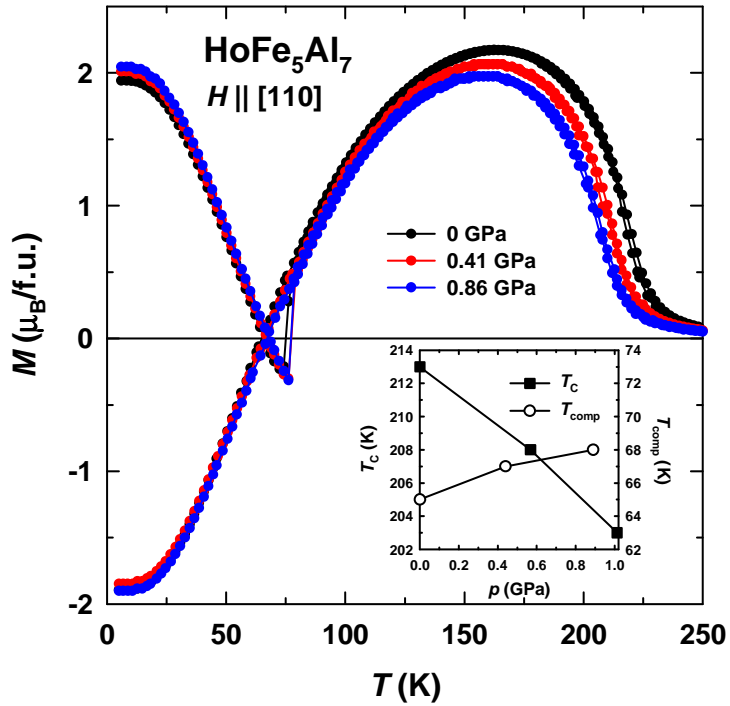


Fig. 5.61. Temperature dependence of the magnetization of the HoFe_5Al_7 single crystal under hydrostatic pressure. The inset shows the variation of T_C and T_{comp} with pressure.

Magnetization isotherms measured at different pressures at $T = 60$ K are shown in Fig. 5.62. The spontaneous magnetic moment increases with a rate $d(\ln M_s)/dp \approx 0.48 \text{ GPa}^{-1}$ as pressure increases up to $p = 0.86$ GPa. Application of pressure shifts $\mu_0 H_{cr,1}$ to higher fields from 3.7 T at $p = 0$ to 5.9 T at $p = 0.86$ GPa [$d(\ln \mu_0 H_{cr,1})/dp \approx 0.54 \text{ GPa}^{-1}$]. The temperature dependence of the transition field at $p = 0, 0.41,$ and 0.86 GPa is presented in the inset of Fig. 5.62. For $T < T_{comp}$, the transition field is much more sensitive to pressure than at $T > T_{comp}$. Figure 5.63 shows magnetization curves measured along the easy [110] axis under $p = 0.86$ GPa for different temperatures between 50 and 80 K (for clarity of the presentation, the magnetization curve at each temperature was shifted down by $0.5 \mu_B/\text{f.u.}$ with respect to the curve at the previous temperature). The field-induced magnetic transition displays very similar behavior as observed at ambient pressure but with higher $\mu_0 H_{cr,1}$ values.

Figure 5.64 shows hysteresis loops in a field applied along the easy [110] axis of the HoFe_5Al_7 single crystal at different temperatures. Very similar hysteresis loops were also observed along the [100] axis. Large coercive field $\mu_0 H_c$, 1.6 T, is found at 2 K. The high H_c reflects the fact that, apart from the anisotropy between the basal plane and the tetragonal axis, the in-plane anisotropy is also very strong in HoFe_5Al_7 . With increasing temperature H_c decreases exponentially (Fig. 5.65), as was observed in the single crystal of highly-anisotropic DyFe_5Al_7 (Fig. 5.25) and TbFe_5Al_7 (Fig. 5.45).

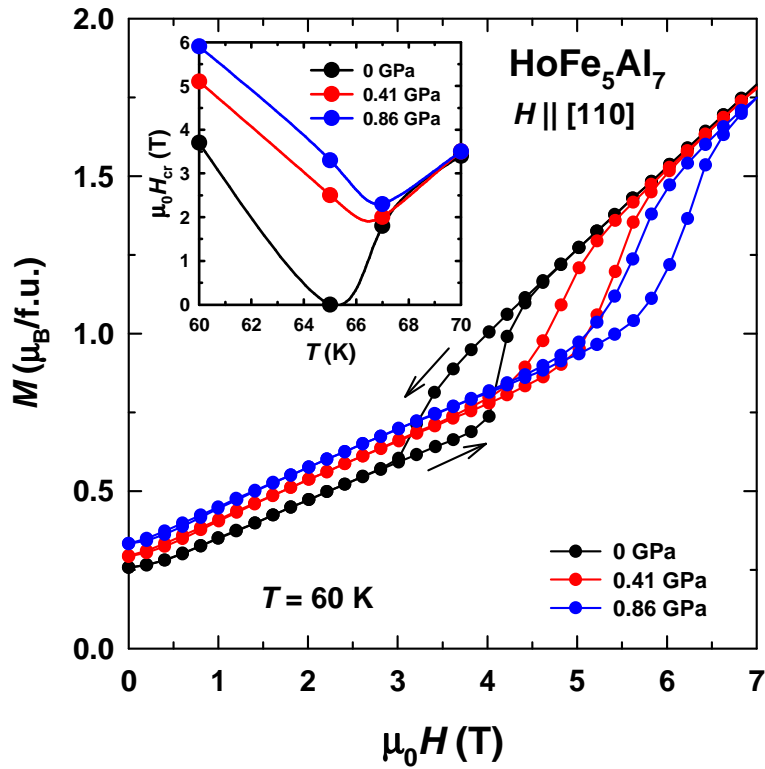


Fig. 5.62. Field dependence of the magnetization measured along the [110] direction at $T = 60$ K under hydrostatic pressure. The inset shows the temperature dependence of the transition field under hydrostatic pressure.

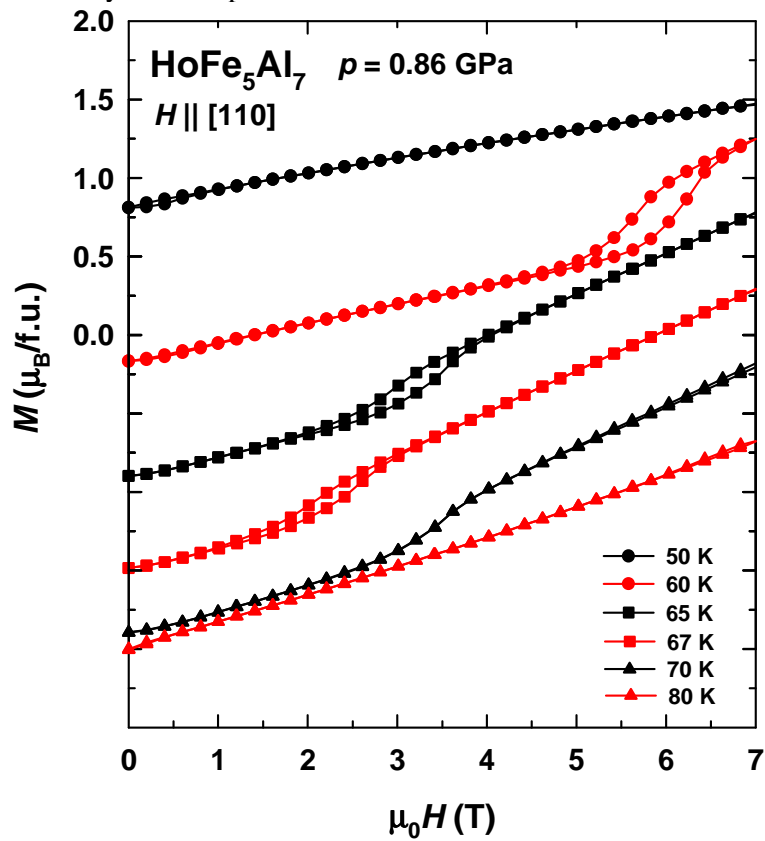


Fig. 5.63. Field dependence of the magnetization measured along the [110] direction under $p = 0.86$ GPa in the vicinity of $T_{\text{comp}} = 68$ K.

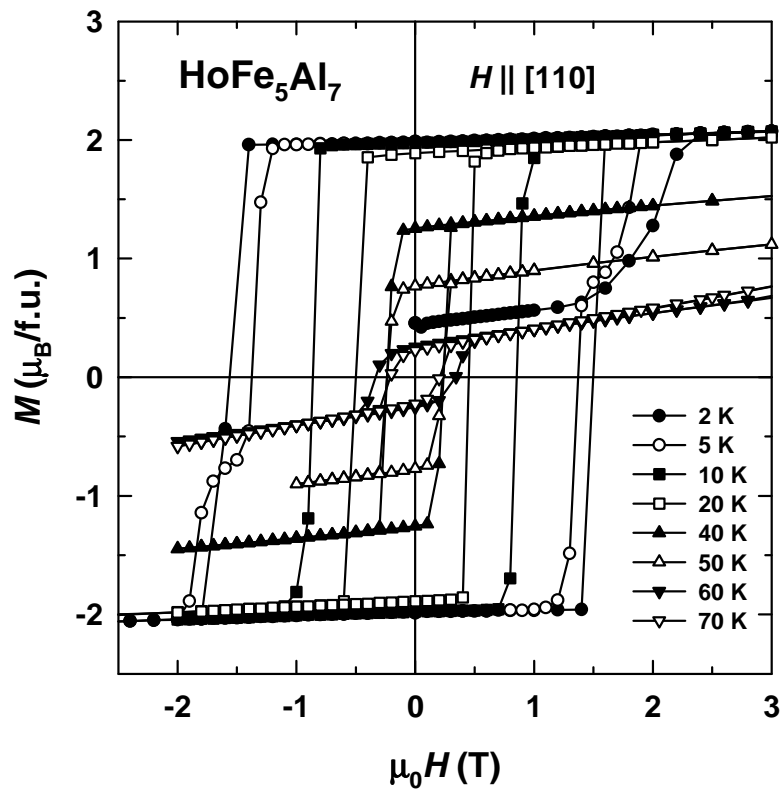


Fig. 5.64. Low-field details of hysteresis loops measured along the [110] axis at different temperatures.

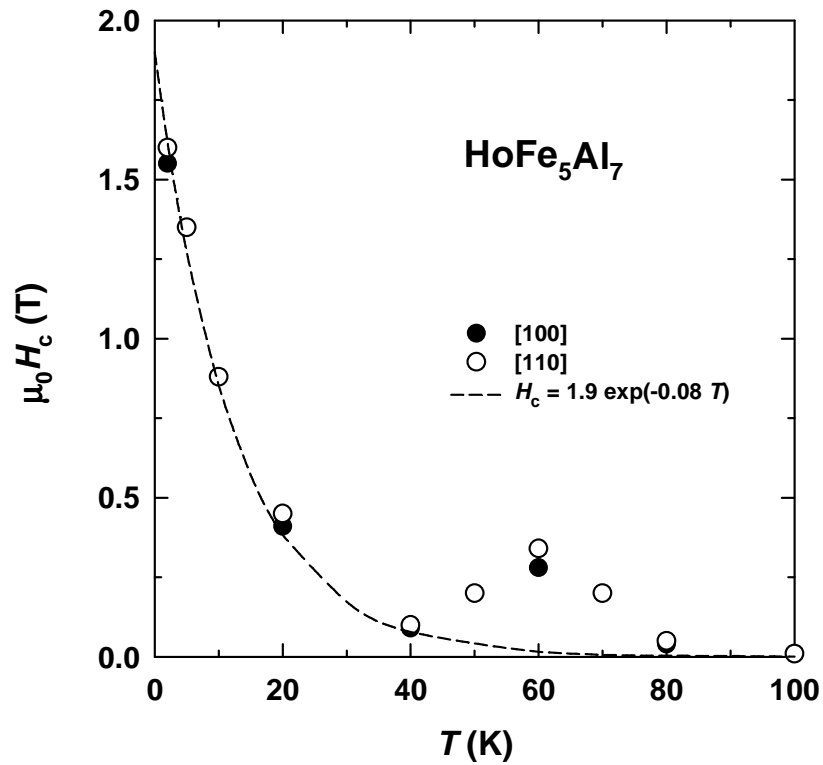


Fig. 5.65. Temperature dependence of the coercive field $\mu_0 H_c$ along the [100] and [110] axes. The dashed lines represent the fit $\mu_0 H_c(T) = \mu_0 H_c(0) \exp(-\beta T)$.

Apart from the field hysteresis, HoFe_5Al_7 also exhibits thermal hysteresis. Figure 5.66 shows the temperature dependence of magnetization measured in a 0.1 T field applied along the main axes in the basal plane upon heating and cooling. First, the sample was cooled down from room temperature to 2 K in a magnetic field of 0.5 T. Since this field is higher than the coercivity just below T_{comp} (Fig. 5.65), the crystal became saturated along the moments of the Ho sublattice. Upon heating this single-domain sample in a field of 0.1 T through the compensation point, the magnetization reorients itself along the moments of the Fe sublattice, i.e., it becomes negative with respect to the applied field of 0.1 T because the coercivity is higher than this field in the vicinity of T_{comp} . However, the magnetization remains negative only in a narrow temperature interval because above 80 K H_c becomes lower than the applied field and the crystal becomes magnetized along the field. Upon subsequent cooling of the sample, since H_c below T_{comp} is always higher than 0.1 T, the crystal remains single-domain after the inversion of magnetization from the Fe to the Ho sublattice, and “the negative magnetization effect” is seen in a wide range to the lowest temperatures.

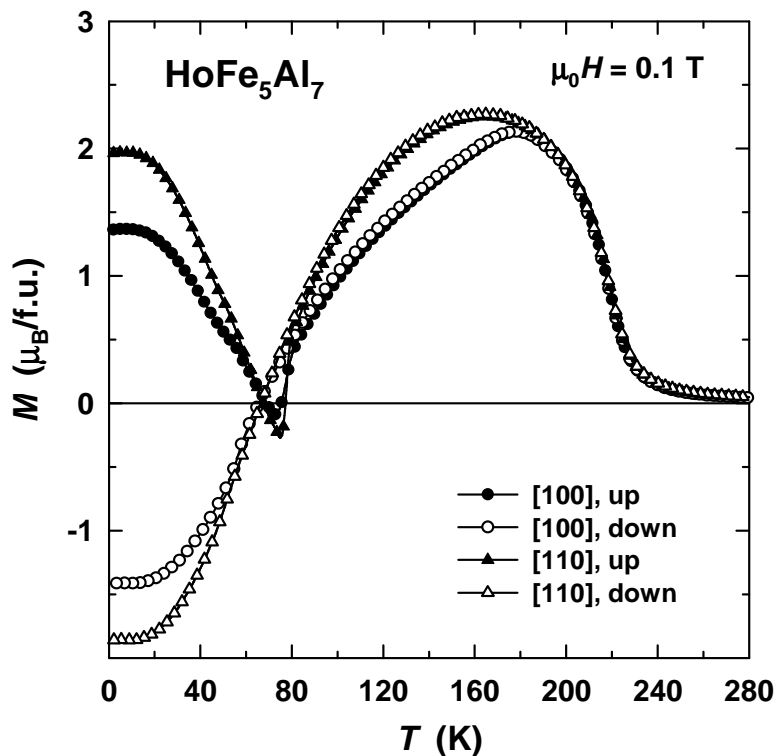


Fig. 5.66. Temperature dependence of magnetization measured in a field of 0.1 T applied along the [100] and [110] axes of the HoFe_5Al_7 single crystal. First, the sample was cooled down to $T = 2$ K in a field of 14 T. Then, the magnetization was measured in 0.1 T upon heating the sample up to $T = 300$ K and subsequent cooling to $T = 2$ K.

5.6. ErFe₅Al₇

The ErFe₅Al₇ compound presents a special case among the RFe₅Al₇ systems described so far since the second-order Stevens' factor is positive for Er³⁺. For this reason, one might expect a uniaxial anisotropy of the Er sublattice, in contrast to the Tb, Dy and Ho sublattices that are planar. This section describes magnetic and magnetoelastic properties of ErFe₅Al₇.

Figure 5.67 presents magnetization curves of the ErFe₅Al₇ single crystal along the principal crystallographic directions at several selected temperatures. The compound displays a spontaneous magnetic moment along the [100] and [110] axes, whereas there is no spontaneous component along the [001] axis. Therefore, the magnetic moments of ErFe₅Al₇ lie in the basal plane of the tetragonal lattice, the [001] axis is the hard-magnetization direction, in agreement with neutron-diffraction data [12]. Anisotropy is also present within the basal plane as evident from the difference between the magnetization curves along the [100] and [110] axes. The EMD is the [100] axis with the spontaneous magnetic moment $M_s = 1.3 \mu_B/\text{f.u.}$ at $T = 2 \text{ K}$. Assuming that the magnetic moment of the Er sublattice is equal to that of a Er³⁺ ion, $M_{\text{Er}} = 9 \mu_B/\text{f.u.}$, the magnetic moment of the Fe sublattice can be determined as $M_{\text{Fe}} = M_{\text{Er}} - M_s = 7.7 \mu_B/\text{f.u.}$ This corresponds to $1.54 \mu_B$ per Fe atom. The spontaneous moment ratio along the [110] and [100] axes, $M_s^{110} / M_s^{100} \approx \cos 45^\circ$,

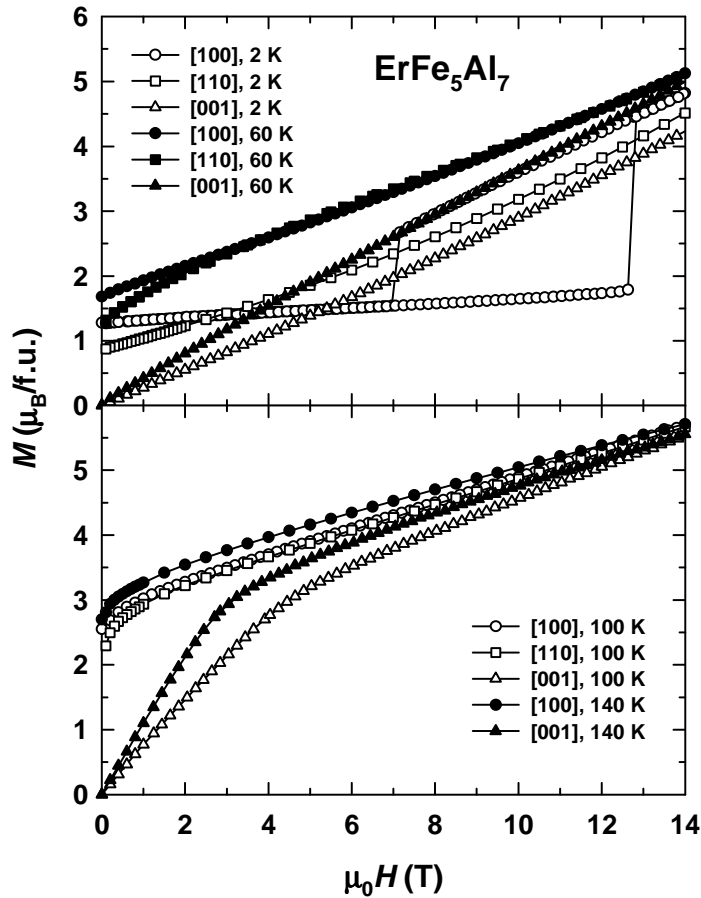


Fig. 5.67. Magnetization isotherms measured along the principal axes of the ErFe₅Al₇ single crystal at selected temperatures.

corresponds well to the tetragonal symmetry and reflects proper orientation of the single crystal. At low temperatures (see the curves at $T = 2$ K in Fig. 5.67) the [110] and [100] magnetization isotherms intersect at about 3 T and then the magnetization along the [110] axis continues to grow and does not follow that along the easy [100] axis as would be expected if 3 T was the field $H_{a,p}$ of the in-plane anisotropy. At elevated temperatures, the field where the [110] curve reaches the [100] one, is indeed $H_{a,p}$, above which both curves coincide (see the curves at $T = 60$ K in Fig. 5.67). The in-plane anisotropy gradually weakens as temperature increases. It is still present at $T = 100$ K but disappears around $T = 140$ K.

It is also seen in Fig. 5.67 that after the domain-wall motion is completed, the signal along the basal-plane directions continues to grow in ErFe_5Al_7 . The reason is the weak Er-Fe exchange interaction that gives rise to the high susceptibility. Field-induced non-collinearity of the magnetic moments appears as the initial collinear ferrimagnetic structure is broken, and the magnetic moments rotate towards the field direction. Strong paraprocess was also observed in GdFe_5Al_7 , TbFe_5Al_7 , DyFe_5Al_7 and HoFe_5Al_7 .

The temperature dependence of the spontaneous magnetization for fields applied along the [100] and [110] axes is presented in the upper panel of Fig. 5.68. For both field directions a ferrimagnetic-like behavior is found. The compensation of the Er and Fe sublattice magnetizations occurs at $T_{\text{comp}} = 34$ K. The spontaneous magnetization is zero around 210 K, whereas the specific heat, shown in the inset in Fig. 5.68, indicates that the phase transition occurs at 201 K (no other anomalies are observed on the $C_p(T)$ dependence to $T = 2$ K). The latter value is the more correct Curie temperature since it was measured in zero magnetic field. The lower panel of Fig. 5.68 shows the relative change of the sound velocity, $\Delta v/v$, of a longitudinal acoustic wave propagating along the [110] axis measured upon heating and cooling. The sound velocity displays a monotonous softening with increasing temperature. In the vicinity of T_C , $\Delta v/v(T)$ displays a weak anomaly which points to a small energy difference between the ferrimagnetic and paramagnetic states in ErFe_5Al_7 . This correlates with a rather small anomaly in the specific heat.

The temperature evolution of the magnetization isotherm along the [100] axis above $T = 40$ K is shown in Fig. 5.69. The magnetization does not display any anomalies. All the curves are characterized by strong linear paraprocess comparable with that at low temperatures in fields above the transition (the curve at $T = 2$ K is repeated here from Fig. 5.67 for a comparison).

The magnetization isotherms along the [110] axis in the temperature range $T = 2 - 220$ K are shown in Fig. 5.70. The curves below $T = 30$ K exhibit a small positive curvature which can be regarded as a precursor to a transition at higher fields. At higher temperatures a steady monotonous growth in magnetization with magnetic field is observed.

Figure 5.71 presents the temperature evolution of the magnetization curve along the hard [001] axis. In the range $T = 2 - 60$ K the magnetization displays linear growth, which means that the anisotropy field H_a of the compound exceeds the

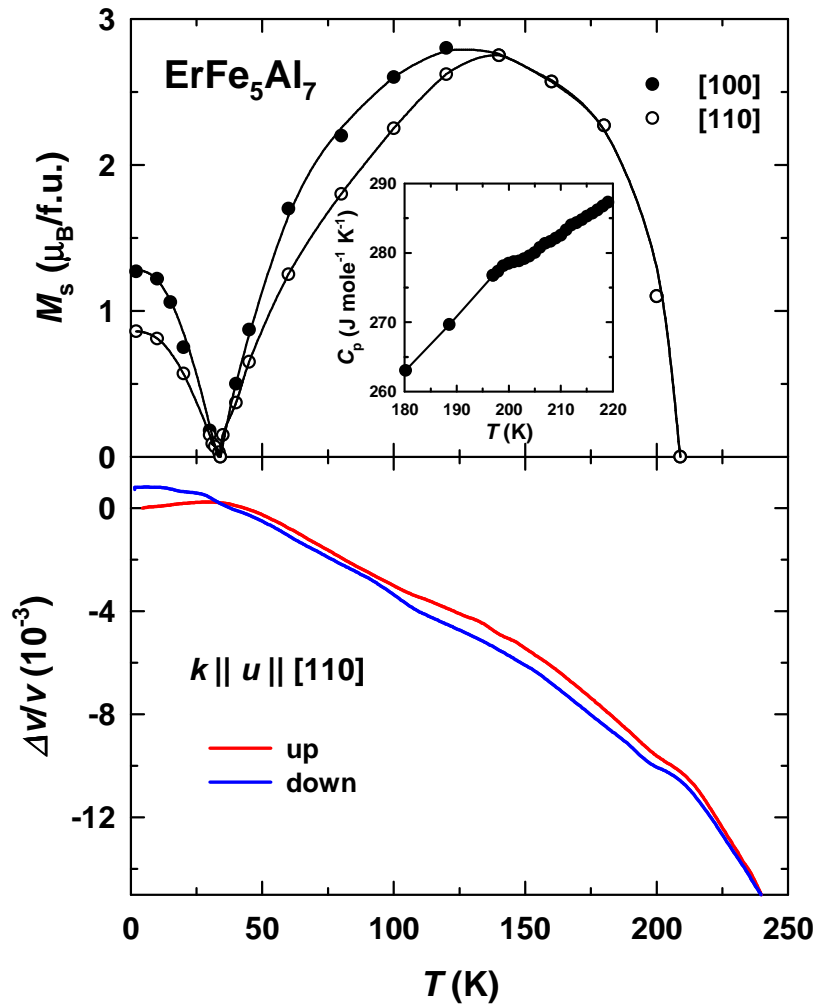


Fig. 5.68. Temperature dependence of the spontaneous magnetic moments along the [100] and [110] axes (upper panel) and of the relative sound-velocity change of longitudinal acoustic waves propagating along the [110] direction (lower panel) of ErFe_5Al_7 . The inset shows the temperature dependence of the specific heat in the vicinity of $T_C = 201$ K.

highest applied magnetic field of 14 T. The slope of the curve reflecting H_a changes in a field of about 6 T at $T = 80$ K and at lower fields at higher temperatures. The temperature dependence of the anisotropy field determined by the SPD method [119] at $T \geq 80$ K is shown in the inset in Fig. 5.71. H_a is a practically linear function of temperature. However, if the linear $H_a(T)$ dependence holds also at $T < 80$ K, the slope of the magnetization curves in this temperature range should change below 14 T as well. Since that is not observed in the experiment, we assume that at $T < 80$ K the anisotropy field depends more strongly on temperature. It should be noted that different temperature variations and higher absolute values of H_a were found for DyFe_5Al_7 and HoFe_5Al_7 (see Figs. 5.10 and 5.50).

It has already been shown that the Tb, Dy and Ho sublattices as well as the Fe sublattice display magnetic anisotropy of the easy-plane type in $R\text{Fe}_5\text{Al}_7$ compounds. Tb^{3+} , Dy^{3+} and Ho^{3+} ions have a negative second-order Stevens' factor α_J . Since $\alpha_J > 0$ for Er^{3+} , within the model of the single-ion anisotropy one could expect the

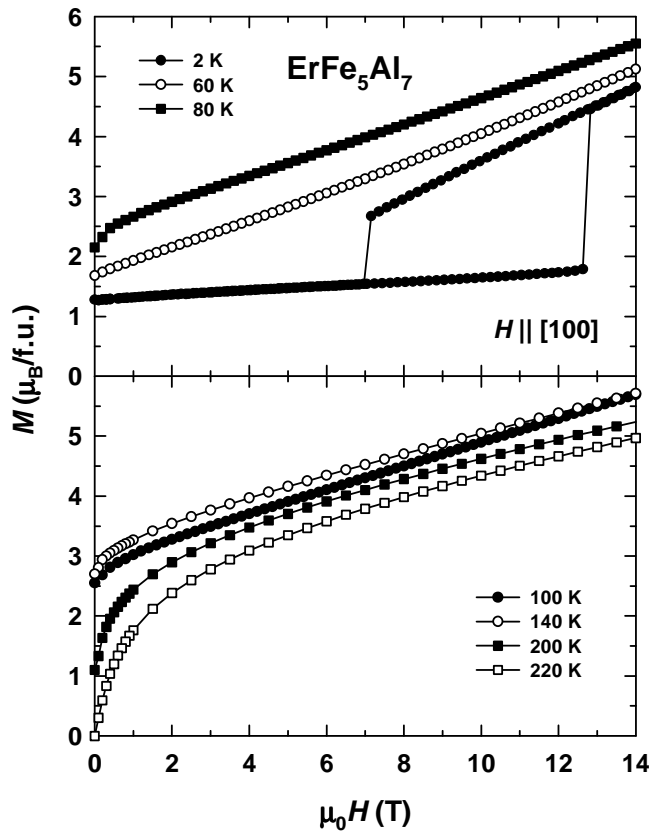


Fig. 5.69. Temperature evolution of the magnetization curve along the [100] axis of the ErFe_5Al_7 single crystal in the range $T = 2 - 220$ K.

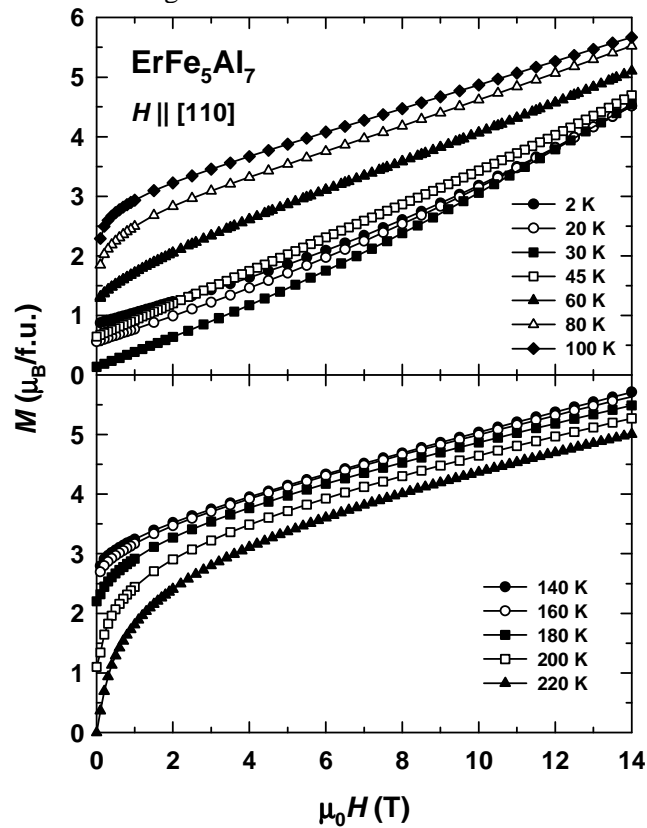


Fig. 5.70. Temperature evolution of the magnetization curve along the [110] axis of the ErFe_5Al_7 single crystal in the range $T = 2 - 220$ K.

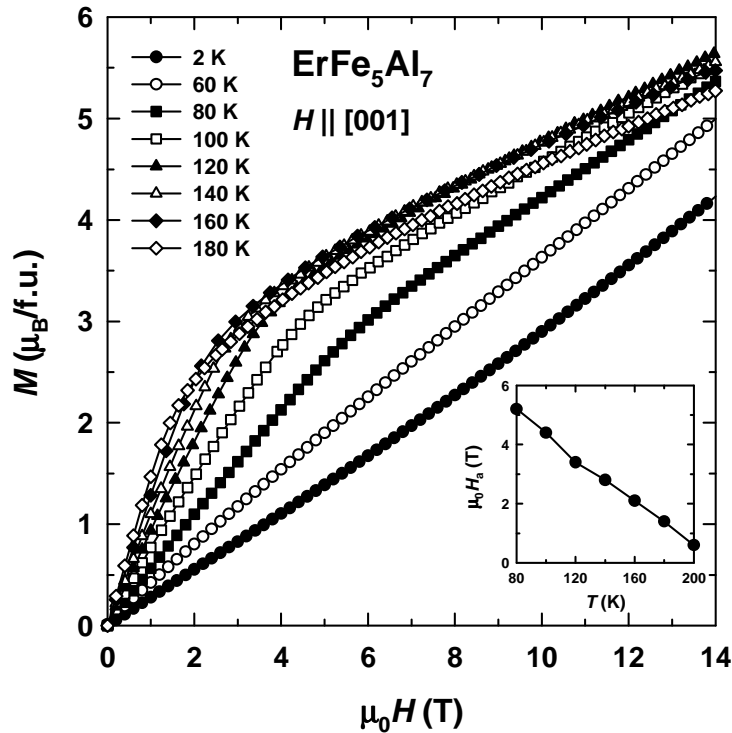


Fig. 5.71. Temperature evolution of the magnetization curve along the [001] axis of the ErFe_5Al_7 single crystal in the range $T = 2 - 180$ K. The inset shows the temperature dependence of the anisotropy field.

ErFe_5Al_7 compound to display uniaxial (or at least out of plane) anisotropy at low temperatures. However, the observed ground-state orientation of the magnetic moments in ErFe_5Al_7 is not consistent with the sign of α_j . This is unlikely to be a result of the competition between different contributions to the anisotropy, easy-plane from the Fe sublattice and easy-axis from the Er sublattice because the Fe anisotropy is not strong. Rather, this discrepancy can be understood as a large negative contribution of higher-order anisotropy terms associated with the Er sublattice. It results in non-uniaxial Er anisotropy in ErFe_5Al_7 . A similar situation has been found in isostructural compounds $\text{ErFe}_{11}\text{Ti}$ and $\text{ErFe}_{10.5}\text{V}_{1.5}$ [100,139]. The Fe sublattice displays easy-axis anisotropy, nevertheless, at low temperatures a considerable projection of the magnetic moment onto the basal plane was observed (a cone of EMDs) reflecting a negative contribution of the Er sublattice to the anisotropy in $\text{ErFe}_{11}\text{Ti}$ and $\text{ErFe}_{10.5}\text{V}_{1.5}$. From this observation it was concluded that the anisotropy of the Er sublattice is not uniaxial as would be expected from the positive sign of α_j for Er^{3+} , and high-order anisotropy terms should be taken into account.

The magnetization curve along the [100] axis of the ErFe_5Al_7 single crystal at $T = 2$ K displays a step-wise anomaly with a broad hysteresis (see Figs. 5.67 and 5.69). The observed first-order field-induced magnetic transition is shown in detail in Fig. 5.72 that presents the temperature evolution of the [100]-axis magnetization curve in the range $T = 2 - 40$ K. Initially, the critical field of the transition $H_{\text{cr},100}$

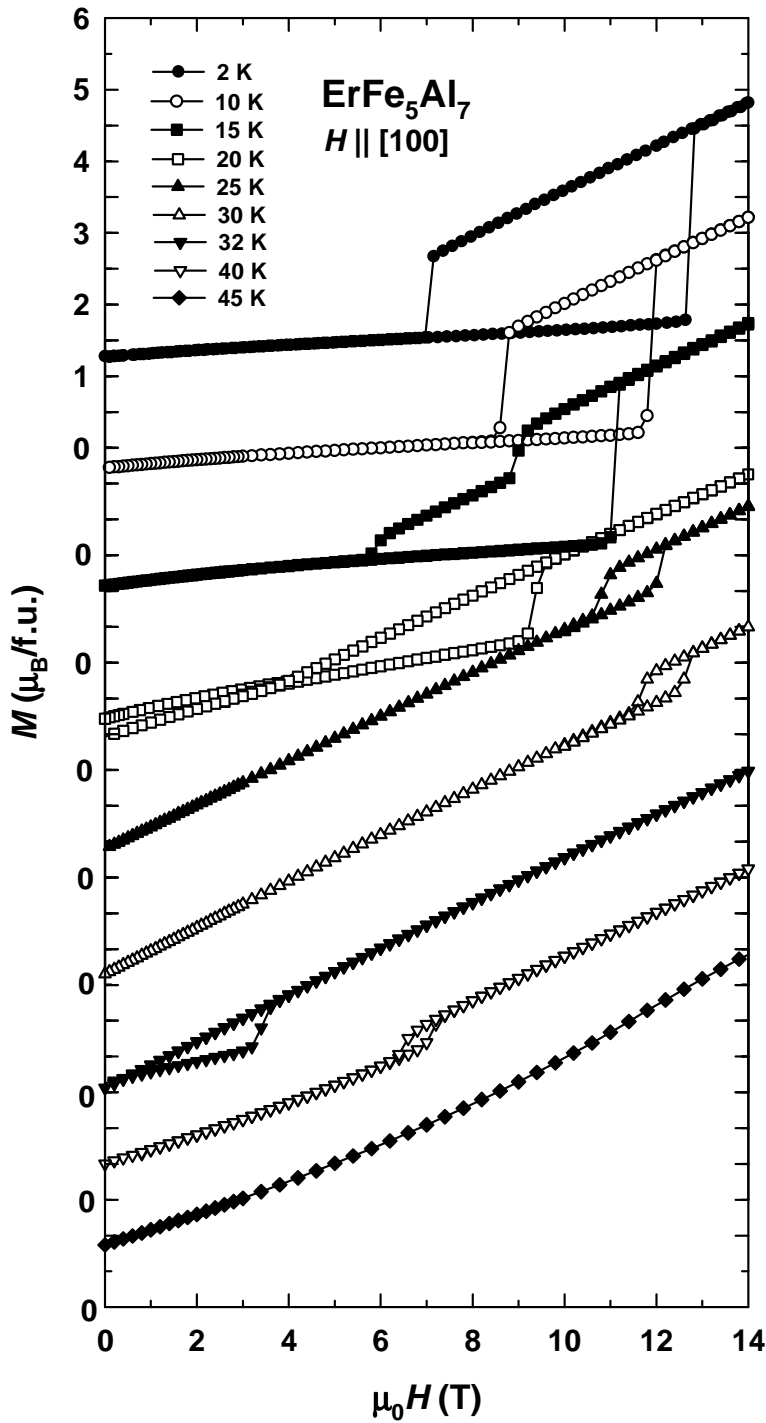


Fig. 5.72. Temperature evolution of the magnetization curve along the [100] axis of the ErFe_5Al_7 single crystal in the range $T = 2 - 40$ K.

(the transition field is marked $H_{\text{cr},100}$ since another magnetic transition is also observed along the [110] axis, see Fig. 5.73) decreases with increasing temperature. At $T = 2$ and 10 K the transition has a trapezoid shape. A more complicated two-step anomaly is observed with decreasing magnetic field at $T = 15$ K. Yet another transition shape is seen at $T = 20$ K: magnetization experiences a jump with increasing magnetic field, whereas with decreasing field the magnetization is a

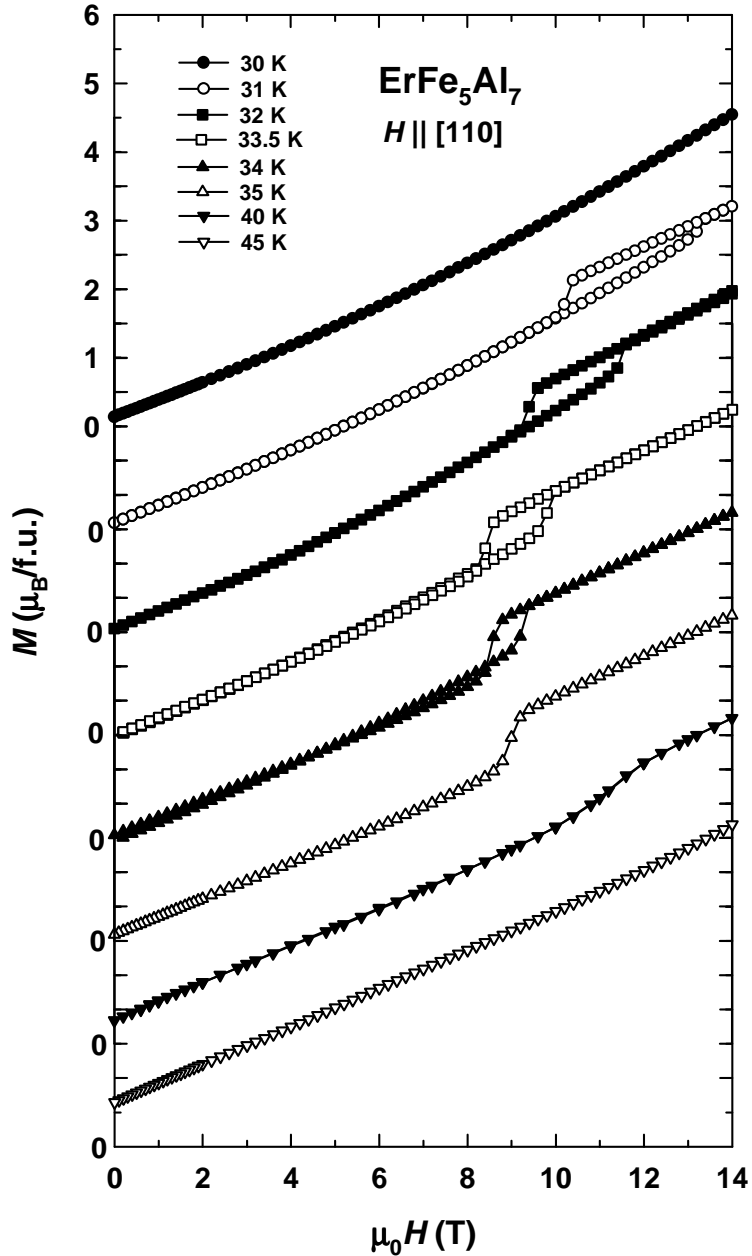


Fig. 5.73. Temperature evolution of the magnetization curve along the [110] axis of the ErFe_5Al_7 single crystal in the range $T = 30 - 45$ K.

smooth function of field without any anomaly. Surprisingly, at $T = 25$ and 30 K the transition field increases with temperature, and the transition shape changes yet again. At $T = 32$ K the transition is observed in a much lower field and looks very similar to that at $T = 20$ K. At $T > T_{\text{comp}}$ magnetization still displays the transition, its field grows with temperature. It means that $H_{\text{cr},100}$ approaches zero at $T = T_{\text{comp}}$. At $T > 40$ K the transition is no longer seen.

The temperature dependence of the transition field, determined only from the ascending branches of the magnetization jumps, is rather complicated (Fig. 5.74a). The initial decrease of $H_{\text{cr},100}$ with increasing temperature is followed by its growth at $T = 25$ and 30 K, after which the transition field rapidly falls down upon approaching

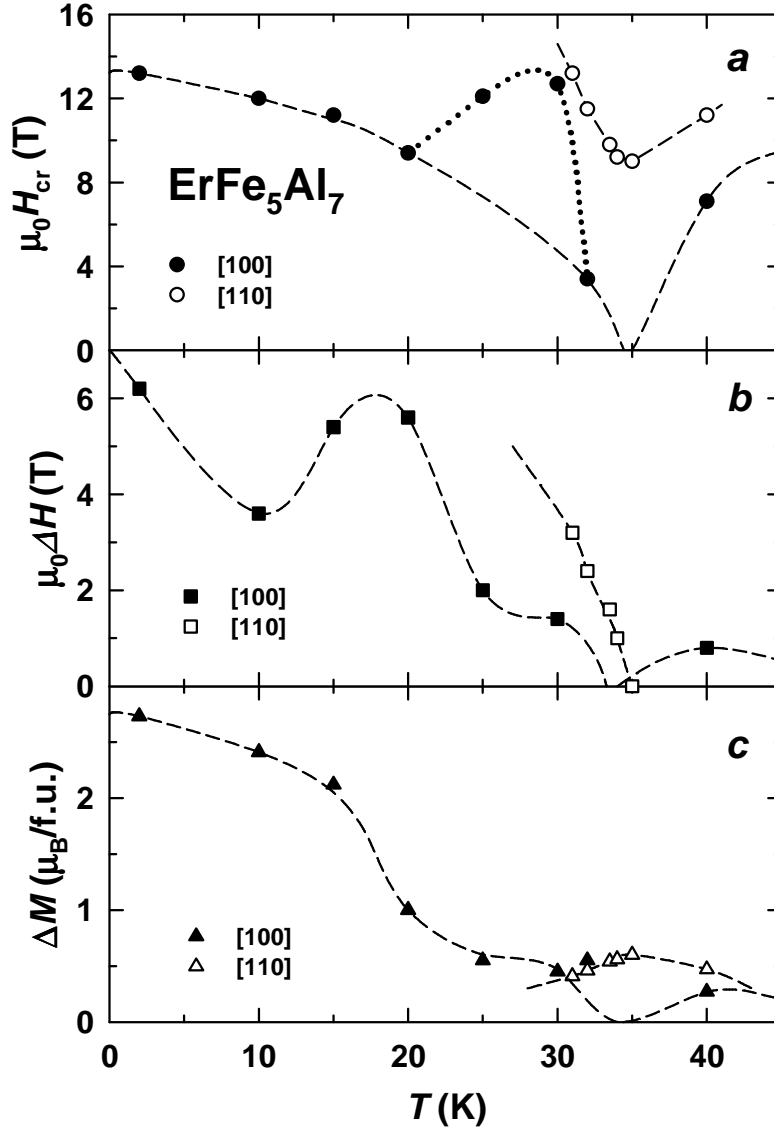


Fig. 5.74. Temperature dependence of the critical field H_{cr} (a), hysteresis ΔH (b) and magnetization jump ΔM (c) for the field-induced magnetic transitions along the [100] and [110] axes of the ErFe_5Al_7 single crystal.

$T = T_{\text{comp}}$. The transition at $T = 32$ K does not appear to be located in the anomalous region but rather follows the initial decrease of the transition field, which is accounted for by the $\mu_0 H_{cr,100}$ value as well as the transition shape. Except for the two points at $T = 25$ and 30 K, the transition field displays a monotonous decrease with temperature up to $T = T_{\text{comp}}$, where it passes through zero and then grows. At $T < T_{\text{comp}}$ this temperature dependence can be fitted to the following quadratic equation:

$$H_{cr,100} = H_{cr,0} \left(1 - \left(\frac{T}{T_{\text{comp}}} \right)^2 \right) \quad (5.20)$$

where $\mu_0 H_{cr,0} = 13.2$ T is the transition field at $T = 0$. The temperature dependence of the transition hysteresis ΔH_{100} is also complex (Fig. 5.74b). At first ΔH_{100} decreases

and then grows in the $T = 15 - 20$ K region where the transition shape changes (Fig. 5.72). Then ΔH_{100} drops to zero at $T = T_{\text{comp}}$ and increases. The magnetization jump ΔM_{100} at the transition (also determined from the ascending branches of the transitions) as a function of temperature is presented in Fig. 5.74c. ΔM_{100} gradually decreases with temperature from about $2.7 \mu_{\text{B}}/\text{f.u.}$ at $T = 2$ K with a somewhat higher rate in the range $T = 15 - 25$ K. Similarly to $H_{\text{cr},100}$ and ΔH_{100} , ΔM_{100} passes through zero $T = T_{\text{comp}}$.

Such a complicated behavior of the magnetic transition in ErFe_5Al_7 contrasts with those in DyFe_5Al_7 and HoFe_5Al_7 , also observed along the EMD (see Figs. 5.13 and 5.54). In the two latter compounds the transition field as well as the magnetization jump at the transition steadily diminish to zero upon approaching $T = T_{\text{comp}}$ from above and below. The magnetization jump in DyFe_5Al_7 and HoFe_5Al_7 is suggested to be a result of simultaneous rotation of the rare-earth and iron magnetic moments. In general, the observed field-induced magnetic transition in ErFe_5Al_7 can also be interpreted in the same way since all three characteristics – $H_{\text{cr},100}$, ΔH_{100} and ΔM_{100} – pass through zero $T = T_{\text{comp}}$. However, the temperature dependence of $H_{\text{cr},100}$ and ΔH_{100} displays sharp anomalies just below $T = T_{\text{comp}}$, which is different from the initial low-temperature behavior and from that at $T > T_{\text{comp}}$ (Fig. 5.74a,b). This implies that the transition undergoes significant changes with temperature. The rich diversity of the transition shapes (Fig. 5.72) supports this assumption.

It is interesting to note that, in contrast to TbFe_5Al_7 , DyFe_5Al_7 and HoFe_5Al_7 , the ErFe_5Al_7 compound displays a field-induced magnetic transition along a different direction. Figure 5.73 shows that a magnetization jump is observed along the [110] axis as well in ErFe_5Al_7 but in a very narrow temperature interval. At $T = 30$ K the magnetization is a featureless function of field up to 14 T. A jump is observed at $T = 31$ K with a broad hysteresis and a rather low magnetization gain $\Delta M_{110} = 0.4 \mu_{\text{B}}/\text{f.u.}$. The transition field $H_{\text{cr},110}$ rapidly decreases with temperature up to $T_{\text{comp}} = 34$ K but does not pass through zero, in contrast to $H_{\text{cr},100}$. At $T > T_{\text{comp}}$ $H_{\text{cr},110}$ grows. In the range $T = 31 - 34$ K the transition exhibits hysteresis that is not visible at higher temperatures. With increasing temperature the magnetization jump becomes more and more smeared out and finally disappears at $T > 40$ K, similarly to the transition along the [100] axis.

The temperature dependence of $H_{\text{cr},110}$ also shown in Fig. 5.74a is very sharp. In the narrow temperature range $T = 31 - 34$ K the transition field decreases from 13 to 9 T and then increases just as rapidly. It is reasonable to assume that the transition will be observed at $T < 31$ K as well but higher magnetic fields are required to verify this assumption. The transition hysteresis displays a rather simple behavior as a function of temperature gradually decreasing to zero at $T = 35$ K (Fig. 5.74b). The magnetization jump at the transition exhibits a maximum of $\Delta M_{110} = 0.6 \mu_{\text{B}}/\text{f.u.}$ in the vicinity of $T = T_{\text{comp}}$ (Fig. 5.74c).

The observed magnetization jump reflects a rotation of the magnetic moments towards the [110] axis since magnetic field is applied along the hard magnetization direction in the basal plane. Very low ΔM_{110} values are probably caused by

significant field-induced non-collinearity of the magnetic moments so that the direction of M_{Er} at $T < T_{\text{comp}}$ or of M_{Fe} at $T > T_{\text{comp}}$ is already rather close to the [110] axis. Moreover, such low ΔM_{110} values also suggest that M_{Er} and M_{Fe} turn simultaneously since either of them is several times higher than ΔM_{110} . The non-monotonous temperature dependence of the transition field displaying a minimum in the vicinity of $T = T_{\text{comp}}$ also confirms the notion of a transition in both magnetic sublattices.

ErFe_5Al_7 displays more complex behavior in an external magnetic field than TbFe_5Al_7 , DyFe_5Al_7 and HoFe_5Al_7 . In particular, the three latter compounds display field-induced transitions only along their EMD, whereas in ErFe_5Al_7 magnetization jumps are observed along the [100] and [110] axes. Moreover, a rather complicated temperature dependence of the transition characteristics was found along the [100] axis.

Below it is demonstrated that changes in the magnetic state at the observed magnetization jumps are accompanied by anomalies in the sound propagation. Figure 5.75a shows magnetization isotherms along the [100] axis for temperatures near the compensation point. The transition field decreases upon approaching T_{comp} and then grows again. At 45 K, a slope change of the magnetization without hysteresis can be identified at 12 T. As seen in Fig. 5.75b, the initially field-independent sound velocity at 2 and 32 K displays a step-wise growth at the same fields where the anomalies in the magnetization appear; as well similar hystereses are found. At 32 K, the hysteresis remains down to zero field. Upon passing through the compensation point, the shape of the acoustic anomaly changes: a deep minimum occurs that indicates a pronounced softening of the acoustic wave.

Field-induced magnetic transitions along the [110] axis cause variations in the spin-phonon coupling as well (Fig. 5.76). At 40 K, a magnetization anomaly is observed at 11 T (Fig. 5.76a). Concomitantly, the sound velocity decreases close to this transition (Fig. 5.76b). A different situation occurs at 45 K: the magnetization is a featureless function of field, whereas the sound velocity, being more sensitive, still displays a non-monotonous behavior. The marked acoustic anomalies at the field-induced magnetic transitions reflect the important role of magnetoelastic interactions in this compound.

Since additional phase transitions are expected to appear in higher magnetic fields, the magnetization and acoustic properties have been measured up to 60 T.

Figure 5.77 shows magnetization isotherms along the principal crystallographic directions of ErFe_5Al_7 at 2 K in pulsed magnetic fields up to 60 T. Along the easy [100] axis the magnetization displays two step-wise anomalies at 8 – 13 T and 38 – 39 T. The first transition was observed as well in static magnetic fields (see Figs. 5.67, 5.69 and 5.72), but the second magnetization jump is only accessible in high pulsed magnetic fields. Both anomalies display hysteresis representing first-order phase transitions. The magnetization jumps at the transitions are approximately equal to $2 \mu_{\text{B}}/\text{f.u.}$ The ferromagnetic saturation can be calculated as the sum of the magnetic moments of the Er and Fe sublattices: $M_{\text{ferro}} = M_{\text{Er}} + M_{\text{Fe}} = 9 + 7.7 = 16.7$

$\mu_B/\text{f.u.}$. Above the second transition the magnetization has almost reached ferromagnetic saturation that is approached around 50 T.

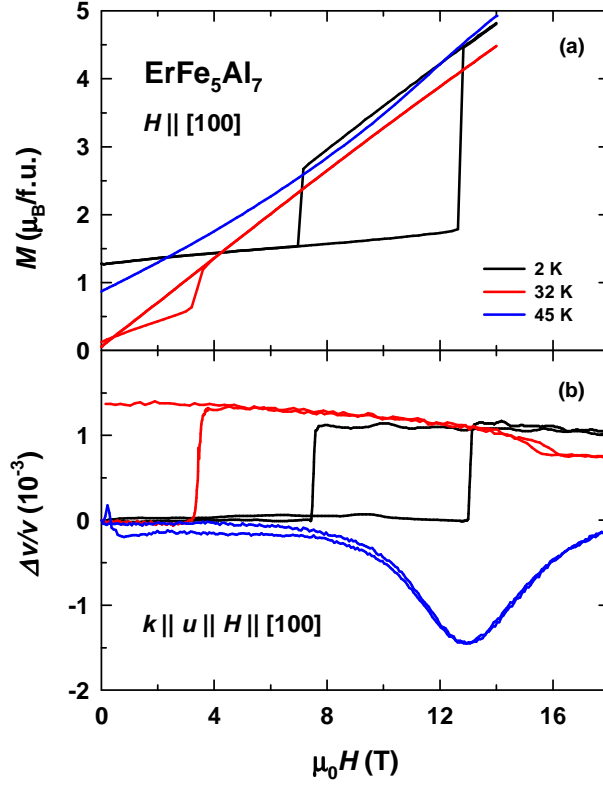


Fig. 5.75. Field dependence of (a) the magnetization and (b) of the relative sound-velocity change of ErFe_5Al_7 for field applied along [100] at 2 K and in the vicinity of $T_{\text{comp}} = 34$ K.

The magnetization for fields applied along the [110] axis increases monotonously up to $16 \mu_B/\text{f.u.}$ at 60 T, the highest available field. There appear no jumps for this field direction at 2 K. Magnetization jumps are observed only in a narrow temperature interval in the vicinity of $T = T_{\text{comp}}$ (see Fig. 5.73).

The magnetization along the hard [001] axis grows up to 50 T where the collinear ferromagnetic state is reached. Above 50 T, the magnetization along the [100] and [001] directions displays identical behavior, whereas the magnetization along the [110] axis is lower in this high-field region and still increases steadily up to 60 T. This may indicate that the anisotropy within the basal plane of ErFe_5Al_7 is stronger than between the basal plane and the [001] axis. However, apart from the anisotropy energy, during the magnetization process the $3d-4f$ inter-sublattice exchange energy and the Zeeman energy change substantially as well. For this reason, a more rigorous analysis is necessary in order to estimate the strength of the anisotropy with respect to the different crystallographic directions.

$M(H)$, $\Delta v/v(H)$, and $\Delta\alpha(H)$ measured at 20 K and 40 K in fields up to 60 T applied along the [100] axis are shown below and above the compensation point in Fig. 5.78. The lower-field transition, clearly resolved on the magnetization curve

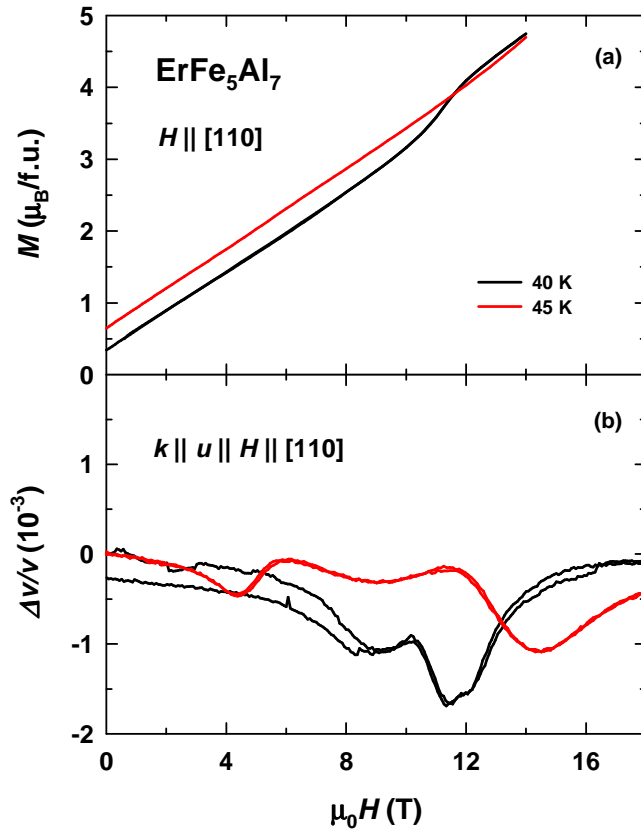


Fig. 5.76. Field dependence of (a) the magnetization and (b) the relative sound-velocity change of ErFe_5Al_7 for field applied along $[110]$ in the vicinity of $T_{\text{comp}} = 34$ K.

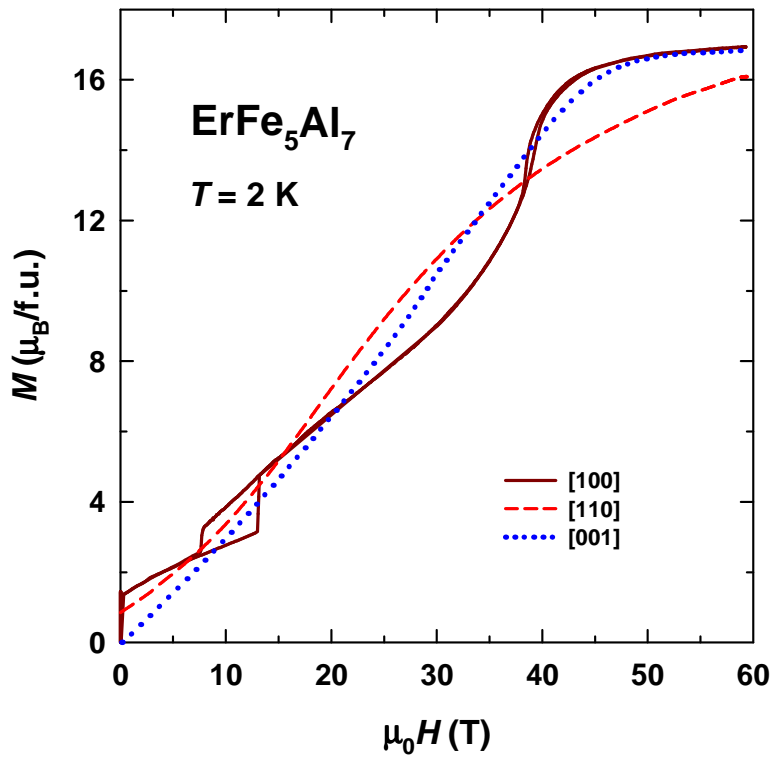


Fig. 5.77. Magnetization measured at 2 K in pulsed magnetic fields up to 60 T applied along the principal axes of ErFe_5Al_7 .

(Fig. 5.78a), results in a relatively weak anomaly in $\Delta v/v$ (this anomaly is seen better in decreasing field, Fig. 5.78c). At the higher-field transition, $\Delta v/v$ displays a pronounced softening with a broad minimum. In the sound attenuation weak anomalies related to both transitions appear slightly above the noise level at 20 K (Fig. 5.78e). With increasing temperature both magnetization jumps smear out. Just above $T = T_{\text{comp}}$, at 40 K, the lower-field anomaly is still visible, whereas the higher-field anomaly has disappeared (Fig. 5.78b). On the other hand, the sound velocity exhibits a strong softening at the lower-field transition (Fig. 5.78d), in contrast to the situation at $T < T_{\text{comp}}$. Changes in $\Delta\alpha$ appear as well at the lower-field transition (Fig. 5.78f).

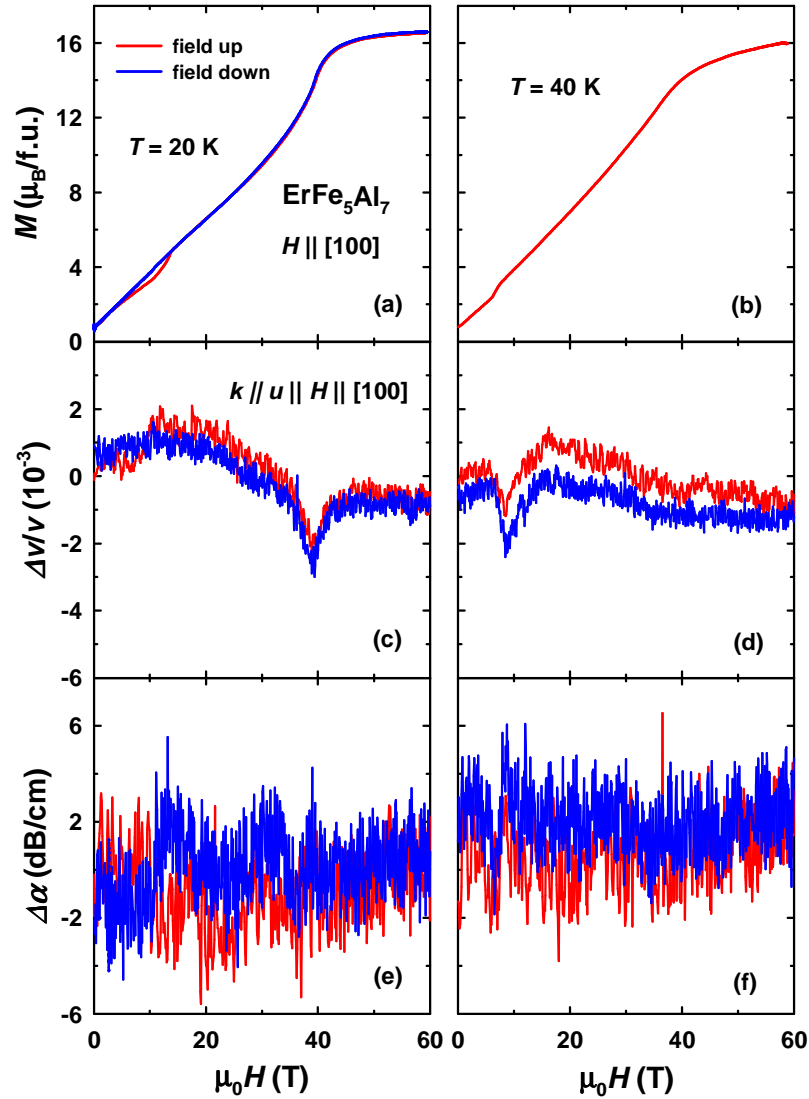


Fig. 5.78. (a, b) Magnetization, (c, d) relative sound-velocity change, and (e, f) sound attenuation measured at 20 and 40 K in pulsed magnetic fields applied along [100].

A similar effect was observed in the isostructural compound HoFe_5Al_7 (see Fig. 5.58). A magnetization jump along the easy [110] axis gradually weakens with increasing temperature. However, upon passing through the compensation point, $T_{\text{comp}} = 65$ K, a very weak anomaly in the field-dependent magnetization is

accompanied by a strong softening of the sound velocity, 4×10^{-3} , and a sharp peak in the sound attenuation of 7 dB/cm.

As shown above (Fig. 5.77), no magnetization jumps occur at 2 K for fields applied along the [110] axis in ErFe_5Al_7 . The same is true at 20 K, as evidenced by measurements of the magnetization and acoustic properties in pulsed fields up to 60 T (Fig. 5.79a, c and e). In static-field measurements up to 14 T, one magnetization jump was identified between 31 and 40 K (Fig. 5.73). In pulsed magnetic fields an additional weak non-hysteretic transition could be resolved in about 30 T at 40 K (Fig. 5.79b). Due to a strong spin-phonon coupling both anomalies in the magnetization at this temperature are accompanied by sharp minima in $\Delta v/v$ (Fig. 5.79d). In the sound attenuation sharp maxima appear at the transitions, reflecting a large energy dissipation (Fig. 5.79f). Although no hysteresis is observed in the magnetization at the higher-field transition, some differences occur in the acoustic

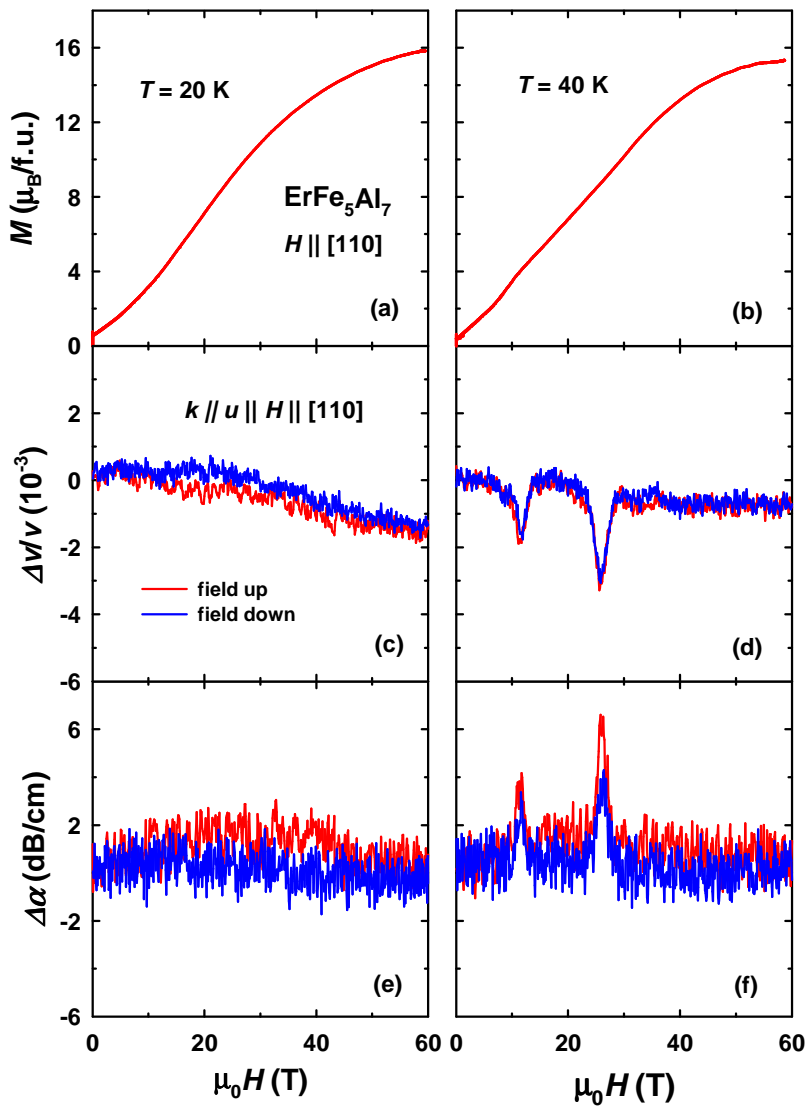


Fig. 5.79. (a, b) Magnetization, (c, d) relative sound-velocity change, and (e, f) sound attenuation measured at 20 and 40 K in pulsed magnetic fields applied along [110].

properties for up and down sweeps. Therefore, we may conclude that this transition is of first order.

In order to determine the critical field $H_{cr,2}^{110}$ of the higher-field transition, the maximum of the susceptibility, dM/dH , was taken. This maximum appears at a slightly higher field than the peaks in the acoustic properties. The transition is weak and broad in the magnetization, whereas it occurs as a sharp peak in the acoustic properties. For this reason, we used the latter anomalies to determine $H_{cr,2}^{110}$.

The magnetic T - H phase diagram of ErFe_5Al_7 for fields applied along the [100] and [110] axes is presented in Fig. 5.80. For $\mathbf{H} \parallel [100]$, two magnetization jumps are observed from the lowest temperatures up to around 40 K. The critical field, $H_{cr,1}^{100}$, of the lower-field transition displays a non-monotonous temperature dependence ($H_{cr,1}^{100}$ was determined only for rising fields). The initial decrease is followed by an increase at 25 and 30 K. This behavior was already presented in Fig. 5.74. Above 30 K, $H_{cr,1}^{100}$ reduces steeply approaching zero at $T_{\text{comp}} = 34$ K. For $T > T_{\text{comp}}$, $H_{cr,1}^{100}$ increases again. In striking contrast, $H_{cr,2}^{100}$ does not change with temperature. This phase diagram is similar to those for fields applied along the easy axes of TbFe_5Al_7 (Fig. 5.40), DyFe_5Al_7 (Fig. 5.19) and HoFe_5Al_7 (Fig. 5.59).

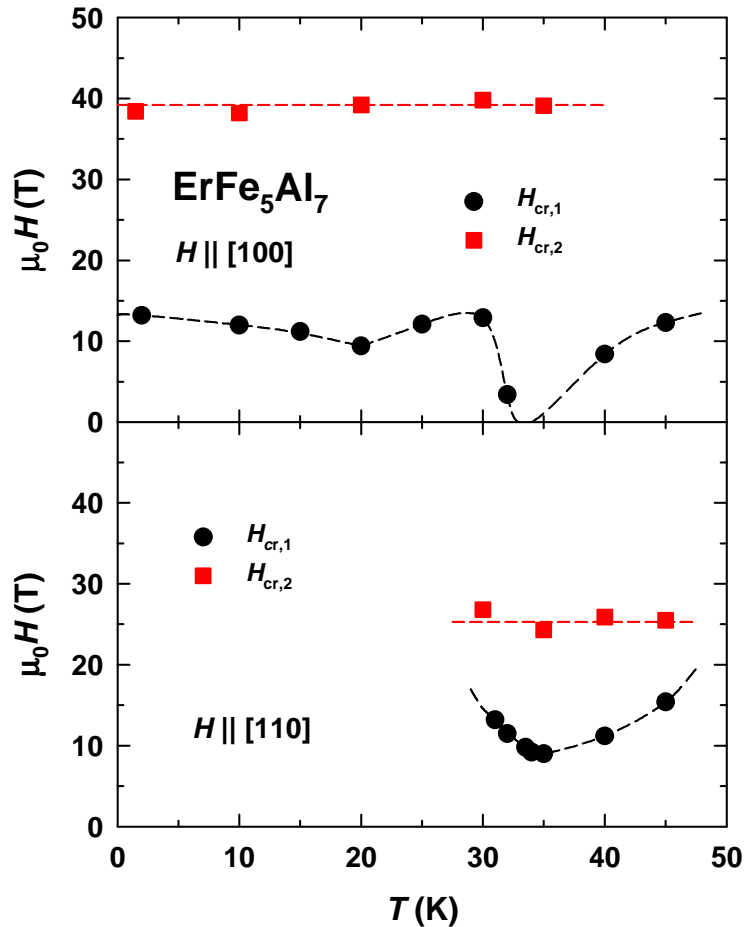


Fig. 5.80. T - H phase diagram for magnetic fields applied along the [100] and [110] axes of ErFe_5Al_7 .

The critical fields of ErFe_5Al_7 for fields applied along the [110] axis are observed only in a narrow temperature interval between 30 and 45 K. Both, $H_{cr,1}^{110}$ and $H_{cr,2}^{110}$ change with temperature in a similar manner as those for $\mathbf{H} \parallel [100]$. $H_{cr,1}^{110}$ passes through a minimum at the compensation point, whereas $H_{cr,2}^{110}$ is temperature independent.

For an interpretation of the field-induced magnetic phase transitions, again it should be noted that within the basal plane of the tetragonal crystal lattice of ErFe_5Al_7 there are two equivalent perpendicular easy magnetization directions, [100] and [010]. In low fields applied along the [100] axis, the response of the magnetic moments is rather weak since they are already aligned along the EMD. However, this situation changes with temperature. In particular, since at the compensation point the ferrimagnet behaves as an antiferromagnet, an energetically more favorable state is realized when the magnetic moments are perpendicular to the applied field. For this reason, the magnetic moments reorient from [100] to the perpendicular direction [010]. The higher the spontaneous magnetic moment, the higher is the field necessary to induce such a transition. With a further field increase, a collinear ferromagnetic state will be stabilized along the field direction. Under these circumstances, an additional reorientation appears from [010] back to the [100] axis. This second transition does not lead to full ferromagnetically aligned moments. As found in this work, after the higher-field anomaly the magnetization still continues to grow as a function of field.

Besides these general well-understood features, details of the magnetic phase diagram and magnetization process remain to be explained. Firstly, the shape of the anomaly at the lower-field transition changes significantly with temperature (Fig. 5.72). Secondly, an anomalous critical-field dependence is observed at 25 and 30 K (Figs. 5.74 and 5.80). For a better understanding of this behavior a microscopic technique, such as neutron diffraction or magnetic X-ray scattering is needed.

The two field-induced magnetic transitions for fields applied along the [110] axis in ErFe_5Al_7 are not observed at low temperatures. Their appearance near the compensation point can be explained by significant changes in the system's energy balance. In general, field-induced step-wise rotation of magnetic moments in ferrimagnets is controlled by the sum of inter-sublattice exchange interactions, the Zeeman energy, and magnetocrystalline anisotropy. A detailed analysis of the free energy for such ferrimagnetic materials was performed for DyFe_5Al_7 in this work. Near $T = T_{\text{comp}}$ the magnetocrystalline anisotropy plays the most important role [138]. At this point a significant increase of the coercivity along the [100] and [110] axes of the ErFe_5Al_7 single crystal appears as well (see Fig. 5.84 below).

The [110] axis is the magnetic hard direction in the basal plane. Therefore, the corresponding magnetization jumps reflect step-wise rotations of the magnetic moments from the easy [100] to the hard [110] axis.

In TbFe_5Al_7 , DyFe_5Al_7 and HoFe_5Al_7 the ferromagnetic saturation was not reached for any field direction up to 60 T (Figs. 5.17, 5.37 and 5.55), in contrast to

ErFe₅Al₇ studied in the present work. One of the reasons is the weaker 3*d*-4*f* exchange interaction since the spin of Er ($S = 3/2$) is lower than those of Tb ($S = 3$), Dy ($S = 5/2$) and Ho ($S = 2$). In order to verify this assumption, we calculate the inter-sublattice exchange parameter n_{ErFe} for ErFe₅Al₇ using molecular field theory and the model for a ferrimagnet with an anisotropic dominant sublattice (similarly to TbFe₅Al₇, DyFe₅Al₇ and HoFe₅Al₇). Figure 5.81 shows the temperature variation of the spontaneous magnetic moment, Fe magnetic moment, $M_{\text{Fe}}(T)$, and the resulting temperature dependence of the Er magnetic moment, $M_{\text{Er}}(T)$. The best fit of $M_{\text{Er}}(T)$ (red line) corresponds to $\mu_0 H_{\text{mol}} = 26$ T which can be re-calculated to $n_{\text{ErFe}} = 3.4$ T f.u./ μ_B .

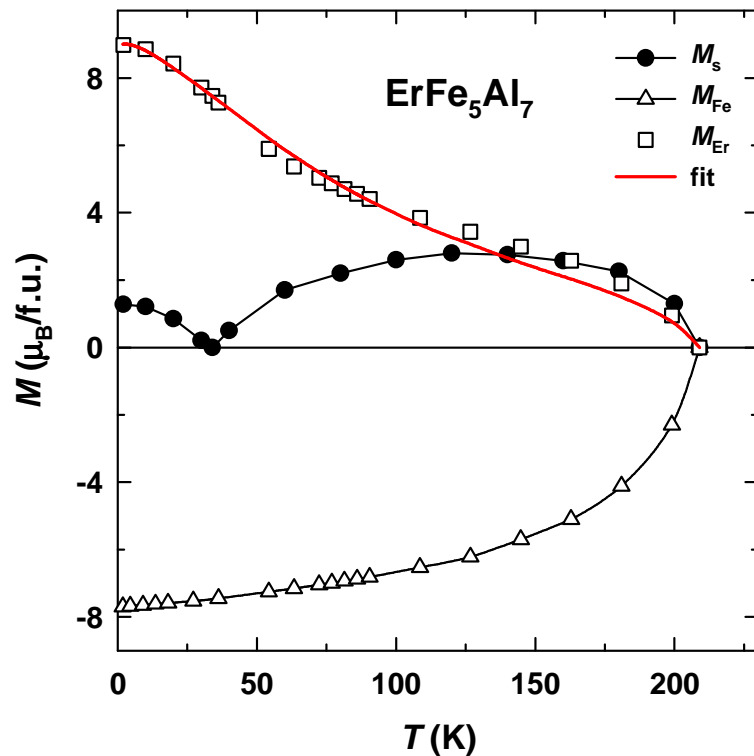


Fig. 5.81. Measured (closed circles) temperature dependence of the spontaneous magnetic moment along the easy magnetization direction together with the calculated temperature dependence of the magnetic moment of the Er and Fe sublattices. The Fe magnetic moment is assumed to be negative as it is antiparallel to the Er magnetic moment. The red line represents the fit according to the molecular-field theory.

Independently, n_{ErFe} can be determined by making use of the field-induced magnetic transition at lower fields applied along the EMD. However, since the transition has a broad hysteresis (Figs. 5.72 and 5.77), the determination of H_{mol} has some ambiguity. Taking $H_{\text{cr},1}^{100} = 13$ T, i.e., the magnetization jump at rising field, we arrive at $\mu_0 H_{\text{mol}} = 33$ T, a value too high in comparison with the result obtained within molecular-field theory. Moreover, such a high value is unreasonable when compared to $\mu_0 H_{\text{mol}} = 32$ T of HoFe₅Al₇. A better estimate can be obtained from the average field, 10 T, of the magnetization jumps at rising (13 T) and decreasing (7 T)

fields. In this case, $\mu_0 H_{\text{mol}} = 25$ T ($n_{\text{ErFe}} = 3.2$ T f.u./ μ_B) is in good agreement with $\mu_0 H_{\text{mol}} = 26$ T obtained within molecular-field theory.

For the inter-sublattice exchange parameter of ErFe_5Al_7 it is reasonable to use the average value of those found by the two first methods, i.e., $n_{\text{ErFe}} = 3.3$ T f.u./ μ_B . This value correlates well with those found within the $R\text{Fe}_5\text{Al}_7$ series: $n_{\text{GdFe}} = 8.3$ T f.u./ μ_B in GdFe_5Al_7 , $n_{\text{TbFe}} = 6.5$ T f.u./ μ_B in TbFe_5Al_7 , $n_{\text{DyFe}} = 5.3$ T f.u./ μ_B in DyFe_5Al_7 , and $n_{\text{HoFe}} = 4$ T f.u./ μ_B in HoFe_5Al_7 .

Figures 5.82 and 5.83 show hysteresis loops measured along the [100] and [110] axes, respectively, of the ErFe_5Al_7 single crystal. Good squaredness of the loops is observed along the [100] axis. The loops along the [110] axis have a slightly different shape as the magnetization grows more intensively in an applied magnetic field. In spite of the easy-plane anisotropy, the compound exhibits strong domain hysteresis with a very high coercive field H_c . Such high H_c values reflect a strong in-plane anisotropy in ErFe_5Al_7 . Along both axes the coercivity attains about $\mu_0 H_c = 2.5$ T at $T = 2$ K. Initially H_c rapidly falls off with temperature (Fig. 5.84). Such a steep decrease along with the high H_c values might be associated with narrow domain walls of a system with high magnetic anisotropy. Very similar $H_c(T)$ dependences at low temperatures were observed in TbFe_5Al_7 , DyFe_5Al_7 and HoFe_5Al_7 (Figs. 5.25, 5.45 and 5.65). The coercivity reaches about $\mu_0 H_c = 1$ T at $T = 20$ K and starts to grow. Upon approaching $T = T_{\text{comp}}$ both curves exhibit a discontinuity as the total magnetization comes close to zero (it is best seen from the hysteresis loop represented by a straight line at $T = 30$ K along the [100] axis, Fig. 5.82). Then H_c displays a steady decrease and becomes negligible at $T \geq 50$ K.

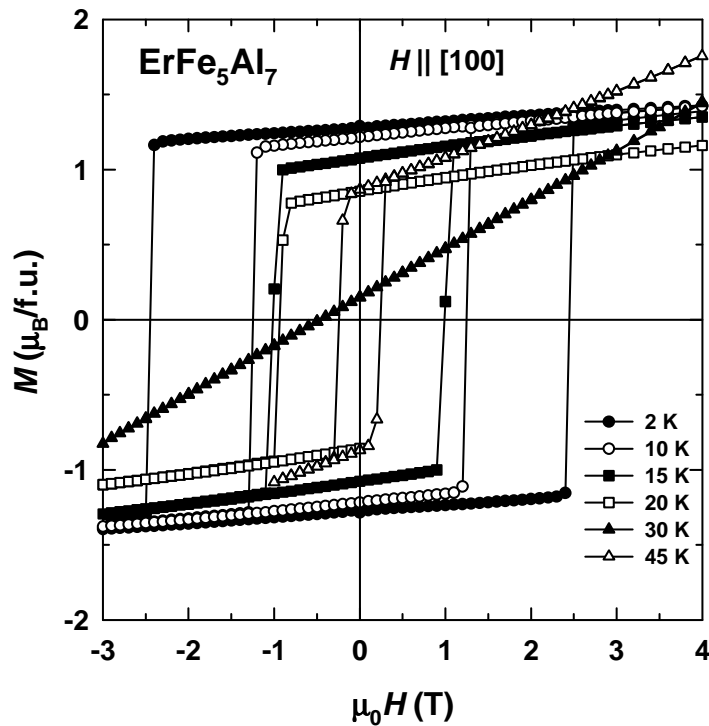


Fig. 5.82. Low-field details of hysteresis loops measured along the [100] axis of the ErFe_5Al_7 single crystal in the range $T = 2 - 45$ K.

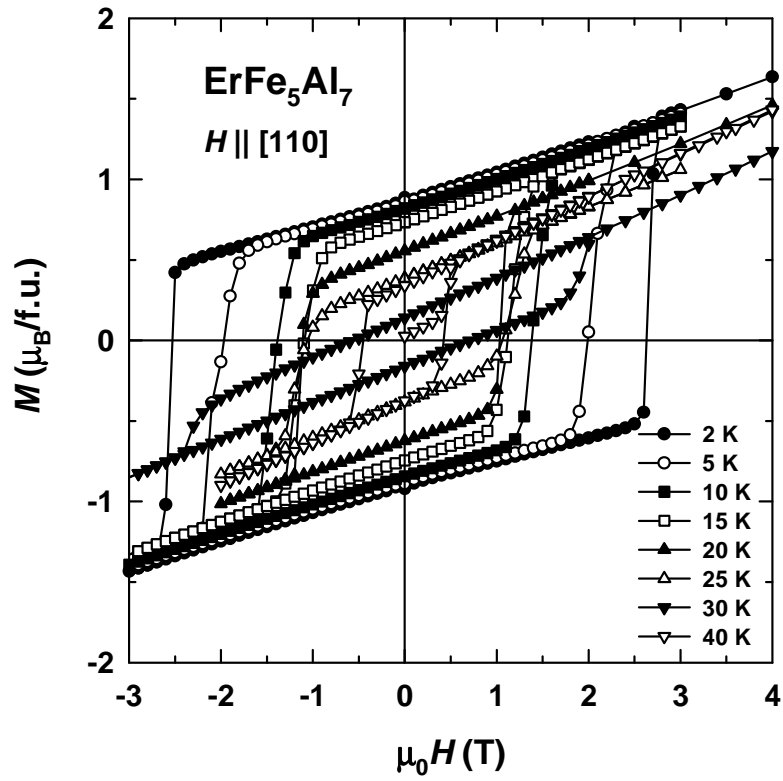


Fig. 5.83. Low-field details of hysteresis loops measured along the [110] axis of the ErFe_5Al_7 single crystal in the range $T = 2 - 40$ K.

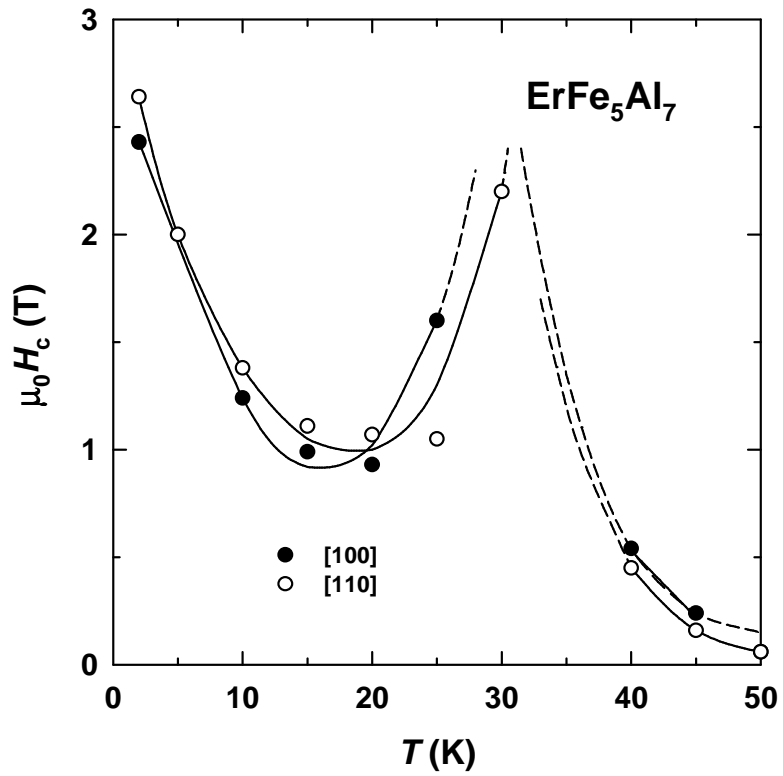


Fig. 5.84. Temperature dependence of the coercive field H_c along the [100] and [110] axes of the ErFe_5Al_7 single crystal.

Apart from the field hysteresis, ErFe_5Al_7 also displays thermal hysteresis (Fig. 5.85), just as was observed on TbFe_5Al_7 , DyFe_5Al_7 and HoFe_5Al_7 single crystals (Figs. 5.26, 5.46 and 5.66). Initially, the sample was cooled down to $T = 2$ K in a field of 14 T. Then the magnetization of the crystal in the single-domain state was measured in 0.1 T along the [100] and [110] axes upon heating followed by subsequent cooling back to $T = 2$ K. Since a field of 0.1 T is lower than the coercive field at $T = T_{\text{comp}}$, the domain structure of the sample does not change at this temperature. In this situation, the re-orientation of the total magnetic moment of ErFe_5Al_7 from the Er to the Fe sublattice upon heating leads to the appearance of “negative magnetization”, i.e., the antiparallel orientation of the sample’s total magnetization and the external magnetic field. However, H_c rapidly decreases with temperature above $T = T_{\text{comp}}$, and M soon turns positive when an external field of 0.1 T exceeds H_c . Upon cooling, the “negative magnetization” effect is seen at all temperatures below $T = T_{\text{comp}}$ since the coercivity exceeds the external applied field.

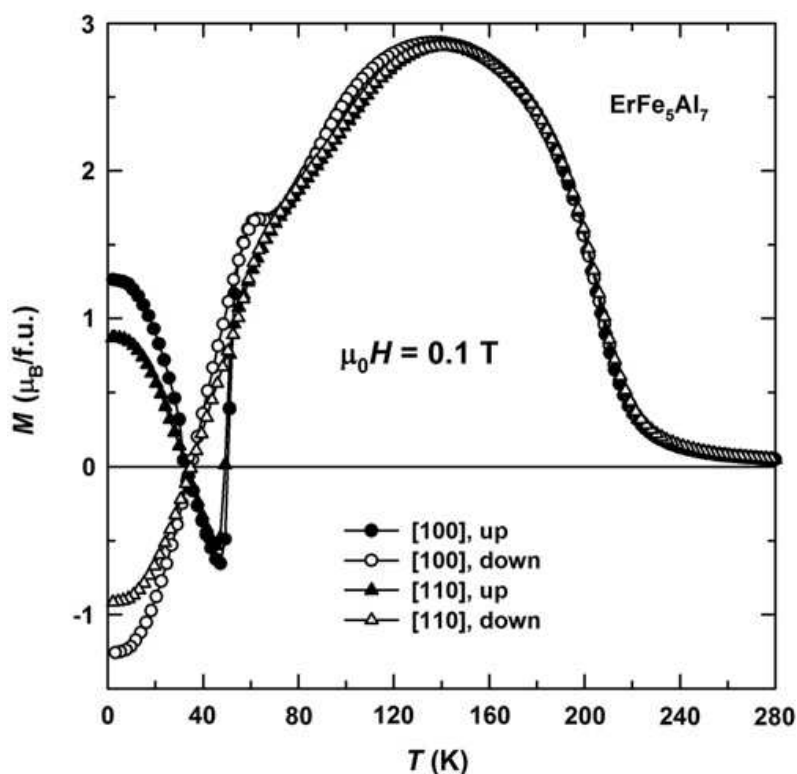


Fig. 5.85. Temperature dependence of the magnetization measured in a field of 0.1 T applied along the [100] and [110] axes of the ErFe_5Al_7 single crystal. First, the sample was cooled down to $T = 2$ K in a field of 14 T. Then, the magnetization was measured in 0.1 T upon heating the sample up to $T = 280$ K and subsequent cooling to $T = 2$ K.

The obtained temperature dependences of the magnetization are different from those of the spontaneous magnetic moment (Fig. 5.68). It can be explained by a relatively low external magnetic field used for the $M(T)$ measurements that could not overcome the sample’s coercive field at $T < T_{\text{comp}}$. On the contrary, the determination of the M_s values requires application of a rather high magnetic field to obtain the

sample in the single-domain state, which is followed by decreasing the field to zero. Apart from the above-mentioned features, a small shoulder is observed in the $M(T)$ dependence along the easy [100] axis around $T = 60$ K. The origin of this feature is not yet clear. The results shown above do not suggest any transition at $T = 60$ K associated with the magnetization along the [100] axis in ErFe_5Al_7 . In order to clarify the nature of this anomaly, a different study seems to be necessary (e.g., neutron diffraction).

5.7. TmFe₅Al₇

All the $R\text{Fe}_5\text{Al}_7$ compounds studied up to now display an easy-plane magnetic anisotropy. It was found that the crystal-field-induced anisotropy of the rare-earth sublattice is not modified as the sign of the second-order Stevens factor α_J of the R^{3+} ion changes ($\alpha_J < 0$ for Tb, Dy, and Ho, but $\alpha_J > 0$ for Er [35]). The apparent controversy for ErFe_5Al_7 was explained by a small α_J value for Er, as a result of which the dominant negative contribution to the anisotropy of the Er sublattice is given by its higher-order terms (fourth- and sixth-order terms).

A way to change the magnetic anisotropy of the rare-earth sublattice in $R\text{Fe}_5\text{Al}_7$ is to use Tm as rare-earth component. For Tm^{3+} , the second-order Stevens factor, $\alpha_J = 0.01$, is positive and much larger than for Er^{3+} , $\alpha_J = 0.00254$ [35]. For this reason, the single-ion magnetocrystalline anisotropy of the Tm sublattice is expected to be uniaxial. The compound should display an easy-axis anisotropy (preferable moment orientation is along the tetragonal axis) at low temperatures where the relative Tm contribution is strongest. A competition between the uniaxial Tm and multiaxial Fe magnetic anisotropies should occur, which may lead to a spontaneous spin-reorientation transition at elevated temperatures.

The magnetic anisotropy also plays an important role in determining the behavior of ferrimagnetically ordered compounds in a magnetic field. Similarly to the $R\text{Fe}_5\text{Al}_7$ compounds with R - Tb, Dy, Ho, and Er, field-induced magnetic transitions are likely to occur in TmFe_5Al_7 in an applied magnetic field because it is also ferrimagnetic. In this sense, TmFe_5Al_7 is a particularly interesting system since its easy magnetization direction is expected to be out of the basal plane leading to a different magnetic symmetry, and, therefore, different field-induced rotations of the magnetic moments. Below the last representative of the $R\text{Fe}_5\text{Al}_7$ family, TmFe_5Al_7 , is studied.

Figure 5.86 shows the magnetization measured at 2 and 120 K for fields up to 8 T applied along the [100] and [001] axes of TmFe_5Al_7 . At $T = 2$ K, the easy magnetization direction (EMD) is along the c axis with a spontaneous magnetic moment of $M_s = 0.5 \mu_B/\text{f.u.}$ In the whole temperature range of the magnetically ordered state the total magnetization is dominated by the Fe sublattice (see Fig. 5.87 below). Assuming that at 2 K the Tm magnetic moment is equal to that of a free Tm^{3+} ion, $7 \mu_B$, and that the compound is a collinear ferrimagnet, the magnetic moment of the Fe sublattice can be calculated as follows: $M_{\text{Fe}} = M_s + M_{\text{Tm}} = 7.5 \mu_B/\text{f.u.}$ This corresponds to $1.5 \mu_B$ per Fe atom, a typical value for $R\text{Fe}_5\text{Al}_7$ compounds. Magnetization curves were also measured for fields applied along the [110] axis showing no difference to the data for $\mathbf{H} \parallel [100]$. This reflects a negligible anisotropy within the basal plane at all temperatures, whereas this anisotropy is large in other $R\text{Fe}_5\text{Al}_7$ compounds with magnetic R . Figure 5.86 also shows that at 120 K the EMD is along the [100] axis, in contrast to the situation at 2 K. Therefore, a spin-reorientation transition occurs in TmFe_5Al_7 from the [001] axis to the (001) plane with increasing temperature.

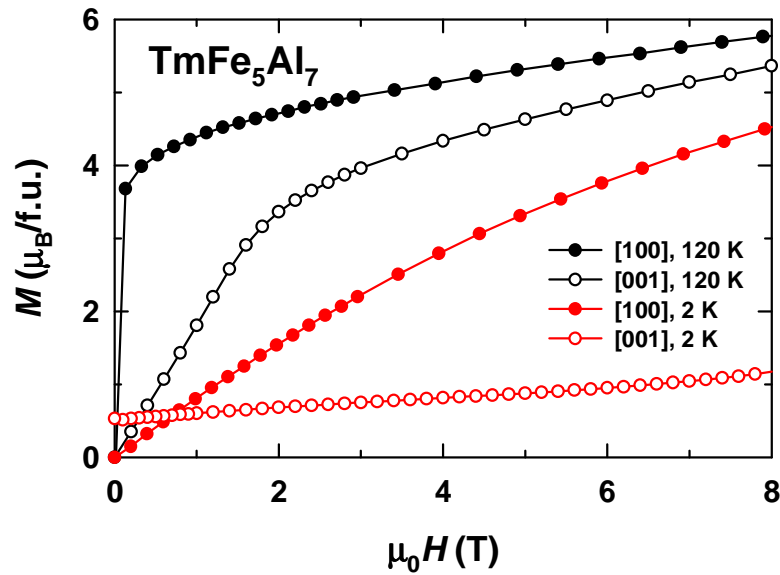


Fig. 5.86. Magnetization curves along the [100] and [001] axes of TmFe_5Al_7 at 2 and 120 K.

Figure 5.87 shows the temperature dependence of the magnetization for a field of 0.1 T applied along the [100] and [001] axes of TmFe_5Al_7 . Growing from low temperatures, the magnetization for $H \parallel c$ (the EMD) shows a pronounced maximum at about 60 K, then at about 70 K the magnetization reduces drastically and the spin-reorientation transition occurs. With increasing temperature the magnetization falls off in the vicinity of 200 K as the compound becomes paramagnetic.

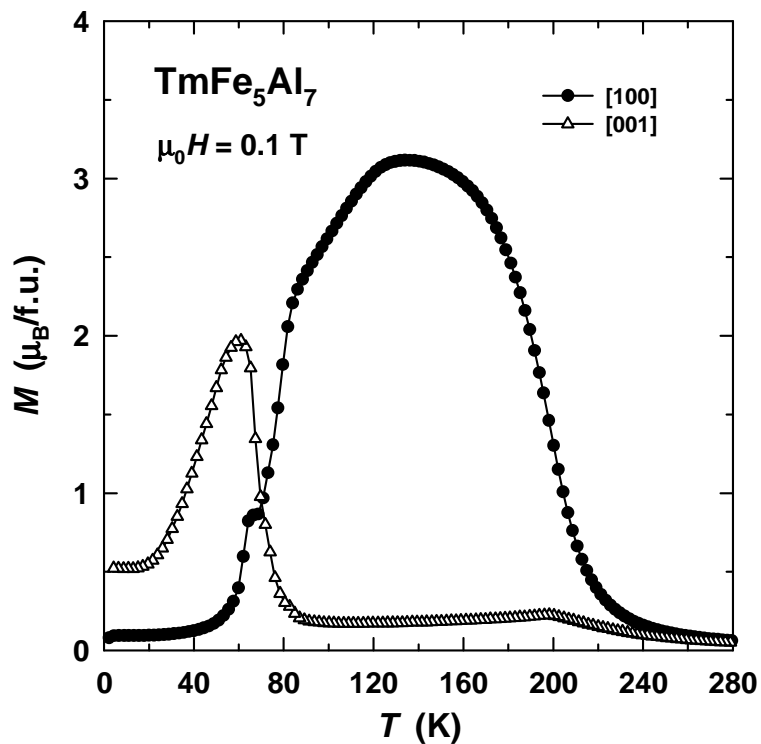


Fig. 5.87. Temperature dependence of the magnetization for a field of 0.1 T applied along the [100] and [001] axes.

In the specific heat two anomalies at 63 and 72 K appear as shown in Fig. 5.88a. In the sound velocity of a longitudinal acoustic mode as well an anomaly appears around 63 K (Fig. 5.88b). In addition, a weak feature is seen in $\Delta v/v$ at 193 K (shown by arrow) that is related to the phase transition into the paramagnetic state.

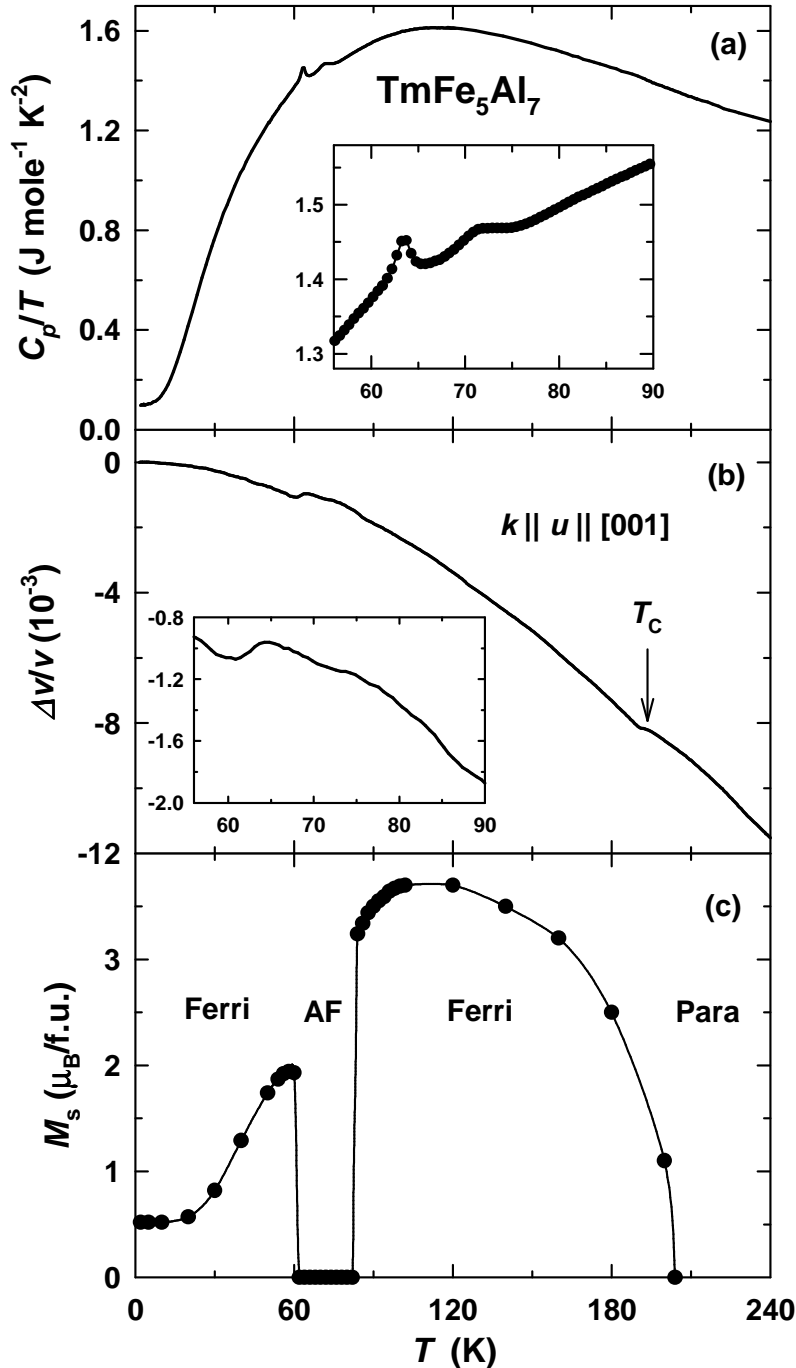


Fig. 5.88. Temperature dependence of (a) the specific heat plotted as C_p/T , (b) the relative sound-velocity change, $\Delta v/v$, of a longitudinal acoustic wave propagating along the [001] axis, and (c) the spontaneous magnetic moment, M_s , of TmFe_5Al_7 . The insets in the upper and middle panels show C_p/T and $\Delta v/v$, respectively, in the vicinity of the spin-reorientation transition. The ferrimagnetic state is denoted by Ferri, antiferromagnetic by AF and paramagnetic by Para.

However, the spontaneous magnetic moment drops to zero only slightly above 200 K (Fig. 5.88c). A small applied magnetic field induces a small moment even above T_C , and a standard Arrott-plot treatment does not provide a proper T_C value. For this reason, T_C can be determined accurately only in zero field. In the specific heat no feature can be resolved in the vicinity of 200 K, which means that the ferrimagnetic phase transition results in a rather small entropy change. In order to elucidate the origin of the anomalies in C_p/T and $\Delta v/v$ around 60 - 70 K, we analyzed the magnetization curves within this temperature interval.

For fields applied along the hard [100] axis, S-shape magnetization curves are found in the temperature range between 50 and 62 K (Fig. 5.89). The observed field-induced magnetic transition is a first-order magnetization process (FOMP). This is a so called type-II FOMP since the magnetization immediately after the transition does not reach the easy-axis value but continues to grow. The FOMP is observed in the temperature range between 40 and 62 K. Below 40 K no magnetization jump is seen along the hard [100] axis in the field range where the FOMP is likely to occur (a magnetization jump is observed at a much higher field ≈ 37 T, however, that has a different origin, see below). This is unexpected since with decreasing temperature the field-induced transition should not disappear but rather become more pronounced. The FOMP is of anisotropic nature, therefore, the observed changes reflect a rather intricate balance between anisotropy constants involved in the process. The FOMP critical field determined as the average field between the ascending and descending branches decreases monotonously with temperature (inset in Fig. 5.89). One would

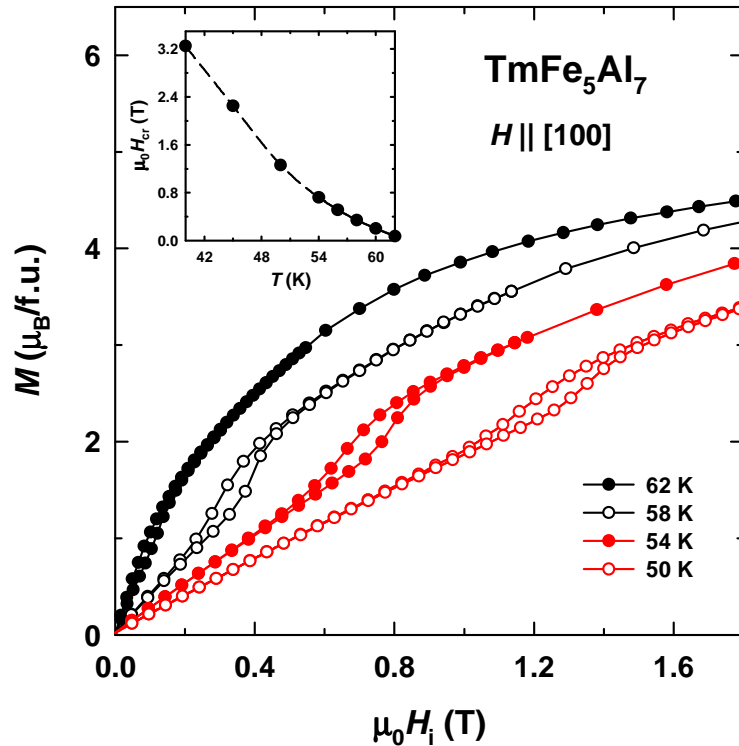


Fig. 5.89. Magnetization as a function of field applied along the [100] axis of TmFe₅Al₇ between 50 and 62 K. The inset shows the temperature dependence of the FOMP critical field.

assume that as soon as the FOMP disappears, that is, when its critical field reaches zero, a spontaneous magnetic moment should appear for $\mathbf{H} \parallel [100]$ axis (just above 62 K). However, this is not observed in experiment.

At 64 K, TmFe_5Al_7 displays no spontaneous magnetic moment for fields applied along the [100] and [001] axes (Fig. 5.90). At low fields the magnetization is still larger for $\mathbf{H} \parallel [001]$. At 66 K, the compound is practically isotropic in the low-field region. With increasing temperature, the slope of the magnetization curve for $\mathbf{H} \parallel [100]$ becomes gradually more vertical. Nevertheless, no spontaneous magnetic moment is observed up to 82 K.

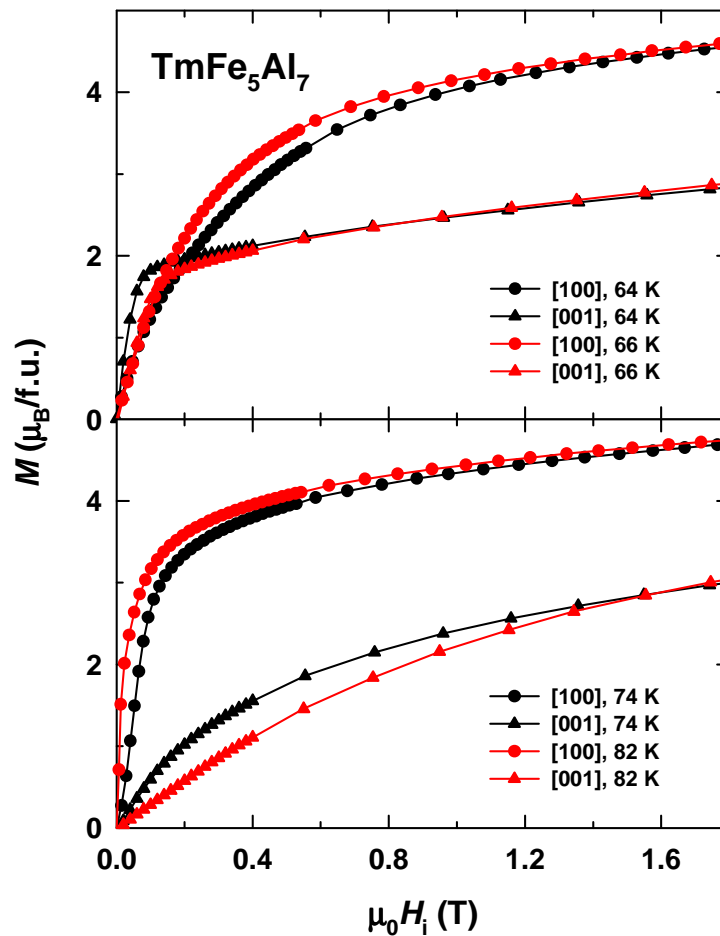


Fig. 5.90. Magnetization as a function of field applied along the [100] and [001] axes of TmFe_5Al_7 between 64 and 82 K.

Low-field details of the magnetization for $\mathbf{H} \parallel [100]$ between 70 and 86 K are shown in Fig. 5.91. Below 74 K, the magnetization is a featureless function of field. At 74 K, a hysteretic magnetization jump develops. This is obviously not a domain hysteresis, the sample's coercivity is very small. With increasing temperature, the jump and its hysteresis become more pronounced. At 86 K, the jump disappears and a spontaneous magnetic moment appears. Moreover, a typical hysteresis caused by ferrimagnetic domains is observed. Above 82 K, a non-zero spontaneous magnetic moment exists along the easy [100] axis with increasing temperature.

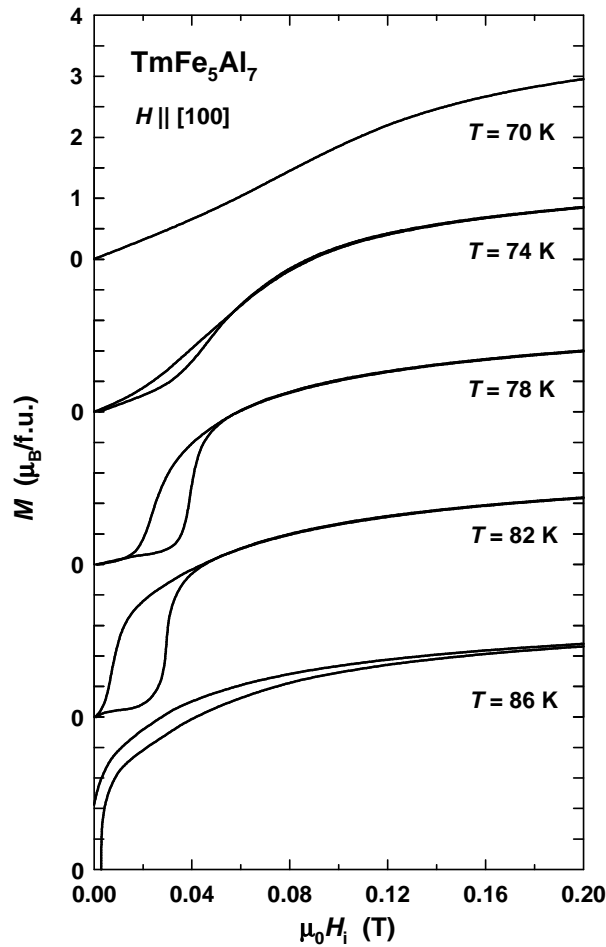


Fig. 5.91. Low-field details of the magnetization for fields applied along [100] between 70 and 86 K.

The temperature dependence of the spontaneous magnetic moment, M_s , of TmFe_5Al_7 in the whole magnetically ordered state is shown in Fig. 5.88c. M_s follows the temperature dependence of the magnetization for $\mathbf{H} \parallel [001]$ below 64 K and for $\mathbf{H} \parallel [100]$ above 82 K. Between 64 and 82 K the spontaneous magnetic moment is zero along both, the [100] and [001], axes.

On the basis of the results presented, the following interpretation of the magnetic behavior of TmFe_5Al_7 is proposed. In accordance with the specific heat and sound-velocity measurements, a phase transition occurs at 64 K when the magnetic moments rotate from the c axis to the basal plane. This is likely a first-order transition since no intermediate easy cone phase was observed. Simultaneously, the spontaneous magnetic moment disappears, with M_s being zero up to 82 K. The absence of a spontaneous magnetic moment can be related either to a paramagnetic or an antiferromagnetic state. The former is not possible since between 82 K and T_C a spontaneous magnetic moment exists, and the compound displays a usual ferrimagnetic behavior. Therefore, the absence of a spontaneous magnetic moment in TmFe_5Al_7 between 64 and 82 K is related to an antiferromagnetic spin arrangement. Around 84 K, the antiferromagnetic structure changes back to ferrimagnetic. In our opinion, the antiferromagnetic-ferrimagnetic phase transition is also of first order

since it occurs when the hysteretic field-induced magnetization jump in the antiferromagnetic state comes to zero field (see Fig. 5.91). Such a set of unusual magnetic transitions may be due to a relatively weak exchange interaction between the Tm and Fe sublattices.

An estimate of the inter-sublattice exchange constant, n_{TmFe} , in TmFe_5Al_7 can be made using molecular field theory. The temperature dependence of the Tm magnetic moment, $M_{\text{Tm}}(T)$, obtained experimentally was fitted by the Brillouin function, B_J , using the molecular field H_{mol} created by the Fe sublattice on Tm:

$$M_{\text{Tm}}(T) = M_{\text{Tm}}(0)B_J\left(\frac{gJJ\mu_B\mu_0H_{\text{mol}}}{k_B T}\right), \quad (5.21)$$

where J and g are the quantum number of the total Tm moment and the Landé factor, respectively (Eq. (5.21) is identical to Eq. (5.3)). Unfortunately, the agreement between the experimental and fitting curves is very poor for a wide range of μ_0H_{mol} values. The reason might be a large error in the estimated $M_{\text{Fe}}(T)$. Moreover, between 64 and 82 K the spontaneous magnetic moment of TmFe_5Al_7 is zero, and the Tm magnetic moment cannot be determined by magnetization measurements. Interestingly, the temperature dependence of the rare-earth magnetic moment can be determined rather precisely using molecular field theory for the isostructural compounds with R - Tb, Dy, Ho, and Er. TmFe_5Al_7 presents a more complicated case. A more thorough approach is necessary in order to calculate H_{mol} , e.g., the needed information on the crystal electric field could be obtained by inelastic neutron scattering.

The molecular field H_{mol} was found to vary linearly with spin, S , of the rare-earth component in the $R\text{Fe}_5\text{Al}_7$ series (Fig. 5.92). Therefore, in order to estimate H_{mol} in TmFe_5Al_7 , a linear extrapolation was made to $S = 1$ as relevant for R - Tm. The obtained value is $\mu_0H_{\text{mol}} = 16$ T (at 2 K), which corresponds to $n_{\text{TmFe}} = 2.1$ T f.u./ μ_B . Using this value of the molecular field, an approximate temperature dependence of the Tm magnetic moment was calculated using Eq. (5.21). Due to the relatively weak Tm-Fe exchange interaction, M_{Tm} decreases much more rapidly at low temperatures than the magnetic moment of the Dy sublattice in isostructural DyFe_5Al_7 (inset in Fig. 5.92). Under these circumstances, the magnetic moment of the Fe sublattice should also decrease more rapidly than, e.g., M_{Fe} of $R\text{Fe}_5\text{Al}_7$ with other magnetic heavy rare-earth elements and of LuFe_6Al_6 [15].

A change of the magnetic ordering within the Fe sublattice is likely to be the driving force behind the ferrimagnetic-antiferromagnetic transition in TmFe_5Al_7 . In the crystal structure of $R\text{Fe}_5\text{Al}_7$, the R atoms are located within the planes filled by Fe and Al atoms ($8j$ site) (see Fig. 2.1). Just above and just below them at equal distances there are planes of the $8f$ sites occupied exclusively by Fe atoms. Competitive exchange interactions were found for $\text{LuFe}_x\text{Al}_{12-x}$ compounds with non-magnetic Lu (see Chapter 4). It is reasonable to assume that within the Fe sublattice there are two types of Fe-Fe exchange interactions. Within the upper and lower planes of the $8f$ site a ferromagnetic exchange interaction is stabilized. There is also

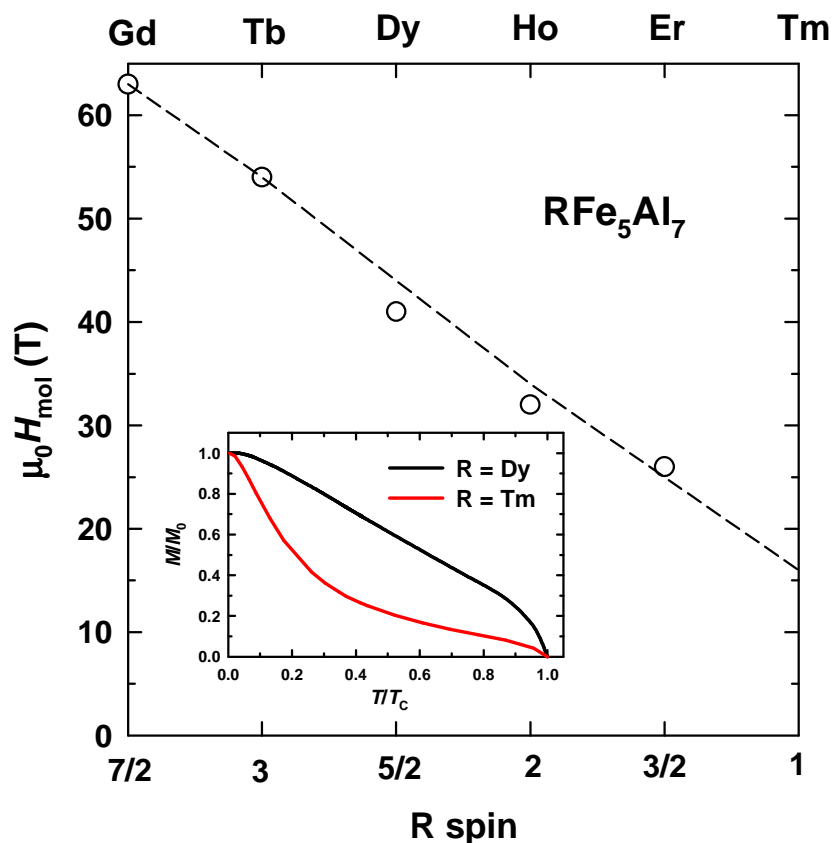


Fig. 5.92. Dependence of the molecular field produced by the Fe sublattice on the rare-earth spin in $R\text{Fe}_5\text{Al}_7$ with R - Gd, Tb, Dy, Ho, and Er. The inset shows the temperature dependence of the specific magnetization of the Dy and Tm sublattices in $R\text{Fe}_5\text{Al}_7$.

an inter-planar Fe-Fe exchange interaction which proceeds through the Fe atoms located in the planes filled by Fe and Al atoms. The sign and strength of the inter-planar interaction depends on the Fe content. In the absence of a magnetic rare-earth component, with increasing temperature the transition from antiferromagnetic to ferromagnetic order appears in LuFe_5Al_7 around $T_0 = 80$ K (see Chapter 4). Therefore, the free energies of the ferromagnetic, E_F , and antiferromagnetic, E_{AF} , phases in LuFe_5Al_7 become equal at T_0 as schematically shown in Fig. 5.93a.

When R is a magnetic heavy rare-earth component, the negative R -Fe exchange interaction is stabilized that strengthens the indirect positive Fe- R -Fe inter-planar exchange interaction whose energy is roughly proportional to the average R magnetic moment (inset in Fig. 5.92). When the R -Fe exchange interaction is strong as in, e.g., DyFe_5Al_7 , the ferromagnetic phase is stable within the Fe sublattice in the whole temperature range of the magnetically ordered state (Fig. 5.93b). When the R -Fe exchange interaction is weak, the ferromagnetic phase can only be stabilized at sufficiently low temperatures $T < T_1$. In the temperature range $T_1 < T < T_2$ the negative inter-planar Fe-Fe exchange interaction results in the formation of an antiferromagnetic order. Finally, at T_2 , slightly lower than T_0 (due to the influence of a negative R -Fe interaction leading to a small positive Fe- R -Fe indirect interaction), the ferromagnetic state is again stabilized (Fig. 5.93c).

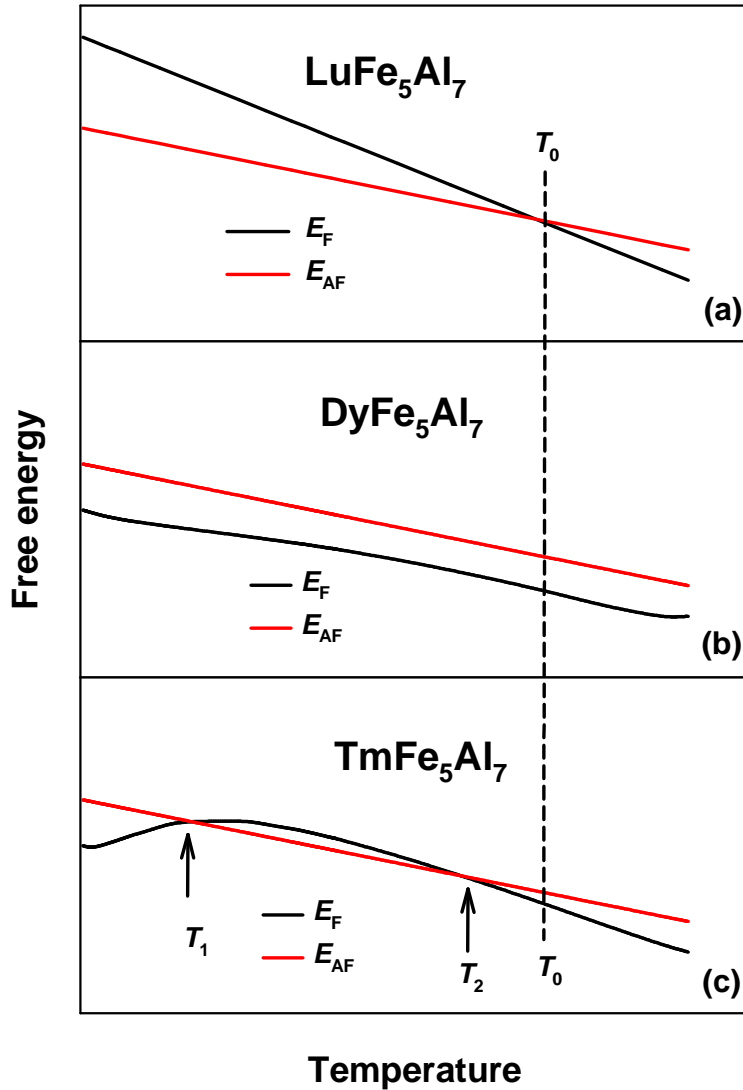


Fig. 5.93. Schematic temperature dependence of the free energy of the ferromagnetic (F) and antiferromagnetic (AF) phases within the Fe sublattice of RFe_5Al_7 with R - Lu (a), Dy (b), and Tm (c).

The spin-reorientation transition in $TmFe_5Al_7$ favors the disappearance of the spontaneous magnetic moment in a limited temperature range. Indeed, the spin reorientation is a result of the competition between the Tm and Fe anisotropies. Due to the weak Tm-Fe exchange interaction, this leads to the formation of a non-collinear magnetic structure in the vicinity of the transition: the Tm moment still sticks to the [001] axis, while the Fe moment tends towards the basal plane. Furthermore, the absolute value of the R moment decreases due to its rotation towards the hard magnetization direction. This effect was observed by use of neutron diffraction in RCO_5 compounds at the spin-reorientation transitions [140]. The non-collinearity and reduced absolute value of the Tm magnetic moment weaken the Tm-Fe exchange interaction and facilitate the formation of the antiferromagnetic structure of the Fe magnetic moments within the basal plane.

Using this model, the unusual shape of the magnetization curves between 74 and 82 K can be explained (Fig. 5.91). The application of a magnetic field along the

[100] axis induces a metamagnetic antiferromagnetic-ferromagnetic transition within the Fe sublattice. The Tm-Fe exchange interaction is strengthened, and the ferrimagnetic order in TmFe_5Al_7 is favored.

The magnetic properties of RMn_6Sn_6 , with R - Er and Tm, with hexagonal crystal structure of the HfFe_6Ge_6 type [141], show some similarities to those of TmFe_5Al_7 . Independent magnetic ordering of the rare-earth and manganese sublattices was found (both the R and Mn sublattices display antiferromagnetic order). The Er and Tm moments vanish at 65 and 40 K, respectively, whereas the Mn moment survives up to about 350 K. Above the magnetic ordering temperatures of the rare-earth sublattices a magnetic field of several Tesla induces a metamagnetic transition along the a and c axes. This reflects the transformation of the antiferromagnetic exchange interactions within the Mn sublattice to ferromagnetic order and, at the same time, the appearance of a ferromagnetic order within the Er and Tm sublattices (since these are heavy rare-earth elements, their magnetic moments are antiparallel to those of Mn, and the compounds become ferrimagnetic in an applied magnetic field). Thus, the Er and Tm magnetic moments order due to strong antiferromagnetic coupling to the ferromagnetically ordered Mn sublattice. The disappearance of the magnetic order within the Er and Tm sublattices at low temperatures probably occurs due to competitive Er-Mn (Tm-Mn) exchange interactions that cause a frustration of the Er (Tm) magnetic moment.

TmFe_5Al_7 displays a field-induced magnetic transition for fields applied along the easy [001] direction at low temperatures as indicated by magnetization measurements up to 14 T (upper panel in Fig. 5.94). A magnetization jump is observed at 2 K with a complicated fine structure. The transition exhibits hysteresis and is of first order. A field of 14 T is not sufficiently high to register the full transition at this temperature. Up to this field, the compound is in a metastable state. This explains why at 11 T with decreasing field the magnetization drops below the values obtained with increasing field. At 5 and 10 K the magnetization jump displays a smaller hysteresis, and a complete transition is seen in spite of the increasing critical field, H_{cr} . At $T = 20$ K, no transition is observed in the magnetization, although the positive curvature implies that a transition might exist above 14 T.

The change in the magnetic state at the magnetization jump modifies the electron-phonon coupling, which results in pronounced anomalies in acoustic properties. The relative change of the sound velocity measured up to 18 T at 2 K demonstrates a broad hysteresis at the transition that extends from 10 to 15 T (lower panel in Fig. 5.94). The transition at 20 K displays a negligible hysteresis. $\mu_0 H_{\text{cr}}$ at this temperature exceeds 14 T.

The inset in Fig. 5.94 shows the temperature dependence of the transition field determined from both, the magnetization and acoustic properties, as the average field between ascending and descending branches. The $\mu_0 H_{\text{cr}}$ value obtained from the magnetization at 2 K turns out to be too low. A more correct value is extracted from the $\Delta v/v$ dependence. Overall, H_{cr} increases linearly between 2 and 20 K, where the transition is observed.

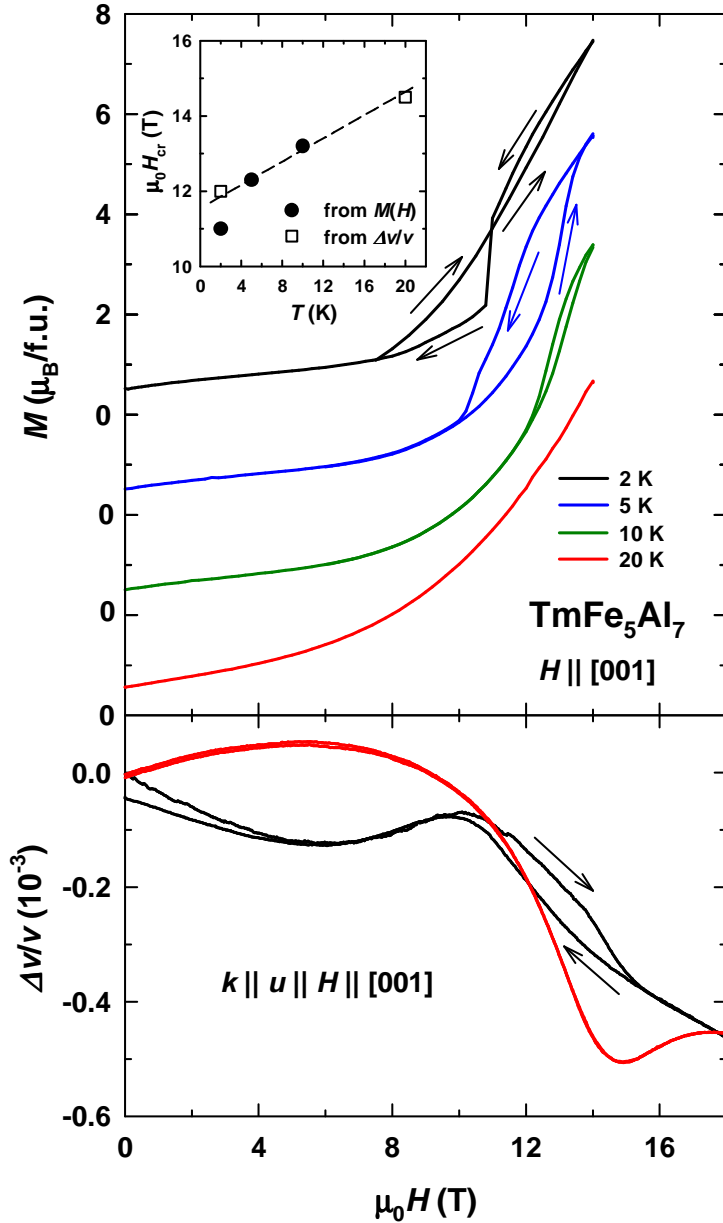


Fig. 5.94. Magnetization (upper panel) and relative sound velocity change (lower panel) as a function of magnetic field applied along the [001] axis of TmFe_5Al_7 between 2 and 20 K. The inset shows the temperature dependence of the critical field of the field-induced transition determined from magnetization and acoustic measurements.

In order to observe all features of the complex magnetization process of TmFe_5Al_7 , the magnetization was measured in pulsed magnetic fields up to 60 T (upper panel in Fig. 5.95). The magnetization for $\mathbf{H} \parallel [100]$ axis changes less fast around 10 T and displays a weak anomaly at about 37 T. At higher fields, the magnetization grows monotonously reaching $11.5 \mu_B/\text{f.u.}$ at 60 T. This value is still far from the forced ferromagnetic state, $M_{\text{ferro}} = M_{\text{Tm}} + M_{\text{Fe}} = 14.5 \mu_B/\text{f.u.}$ The magnetization anomaly at 37 T should reflect the rotation of the Tm and Fe magnetic moments towards the [100] axis since this is the hard magnetization direction in this temperature range. The sound velocity and sound attenuation (not shown) were also

measured along the [100] axis up to 60 T at 2 K. They did not show any anomaly. The anomaly in the magnetization disappears at 40 K.

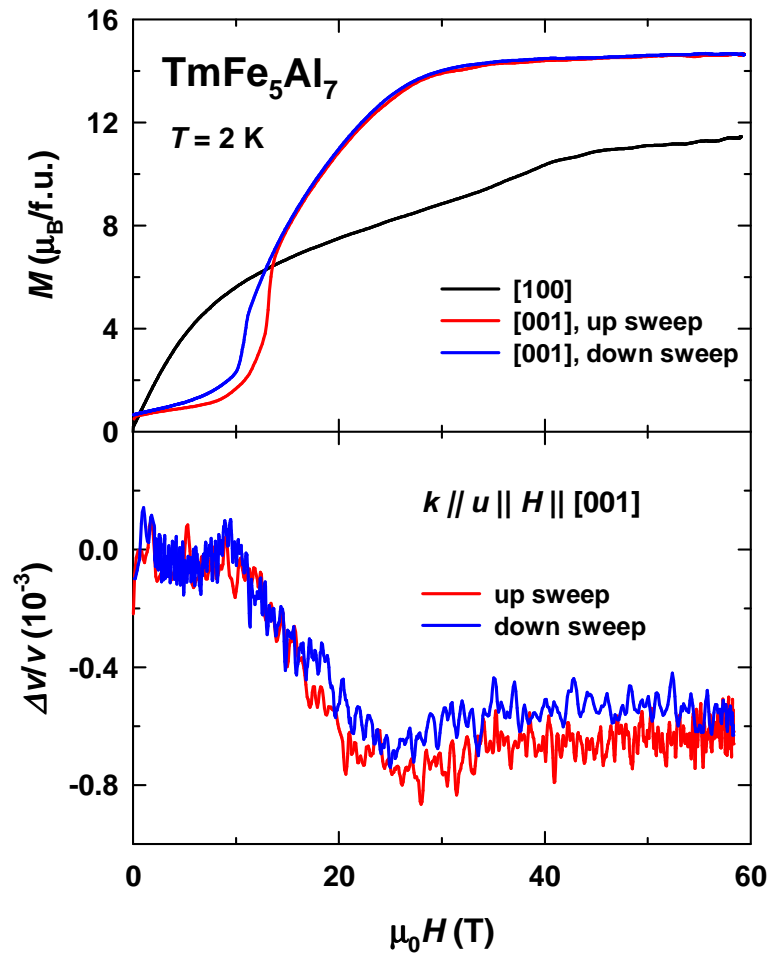


Fig. 5.95. Magnetization (upper panel) and relative sound velocity change (lower panel) in pulsed magnetic fields up to 60 T applied along the [100] and [001] axes of TmFe_5Al_7 at 2 K.

Figure 5.95 also shows that a sharp step-wise anomaly occurs for $\mathbf{H} \parallel [001]$. The magnetization jump amounts to $\Delta M = 6 \mu_B/\text{f.u.}$ Below the magnetization jump, the Tm and Fe magnetic moments are almost antiparallel. The field-induced transition reflects the breaking of this alignment and step-wise rotation of the moments. Above the transition, the magnetization continues to grow as a function of field, as the sublattice moments continue to rotate towards the minimum-energy direction. No other field-induced transitions are observed. The ferromagnetic saturation of $14.5 \mu_B/\text{f.u.}$ is practically reached at about 30 T. The pronounced difference between the magnetization for $\mathbf{H} \parallel [100]$ and [001] points to a high magnetic anisotropy of the compound, whose uniaxial nature is related to the Tm sublattice.

Figure 5.95 also shows the relative sound velocity change of a longitudinal acoustic wave propagating along the [001] axis. The anomaly in $\Delta v/v$ is similar to

that observed in static magnetic fields (see Fig. 5.94). At higher fields, the softening of the acoustic wave continues until the forced ferromagnetic state is reached.

The magnetization and acoustic properties measured for $\mathbf{H} \parallel [001]$ at 20 and 40 K are shown in Fig. 5.96. The field dependence of the magnetization at 20 K (Fig. 5.96a) is very similar to that at 2 K (see Figs. 5.94 and 5.95). In the sound velocity a two-step anomaly appears close to the magnetization jump at about 14 T (Fig. 5.96c). At higher fields in the saturated state no more changes in $\Delta v/v$ are observed. At 40 K, the transition is smeared out and no longer seen in the magnetization (Fig. 5.95b). $\Delta v/v$ displays a change in slope at about 10 T (Fig. 5.96d). Typically, the acoustic properties are very sensitive to magnetic phase transitions, and one might assume that this feature reflects a step-wise rotation of the magnetic moments in TmFe_5Al_7 . A similar situation was observed as well in the $R\text{Fe}_5\text{Al}_7$ compounds with R - Tb, Ho, and Er: hardly any anomaly was seen in the magnetization, whereas the acoustic properties displayed pronounced anomalies (Figs. 5.39, 5.58 and 5.79). However, the feature in $\Delta v/v$ of TmFe_5Al_7 at 40 K (Fig. 5.96d) has a shape different than at lower temperatures, without an abrupt decrease. Moreover, the transition field was found to increase with temperature (see inset in Fig. 5.94), which is not in line with the decrease in $\Delta v/v$ at about 10 T. From these considerations it follows that at 40 K the field-induced transition is no longer observed.

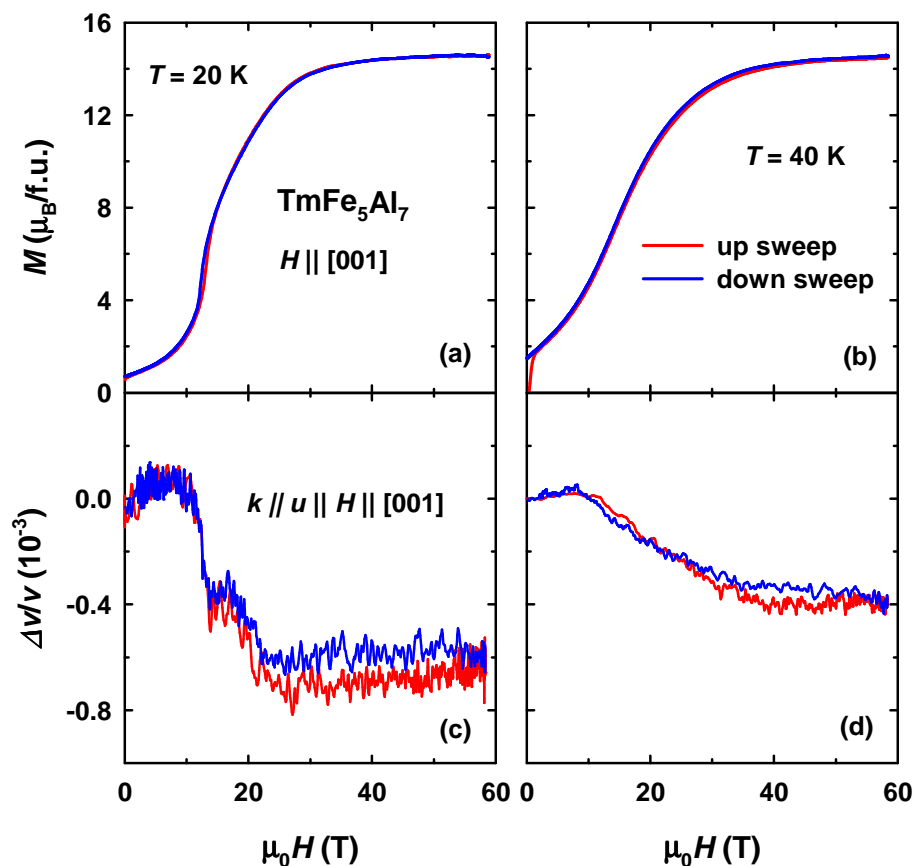


Fig. 5.96. Magnetization (a and b) and relative sound velocity change (c and d) measured in pulsed magnetic fields up to 60 T along the [001] axis of TmFe_5Al_7 at 20 and 40 K.

For completeness, the hysteresis due to domains in TmFe_5Al_7 is discussed. Figure 5.97 shows hysteresis loops measured for $\mathbf{H} \parallel [001]$ between 2 and 40 K. TmFe_5Al_7 , being an easy-axis ferrimagnet at these temperatures, displays strong magnetic hysteresis. The coercive field, $\mu_0 H_c$, is nearly 4 T at 2 K and rapidly falls off with increasing temperature (inset in Fig. 5.97). It should be noted that the loop shape is not rectangular due to the low magnetization and high susceptibility in a magnetic field. As a consequence, the $\mu_0 H_c$ values are much smaller than the loop half width, $\mu_0 H_c^*$, that reflects the field at which the magnetic hysteresis disappears completely. $\mu_0 H_c^*$ is just below 8 T at 2 K and decreases exponentially with temperature according to $H_c^*(T) = H_c^*(0)\exp(-\beta T)$, where $\mu_0 H_c^*(0) = 9.2$ T and $\beta = 0.065$ K⁻¹. Around 50 K, the loop half width is negligible. The strong magnetic hysteresis of the highly-anisotropic ferrimagnet TmFe_5Al_7 with the strong temperature dependence may be related to a high intrinsic coercivity of narrow domain walls [132].

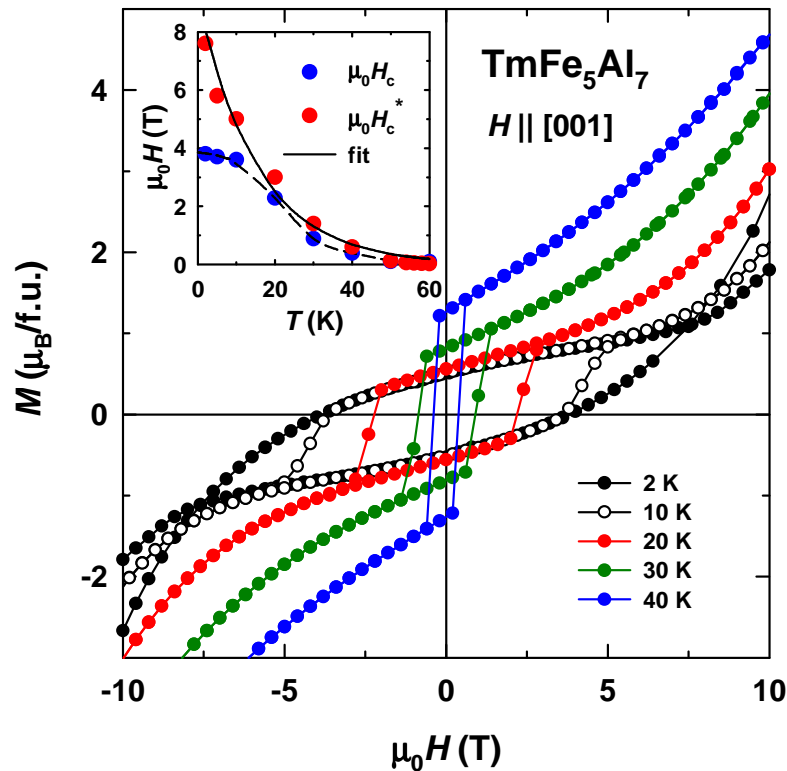


Fig. 5.97. Hysteresis loops for $\mathbf{H} \parallel [001]$ of TmFe_5Al_7 between 2 and 40 K. The inset shows the temperature dependence of the coercivity, H_c , and loop half width, H_c^* . In the inset the dashed line is a guide to the eye, the solid line is the fit $H_c^*(T) = 9.2\exp(-0.065T)$.

5.8. Summary

Figure 5.98 summarizes fundamental magnetic properties of $R\text{Fe}_5\text{Al}_7$ compounds with R - Gd, Tb, Dy, Ho, Er and Tm. Their ferrimagnetic order results in low spontaneous magnetic moments at low temperatures. The M_s variation is consistent with the magnetic moment of the rare-earth component. With increasing temperature M_s values increase, and $M_s(T)$ dependences have a dome-like shape.

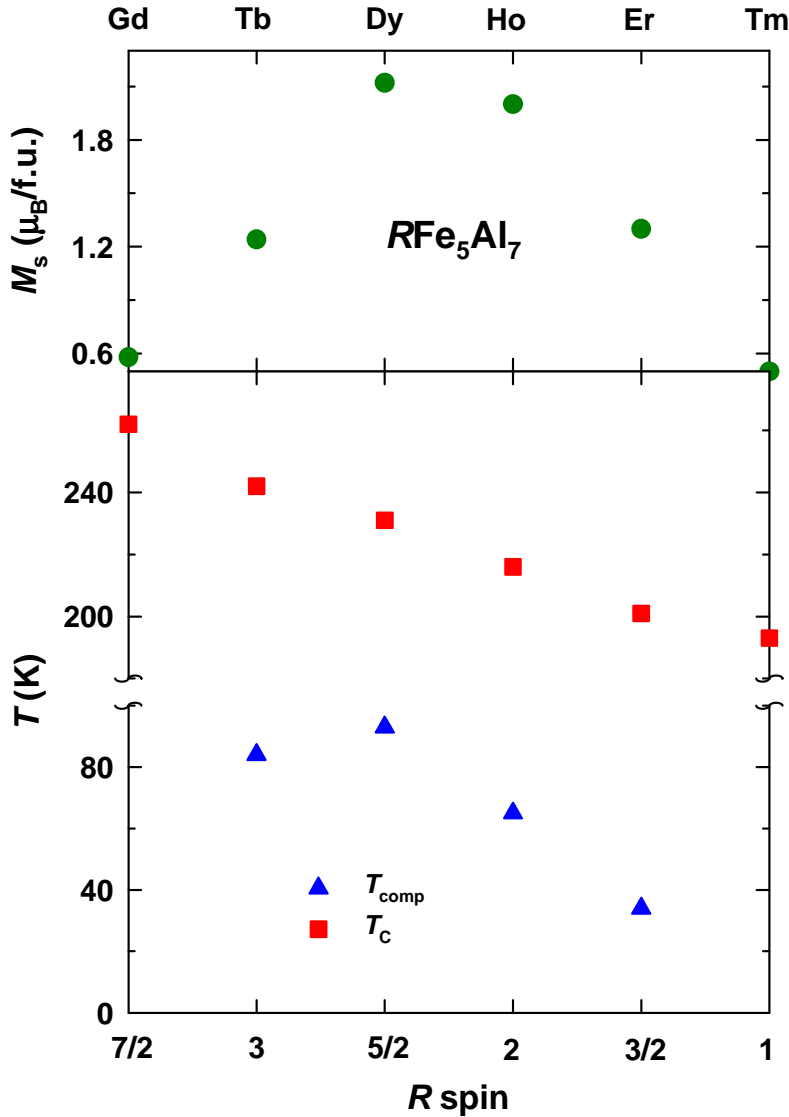


Fig. 5.98. Spontaneous magnetic moment (upper panel) and compensation point and magnetic ordering temperature (lower panel) in $R\text{Fe}_5\text{Al}_7$ with R - Gd, Tb, Dy, Ho, Er, and Tm.

The magnetic moment of the Fe sublattice in $R\text{Fe}_5\text{Al}_7$ is $M_{\text{Fe}} = 7.6 - 8 \mu_B$ at $T = 2$ K. GdFe_5Al_7 and TmFe_5Al_7 do not have a compensation point since $M_R < M_{\text{Fe}}$ at all temperatures in the magnetically-ordered state. In the other systems $M_R > M_{\text{Fe}}$ at low temperatures. With increasing temperature the rare-earth magnetic moment decreases more rapidly than the iron magnetic moment, which leads to a

compensation of the two sublattices. Except for the compound with R - Tb, T_{comp} diminishes as the spin S of the rare-earth component decreases. It is best seen from a comparison between the compounds with R - Dy and Ho. In the ground state both R elements carry the same magnetic moment, $10 \mu_{\text{B}}$. But $S = 5/2$ for Dy and $S = 2$ for Ho. As a result, T_{comp} is higher for DyFe₅Al₇ (93 K) than for HoFe₅Al₇ (65 K). For the compound with R - Tb $T_{\text{comp}} = 84$ K, which is lower than for the compound with R - Dy. The reason is a lower Tb magnetic moment, $9 \mu_{\text{B}}$, in the ground state.

A decrease in the spin of the rare-earth elements results also in a monotonous decrease of the Curie temperatures of RFe₅Al₇. It can be explained mainly by a weakening of the inter-sublattice R -Fe exchange interactions. The intra-sublattice R - R exchange weakens as well but its influence on T_{C} should be much less pronounced.

Since the Fe sublattice is significantly diluted with Al, the Fe-Fe and R -Fe exchange interactions are rather weak. In this situation, a non-collinear magnetic structure can form in zero magnetic field. However, a rather high magnetic moment per Fe atom, $1.5 - 1.6 \mu_{\text{B}}$, obtained for all RFe₅Al₇, practically excludes this hypothesis. It should be noted that in the LuFe₅Al₇ compound a non-collinear magnetic structure was found (Chapter 4). Collinear ferrimagnetic structures appear to be stabilized in RFe₅Al₇ by the inter-sublattice R -Fe exchange interactions.

Non-collinear magnetic structures are formed in an applied magnetic field, which is reflected in an intensive growth of the magnetization after domain wall motion is completed. The magnetization grows the least in GdFe₅Al₇. As the rare-earth spin decreases, the magnetization increases more rapidly. Therefore, this paraprocess can be explained by changes in the relative orientation of the R and Fe magnetic moments. The Fe sublattice might also display a non-collinear magnetic structure but it should contribute less to the growth in the magnetization.

Magnetic moments of RFe₅Al₇ lie in the basal plane of the tetragonal lattice except for TmFe₅Al₇ which is uniaxial at low temperatures. GdFe₅Al₇ was found to display a strong easy-plane anisotropy that originates from the Fe sublattice. A substitution of Gd with rare-earth components having a non-zero orbital momentum significantly strengthens the anisotropy. This was observed for R - Tb, Dy and Ho ($\alpha_J < 0$) and for R - Er and Tm ($\alpha_J > 0$). Unfortunately, a quantitative description of the anisotropy is complicated. The reason is an intensive growth of the magnetization in an applied magnetic field. It renders ineffective the determination of anisotropy constants by existing methods. The anisotropy constants and anisotropy field of the isostructural uranium analogue, UFe₅Al₇, are $K_1 = -6.9$, $K_2 = 0.5 \text{ MJ/m}^3$ and $\mu_0 H_a = 27 \text{ T}$, respectively, at $T = 2 \text{ K}$ [142].

A magnetic anisotropy is observed within the basal plane of all RFe₅Al₇ except for the compound with R - Tm. In GdFe₅Al₇ the presence of the in-plane anisotropy is unusual since it arises exclusively from the Fe sublattice. It is explained by a closeness of the compound to compensation at low temperatures. As a result, the in-plane anisotropy is strongly manifested despite being weak in energy terms. The anisotropy within the basal plane of the compounds with R - Tb, Dy, Ho and Er stems from a large rare-earth contribution. In this connection, it is unexpected that no

in-plane anisotropy was detected in TmFe_5Al_7 since the Tm sublattice should make an equally large contribution. It should be noted that the compound displays a FOMP transition which requires non-zero anisotropy constants at least up to the sixth order. Therefore, it should lead to a non-negligible in-plane anisotropy. However, the transition is not observed at low temperatures but rather appears in a narrow interval $T = 40 - 62$ K. It suggests a complex balance between anisotropy constants, and a more detailed study is necessary.

The magnetic anisotropies between the basal plane and the c axis of $R\text{Fe}_5\text{Al}_7$ can be qualitatively compared on the basis of their anisotropy fields found upon approaching to the magnetic ordering temperatures. For the compound with R - Tb $\mu_0 H_a = 8$ T at $T = 220$ K in the vicinity of $T_C = 242$ K. TbFe_5Al_7 displays the strongest anisotropy in the $R\text{Fe}_5\text{Al}_7$ family. It should be noted that Tb^{3+} ion has the highest value of the second-order Stevens factor, $\alpha_J = -0.01$, among the heavy rare-earth elements with negative α_J [35]. In the sequence Tb, Dy ($\alpha_J = -0.006349$) and Ho ($\alpha_J = -0.002222$) the absolute value of α_J gradually decreases. The anisotropy field decreases from DyFe_5Al_7 ($\mu_0 H_a = 8$ T at $T = 160$ K) to HoFe_5Al_7 ($\mu_0 H_a = 3.6$ T at $T = 160$ K). The sign of α_J changes on going from Ho^{3+} to Er^{3+} . Despite positive second-order Stevens factor for Er^{3+} , ErFe_5Al_7 exhibits an easy-plane anisotropy. The planar contribution is provided by both, the Fe and Er sublattices. The sign of α_J and the type of the Er anisotropy are not in accord. The most likely reason is a small $\alpha_J = 0.00254$ value for Er^{3+} [35]. As a result, a big negative contribution is provided by high-order terms of the Er sublattice. The anisotropy field of ErFe_5Al_7 is lower than those of the compounds with R - Tb, Dy and Ho.

The TmFe_5Al_7 compound presents a special case since at low temperatures it displays an easy-axis anisotropy due to a uniaxial contribution of the Tm sublattice. For Tm^{3+} ion $\alpha_J = 0.01$ is positive and much higher in absolute value as compared to that of Er^{3+} [35]. A competition between a uniaxial Tm anisotropy and a planar Fe anisotropy results in a spin-reorientation transition as the magnetic moments rotate from the c axis to the basal plane.

5.9. Conclusions

1. The $R\text{Fe}_5\text{Al}_7$ compounds with R - Gd, Tb, Dy, Ho, Er and Tm crystallizing in the tetragonal crystal structure of the ThMn_{12} type are ferrimagnets. With increasing atomic number of the rare-earth component the Curie temperature monotonously decreases from $T_C = 262$ K for GdFe_5Al_7 to $T_C = 193$ K for TmFe_5Al_7 mainly due to a weakening of the R -Fe inter-sublattice exchange interaction. The systems with R - Tb, Dy, Ho and Er have a compensation point. Due to a low Fe content a non-collinear structure of the magnetic moments is induced in an applied magnetic field after domain wall motion is completed.

2. Magnetic moments of the $R\text{Fe}_5\text{Al}_7$ compounds with R - Gd, Tb, Dy, Ho and Er lie in the basal plane. In GdFe_5Al_7 a strong anisotropy originating from the Fe sublattice was found between the c axis and the basal plane. The magnetic anisotropy is significantly strengthened in the compounds with R elements having a non-zero orbital momentum due to a strong single-ion contribution. The Tb, Dy, Ho and Er sublattices also make a planar contribution to the anisotropy. A change in the sign of the second-order Stevens factor upon going from R - Ho to R - Er does not modify the anisotropy type.

3. The TmFe_5Al_7 compound displays an easy-axis anisotropy at low temperatures. The second-order Stevens factor is positive for R - Tm, and the Tm sublattice makes a uniaxial contribution to the anisotropy. It competes against the planar Fe anisotropy, which results in a spin-reorientation transition as the magnetic moments rotate from the c axis to the basal plane.

4. Anisotropy was also found within the basal plane of the $R\text{Fe}_5\text{Al}_7$ compounds with R - Gd, Tb, Dy, Ho and Er. Despite being weak in GdFe_5Al_7 , it can be detected due to a closeness of the compound to compensation at low temperatures. In other systems the in-plane anisotropy is much stronger since it originates from the rare-earth sublattice. In TmFe_5Al_7 no anisotropy was detected within the basal plane, presumably due to a complex balance between low- and high-order anisotropy constants.

5. A quantitative description of the magnetocrystalline anisotropy of the $R\text{Fe}_5\text{Al}_7$ compounds with R - Gd, Tb, Dy, Ho, Er and Tm is complicated. The anisotropy can be estimated on the basis of anisotropy fields determined upon approaching magnetic ordering temperatures. It indicates that TbFe_5Al_7 displays the strongest anisotropy. The anisotropy of the other compounds is weaker, in accordance with a decrease in the absolute value of the second-order Stevens factor of the rare-earth components.

6. With increasing temperature the TbFe_5Al_7 compound displays a spin-reorientation transition within the basal plane from $[100]$ to $[110]$ in the vicinity of the compensation point $T_{\text{comp}} = 84$ K. Elastic properties exhibit anomalies in the vicinity of the transition.

7. Field-induced magnetic phase transitions occur in $R\text{Fe}_5\text{Al}_7$ compounds with rare-earth components having a non-zero orbital momentum. In fields up to 60

T magnetization jumps are observed along basal plane directions of TbFe_5Al_7 , DyFe_5Al_7 , HoFe_5Al_7 and ErFe_5Al_7 and along the c axis in TmFe_5Al_7 . The jumps are controlled by a balance between the R -Fe inter-sublattice exchange interaction, magnetocrystalline anisotropy and Zeeman energy. Most of the jumps can be explained within the model for a ferrimagnet with weak inter-sublattice exchange interaction. The strength of this interaction can be determined from the field-induced phase transitions.

8. Highly-anisotropic $R\text{Fe}_5\text{Al}_7$ compounds with R - Tb, Dy, Ho, Er and Tm display strong magnetic hysteresis at low temperatures. The coercive field reaches several Tesla at $T = 2$ K and exponentially decreases with increasing temperature. The strong magnetic hysteresis with a sharp temperature dependence is related to narrow domain walls of the highly-anisotropic ferrimagnets.

9. The strong magnetic hysteresis is the reason for a strong thermal hysteresis of the $R\text{Fe}_5\text{Al}_7$ compounds with R - Tb, Dy, Ho, Er near their compensation point. In a low magnetic field a high coercivity prevents domain structure from changing upon passing through the compensation point. As a result, the total magnetization and the applied magnetic field become antiparallel to each other.

References

- [1] K. Strnat, G. Hoffer, J. Olson, W. Ostertag, J.J. Becker, *J. Appl. Phys.* 38 (1967) 1001.
- [2] M. Sagawa, S. Fujimura, M. Togawa, Y. Matsuura, *J. Appl. Phys.* 55 (1984) 2083.
- [3] K.H.J. Buschow, in: K.H.J. Buschow (Ed.), *Handbook of Magnetic Materials*, vol. 10, Elsevier, Amsterdam, 1997, p. 463.
- [4] K.H.J. Buschow, in: E.P. Wohlfarth and K.H.J. Buschow (Eds.), *Handbook of Magnetic Materials*, vol. 4, Elsevier, Amsterdam, 1988, p. 1.
- [5] H.-S. Li, J.M.D. Coey: in: K.H.J. Buschow (Ed.), *Handbook of Magnetic Materials*, vol. 6, Elsevier, Amsterdam, 1991, p. 1.
- [6] J.J.M. Franse, R.J. Radwański, in: K.H.J. Buschow (Ed.), *Handbook of Magnetic Materials*, vol. 7, Elsevier, Amsterdam, 1993, p. 307.
- [7] N.H. Duc, in: K.A. Gschneidner, Jr. and L. Eyring (Eds.), *Handbook on the Physics and Chemistry of Rare Earths*, vol. 24, Elsevier, Amsterdam, 1997, p. 339.
- [8] A. Chełkowski, E. Talik, J. Szade, J. Heimann, A. Winiarska, A. Winiarski, *Physica B* 168 (1991) 149.
- [9] P. Gaczyński, F.G. Vagizov, W. Suski, B. Kotur, K. Wochowski, H. Drulis, *J. Magn. Magn. Mater.* 214 (2000) 37.
- [10] P. Gaczyński, F.G. Vagizov, W. Suski, B. Kotur, W. Iwasieczko, H. Drulis, *J. Magn. Magn. Mater.* 225 (2001) 351.
- [11] H. Misiorek, J. Stępień-Damm, W. Suski, E. Talik, B.Y. Kotur, V.M. Dmitriev, *J. Alloys Comp.* 363 (2004) 81.
- [12] B. Andrzejewski, A. Kowalczyk, T. Toliński, *Acta Phys. Pol. A* 109 (2006) 561.
- [13] T. Toliński, B. Andrzejewski, A. Kowalczyk, G. Chełkowska, A. Szlaferek, J. Frąckowiak, *J. Phys. Chem. Solids* 67 (2006) 751.
- [14] W. Schäfer, W. Kockelmann, S. Fredo, I. Halevy, J. Gal, *J. Magn. Magn. Mater.* 177–181 (1998) 808.
- [15] A.V. Andreev, *Physica B* 404 (2009) 2978.
- [16] W. Kockelmann, W. Shafer, G. Will, P. Fischer, J. Gal, *J. Alloys Comp.* 207–208 (1994) 311.
- [17] P. Schobinger-Papamantellos, K.H.J. Buschow, C. Ritter, *J. Magn. Magn. Mater.* 186 (1998) 21.
- [18] J.A. Paixão, M.R. Silva, J.C. Waerenborgh, A.P. Gonçalves, G.H. Lander, P.J. Brown, M. Godinho, P. Burlet, *Phys. Rev. B* 63 (2001) 054410.
- [19] I. Felner, I. Nowik, K. Baberschke, G.J. Nieuwenhuys, *Solid State Commun.* 44 (1982) 691.
- [20] I. Felner, I. Nowik, M. Seh, *J. Magn. Magn. Mater.* 38 (1983) 172.
- [21] S. Legvold, in: E.P. Wohlfarth (Ed.), *Handbook of Magnetic Materials*, vol. 1, Elsevier, Amsterdam, 1980, p. 183.

- [22] B.N. Harmon, A.J. Freeman, *Phys. Rev. B* 10 (1974) 1979.
- [23] S. Blundell, *Magnetism in Condensed Matter* (Oxford University Press, Oxford, 2003).
- [24] K.H.J. Buschow, F.R. de Boer, *Physics of Magnetism and Magnetic Materials* (Kluwer Academic Publishers, New York, 2003).
- [25] E.P. Wohlfarth, in: E.P. Wohlfarth (Ed.), *Handbook of Magnetic Materials*, vol. 1, Elsevier, Amsterdam, 1980, p. 1.
- [26] T. Moriya, *Spin Fluctuations in Itinerant Electron Magnetism*, Springer Series in Solid State Sciences, vol. 56, Springer-Verlag, Berlin, 1985, p. 247.
- [27] C. Kittel, *Introduction to Solid State Physics* (John Wiley and Sons, Inc., New York, 1996).
- [28] J. Stöhr, H.C. Siegmann, *Magnetism From Fundamentals to Nanoscale Dynamics* (Springer-Verlag, Berlin, Heidelberg, 2006).
- [29] J.C. Slater *Phys. Rev.* 36 (1930) 57.
- [30] C. Herring, in: G.T. Rado and H. Suhl (Eds.) *Magnetism*, Vol. IIB, Academic Press, New York, 1966, p. 1.
- [31] I.A. Campbell, *J. Phys. F: Met. Phys.* 2 (1972) L47.
- [32] Hutchings, *Solid State Phys.* 16 (1964) 227.
- [33] A.J. Freeman, J.P. Desclaux, *J. Magn. Magn. Mater.* 12 (1979) 11.
- [34] H.B. Callen, E. Callen, *J. Phys. Chem. Solids* 27 (1966) 1271.
- [35] M.D. Kuz'min, A.M. Tishin, in: K.H.J. Buschow (Ed.), *Handbook of Magnetic Materials*, vol. 17, Elsevier, Amsterdam, 2008, p. 149.
- [36] W.D. Corner, W.C. Roe, K.N.R. Taylor, *Proc. Phys. Soc.* 80 (1962) 927.
- [37] A.V. Deryagin, E.N. Tarasov, A.V. Andreev, V.N. Moskalev, A.I. Kozlov, *JETP Lett.* 39 (1984) 629.
- [38] D. Givord, H.S. Li, R. Perrier de la Bâthie, *Solid State Comm.* 51 (1984) 857.
- [39] H.B.G. Casimir, J. Smit, U. Enz, J.F. Fast, H.P.J. Wijn, E.W. Gorter, A.J.W. Duyvesteyn, J.D. Fast, J.J. de Jong, *J. Phys. Rad.* 20 (1959) 360.
- [40] W. Sucksmith, J.E. Thompson, *Proc. Roy. Soc. London A* 225 (1954) 362.
- [41] G. Asti, in: K.H.J. Buschow and E.P. Wohlfarth (Eds.), *Handbook of Magnetic Materials*, vol. 5, Elsevier, Amsterdam, 1990, p. 397.
- [42] G. Asti, F. Bolzoni, *J. Magn. Magn. Mater.* 20 (1980) 29.
- [43] B. Lüthi, *Physical Acoustics in the Solid State* (Springer, Heidelberg, 2007).
- [44] B. Lüthi, T.J. Moran, R.J. Pollina, *J. Phys. Chem. Solids* 31 (1970) 1741.
- [45] V.N. Kashcheev, *Phys. Lett. A* 25 (1967) 71.
- [46] H.S. Bennett, *Phys. Rev.* 185 (1969) 801.
- [47] T.J. Moran, B. Lüthi, *Phys. Lett. A* 29 (1969) 665.
- [48] A.E. Clark, in: E.P. Wohlfarth (Ed.), *Handbook of Magnetic Materials*, vol. 1, Elsevier, Amsterdam, 1980, p. 531.

- [49] O. Mathon, F. Baudelet, J. P. Itié, A. Polian, M. d'Astuto, J. C. Chervin, S. Pascarelli, *Phys. Rev. Lett.* 93 (2004) 255503.
- [50] V. Iota, J.-H. Park Klepeis, C.-S. Yoo, J. Lang, D. Haskel, G. Srajer, *Appl. Phys. Lett.* 90 (2007) 042505.
- [51] K. Shimizu, T. Kimura, S. Furomoto, K. Takeda, K. Kontani, Y. Onuki, K. Amaya, *Nature (London)* 412 (2001) 316.
- [52] N.D. Lang, H. Ehrenreich, *Phys. Rev.* 168 (1968) 605.
- [53] A. Jayaraman, in: K.A. Gschneidner, Jr. and L. Eyring (Eds.), *Handbook on the Physics and Chemistry of Rare Earths*, vol. 1, Elsevier, Amsterdam, 1978, p. 707.
- [54] D.B. McWhan, A.L. Stevens, *Phys. Rev.* 139 (1965) A682.
- [55] L.B. Robinson, F. Milstein, A. Jayaraman, *Phys. Rev.* 134 (1964) A187.
- [56] A. Jayaraman, R.C. Sherwood, *Phys. Rev. Lett.* 12 (1964) 22.
- [57] Z. Arnold, O. Isnard, H. Mayot, Y. Skorokhod, J. Kamarád, M. Míšek, *Solid State Comm.* 152 (2012) 1164.
- [58] M.R. Ibarra, L. Morellon, P.A. Algarabel, C. Marquina, Z. Arnold, J. Kamarád, *J. Magn. Magn. Mater.* 104-107 (1992) 1371.
- [59] W. Suski, in: K.A. Gschneidner Jr., L. Eyring (Eds.), *Handbook on the Physics and Chemistry of Rare Earths*, vol. 22, Elsevier, Amsterdam, 1996, p. 143.
- [60] F.J. Cadieu, H. Hegde, A. Navarathna, R. Rani, K. Chen, *Appl. Phys. Lett.* 59 (1991) 875.
- [61] D. Wang, S.H. Liou, P. He, D.J. Sellmyer, G.C. Hadjipanayis, Y. Zhang, *J. Magn. Magn. Mater.* 124 (1993) 62.
- [62] J.V. Florio, R.E. Rundle, A.I. Snow, *Acta Cryst.* 5 (1952) 449.
- [63] K.H.J. Buschow, *J. Appl. Phys.* 63 (1988) 3130.
- [64] R. Verhoef, F.R. de Boer, Z.D. Zhang, K.H.J. Buschow, *J. Magn. Magn. Mater.* 75 (1988) 319.
- [65] P. Stefański, A. Wrzeciono, *J. Magn. Magn. Mater.* 82 (1989) 125.
- [66] Q. Li, Y. Lu, R. Zhao, O. Tegus, F. Yang, *J. Appl. Phys.* 70 (1991) 6116.
- [67] D.B. de Mooij, K.H.J. Buschow, *J. Less.-Common. Met.* 136 (1988) 207.
- [68] K.H.J. Buschow, *J. Magn. Magn. Mater.* 100 (1991) 79.
- [69] O. Moze, R.M. Ibberson, K.H.J. Buschow, *J. Phys.: Condens. Matter.* 2 (1990) 1677.
- [70] I. Felner, I. Nowik, *J. Phys. Chem. Solids* 39 (1978) 951.
- [71] P. Schobinger-Papamantellos, K.H.J. Buschow, I. Hagemusa, F.R. de Boer, C. Ritter, F. Fauth, *J. Magn. Magn. Mater.* 202 (1999) 410.
- [72] G.M. Kalvius, F.E. Wagner, I. Halevy, J. Gal, *Hyperfine Interact.* 151/152 (2003) 195.
- [73] M. Kuznietz, A.P. Gonçalves, J.C. Waerenborgh, M. Almeida, *Phys. Rev. B.* 60 (1999) 9494.
- [74] J.C. Waerenborgh, P. Sakamakha, O. Sologub, S. Sérgio, M. Godinho, A.P. Gonçalves, M. Almeida, *J. Alloys Compd.* 323-324 (2001) 78.

- [75] S. Sérgio, J. C. Waerenborgh, M. Almeida, M. Godinho, J. Magn. Magn. Mater. 265 (2003) 33.
- [76] F.G. Vagizov, W. Suski, K. Wochowski, H. Drulis, J. Alloys Compd. 219 (1995) 271.
- [77] J.C. Waerenborgh, A.P. Gonçalves, M. Almeida, Solid State Commun. 110 (1999) 369.
- [78] S. Sérgio, J.C. Waerenborgh, A.P. Gonçalves, M. Almeida, M. Godinho, J. Magn. Magn. Mater. 302 (2006) 282.
- [79] W. Schäfer, W. Kockelmann, G. Will, P. Fischer, J. Gal, J. Alloys Compd. 225 (1995) 440.
- [80] K. Rećko, M. Biernacka, L. Dobrzyński, K. Perzyńska, D. Satuła, K. Szymański, J. Waliszewski, W. Suski, K. Wochowski, G. André, F. Bourée, J. Phys.: Condens. Matter. 9 (1997) 9541.
- [81] W. Schäfer, W. Kockelmann, G. Will, P. Fischer, J. Gal, J. Alloys Compd. 207/208 (1994) 316.
- [82] I. Felner, M. Seh, M. Rakavy, I. Nowik, J. Phys. Chem. Solids. 42 (1981) 369.
- [83] I. Nowik, I. Felner, M. Seh, J. Magn. Magn. Mater. 15-18 (1980) 1215.
- [84] E.S. Popiel, W. Zarek, M. Tuszyński, Hyperfine Interact. 51 (1989) 975.
- [85] I. Felner, I. Nowik, J. Magn. Magn. Mater. 54-57 (1986) 163.
- [86] I. Felner, I. Nowik, J. Magn. Magn. Mater. 58 (1986) 169.
- [87] I. Felner, I. Nowik, J. Magn. Magn. Mater. 74 (1988) 31.
- [88] M. Angst, A. Kreyssig, Y. Janssen, J.-W. Kim, L. Tan, D. Wermeille, Y. Mozharivskiy, A. Kracher, A.I. Goldman, P.C. Canfield, Phys. Rev. B 72 (2005) 174407.
- [89] M.O. Bargouth, G. Will, K.H.J. Buschow, J. Magn. Magn. Mater. 6 (1977) 129.
- [90] K.H.J. Buschow, A.M. van der Kraan, Physica B+C 86-88 (1977) 93.
- [91] K.H.J. Buschow, A.M. van der Kraan, J. Phys. F. 8 (1978) 921.
- [92] J.A. Paixão, S. Langridge, S.A. Sørensen, B. Lebech, A.P. Gonçalves, G.H. Lander, P.J. Brown, P. Burlet, E. Talik, Physica B 234-236 (1997) 614.
- [93] J.A. Paixão, M. Ramos Silva, S.A. Sørensen, B. Lebech, G.H. Lander, P.J. Brown, S. Langridge, E. Talik, A.P. Gonçalves, Phys. Rev. B 61 (2000) 6176.
- [94] S. Sérgio, L.C.J. Pereira, M. Godinho, J.C. Waerenborgh, Intermetallics 16 (2008) 1219.
- [95] N.P. Duong, E. Brück, F.R. de Boer, K.H.J. Buschow, Physica B 294–295 (2001) 212.
- [96] N.P. Duong, E. Brück, F.R. de Boer, K.H.J. Buschow, J. Alloys Compd. 338 (2002) 213.
- [97] H. Shaked and M. Melamud, private communication.
- [98] S.A. Nikitin, I.S. Tereshina, V.N. Verbetsky, A.A. Salamova, J. Alloys Compd. 316 (2001) 46.

- [99] C. Abadía, P.A. Algarabel, B. García-Landa, M.R. Ibarra, A. del Moral, N.V. Kudrevatykh, P.E. Markin, *J. Phys.: Condens. Matter.* 10 (1998) 349.
- [100] A.V. Andreev, V. Sechovský, N.V. Kudrevatykh, S.S. Sigaev, E.N. Tarasov, *J. Less-Common Met.* 144 (1988) L21.
- [101] L.A. Aslanov, G.V. Fetisov, J.A.K. Howard, in: J.A.K. Howard (Ed.), *Crystallographic Instrumentation* (Oxford University Press, Oxford, 1998).
- [102] J. Rodríguez-Carvajal, L. Chapon, FULLPROF Suite, Version 2.0, 2008.
- [103] H.M. Rietveld, *J. Appl. Cryst.* 2 (1969) 65.
- [104] Y. Skourski, M.D. Kuz'min, K.P. Skokov, A.V. Andreev, J. Wosnitza, *Phys. Rev. B* 83 (2011) 214420.
- [105] G.P. Felscher, R. Kleb, *Europhys. Lett.* 36 (1996) 455.
- [106] J. Kamarád, Z. Machátová, Z. Arnold, *Rev. Sci. Instrum.* 75 (2004) 5022.
- [107] A.M. Gurevich, V.M. Dmitriev, V.N. Eropkin, L.A. Ishchenko, N.N. Prentslau, L.V. Shlyk, *Low Temp. Phys.* 25 (1999) 10.
- [108] D.I. Gorbunov, A.V. Andreev, M.D. Kuz'min, *Phys. Rev. B* 86 (2012) 024407.
- [109] D.I. Gorbunov, A.V. Andreev, M.D. Kuz'min, *J. Korean Phys. Soc.* 62 (2013) 1517.
- [110] D.I. Gorbunov, A.V. Andreev, *J. Alloys Compd.* 577 (2013) 203.
- [111] D.I. Gorbunov, A.V. Andreev, N.V. Mushnikov, *J. Alloys Compd.* 514 (2012) 120.
- [112] D.I. Gorbunov, A.V. Andreev, *Solid State Phen.* 194 (2013) 54.
- [113] D.I. Gorbunov, A.V. Andreev, *J. Alloys Compd.* 556 (2013) 109.
- [114] D.I. Gorbunov, S. Yasin, A.V. Andreev, N.V. Mushnikov, Ye. Rozenfel'd, Y. Skourski, S. Zherlitsyn, J. Wosnitza, submitted for publication.
- [115] F.R. de Boer, Ying-Kai Huang, D.B. de Mooij, K.H.J. Buschow, *J. Less-Common Met.* 135 (1987) 199.
- [116] A.V. Andreyev, A.N. Bogatkin, N.V. Kudrevatykh, S.S. Sigaev, Ye.N. Tarasov, *Phys. Met. Metallogr.* 68 (1989) 68.
- [117] A.V. Andreev, Ye.V. Scherbakova, T. Goto, W. Suski, *J. Alloys Comp.* 198 (1993) 43.
- [118] A.V. Andreev, V. Sechovský, N.V. Kudrevatykh, S.S. Sigaev, E.N. Tarasov, *J. Less-Common Met.* 144 (1988) L21.
- [119] G. Asti, S. Rinaldi, *J. Appl. Phys.* 45 (1974) 3600.
- [120] M. Loewenhaupt, P. Tils, K.H.J. Buschow, R.S. Eccleston, *J. Magn. Magn. Mater.* 152 (1996) 10.
- [121] A.V. Andreev, *J. Alloys Compd.* 475 (2009) 13.
- [122] A.V. Andreev, M.I. Bartashevich, T. Goto, S.M. Zadvorkin, *J. Alloys Comp.* 262-263 (1997) 467.
- [123] J.P. Liu, F.R. de Boer, P.F. de Châtel, R. Coehoorn, K.H.J. Buschow, *J. Magn. Magn. Mater.* 132 (1994) 159.

- [124] M.D. Kuz'min, Y. Skourski, K.P. Skokov, K.-H. Müller, *Phys. Rev. B* 75 (2007) 184439.
- [125] Y. Skourski, M.D. Kuz'min, K.P. Skokov, A.V. Andreev, J. Wosnitza, *Phys. Rev. B* 83 (2009) 214420.
- [126] E.A. Tereshina, I.S. Tereshina, M.D. Kuz'min, Y. Skourski, M. Doerr, O.D. Chistyakov, I.V. Telegina, H. Drulis, *J. Appl. Phys.* 111 (2012) 093923.
- [127] M.D. Kuz'min, *J. Magn. Magn. Mater.* 323 (2011) 1068.
- [128] M.D. Kuz'min, L.M. García, M. Artigas, J. Bartolomé, *Phys. Rev. B* 54 (1996) 4093.
- [129] Bo-Ping Hu, Hong-Shuo Li, J.M.D. Coey, J.P. Gavigan, *Phys. Rev. B* 41 (1990) 2221.
- [130] L.M. García, J. Bartolomé, P.A. Algarabel, M.R. Ibarra, M.D. Kuz'min, *J. Appl. Phys.* 73 (1993) 5908.
- [131] A.V. Andreev, M.I. Basrtashevich, N.V. Kudrevatykh, S.M. Razgonyaev, S.S. Sigaev, E.N. Tarasov, *Physica B* 167 (1990) 139.
- [132] H.R. Hilzinger, H. Kronmüller, *Phys. Status Solidi B* 54 (1972) 593.
- [133] A.V. Andreev, S.M. Zadvorkin, *Physica B* 225 (1996) 237.
- [134] A.V. Andreev, S.M. Zadvorkin, *Philos. Mag.* 77 (1998) 147.
- [135] A. Sarkis, E. Callen, *Phys. Rev. B* 26 (1982) 3870.
- [136] D.I. Gorbunov, A.V. Andreev, Y. Skourski, M.D. Kuz'min, *J. Alloys Compd.* 553 (2013) 358.
- [137] J.H.V.J. Brabers, G.F. Zhou, J.H.P. Colpa, K.H.J. Buschow, F.R. de Boer, *Physica B* 202 (1994) 1.
- [138] A.K. Zvezdin, in: K.H.J. Buschow (Ed.), *Handbook of Magnetic Materials*, vol. 9, Elsevier, Amsterdam, 1995, p. 405.
- [139] A.V. Andreev, A.N. Bogatkin, N.V. Kudrevatykh, S.S. Sigaev, Ye.N. Tarasov, *Phys. Met. Metallogr.* 68 (1) (1989) 68.
- [140] A.S. Ermolenko, E.V. Rozenfel'd, Yu.P. Irkhin, V.V. Kelarev, A.F. Rozhda, S.K. Sidorov, A.N. Pirogov, A.P. Vokhmyanin, *Zh. Eksp. Teor. Fiz.* 69 (1975) 1743.
- [141] D.M. Clatterbuck, K.A. Gschneidner Jr., *J. Magn. Magn. Mater.* 207 (1999) 78.
- [142] A.V. Andreev, E.A. Tereshina, E. Šantavá, J. Šebek, K. Koyama, K. Watanabe, *J. Alloys Compd.* 492 (2010) 52.